# AN ABSTRACT OF THE DISSERTATION OF

Tyler J. Deboodt for the degree of Doctor of Philosophy in Civil Engineering presented on June 1, 2018.

Title: Investigation of x-ray computed tomography for portland cement phase quantification

Abstract approved: _____
Jason H. Ideker O. Burkan Isgor

Cementitious materials are often characterized through the use of advanced analytical techniques to understand the macro-, micro-, and nano-scale properties, including phase formation during hydration, and subsequent potential deterioration mechanisms which can affect service life. A major limitation with using such analytical techniques to quantify solid phases in cementitious systems is that many techniques are destructive in nature. If one wants to monitor changes over time, samples must be extracted from different locations of the same sample, or from a different sample, at different times. This limitation can hinder the ability continually monitor the desired property. One method to extract quantifiable information non-destructively is x-ray computed tomography (x-ray CT). X-ray CT is a non-destructive, non-contact technique that uses computer-processed x-rays to produce three-dimensional tomographic images of specific zones of a sample. This technique has been successfully used in many different aspects of research, including medicine, geo-sciences, and materials science. The use of x-ray CT has been applied to cementitious systems but has been predominately limited to qualitative or semi-quantitative analysis. Quantification of cementitious properties has been hindered through two means, spatial resolution and low contrast between solid phases, including the unhydrated and hydrated phases. This low contrast has often led to quantification of void space within the cementitious sample. The work presented in this dissertation addresses methods to resolve the expected low contrast in x-ray CT images on cementitious and the potential for segmentation of the four main hydration products found in portland cement. This was achieved through an investigation of different image segmentation algorithms and a creative use of contrast agents to be bound into specific hydration

products using a synchrotron x-ray CT. Advancements in x-ray CT optics and data collection are continually improving image resolution, therefore it is not discussed in this dissertation.

Published literature on the use of x-ray CT in cementitious materials often does not include a thorough description of the image processing procedures used for analysis. The use of arbitrary, histogram-based threshold values can lead to biased segmentation and misclassification of the voxels in the image volume. Presented in this dissertation is a method to deconstruct the greyscale values of a histogram into individual Gaussian curves in an unbiased manner. The greyscale values of laboratory synthesized calcium-silicate-hydrate (C-S-H), calcium hydroxide (CH), monosulfate (AFm), and ettringite (AFt) were determined to provide a baseline for threshold values. Pure phase, binary, and quaternary mixture samples of the four aforementioned phases were studied. A Gaussian probability density function was applied to each phase and proportioned to the known mass of each phase in the binary and quaternary mixtures. Intersections of the Gaussian curves was determined as the threshold value. Quantification of binary mixtures was successfully done with exception to C-S-H and AFm mixtures. Low contrast between the phases was observed leading to difficulties accurately quantifying such mixtures. Similar success was observed in quaternary mixtures of phases. However, difficulties in segmentation were compounded segmenting AFm, C-S-H, and CH in these mixtures.

One method to resolve low contrast is to incorporate the use of contrast agents. Success in the medical field, and other limited successes in geo-sciences, provided the motivation to determine methods to incorporate contrast agents into portland cement hydrates. Literature reports a myriad of ions which can be incorporated into the structure of C-S-H, AFm, and AFt through various mechanisms, including substitution and absorption. Due to the limitations in segmenting AFm and C-S-H in their pure form, investigations for incorporating contrast agents to improve segmentation was done. Iodine was selected as the contrast agent to be substituted for the sulfate ion in AFm. Dual energy scans above and below the absorption edge of iodine was done, and the use of image subtraction allowed for quick and accurate segmentation of the C-S-H and modified AFm phases. However, difficulties segmenting C-S-H and CH were observed in quaternary mixtures of AFt, CH, C-S-H, and a modified AFm using the Gaussian deconstruction method to determine threshold values for segmentation.

Lastly, due to the difficulties achieving consistent results during segmentation when using histogram-based threshold values, a study determining the feasibility of local segmentation algorithms was done on binary and quaternary mixtures of the four phases. These algorithms often result in more desirable results by accounting for the spatial arrangement of the greyscale values throughout the image volume. Two local segmentation algorithms, watershed and Bayesian Markov random fields, were compared to the Gaussian deconstruction method. Results indicated both local segmentation algorithms resulted in more accurate quantification of the four phases, thus providing promise for future applications to hydrating portland cement.

# Investigation of x-ray computed tomography for portland cement phase quantification

by
Tyler J. Deboodt

A DISSERTATION

submitted to

Oregon State University

in partial fulfillment of
the requirements for the
degree of

Doctor of Philosophy

Presented June 1, 2018
Commencement June 2018

Doctor of Philosophy dissertation of Tyler J. Deboodt presented on June 1, 2018

APPROVED:

Co-Major Professor, representing Civil Engineering

Co-Major Professor, representing Civil Engineering

Head of the School of Civil and Construction Engineering

Dean of the Graduate School

I understand that my dissertation will become part of the permanent collection of Oregon State University libraries. My signature below authorizes release of my dissertation to any reader upon request.

Tyler J. Deboodt, Author

# ACKNOWLEDGEMENTS

Where to begin. So many people have influenced and encouraged me during my time as a graduate student at Oregon State University. The work presented in this dissertation could not have been completed without the effort and advice of so many people. My success is owed to an amazing group of friends, mentors, and colleagues. If it were not for all of these people and encouragement during the experimental failures and difficult classes this dissertation and the experimental work presented herein would never have been completed. This list is long, and I will try my best to include everyone. I greatly apologize if I unintentionally left anyone important off of this list.

First and foremost, I want to thank my family for their unending support during my seemingly never ending tenure as a student. The support and encouragement I have received during my graduate studies has meant the world to me. Thank you from the bottom of my heart for everything you have done for me.

Thank you to Dr. Jennifer Tanner, at the University of Wyoming, for taking me under your wing as an undergraduate to show me that creating concrete is not as miserable as many of the days we had creating concrete in the lab at Wyoming. There were plenty of days we swore concrete off after moving an unending supply of aggregates and cement by hand to the Engineering Building just to move them again and again. Your caring nature, teaching style, expertise (I still teach students your concrete finishing technique), trust, and support allowed me to be successful as a graduate student. It is always a pleasure to catch up.

To all of the past, present, and future, members of the Corvallis Mountain Rescue Unit. I owe so much to all of you. I honestly did not know what I was getting myself into when I went to my first meeting in January 2012. I was looking for some guidance as a new climber and found so much more. Thank you for all of the good times and making the shitty times bearable. It is amazing what a group of dedicated individuals that care about a stranger, who has found themselves in a bad situation, in near freezing temperatures, with a driving rain can accomplish. Thank you to all for trusting your life in my hands on trainings and missions to better serve those that really need someone like you. I will always remember the times we have shared together.

Thank you to the friends I have met along the way. While many of my colleagues have become great friends, there are people I want to share my appreciation for. John Stevenson and Anna Pakenham-Stevenson, thank you for teaching me the ways of backcountry skiing. It can be a hard sell to suggest skiing (walking) uphill for hours in bad weather only to scratch down an icy or rocky slope, have a good time, and do it again the next week. While I may not have fully embraced your philosophy of "if you can't ski it, it isn't worth going up," but it is always in the back of my head when I am trip planning. Todd Lemein, Joe McCormick, and Landon Harman, thanks for all of the great times we have had climbing in the mountains. Mountaineering is such a hard thing to explain. Walking uphill for endless hours in the dark, only to walk back down is a difficult concept to wrap your head around. I have enjoyed all of our trips, even the ones that did not go well, and look forward to many more adventures together. Jerry Heilman, thank you for taking me under your wing as a mentor in the Corvallis Mountain Rescue Unit. I have appreciated our conversations to and from trainings, you have become a great friend that I look to for advice. Many other friends are not mentioned, as this list would be never ending, but you are all greatly appreciated!

Andrea Brush, thank you for all of your patience during my time as a PhD student. Thank you for your support during the tough times. Extra special thanks for your patience for the often ill-advised and under researched trips into the mountains we have had. Whether it be running down the trail to make sure I haven't led us astray, or rushing down steep trails to get back before dark because we forgot our headlamps. I look forward to what the future holds.

I want to personally thank many of my colleagues I have worked with. Dr. Tengfei Fu, you were one of the first graduate students I met to help with a concrete mix. Corvallis isn't the same place without you around, but I am looking forward to watching you succeed in your career. Dr. Matthew Adams, your inspiration and encouragement through our conversations, although not always about concrete materials, have kept my motivation to do high level research. Many times I wanted to cave in and take the easy way out, I appreciate all of your encouragement. Dr. Chang Li, thank you for showing me what hard work and dedication really look like. The three of you really set the bar for the Infrastructure Materials group and we would be nothing without the hard work you all provided. Extra special thanks to other students that have come through the program, Kelsea Schumacher, Monica Morales, David Rodriguez, and Jose Bañuelos. You have all become great friends, and while we may not keep in touch as much as I would like, I owe you all so much for

your help in the past. Thank you to Dr. Prannoy Suraneni and Dr. Vahid Azad for all of your assistance in getting the analysis portion of my PhD research up and going. I couldn't have done it without you. Siva Chopperla, thank you for your assistance and friendship for the past two years. You will do great things in your career with your enthusiasm and energy. Dr. Fred Aguayo, thank you for all of your encouraging words over my tenure as a graduate student, I have not taken them lightly. Thank you to all of the members that I have worked with in the past at OSU. I will not attempt to name everyone, as this is where I will forget specific people, but thank you to all the past and present researchers I have worked with to make the Infrastructure Materials group what is has become.

Extra special thanks to Dr. Dorthe Wildenschild and her research group for all of their help and support on the experimental design, image analysis, and the ins and outs of the Advanced Photon Source. Linnea Andersson, Chris Brueck, Doug Meisenheimer, and Rebecca Paustian, thank you so much for the never ending stream of questions from me, the late nights at APS, the relief of the end of beamtime, and the surreal nature of coming back into society after 5 days at APS. I could not have completed this dissertation without the help of all of you.

Thank you to the staff at the 13-BMD beamline at the Advanced Photon Source at Argonne National Laboratory. Dr. Mark Rivers, I greatly appreciate your patience to help me understand the endless array of monitors and program windows to collect data, reconstruction, the 2 a.m. phone call when the last image will not take, and advice on sample preparation. Thank you to Nancy Lazarz for helping navigate the paperwork and steps to gain access to the APS, making sure proposals were submitted on time, and ESAFs were completed before coming. It was always great to see a smiling face at the beginning of the second 24 hour shift.

Thank you to the staff in the Civil and Construction Engineering department. Cindy Olson, thank you for your never ending help and ability to answer nearly every question I have asked off the top of your head. Dana Ainsworth, thank you for never ending energy and upbeat attitude amongst a never ending pile of papers and work. Kathy Westberg, you were one of the first people I met when I came to Corvallis. Thank you for all of the conversations we have had, and all of the help you have provided to me and the entire department. I would not have been able to complete my graduate work without the help from the three of you. Your upbeat attitudes always made long days easier to bear. My gratitude cannot be expressed in words on paper. Thank you to James Batti

for all of your help getting equipment up and running, and extra special thanks for bailing me out of equipment fixes when I was in over my head. Thank you to Greyson Termini and Manfred Dittrich. Greyson, thank you for your ability to build the equipment I needed from the napkin scratches I provided for you. Manfred, thank you for all of the work you have done for the Infrastructure Materials group in the past. Your smile, friendship, and legacy is not forgotten. Those of us that met and worked with you were truly lucky.

Thank you to Dr. W. Jason Weiss, Dr. Fred Kamke, and Dr. Dorthe Wildenschild for agreeing to serve on my committee. I chose the experts for my committee, and I appreciate all of your comments and feedback to make this dissertation what it is.

Last, but definitely not least, thank you to my advisers, Dr. O. Burkan Isgor and Dr. Jason H. Ideker. Words can't express truly how grateful I am. Burkan, thank you for challenging me to branch outside of my comfort zone for my PhD research. While we may not have always saw eye-to-eye, your compassion, encouragement, and support truly made me a better researcher and writer. Jason, thank you for going on a limb and taking a chance on me as a master's student. You have done so much for me over the years. I truly cannot express my appreciation for everything, I can only hope I hold as much respect as you hold in my career. You are one of a kind.

# CONTRIBUTION OF AUTHORS

Dr. Jason H. Ideker and Dr. O. Burkan Isgor advised on data collection, analysis, and interpretation of results, as well as edits for the entire document. Dr. Dorthe Wildenschild and Dr. Mark Rivers assisted in experimental design and image processing on the x-ray tomography datasets. Appreciation to Dr. Prannoy Suraneni and Dr. Vahid Azad for their assistance in analyzing data collection and processing for material collection. Special thanks to Doug Meisenheimer and Rebecca Paustian for their assistance on image processing, particularly on Chapter 5. Andrew Wilson and Dr. Matthew P. Adams assisted in data collection, analysis, and writing of Appendix C.

# TABLE OF CONTENTS

TABLE OF CONTENTS (Continued)

Page

TABLE OF CONTENTS (Continued)

Page

TABLE OF CONTENTS (Continued)

TABLE OF CONTENTS (Continued)

Page

TABLE OF CONTENTS (Continued)

# LIST OF FIGURES

Figure Page

# LIST OF FIGURES (Continued)

Figure Page

# LIST OF FIGURES (Continued)

Figure Page

# LIST OF FIGURES (Continued)

Figure Page

# LIST OF FIGURES (Continued)

Figure Page

# LIST OF FIGURES (Continued)

Figure Page

# LIST OF TABLES

# LIST OF APPENDICIES

Appendix Page

# LIST OF APPENDICIES (Continued)

Appendix Page

# LIST OFAPPENDIX FIGURES

Figure Page

# LIST OFAPPENDIX TABLES

# 1. General introduction and literature review

## 1.1. Scope and layout of this dissertation

This doctorate thesis follows the manuscript option for the Doctor of Philosophy as described in the Oregon State University Graduate School Thesis Guide 2017-2018. The research presented in this dissertation moves beyond the typical use of x-ray computed tomography in cementitious materials of void and microstructure characterization addresses to determine the potential for non-destructive, three-dimensional imaging to provide quantifiable information on the major phases that form in hydrated portland cement. The dissertation is presented through a literature review, experimental methods, three manuscripts, and general conclusions. The details of each chapter is described as follows:

Chapter 1: *General Introduction and Literature Review* – This chapter provides an introduction and background for the work presented in this dissertation, as well as the motivation for this research. An in-depth literature review provides discussion on the critical need to quantify portland cement hydrates non-destructively. This literature review focuses on phase assemblage, methods to quantify hydration products, challenges using x-ray computed tomography in cementitious systems, and potential improvements to low contrast using contrast agents are presented.

Chapter 2: *Experimental Methods* – This chapter provides an overview of the experimental methods that were implemented for the research completed in this dissertation. Background information and how the explicit pieces of equipment were used are discussed in this section.

Chapter 3: *Manuscript 1* – The first manuscript in this dissertation is titled "Quantification of synthesized hydration products using synchrotron microtomography and spectral analysis." This chapter focuses on the potential to quantify synthesized hydration products using x-ray computed tomography using a synchrotron radiation facility. Pure phases were created and the greyscale signature of each phase was recorded. The signature was then applied to tomographic data sets of binary and quaternary mixtures of similar pure phases to determine the potential for quantification through image processing. Calcium silicate hydrate, calcium hydroxide, ettringite, and

monosulfate were the hydration products studied. This manuscript has been published in Construction and Building Materials in December 2017[1].

Chapter 4: *Manuscript 2* – The second manuscript in this dissertation is titled "Use of iodine for improving phase quantification using x-ray tomography." This chapter addresses methods to improve low contrast between synthesized, hydrated portland cement phases using x-ray computed tomography, particularly between calcium silicate hydrate and monosulfate, as discovered in Chapter 3. Novel techniques were implemented to incorporate contrast agents into monosulfate through ionic substitution. This research lays the groundwork for partial substitution, or absorption, into the crystalline or semi-crystalline structure for calcium silicate hydrate and ettringite. This manuscript has been submitted for review for publication in Cement and Concrete Research in March 2018.

Chapter 5: *Manuscript 3* – The third chapter in this dissertation is titled "Comparison of segmentation algorithms for quantifying portland cement hydrates using synchrotron microtomography." This manuscript focuses on existing advanced thresholding techniques to address the potential for misclassification of voxels found in x-ray tomography data sets discussed in Chapters 3 and 4, particularly in low contrast images. Global and local thresholding techniques were used to assess methods for appropriately assigning and quantifying amounts of each phase. This manuscript will be submitted to Cement and Concrete Composites.

Chapter 6: *General Conclusions* – This chapter summarizes the major findings of this research and provides conclusions for the research completed in this dissertation

Chapter 7: *References* – This chapter is a comprehensive list of references used to create this dissertation, including those given in the introduction.

[1] T. Deboodt, J.H. Ideker, O.B. Isgor, D. Wildenschild, Quantification of synthesized hydration products using synchrotron microtomography and spectral analysis, Construction and Building Materials 157 (2017) 476-488.

Appendix A: *Additional Data* – This section includes additional data on preliminary work on investigating alkali-silica reaction using x-ray computed tomography, particularly using fast tomography with 'pink' beam. Initial work will be described and future work will be outlined.

Appendix B: *Additional Manuscript 1* – An additional manuscript, included in Appendix B, is titled "Limitations and recommendations for measuring setting time, autogenous deformation, and chemical shrinkage of paste." This paper was written from research that was done during his time as a Ph.D. student. This work looks at nuances and errors in measured autogenous deformation of pastes that may be created from improperly determining the setting time using standard test methods caused by temperature variations between the autogenous deformation sample and the setting time sample. This manuscript was published in the Proceedings of the 14$^{th}$ International Congress on Cement Chemistry held in Beijing, China, in 2015.

Appendix C: *Additional Manuscript 2* – The additional manuscript included in Appendix C is titled "Re-evaluation of testing parameters in the accelerated mortar bar test." This paper was written from research that was done during his time as a Ph.D. student. This work focuses on the main testing variables used in the accelerated mortar bar test. A locally sourced, siliceous fine aggregate was subjected to different temperatures, normality of soak solution, and gradation. Each parameter affected the reactivity of the aggregate and the measured expansion at 14- and 28-days. This manuscript was published in the 15$^{th}$ International Conference on Alkali-Aggregate Reactivity held in São Paulo, Brazil, in 2016.

## 1.2. Notation

Cement chemistry notation is used in addition to conventional chemistry notation throughout this dissertation. Standard chemical notation will be used in the event that cement chemistry notation could not be used. Below is a detailed list of abbreviations used throughout this dissertation.

### *1.2.1. Cement chemistry notation for oxide compounds*

A: $Al_2O_3$ C: CaO S: $SiO_2$ F: $Fe_2O_3$ $: $SO_3$ H: $H_2O$

### *1.2.2. Cement chemistry notation and standard chemical notation of phases*

Tricalcium silicate, $C_3S$: $3CaO \cdot SiO_2$

Dicalcium silicate, $C_2S$: $2CaO \cdot SiO_2$

Tricalcium aluminate, $C_3A$: $3CaO \cdot Al_2O_3$

Tetracalcium aluminoferrite, $C_4AF$: $4CaO \cdot Al_2O_3 \cdot Fe_2O_3$

Calcium-silicate-hydrate (C-S-H), [0.7-2.0]CS[1.0-2.5]H: ([0.7-2.0]$CaO \cdot SiO_2 \cdot$[1.0-2.5]$H_2O$[*]

Calcium hydroxide, CH: $Ca(OH)_2$

Ettringite (AFt): $C_6A\$_3H_{32}$: $3CaO \cdot Al_2O_3 \cdot 3CaSO_4 \cdot 32H_2O$

Monosulfate (AFm): $C_4A\$H_{12}$: $3CaO \cdot Al_2O_3 \cdot CaSO_4 \cdot 12H_2O$

(*[*]Chemical composition varies by constituents of raw materials, temperature, curing, etc.)*

*1.2.3. Analytical techniques*

XRD: X-ray diffraction

TGA: Thermogravimetric analysis

SEM: Scanning electron microscopy

EDX: Energy dispersive x-ray

X-ray CT: X-ray computed tomography

## 1.3. Background and literature review

*1.3.1. Critical need*

Portland cement concrete is the most widely used construction material in the world. As a result, the economic, social, and environmental cost of deterioration of concrete structures is a major contributor to the infrastructure deficit in the United States. The gravity of the problem has been the driving force behind the increasing number of studies to develop a fundamental understanding of hydration and deterioration mechanisms that may occur in concrete, and to discover new cementitious materials with superior mechanical and durability properties. Recent interest in the development or improvement of alternative inorganic binders [1-8] and innovative attempts to

change the nano-structure of hydrated cement phases for better durability [9-15] are also clear indicators of the demand for additional research.

The use of advanced material characterization techniques has had an irrefutable impact on the progress during the past several decades. It is now common to use advanced microscopic, spectroscopic, and crystallographic techniques to understand macro-, micro-, and nano-scale properties of concrete components, their formation, and deterioration mechanisms. Despite the progress enabled by these advanced characterization techniques, further advancement of our understanding of concrete hydration, and subsequent deterioration of those phases, is also hindered by their limitations. One limitation is the inability to non-destructively monitor compositional changes in three-dimensional (3D) concrete (or hydrated cement or mortar). It is routine to characterize crystalline phases in concrete using x-ray diffraction (XRD) on powdered samples. However, the powder analysis only gives averaged information from the extracted sample domain. If one wants to monitor changes over a period of time, additional powder samples need to be extracted from different locations of the same specimen, or from different specimens at different times. Optical and electron microscopic studies on concrete or its components are also limited in that they are performed on two-dimensional (2D) surfaces that need to be prepared for analysis; such preparation can induce artifacts in the microstructure [16] — such as loss of structure by grinding and polishing [17], changes in structure caused by drying [17, 18], or cracking caused by cutting or drying [19]. After collecting microscopic data, image analysis can be done to extract quantitative information on the microstructure of the observed surface. Microscopy techniques can be coupled with spectroscopic tools to extract elemental mapping of the surface — for example, by using energy-dispersive x-ray spectroscopy (EDX). In some cases, 3D information can be extrapolated from the 2D microstructural and/or elemental measurements; however, 2D analysis is generally inadequate for accurate characterization when direct 3D information is needed, such as connectivity and distribution of phases within a complex structure. Again, in order to monitor changes over time, new cross sections need to be extracted from additional specimens at different times.

One method to obtain quantifiable 3D information is through the use of x-ray computed tomography (x-ray CT). X-ray CT is a non-destructive, non-contact technique that uses computer-processed x-rays to produce 3D tomographic images of specific zones of a scanned object,

allowing the user to see inside the object without damaging the specimen [20-23]. Although x-ray CT has been used in a number of applications, including geosciences [20, 22, 24] and material science [25-29], it has been particularly successful in medical fields as an imaging technique used for research and clinical applications [30]. However, in previous research on portland cement systems, similar greyscale values of different components of concrete and phases in hydrated cement have been reported. This has predominately limited the use of x-ray CT to the qualitative or semi-quantitative characterization of internal pore structure [31-40], cracking, and mechanical damage [17, 36, 41-44].

The main hypothesis of this thesis is to expand the use of x-ray CT beyond its current limited application for quantification in cementitious systems, namely pore structure and crack characterization, to provide quantitative 3D information on primary and secondary hydrated phases as well as lay the groundwork for monitoring changes in those phases that may be associated with subsequent deterioration of the hydrated phases. Synchrotron x-ray CT will be used as the framework of the proposed research. The contrast of primary hydrate phases, calcium silicate hydrate (C-S-H) and calcium hydroxide (CH), and secondary hydrate phases, ettringite (AFt) and monosulfate (AFm), of portland cement will be determined. In instances of low contrast, one or more phases will be manipulated through the use of contrast agents - either elemental, ionic, or molecular substitutions or interstitials so that these phases can be easily identified by x-ray CT. This non-destructive approach will also allow the samples to be monitored repeatedly over time so that the progressive changes in these can be recorded.

## 1.4. Manufacturing of portland cement

In order to improve contrast in x-ray CT, the hydration and subsequent formation of hydration products of portland cement must first be understood. This section discusses the raw materials, clinker phases, and hydration products that are typically found in ordinary portland cement.

### *1.4.1. Raw materials used in portland cement manufacturing*

Portland cement clinker is typically created from the intermixing of a calcareous material, usually limestone, with an argillaceous, clay or shale. Other minor quantities of materials are added to correct the bulk composition (i.e. iron ore, bauxite, or sand). The raw materials are ground and

then heated to approximately 1450 °C in a rotary kiln. During this process, three main reactions occur:

- Below 1300 °C decomposition of calcite ($CaCO_3$) to lime (CaO), decomposition of clay minerals, and the reaction of the lime with quartz and decomposed clay minerals. There is minimal liquid formed below this temperature, but can play a significant role in promoting the aforementioned reactions. Formation of belite ($C_2S$), lime, aluminate, and ferrite occur during this stage of manufacturing.
- The solids begin to melt between 1300 – 1450 °C, and approximately 20-30% of the material is a liquid. The belite reacts with the lime and silica to form alite ($C_3S$), and the materials begin to nodulize to form clinker.
- As the material cools, the liquid crystallizes to form aluminate and ferrite phases. Polymorphs of the alite and belite phases also occur during cooling [45]. The rate of cooling will affect the degree of crystallinity and amount of polymorphs found in the clinker material [46]. After the material has cooled, it is ground to a powder with a specific fineness.

The formation of the major and minor phases depends on the composition of the raw materials, as well as the heating and cooling process. Typically, portland cement is composed of approximately 45-60% of $C_3S$, 15-30% of $C_2S$, 6-12% of $C_3A$, and 6-8% of $C_4AF$ [47].

## 1.5. Hydration of portland cement

Due to the complexities of the composition of portland cement, hydration of individual phases is often studied. Therefore, the hydration of individual unhydrated phases will be discussed. The following is a discussion on the hydration of the four main unhydrated phases in portland cement. These will be broken into the silicate phases and the aluminate phases.

### *1.5.1. Hydration of silicate phases*

The main silicate phases in portland cement are belite ($\beta$-$C_2S$) and alite ($C_3S$). The rates of reactions of these two phases differ significantly. The reaction of alite and water is quicker than the reaction of belite and water. However, the hydration of these two phases yields a family of

calcium silicate hydrates. These include the formation of C-S-H and CH [46]. The stoichiometric reactions for $C_3S$ and $C_2S$ are seen below [47]:

$2C_3S + 6H \rightarrow C_3S_2H_3 + 3CH$ Equation 1-1

$2C_2S + 4H \rightarrow C_3S_2H_3 + CH$ Equation 1-2

However, the chemical composition of C-S-H can vary significantly. For example, the calcium to silica ratio and amount of chemically combined water can vary [47]. These two phases will be discussed in more detail in section 1.6.

### *1.5.2. Hydration of aluminate phases*

The main aluminate phases found in portland cement are tricalcium aluminate ($C_3A$) and tetra-calcium aluminoferrite ($C_4AF$). Hydration of $C_3A$ is a quick reaction, on the order of tens of minutes. This is typically controlled with the addition of a small amount of gypsum ($C\$H_2$), usually less than 5% by mass. $C_4AF$ reacts much more slowly, on the order of months and years. The addition of gypsum into the system results in the formation of similar hydration products when $C_3A$ and $C_4AF$ react with water, but at a manageable rate for ease of workability and placement in the first few hours after initial mixing. Quantities of the hydration products formed by the hydration of $C_4AF$ are minor in comparison to those formed by the hydration of $C_3A$. The two main hydrated phases are ettringite ($C_6A\$_3H_{32}$) and monosulfate ($3C_4A\$H_{12}$) [47, 48]. Stoichiometric reactions for $C_3A$ form ettringite and monosulfate are seen below [48]:

$C_3A + 3C\$H_2 + 26H \rightarrow C_6A\$_3H_{32}$ Equation 1-3

$C_6A\$_3H_{32} + 2C_3A + 4H \rightarrow 3C_4A\$H_{12}$ Equation 1-4

Reactions for $C_4AF$ in the presence of $C\$H_2$ are seen below [47]. Note these reactions are not stoichiometric:

$C_4AF + C\$H_2 + H \rightarrow C_6A(F)\$_3H_{32}$ Equation 1-5

or

$C_4AF + C\$H_2 + H \rightarrow C_4A(F)\$H_{18}$ Equation 1-6

The $C_6A\$_3H_{32}$ (AFm) $3C_4A\$H_{12}$ (AFt) phases will be discussed in more detail in section 1.6.

## 1.6. Hydration products in portland cement

Four major hydration products form during the hydration of portland cement. These are C-S-H, CH, AFt, and AFm. Chemical variations of these phases, and subsequent minor phases, occur depending on the initial composition of the raw materials, as well as the service environment during the entire life of the concrete. These four main hydration products were studied in this research, and will only be discussed.

### *1.6.1. C-S-H*

C-S-H is the primary hydrated phase when portland cement reacts with water. C-S-H is often referred to as tobermorite, which has similarities in crystal structure assembly to clay minerals. This hydrate occupies approximately 50-60% by volume of all hydrated phases [47]. It is an important hydrate that contributes to several properties, such as strength, volume stability, and durability. The composite is formed by distorted calcium hydroxide sheets with parallel rows of wolloastonite-type chains ($Ca_4Si_6O_{18}$) on the sides [49]. Differences between morphology with varying degrees of structural order of the inner and outer products of C-S-H formed in pure portland cement systems have also been found [50-52]. The formation of C-S-H tends to create a fibrous particle in portland cement ranges from 0.5 μm to 2 μm long and less than 0.2 μm across [46]. The aggregation of C-S-H can be as large as several μm in size [47]. However, the structure is typically amorphous or poorly crystalline and exact stoichiometric composition can vary [53]. It has been reported the calcium to silica ratio (Ca/Si) can range from 1.4 to 2.0, with a value of 1.7 as likely being the Ca/Si ratio that typically forms [54]. While the Ca/Si ratio can deviate, larger deviations in the stoichiometry of the structural water are typical [47, 54]. Variation of the composition, nanostructure, and morphology of C-S-H depends on several factors. The water to cement ratio, curing temperature, chemical composition of raw materials, degree of hydration, and the presence of chemical and mineral admixtures all affect the chemical composition of C-S-H [55, 56].

### *1.6.2. CH*

The formation of CH in hydrating portland cement constitutes approximately 20-25% of the volume of paste that forms. The formation of CH in portland cement has a definitive stoichiometry of $Ca(OH)_2$, and form large crystals with hexagonal plate morphology. The morphology is

dependent on several factors, including available space, temperature, and impurities. Due to the large size of crystals, up to tens of microns [48], CH contributes little to the overall strength development [47].

### *1.6.3. AFt*

The AFt phase is part of a large group of minerals with a general formula of $3CaO{\cdot}(Al,Fe)_2O_3{\cdot}3CaX_2{\cdot}nH_2O$, where X is one monovalent anion or half divalent anion [57]. The ettringite crystal structure is composed of two distinct components. These include columns with a typical chemical formulation of $[Ca_6(Al(OH)_6)_2{\cdot}24H_2O]^{6+}$, and channels with the chemical formulation of $[(oxyanion)_{2-4}(OH)_{0-4}(H_2O)_{0-6}]^{6-}$ [58, 59]. Variations in the oxyanion occur, but typically the anion present in cement hydration is $SO_4^{2-}$. Typical crystalline structure of AFt contains three distinct types of water. These include the water in the columns, the water bound to the columns, and the water as hydroxide ions on the columns [60]. Dehydration of AFt can result in a shift in the XRD patterns, particularly once the structure has less than 36 molecules of water per structural unit. When this occurs, there is a shift in the XRD basal peak from 0.97 nm to 0.73 nm [61]. Stoichiometry of ettringite can have an excess or deficiency in several components, without changing the crystal structure. Therefore, compositions vary depending on available concentrations of available constituents [62]. However, in hydration of portland cement, the composition typically is $3CaO{\cdot}Al_2O_3{\cdot}3CaSO_4{\cdot}26\text{-}32H_2O$ [63], with minor variations occurring due to raw material constituents. AFt in portland cement systems are space opportunistic. They are needlelike and can be up to 10s of μm in length [47, 63].

### *1.6.4. AFm*

AFm phases belong to the lamellar double hydroxide (LDH) family, which is a type of anionic clay material with cationic brucite layers that have exchangeable interlayer anions [64]. Most LDHs have relatively weak interlayer bonding, which results in the ability to capture inorganic anions by both surface adsorption and anion exchange [65, 66]. LDHs can be nominally expressed as the following chemical formula $[M_{1-x}^{2+}M_x^{3+}(OH)_2]^{X+}(A^{n-})_{x/n}{\cdot}mH_2O$. $M^{2+}$ and $M^{3+}$ are divalent and trivalent metal cations with an anionic radius similar to $M^{2+}$. $A^{n-}$ is an n-valent exchangeable anion. This anion can be either organic or inorganic.

However, the AFm structure found in portland cements is composed of positively charged outer layers $[Ca_2Al(OH)_6]^+$ and negatively charged interlayers $[X{\cdot}xH_2O]^-$, where X is an exchangeable singly charged (e.g. chloride) or half-doubly charged anion (e.g. sulfate, carbonate, aluminosilicate). The value for *x* ranges from 0.17 to 0.33 [67]. The anion present in the AFm phase is sensitive to the cement composition, as well as the service environment [63, 68]. Anions that may be present in portland cement systems are hydroxide, sulfate, and carbonate [45, 63]. In blended cements, aluminosilicate anions are typically present [63]. In the presence of chlorides in cement paste, the diffusion profiles are affected by ion exchange and chloride binding in the AFm phase. These phases collect and bind the chlorides and retards the diffusion [68].

Under ideal conditions, AFm phases are platey, hexagonal crystals with cleavage on the (0001) plane, and are approximately 4-10 µm in diameter [45, 63]. However, during formation of AFm phases in portland cement systems, they have a poorly crystalline structure and are intermixed with C-S-H [45] resulting in difficulties to analyze due to its low crystallinity, polytypism, variations in the composition, and changes in the composition during service. For example, during service, chlorides often displace the anions that are in the AFm phase, thus changing the structure [63]. The most common AFm phase in freshly hydrated portland cement is monosulfate with the chemical formulation of $C_4A\$H_{12}$: ($3CaO{\cdot}Al_2O_3{\cdot}CaSO_4{\cdot}12H_2O$). Other AFm phases found in portland cement systems include Friedel's salt, which form in the presence of chloride ions [68]. The typical crystal morphology is hexagonal or pseudohexagonal with a chemical formula of $3CaO{\cdot}Al_2O_3{\cdot}CaCl_2{\cdot}10H_2O$ [64].

## 1.7. Methods to quantify hydration products in cementitious systems

As discussed in section 1.3.1, there is a critical need to quantify cementitious materials in a non-destructive manner. While many test methods to characterize and quantify hydration products in cementitious systems exist. This section describes the test methods that were used in this research for phase verification and quantification. Details on the specific pieces of equipment used are found in Chapter 2.

### *1.7.1. XRD*

XRD is used for characterization of the structure, namely crystalline structure, of a material. Two processes can occur when an x-ray interacts with a solid object. The x-ray may be absorbed,

resulting in an ejection of electrons from the atom, or it may be scattered [69]. In XRD there is an "elastic scattering of x-ray photons by atoms in a periodic lattice [70]." The diffraction of x-rays by periodic crystal planes can be described by Bragg's law:

$$n\lambda = 2d\sin(\theta) \qquad \text{Equation 1-7}$$

Where *n* is the order of reflection (an integer), $\lambda$ is the wavelength of the incident x-ray, *d* is the lattice spacing of the crystalline planes, and $\theta$ is the angle between the x-ray beam and the normal to the lattice plane. The lattice spacing can be determined for each crystallographic phase through the measurement of theta. Crystalline materials can be assessed qualitatively by matching the XRD pattern of the material to characteristic patterns of known crystals. The material can also be assessed through quantitative XRD using the internal standard method, diffraction absorption method, or dilution method [70]. This research used qualitative analysis to match the XRD patterns of synthesized phases to known patterns of the phases. Therefore, the quantitative methods will not be discussed in detail.

### *1.7.2. Thermal analysis*

A material may undergo a variety of physical or chemical changes when it is subjected to thermal treatment. These changes include, but are not limited to, dimensional changes, magnetic properties, weight, crystal structure, mechanical properties, acoustic properties [70]. During thermal analysis, the material is heated and a potential change in a certain physical or chemical property is measured at a regular interval [71]. During dynamic thermal analysis, such as thermogravimetric analysis (TGA) or differential thermal analysis (DTA), the desired change in material property is monitored continually during a uniform heating. This research implemented the use of TGA and differential thermogravimetric analysis (DTG). In DTG, the first derivative of the change of mass is determined and results in sharp peaks in the DTG curve, which aids in material classification [70].

### *1.7.3. X-ray computed tomography*

X-ray computed tomography (x-ray CT) is a non-destructive, non-contact technique that uses computer-processed x-rays to produce 3D tomographic images of specific zones of a scanned object, allowing the user to see inside the object without damaging the specimen [20-23]. Medical imaging is the most common application of x-ray CT [30]; however, its use to characterize concrete has gained increasing attention in recent years. Due to similar greyscale properties of different

components of concrete and phases in hydrated cement, the use of x-ray CT has been limited to the qualitative or semi-quantitative characterization of internal pore structure [31-40], cracking, and mechanical damage [17, 36, 41-44]. A detailed summary of the use of x-ray CT in cementitious systems is found in section 1.8.

In x-ray CT, a sample is placed between the x-ray source and a detector. X-ray beams are sent through a sample and the transmitted beams are recorded on a detector after passing through a scintillator to convert the x-rays to visible light [16, 72]. The sample is rotated (up to 360°) along its vertical axis to obtain a multitude of projections. In x-ray tube CT, the sample is placed between the x-ray source and the detector and can be moved to adjust the resolution. The resolution can range, typically between 10 and 500 μm. A compromise between sample size and resolution must be found for scans. Helicoidal rotation of the sample may be done during the scan in order to scan larger objects. The time for a complete scan depends on resolution, size of detector, and the x-ray source [73].

There are two primary methods to produce x-rays used to obtain data using x-ray CT, which are the use of x-ray tubes or synchrotron radiation to produce x-rays. X-ray tubes emit an x-ray from a metallic target and a polychromatic, divergent beam is generated, as seen in Figure 1-1 [73]. The accelerated electrons release electromagnetic radiation in the form of x-rays and the maximum energy of the radiation is limited by the energy of the incident electron [72]. In the case of a 1D line detector, only one line of data from a fan beam is recorded at a time, and a series of vertical scans are needed to image the entire sample. A 2D CCD detector records data from a cone beam, and allows for a shorter acquisition time. However, if the vertical angle of the sample is off from vertical geometric artifacts may be present. This is due to reconstruction algorithms which are based on a parallel beam configuration [73]. Synchrotron sources deliver a very high flux at small source size (at least 1000 times larger than x-ray tubes). A monochromator is typically placed in front of the sample to create a monochromatic, white beam. The beam is practically parallel and there is no magnification of the image on the detector. The parallel, monochromatic beam set-up makes an exact and quantitative reconstruction free of geometrical and beam artifacts. A crucial element in the set-up is a high- resolution detector. The scan time for synchrotron tomography is much less than that of x-ray tube tomography. The scan time can range from 30 sec to 30 min.

This short scan time allows for scanning of in situ experiments. A schematic of the two types of x-ray CT configurations is seen in Figure 1-1.

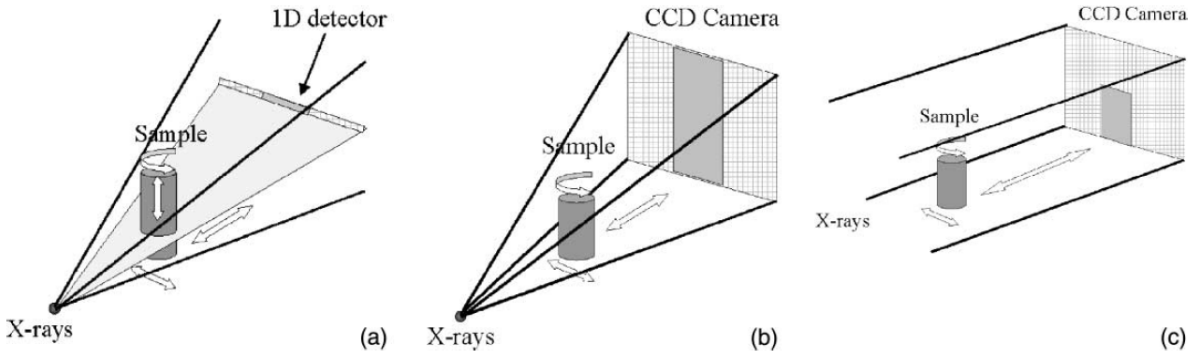


Figure 1-1: Figure 1-1a) and b) represent the configuration for x-ray CT using an x-ray tube as the source of the x-rays. Figure 1-1a) displays a fan beam configuration using a 1D line detector. Figure 1-1b) represents a typical cone beam emitted from an x-ray tube source using a 2D detector. The sample is magnified on the detector relative to its position to the x-ray source. Figure 1-1c) represents the configuration for x-ray CT using a synchrotron x-ray source. This method produces a parallel beam, and no magnification occurs on the detector [73]

Synchrotron radiation sources are particularly well suited to high-resolution tomographic imaging because of the extremely high photon flux. A comparison of the photon flux intensity between an x-ray tube and synchrotron radiation source is presented in Figure 1-2.

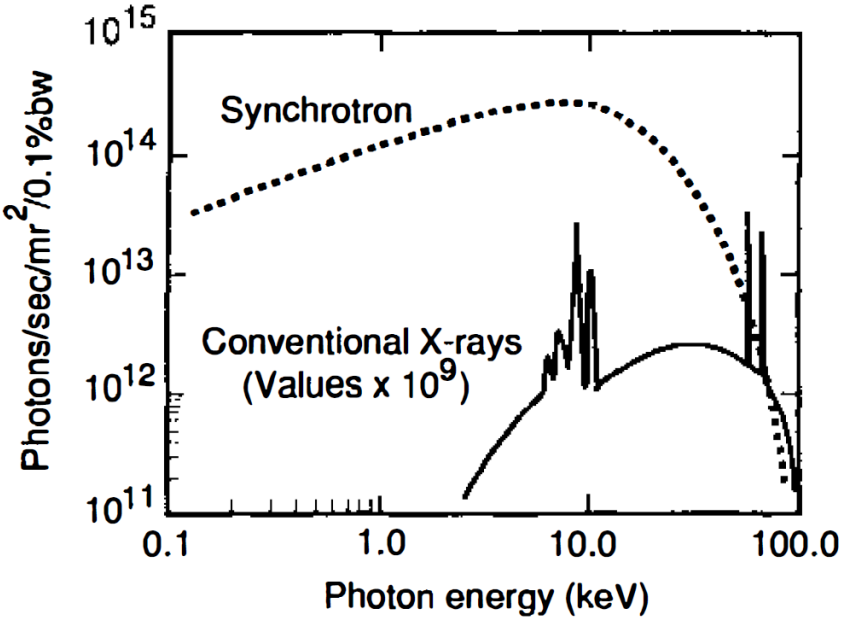


Figure 1-2: Difference in flux between conventional x-ray tube source and synchrotron radiation source. The synchrotron source was measured at the Stanford Synchrotron Radiation Laboratory. Whereas, the flux of the x-ray tube source was measured using a tungsten anode with a voltage of 100 kV and a current of 5 mA. The maximum values of flux intensity measured from the x-ray tube source were in the $10^9$ photons/sec/mr$^2$/0.1%bw, which was much smaller compared to the intensity measured from the synchrotron source ($10^{14}$ photons/sec/mr$^2$/0.1%bw) [74].

Furthermore, the white synchrotron light can be filtered to the desired energy level with a monochromator. This can be used to enhance the contrast between different phases/features in an object by scanning at the peak absorption energy of an added chemical contrast agent or by scanning at multiple energy levels and using subtraction algorithms. This latter approach can prove highly valuable for the work proposed here, as the contrast of compounds containing specific elements can be achieved through multi-energy scanning.

As monochromatic x-rays pass through solid materials, their intensities attenuate to varying degrees as a function of the materials along the path of the beam, a phenomenon described by the Beer-Lambert Law [22]:

$$I(x) = I_o e^{(-\mu x)} \qquad \text{Equation 1-8}$$

where, $I$ is the attenuated intensity of the x-ray after passing through the solid with a thickness of $x$, $I_o$ is the initial intensity of the radiation, and $\mu$ is the linear attenuation coefficient. According to the Beer-Lambert Law, the ratio of the number of transmitted to incident photons is related to the

integral of the linear attenuation coefficient(s) of the materials along the path that the photons travel through the sample. The linear attenuation coefficient is linked to the density, the atomic number, and the energy of the beam [73]. Materials with higher density or high atomic number tend to absorb x-rays better. The relationship between density, atomic number and linear attenuation coefficient of an element is given as [72]:

$$\mu = \frac{\rho Z^4}{AE^3} \qquad \text{Equation 1-9}$$

where, *A* is the atomic mass, *Z* is the atomic number, $\rho$ is the density, and *E* is the x-ray energy. Materials with a high linear attenuation coefficient allow x-rays to only penetrate a short distance, whereas materials with a low linear attenuation coefficient allow x-rays to pass through more easily [22].

At energies relevant to most CT applications, the linear attenuation coefficient of a material depends on its density, atomic number of its elements, and the energy of the beam [73], such that materials with higher density or high atomic number tend to absorb x-rays more effectively [72]. A consequence of this is that materials with a high linear attenuation coefficient allow x-rays to only penetrate a short distance into the material and sufficiently highly energetic x-rays are needed to obtain a good signal-to-noise ratio when the x-rays are detected upon exit [22].

When an x-ray with energy equal to or slightly greater than the binding energy of the k-shell electron of a particular element, the resulting interaction with the material causes a significant increase in absorption. This value is known as the absorption (k) edge, and the value of the k-edge energy level increases with the atomic number of the elements in the material. In synchrotron facilities, the energy of the x-ray source can be adjusted using a monochromator to closely match the absorption edge to generate images with optimal contrast [22, 72].

Upon completion of a scan, the series of acquired projections (2D maps of linear attenuation coefficients) can be mathematically reconstructed into a 3D rendition of the object [72]. This image is composed of a 3D volume of pixels, that encompass the weighted average linear attenuation coefficients of all components within the voxel which determine the greyscale value, and ultimately the contrast seen in the reconstructed image [75]. The contrast between different materials is manifested if intensities are plotted as a histogram. These 3D greyscale images need to undergo segmentation to isolate features in the 3D image stack. The resolution of the image can

range from sub-microns to several hundred microns depending on the x-ray source and the size of the sample. The time for a complete scan depends on resolution, detector size, and the x-ray source. In synchrotron facilities the total scan time can be in the range of 30 sec to 30 min, whereas in lab-based systems, it may be from 15 min to 24 h [22].

### 1.8. Use of x-ray CT in cementitious systems

Medical imaging is the most common application of x-ray CT [30]. However, its use to characterize concrete and cementitious materials has gained increasing attention in recent years. The use of x-ray CT has been used to study a variety of properties of cement and concrete. These include characterizing physical properties, such as internal pore structure and tortuosity [31-40, 76-79], morphology of aggregates [80-83], crack formation, propagation, and subsequent healing of cracks [36, 41-44, 84-88], distribution of fiber reinforcement [89-91], microstructure formation during hydration [92-94], microstructure development [34, 39, 79, 95-99], segregation resistance [100], and mass diffusivity [101]. Furthermore, x-ray CT has been used to study deterioration of the cement paste matrix. These studies included detection of freeze-thaw damage [16, 102], alkali silica reaction [16, 103], formation of calcium carbonate caused by carbonation [75], rebar location and formation corrosion products [104-106], delayed ettringite formation [17], sulfate attack [107-109], and leaching of calcium hydroxide [35, 43, 110-112].

A major challenge related to the application of x-ray CT to characterize cementitious systems is the difficulty of the technique to distinguish different solid phases due to relatively similar greyscale values that hinder differentiation [17], including differentiating unhydrated and hydrated phase. This challenge has resulted in the limitations of x-ray CT for extracting quantifiable information on cementitious materials, and resulted in many of the aforementioned studies being limited to qualitative or semi-quantitative analysis. However, recent success using x-ray CT coupled with other analytical techniques has allowed for extracting quantifiable information, such as chemical composition and water movement within the cement matrix. Research by Trtik et al. used x-ray CT to analyze the pore size distribution of a fine lightweight aggregate (FLWA) in cement paste. The results from x-ray CT were compared to water movement detected with neutron tomography and discovered the resolution was not capable of detecting the fine pores in the FLWA. It was found during the comparison of images that the water was being stored in the solids, and not in pores. It was concluded the resolution (~16 μm) was not sufficient for detecting all pores

in the FLWA [83]. Furthermore, a combination of x-ray CT and electron probe microanalysis has been achieved to characterize chemical constituents in fly ash, a commonly used supplementary cementitious material [113]. While this method was successful at mapping 3D locations of the chemical components of the fly ash, subsequent x-ray CT scans of the same sample could not be achieved due to the need for a polished flat surface for electron probe microanalysis.

While x-ray CT has been used to characterize several aspects of concrete and cementitious materials, there are limitations on the ability to extract quantifiable information, particularly on the hydrated phases. Section 1.9 describes two of the major limitations that exist with x-ray CT as a standalone method to quantify phases. These include spatial resolution and low contrast in the solid phases. The author acknowledges the limitations on spatial resolution for use in cementitious materials, however, emerging technologies in x-ray CT are improving the resolution in reconstructed image volumes of both x-ray tube and synchrotron sources. The primary focus of this research is to investigate methods to resolve low contrast issues with the use of contrast agents and segmentation algorithms to use x-ray CT as a standalone method for cementitious materials. This will provide fundamental understanding that can be used as the resolution of x-ray CT devices improves in the future.

## 1.9. Limitations of x-ray CT for cementitious materials

Applications of x-ray CT as a standalone method to characterize cementitious materials and concrete have a number of challenges. These include distinct, quantifiable detection of hydrated phases due to low image contrast in the solid phases, as well as issues related to the sample size and spatial resolution of x-ray CT. This section discusses the current limitations of using x-ray CT in cementitious systems, and methods researchers have used to overcome these limitations.

### *1.9.1. Spatial resolution*

One limitation in using x-ray CT is obtaining adequate spatial resolution in the reconstructed image volume. Spatial resolution depends on the sample size, the optics used for magnification, and the resolution of the detector. In order to increase the accuracy of quantitative measurements (e.g. porosity), the resolution needs to be optimized as well, which typically implies the use of a smaller samples. Distinction between phases in a bulk system (e.g. hydrated cement paste, void, or aggregate) becomes challenging as the size of the voxel is increased. If a particular phase does not

encompass an entire voxel, errors in segmentation of the image may occur. This artifact, called partial volume effects, increases as the voxel size increases [99]. In particular, high spatial resolution is key to extracting accurate pore structure information from an image stack. Therefore, a compromise between sample size and resolution must be found for x-ray CT imaging in cementitious systems, particularly in systems where aggregate-cement interaction and identification of phases in hydrated cement are of interest [16]. Currently, maximum resolution achievable in x-ray CT is approximately 50 nm/voxel, and it is expected to be reduced as low as 15 nm/voxel with emerging technologies [114].

Examples of the importance for high resolution include work by Gallucci et al. [96], showing that an increase in the resolution from 2.67 to 0.67 μm resulted in an increase in measured porosity from 5.03% to 18.6%. Similar work by Promentilla et al. [38] indicated a reduction in measured porosity and increase in tortuosity of a cement paste due to an increase in the voxel size, as seen in Figure 1-3. It was found that changing the voxel resolution from 2.0 μm/voxel to 0.5 μm/ voxel resulted in higher tortuosity of the connected pores due to the inability to properly image the smaller pores at the 2 μm/voxel resolution. It was concluded that when the voxel size was greater than 1.0 μm/voxel, the pore structure was no longer connected in the three orthogonal directions in a cement paste that had been hydrating for 28 d.

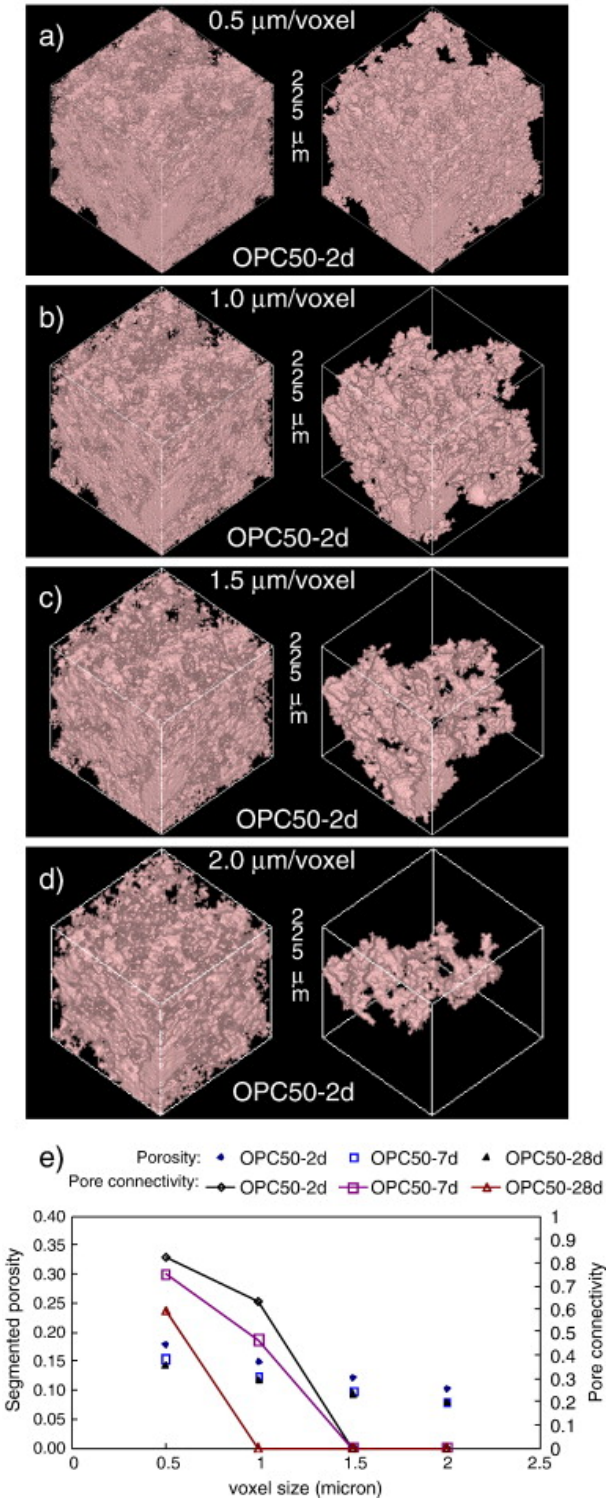


Figure 1-3: Decreasing resolution resulted in a decrease in porosity and an increase in tortuosity due to the inability to adequately capture small pores in reconstructed image volumes [38]

An approach to improving the voxel resolution is to reduce the dimensions of the sample. Bossa et al. [35] were able to improve the resolution of x-ray CT measurements in cementitious system from micro-scale to nano-scale by reducing the sample size. The resolution improved from 1.81 μm/voxel to 63.5 nm/voxel by reducing the dimensions of sample from 5 mm to 0.4 mm. However, there is still insufficient resolution to detect the gel and some of the capillary pores in hydrated cement phases that are in the low nanometer range [40, 96].

One method that takes advantage of small sample sizes to result in high voxel resolution is ptychographic x-ray CT. Resolutions in below 50 nm/voxel can be achieved. In this method a small sample, typically less than 100 μm, is placed on a three-dimensional rotation stage having nanometer precision in all directions. An x-ray beam produced from synchrotron radiation is focused with a pinhole to produce a spatially defined x-ray beam on the sample. Coherent diffraction patterns of the x-rays are collected, and a tomographic volume of the sample can be created [115]. A typical setup for ptychographic x-ray tomography is seen in Figure 1-4.

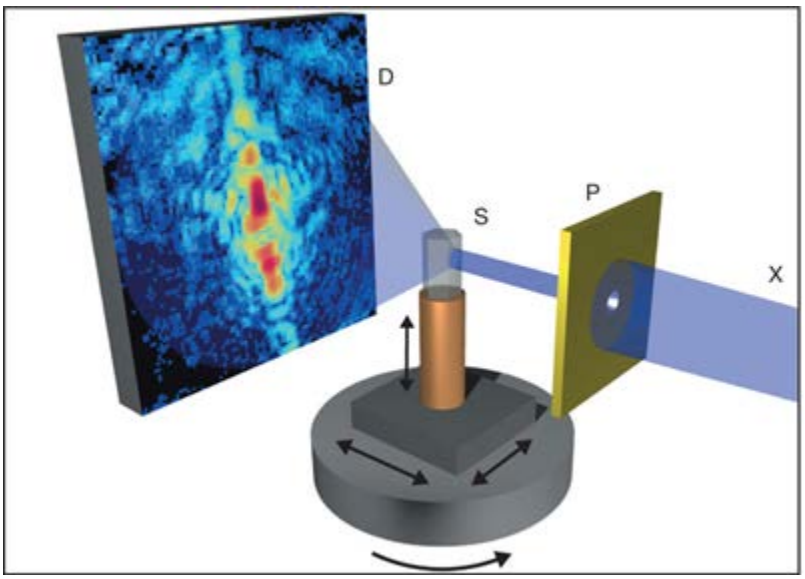


Figure 1-4: Ptychographic setup, where (X) is the x-ray beam created from a synchrotron source. A focusing element (P) is used to produce localized illumination on the sample (S). The coherent diffraction patterns from the focused x-ray source is recorded on a 2-D detector (D) [116]

This technique has been successfully used in characterizing cementitious materials by measuring mass densities of hydrated phases. The high resolution (up to 40.8 nm/pixel [117]) allowed for the determination of mass densities based on the measured electron density and the known chemical composition of unhydrated and hydrated phases [115], hydration products of alite [118], and

hydration products of alternative, eco-cements [117]. While this method has been successful at quantifying hydrated phases, the samples prepared for ptychographic x-ray CT are created using focused ion beam (FIB) milling, as seen in Figure 1-5, to produce a sample small enough (sub-100 μm in diameter) for scanning [115, 117-119]. This requirement makes the use of this method limited to those with access to such high precision milling capabilities.

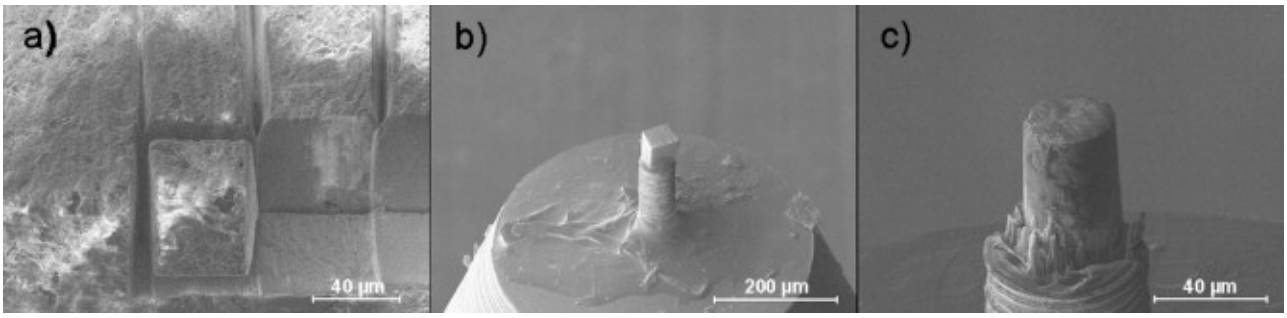


Figure 1-5: Creation of a sample for ptychographic CT using FIB milling to create a cylindrical sample with a diameter of 30 μm [115]

### *1.9.2. Low contrast in reconstructed images*

The main motivation for this research is to investigate the limitations of low contrast in phases and quantify the amounts of each phase present in a cementitious system. There have been a limited number of studies that attempted to identify different solid phases in hydrated cement. For example, Tosun and Baradan [17] used synchrotron x-ray CT to detect delayed ettringite formation (DEF) in aged concrete. As seen in Figure 1-6, ettringite was detectable only in pores, cracks, and aggregate-paste interfaces with the cementitious matrix, but it was difficult to identify in the bulk cementitious matrix because the greyscale values of ettringite are similar to those of the bulk paste and the aggregates.

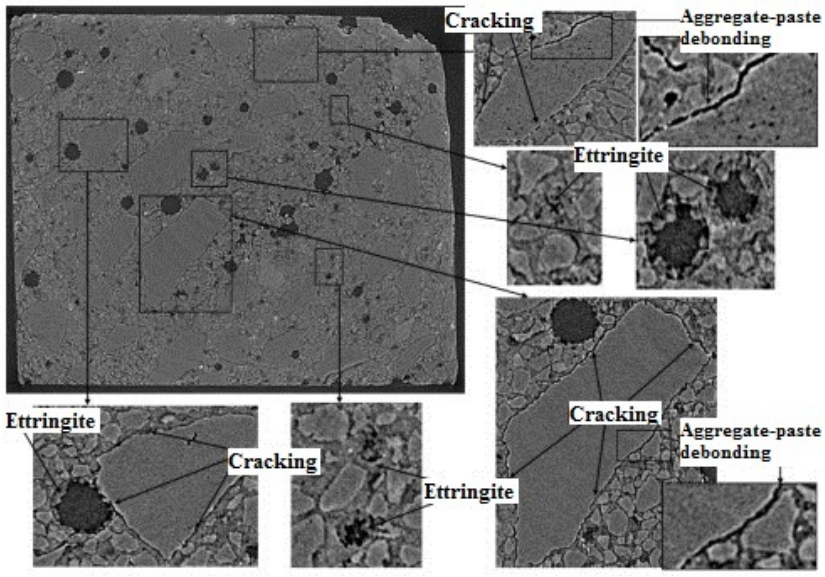


Figure 1-6: Reconstructed 2D x-ray CT image showing cracking caused by DEF and ettringite pockets in the pores and aggregate-paste interface. Cracking was observed around the aggregates due to the expansive nature of DEF, and there was no bonding in the between the aggregates and the bulk paste. Enhancement of the pores revealed the presence of ettringite after steam curing after 1.5 years from casting as seen in the images above. Changes in the greyscale values in the pores indicated the presence of ettringite. The x-ray CT images were compared to SEM images taken at the same age to confirm ettringite had formed in the pores [17].

The lack of contrast between solid phases has proven to be difficult to choose an unbiased threshold value to segment the image volume. Often times the resultant histogram of the image volume results in overlapping peaks. Research by Provis et al. [32] investigated hydration of alkali activated binders which composed of varying ratios of ground granulated blast furnace slag and fly ash. While the primary focus of this research was to investigate the tortuosity of the microstructure as it hydrates, the authors also investigated the ability to differentiate between the anhydrous and hydrate phases. The authors chose a distinct greyscale value (approximately 125) as their threshold value, yet there was no separation between histogram peaks, potentially leading to misclassification of voxels.

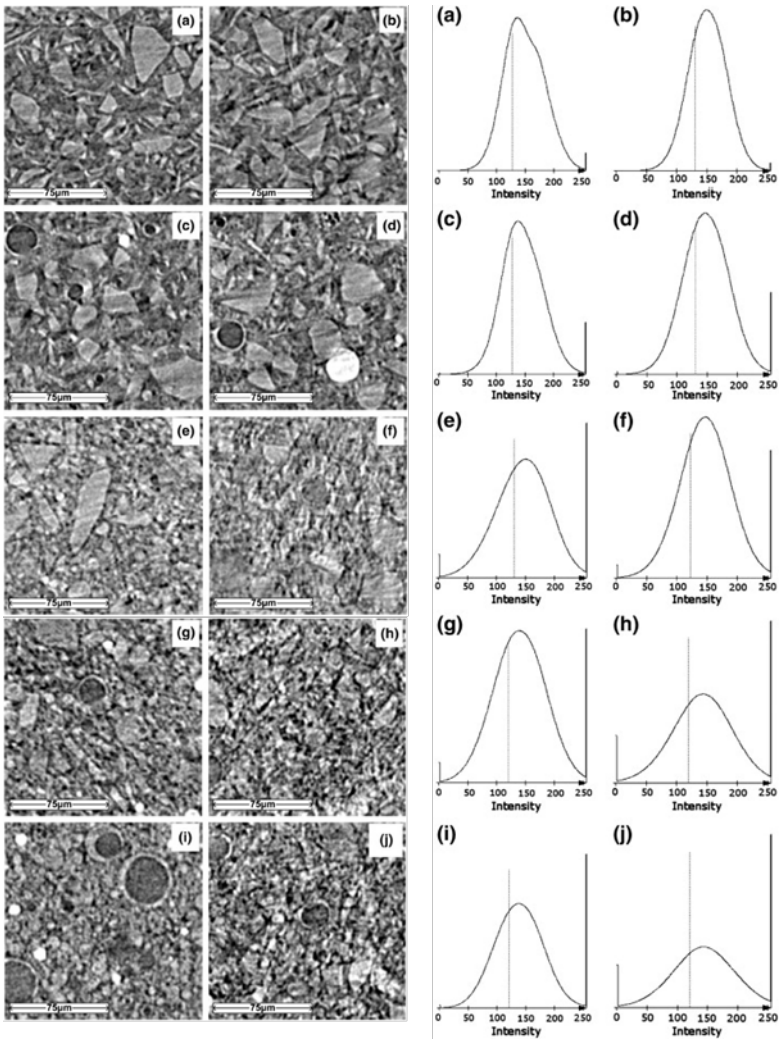


Figure 1-7: Low contrast in images leads to difficulty segmenting. Left) shows a reconstructed region of interest of a hydrating slag system. The vertical line in the histogram was determined to be the threshold value to segment the anhydrous particles from the hydration particles [32]

Another approach is to deconstruct the histogram into separate Gaussian curves. Research by Bossa et al. [35] used this approach to differentiate between voids, hydration products, and unhydrated dicalcium silicate ($C_2S$) and tricalcium silicate ($C_3S$). However, issues with thresholding to isolate solids from pores can be difficult as illustrated in Figure 1-8, which contains two histograms of a hydrated portland cement system subjected to leaching. Histogram A represents an unaltered layer that was not subjected to leaching, whereas histogram B experienced leaching [35]. In histogram A, there is no distinction between the void and solid phases; but some separation is observed in histogram B. While there was an attempt to segment between voids and solids (hydrated and unhydrated phases) using histogram deconstruction, there is no distinction

within the deconstructed Gaussian curves to differentiate distinct hydrated phases. As illustrated, the histogram deconstruction alone does not provide adequate segmentation of the image stack, particularly in the hydrated cement phases.

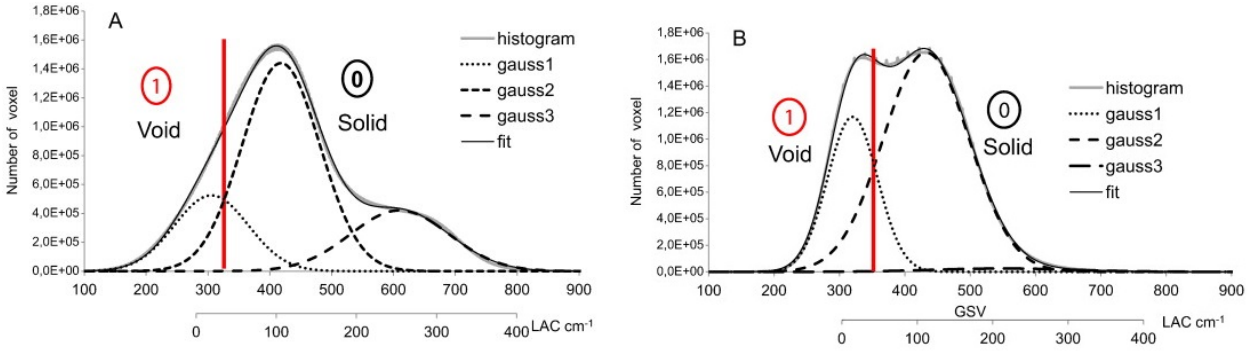


Figure 1-8: Histogram of the filtered volume and the best fit of the three calculated Gaussian curves, where gauss1 represents voids, gauss2 the solid hydrated phases, and gauss3 the solid unhydrated C2S and C3S phases. Histogram A is an unaltered layer of the cement paste not subjected to leaching. Histogram B is an altered layer of the cement paste subjected to leaching. Gauss3 disappears in histogram B due to dissolution from the leaching process. The vertical red line indicates the distinction between the void space and the solid phases. In histogram A, there is difficulty discerning between gauss1 and gauss2 prior to the deconstruction of the histogram. There is a slight difference between gauss1 and gauss2 in histogram B [35]. Significant improvements to the histograms, and therefore vastly more reliable segmentation, could be achieved with the addition of contrast agents that target specific hydrated phases.

Other researchers have shown limited success in differentiating phases in portland cement mortars using x-ray CT methods while characterizing the calcium leaching (decalcification) of C-S-H and CH phases [43, 110]. It was found in these studies that prior to leaching the hydrated phases of the samples had a nearly uniform linear attenuation coefficient. After 24 h of leaching, two main zones were observed in the cement paste phase, as shown in Figure 1-9. While these studies show promise in detecting different hydrated phases after exposure to deterioration (decalcification of C-S-H and CH), there is still little ability to accurately segment (in an unbiased and automated manner) the image between more than two hydrated cement phases [79], and often times between the hydrated cement phases and the aggregates.

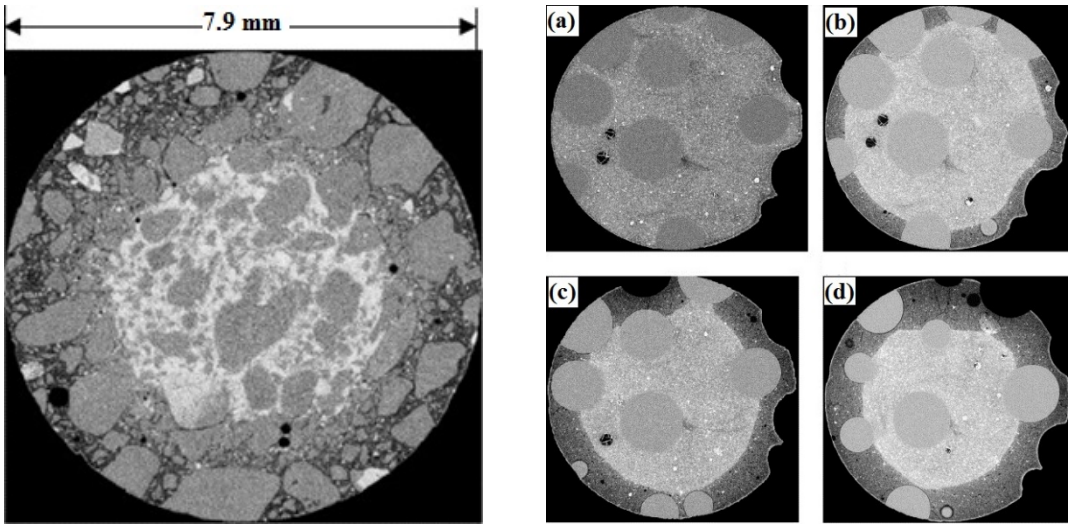


Figure 1-9: Enhancement of attenuation coefficient after decalcification of C-S-H and CH through leaching process. Left: Mortar sample made with natural sand aggregates after exposure to leaching conditions for 24 h. Two distinct zones are seen in the cement paste phase. An outer (darker) range with a lower density and an inner (lighter) section with a higher density, whereas the aggregate remains unchanged [110]. Right: Evolution of leaching in a mortar with round, glass aggregates. In image (a) the sample has not been exposed to leaching conditions. A near uniform greyscale value for the bulk paste is observed. The subsequent images [(b)-(d)] show the progression of the leaching process and an increase in the size of the leached zone. In image (b), after 11 hrs of exposure to leaching conditions, there was a prominent dissolution front approximately 600 μm from the face of the sample resulting in a distinct difference in the linear attenuation coefficient [43].

Few researchers have used x-ray CT to try to quantify solid phases found in cement paste. Work by Gallucci et al. [96] investigated the microstructural development of an ordinary portland cement paste with a water/cement ratio of 0.5. The sample size was 600 μm in diameter and were scanned at 1 d, 3 d, 7 d, 14 d, 28 d, and 60 d of hydration. In this research, the investigators were able to quantify the changes in porosity, volume of hydration products, and the amount of anhydrous cement grains during hydration at various ages. A resolution of 0.6835 μm/voxel allowed for differentiation of the phases and resulted in a histogram that was able to be segmented for quantification, as seen in Figure 1-10. While this research was successful at quantifying hydrated and unhydrated phases, they were unable to differentiate between individual hydration products.

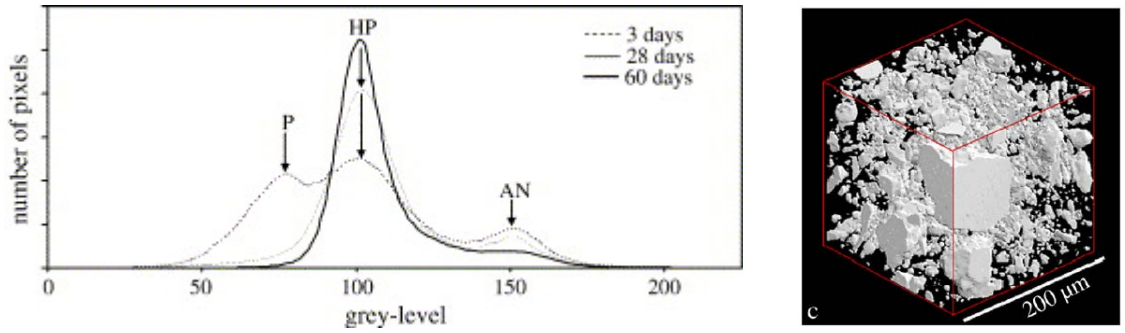


Figure 1-10: Left) Histogram of reconstructed image volumes at 3 d, 28 d, and 60 d. The histogram shows the ability to detect changes in porosity (P), hydration products (HP), and anhydrous phases (AN). Right) segmented quantity of unhydrated cement grains from a selected region of interest [96].

Similar to the work by Gallucci et al., work by Gastaldi et al. [94] investigated hydration behaviors of ordinary portland cement (OPC), calcium sufloaluminate cement (CSA), and a mix of OPC and CSA. The hydrating samples were scanned every 36 min for 12 h. Four pure phases were investigated in x-ray CT to correlate the measured greyscale value to the linear attenuation coefficient to be able to identify them in the hydrated cement pastes. These included the glass tube sample holder, gypsum, portlandite (represented by calcium hydroxide), and tetracalcium aluminoferrite ($C_4AF$). Good correlation, with an $R^2$ value of 0.99, indicated the ability to differentiate the variety of materials and phases. Theoretical greyscale values were determined based on the assumed linear attenuation coefficient for the remaining hydrated and unhydrated phases. Changes in the histogram were discovered as the cement paste hydrated in all three sample types, as seen in Figure 1-11. While the authors were able to quantify the changes in porosity of all three sample types, the quantity of individual hydration products was not reported. This research began investigating the ability to measure greyscale values of individual phases, but the ability to segment each phase became difficult due to the similar greyscale values reported and overlapping peaks in the histogram.

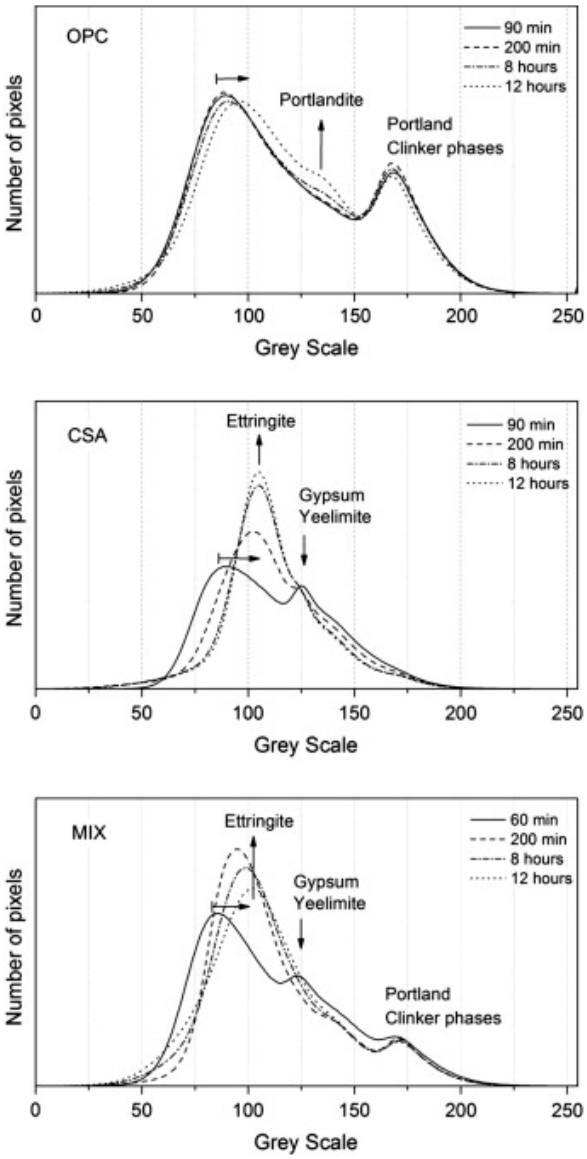


Figure 1-11: Changes in greyscale values of phases in OPC, CSA, and combination of OPC and CSA [94]

## 1.10. Improving contrast in x-ray CT images

A common approach used in soft tissue imaging to improve image contrast, and subsequent histogram segmentation, is to implement contrast agents. The success of using contrast agents in image segmentation and phase identification in the medical sciences provides promise that such an approach might also be used in applications in cementitious systems. The use of contrast agents to improve segmentation in mortars has been done. Soaking a hardened mortar sample in a 3% iodine solution in ethanol allowed for improved segmentation between the aggregates and the cement paste matrix. Although this improved the ability to isolate the aggregates from the cement

paste matrix, but not isolate individual hydrated phases [120]. Recently, it was shown that iodine could be used as an indicator in transmission x-ray microscopy to determine sorptivity of ions with varying degrees of saturation. It was shown that the iodine provided adequate in the radiographic projects to determine the sorptivity [121]. However, such an approach to improve contrast between individual primary and secondary phases has not been extensively studied, and cementitious systems have additional challenges over traditional medical imaging applications using contrast agents. This research aims to fill these gaps in knowledge.

Several requirements should be satisfied for contrast agents to be used to identify different phases in portland cement systems. Ideally, a contrast agent should exist in adequate quantity so that it will improve the absolute attenuation difference between the target phases by approximately two times [72], although this level of difference may not always be practical. In the case of concrete samples, contrast agents should be bound in the primary and secondary phases for continual monitoring. However, since different phases can form at different times (as in the case of AFm and AFt phases), and signature products of deterioration may form later (e.g. ettringite, Friedel salt, gypsum), contrast agents need to be activated as the target phases form. In other words, x-ray CT needs to distinguish between the primary and secondary hydrated phases (i.e., C-S-H, CH, AFm, AFt) and subsequent phases that form during deterioration processes. This will require the identification of optimum x-ray CT scanning energies for individual phases with contrast agents. The resultant mineral structures that form with the contrast agents should be thermodynamically stable for an adequate duration to scan the sample. Several researchers have shown that such incorporations of different phases with contrast agents are possible and is discussed in detail in section 1.11.

In order to achieve higher levels of x-ray attenuation, elements of higher atomic number are often used. Iodinated contrast agents (iodine) can be classified as either ionic or nonionic. Several techniques in the medical field have been implemented for dispersing contrast agents. These methods include small-molecule iodinated contrast agents, nanoparticle iodine-containing contrast agents, liposomal contrast agents, nanosuspensions, polymeric nanoparticles, lanthanide based contrast agents, gold nanoparticles, bismuth, and xenon gas [72]. While these methods have been successful in the past improving contrast in the medical field, it may be more difficult to achieve

adequate contrast in solids. Therefore, an understanding of solid formation and substitutions must be understood in hydrated portland cement phases to determine potential contrast agents.

### 1.11. Potential contrast agents

Mixing of heavy ions, that are potential contrast agents, into anhydrous cement with water can result in ion incorporation during the hydration process [122]. During this hydration the ions may be chemisorbed, precipitated, formed a surface compound to any of several cement component surfaces, formed inclusions, or have simultaneous occurrence of several of the aforementioned scenarios [123], as seen in Figure 1-12.

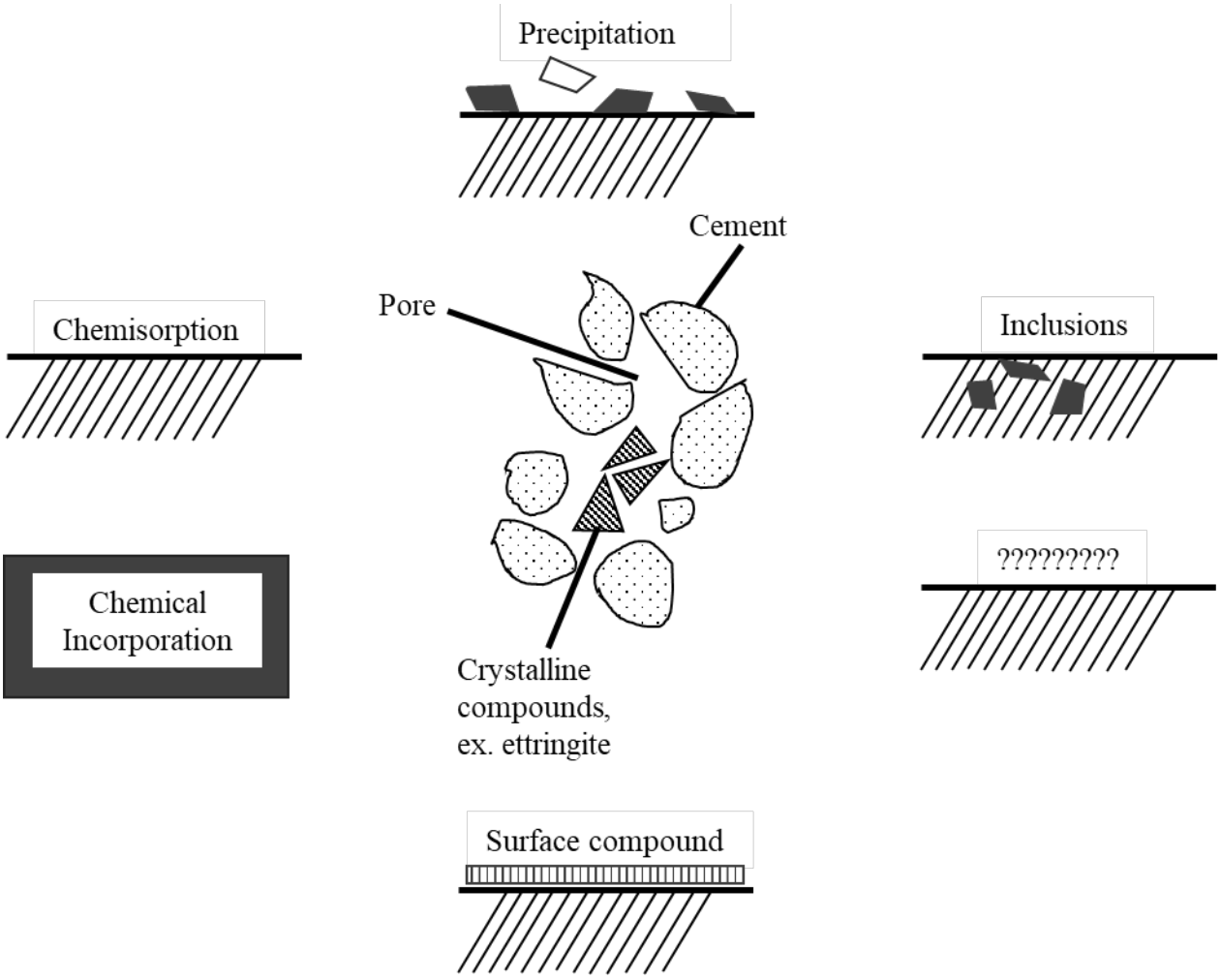


Figure 1-12: Possible incorporation mechanisms of ions in hydrated cement phases, redrawn from [123]

Hydration products from unhydrated calcium aluminate phases found in portland cement, $C_3A$, and to a lesser extent $C_4AF$, have the capability to incorporate ions that are known contrast agents

into the composition. Both AFm and AFt phases have been documented to allow various substitutions in their cationic or anionic positions [62, 122, 124-126]. Due to the relatively stable crystalline structure of CH, incorporating contrast agents to this phase will not be attempted; however, by incorporating contrast agents to other primary and secondary phases, the CH phase will be recognized through x-ray CT as an abundant unmarked phase. Discussion of potential contrast agents for C-S-H, AFt, and AFm can be found in sections 1.11.1, 1.11.2, 1.11.3, respectively.

*1.11.1. Potential contrast agents for C-S-H*

Several successful modifications to the C-S-H structure has been reported [127-129]. This includes sodium, hexadecyltrimethylammonium [127], lead, chromium [129], and the interaction of methylene blue dye [128]. There is great potential for incorporation of other contrast agents due to the large number of structural sites for cations and anions to bind. Due to the amorphous nature of C-S-H, crystal substitutions are unlikely [122]. Ion immobilization in C-S-H can help be described by the Richardson-Groves model [130], as follows:

- $Ca_xH_{(6n-2x)}(Si_{1-a}R_a^{[IV]})_{(3n-1)}O_{(9n-2)}\cdot A^{c+}_{a(3n-1)/c}\cdot zCa(OH)_2\cdot mH_2O$ Equation 1-10
  - Where: $x = 0.5(6n-w)$
  - And: $z = 0.5[w+n(y-2)]$
  - And for: $0 < y < 2$; $n(2-y) < w < 2n$
    - $2 < y < 4$; $0 < w < 2n$
    - $4 < y < 6$; $0 < w < n(6-y)$
  - And $0 < a < n-1/3n-1$
  - $R^{[IV]}$ is a trivalent cation in tetrahedral coordination. This is typically $Al^{3+}$ or $Fe^{3+}$
  - $A^{c+}$ is an interlayer ion which charge balances the $R^{3+}$ substitution for $Si^{4+}$. $A^{c+}$ is typically a monovalent alkali cation or $Ca^{2+}$

Alkali cations are thought to substitute into the interlayer sites, which corresponds to the $A^{c+}$ position in the Richardson-Groves model [130]. Potential contrast agents, such as cadmium [129, 131] and alkali metals [127], have been substituted into the C-S-H structure. Cadmium has a k-shell binding energy of 26.7 keV, which would be suitable for the expected scanning energies at a synchrotron facility. Past research indicated cadmium can be immobilized through precipitation as

hydroxides and carbonates, but not through substitution in C-S-H [132]. Further research indicated that cadmium was stabilized in the form of $Cd(OH)_2$. This hydroxide was incorporated into the layer structure of C-S-H [133]. Iodine was another potential candidate as a contrast agent for C-S-H, and thermodynamic modeling suggests iodine ($I^-$) can be immobilized through sorption into C-S-H. Iodine was absorbed as $I^-$ at an uptake value of 19% in C-S-H with a Ca/Si ratio of 1.7 [134]. Lastly, in 1.1-nm tobermorite, it was discovered a small amount of cesium would pair with aluminum in substitution of silica [135]. A summary of species that have been reported to be incorporated into C-S-H are summarized in Table 1-1.

Table 1-1: Reported ions that can be immobilized by C-S-H. Recreated from [122]

| **Species Reported as Immobilized by Calcium Silicate Hydrate Gel (C-S-H)** |
|---|
| Li, Na, K, Rb, Cs |
| Mg, Ni, Co, Hg, Zn, Cd |
| Al, Fe, Cr |
| Pb, U |
| Cl, I |
| $OH^{-1}$, $CO_3^{-2}$, $SO_4^{-2}$ |

Several of the ions reported by Gougar [122] would be candidates for the expected energy range used in synchrotron tomography. Cesium was chosen as a candidate for further investigation due to the availability of Cs containing compounds.

*1.11.2. Potential contrast agents for AFt*

The AFt phase is a large group of minerals with a general formula of $3CaO{\cdot}(Al,Fe)_2O_3{\cdot}3CaX_2{\cdot}nH_2O$, where X is one monovalent anion or half divalent anion [57]. The crystalline structure is composed of two parts; positively charged columns $[Ca_3Al\,(OH)_6{\cdot}12H_2O]^{3+}$ and negatively charged channels $[3X{\cdot}nH_2O]^{3-}$. The AFt phase is known to bind a variety of anions [57, 58, 62, 126, 136-139] and cationic substitutions can occur [124, 140]. AFt has the ability to withstand modest deviations in the chemical composition without changing its crystalline structure. The change in composition typically occurs as ionic substitution at the crystal chemical level. Several ions in ettringite can participate in ionic substitution. These ions are $Ca^{2+}$, $Al^{3+}$, $SO_2^{2-}$

, and $OH^-$ [122]. Replacement of the sulfate in AFt is achieved relatively easy with oxyanions of similar structure and radius, such as chromate, arsenate, vanadate, and selenite [62, 137, 141, 142].

While some of these substitutions have -shell binding energies outside the expected range, there is potential within the same group for incorporation into the AFt structure. Success in substitution with $SO_4^{2-}$ with $MoO_4^-$ [62] in the anion structure and $Sr^{2+}$ [143] and the potential for $Ba^{2+}$ replacing $Ca^{2+}$ [144] in the cationic structure has been observed. These ions have k-shell binding energies in the expected synchrotron radiation energy. A summary of known ions that will substitute in to the various sites in the crystalline structure of AFt are found in Table 1-2. Furthermore, it should be noted the crystalline lattice site for substitution in AFt can accommodate a specific range of ionic radii without changing the crystalline structure. A summary of the ionic radii sizes for substitution sites is found in Table 1-3.

Table 1-2: Reported ion substitutions in ettringite. Adapted from [122, 126]. Results from previous research indicated that AFt will not uptake $I^-$ [145]

| **$(Ca^{+2})^{VIII}$ site** | **$(Al^{+3})^{VI}$ site** | **$(SO_4^{-2})$ site** | **$(OH^{-1})$ site** |
|---|---|---|---|
| $Sr^{+2}$ | $Cr^{+3}$ | $B(OH)_4^{-1}$ | $O^{-2}$ |
| $Ba^{+2}$ | $Si^{+4}$ | $CO_3^{-2}$ | |
| $Pb^{+2}$ | $Fe^{+3}$ | $Cl^{-1}$ | |
| $Cd^{+2}$ | $Mn^{+3}$ | $OH^{-1}$ | |
| $Co^{+2}$ | $Ni^{+3}$ | $CrO_4^{-2}$ | |
| $Ni^{+2}$ | $Co^{+3}$ | $AsO_4^{-3}$ | |
| $Zn^{+2}$ | $Ti^{+3}$ | $SeO_4^{-2}$ | |
| | | $VO_4^{-3}$ | |
| | | $BrO_3^{-1}$ | |
| | | $NO_3^{-1}$ | |
| | | $MoO_4^{-2}$ | |
| | | $ClO_3^{-1}$ | |
| | | $SO_3^{-2}$ | |
| | | $IO_3^{-1}$ | |

Table 1-3: Ionic radii limitations for crystal substitutions at different lattice sites for AFt. Adapted from [122]

| Substitution site | Ionic radii range (Å) |
|---|---|
| $Ca^{2+}$ | 0.90-1.42 |
| $Al^{3+}$ | 0.42-0.76 |
| $SO_4^{2-}$ | 0.62-3.71 |
| $OH^{1-}$ | 0.62-1.38 |

*1.11.3. Potential contrast agents for AFm*

AFm phases belong to the lamellar double hydroxide (LDH) family, which is a type of anionic clay material with cationic brucite layers with exchangeable interlayer anions [64]. Most LDHs have relatively weak interlayer bonding, which results in the ability to capture inorganic anions by both surface adsorption and anion exchange [65, 66]. The structure is composed of positively charged outer layers $[Ca_2Al(OH)_6]^+$ and negatively charged interlayers $[X{\cdot}xH_2O]^-$, where X is an exchangeable singly charged (e.g. chloride) or half-doubly charged anion (e.g. sulfate, carbonate, aluminosilicate). The anion present in the AFm phase is sensitive to the cement composition, as well as the service environment. Anions that may be present in portland cement systems are hydroxide, sulfate, and carbonate. In blended cements, aluminosilicate anions are typically present. The AFm phase is known to incorporate singly charged or half doubly charged anions [63]. Several studies have shown that the AFm phase has successfully incorporated singly charged anions into the interlayer [57, 146-157], half doubly charged anions [57, 146, 155, 158-162], and multiple anionic compounds [155, 158-162]. While successful substitution of anions into the AFm structure has occurred, the k-shell binding energy for these ions is not necessarily within the appropriate x-ray energy range for providing additional contrast during scanning. One potential contrast agent for the AFm phase with a k-shell binding energy within the potential scanning range is iodine (33.2 keV), which is a known anion that may be incorporated [155-157].

## 1.12. Summary

The goal of this literature review was to inform the reader of phase formation in hydrating portland cement systems, success and limitations in test methods to characterize and quantify these phases. The primary focus was limitations on using x-ray CT to quantify solid phases due to low contrast

in the reconstructed image volume. A discussion on potential uses of contrast agents in x-ray CT could be implemented to quantify the four main hydrated phases in a non-destructive manner, and the potential for long-term monitoring of changes in these phases caused by continued hydration or deterioration mechanisms. From the literature review, several knowledge gaps were identified leading to the following three research objectives:

- Objective 1: Perform experimental studies to develop techniques to best incorporate elements or molecules as contrast agents in synthesized primary and secondary phases.

- Objective 2: Implement x-ray CT studies to differentiate synthesized phases with and without contrast agents. Pure phase imaging will allow for a basic understanding of potentially difficult phases to segment. The potential for low contrast will provide the understanding of which phases may need contrast agents to properly quantify.

- Objective 3: Determine appropriate segmenting algorithms to accurately segment image volumes where phases may exhibit low contrast, as well as phases with contrast agents.

The following chapters in this dissertation describe the research methods used to fulfill these objectives. Chapter 2 summarizes the experimental techniques and methods used throughout the dissertation. Chapters 3-5 presents the work completed to fulfill the research objectives defined in this chapter. Chapter 6 concludes the work presented and suggested research to continue. This work provides a significant contribution by expanding the role of x-ray CT as a viable tool for non-destructive evaluation of cementitious systems.

## 1.13. References

[1] I. Chen, M.G. Juenger, Synthesis and hydration of calcium sulfoaluminate-belite cements with varied phase compositions, Journal of Materials Science, 46 (2011) 2568-2577.

[2] P. Duxson, A. Fernández-Jiménez, J.L. Provis, G.C. Lukey, A. Palomo, J.S.J. van Deventer, Geopolymer technology: The current state of the art, Journal of Materials Science, 42 (2007) 2917-2933.

[3] E. Gartner, Are there any practical alternatives to the manufacture of portland cement clinker?, Journal of the Chinese Ceramic Society, 40 (2012) 61-68.

[4] C. Gosselin, E. Gallucci, K. Scrivener, Influence of self heating and $Li_2SO_4$ addition on the microstructural development of calcium aluminate cement, Cement and Concrete Research, 40 (2010) 1555-1570.

[5] J.H. Ideker, C.G. Gosselin, R. Barborak, An alternative repair material: Basics and practical testing calcium aluminate cements, Concrete International, 35 (2013) 33-37.

[6] M.C.G. Juenger, F. Winnefeld, J.L. Provis, J.H. Ideker, Advances in alternative cementitious binders, Cement and Concrete Research, 41 (2011) 1232-1243.

[7] A. Radlińska, J. Yost, M. Salera, Material properties of structurally viable alkali-activated fly ash concrete, Journal of Materials in Civil Engineering, 25 (2013) 1456-1464.

[8] C. Shi, A.F. Jiménez, A. Palomo, New cements for the 21st century: The pursuit of an alternative to portland cement, Cement and Concrete Research, 41 (2011) 750-763.

[9] R. Alizadeh, J.J. Beaudoin, L. Raki, V. Terskikh, C-S-H/polyaniline nanocomposites prepared by in situ polymerization, Journal of Materials Science, 46 (2011) 460-467.

[10] J.J. Beaudoin, H. Drame, L. Raki, R. Alizadeh, Formation and characterization of calcium silicate hydrate-hexadecyltrimethylammonium nanostructure, Journal of Materials Research, 23 (2008) 2804-2815.

[11] J.J. Beaudoin, H. Drame, L. Raki, R. Alizadeh, Formation and properties of C-S-H-PEG nano-structures, Materials and Structures, 42 (2009) 1003-1014.

[12] R. Khoshnazar, L. Raki, J. Beaudoin, R. Alizadeh, Solvent exchange in sulphoaluminate phases. Part I: Ettringite, Advances in Cement Research, 25 (2013) 314-321.

[13] R. Khoshnazar, L. Raki, J. Beaudoin, R. Alizadeh, Solvent exchange in sulfoaluminate phases. Part II: Monosulfate, Advances in Cement Research, 25 (2013) 322-331.

[14] F. Sanchez, K. Sobolev, Nanotechnology in concrete – A review, Construction and Building Materials, 24 (2010) 2060-2071.

[15] M. Vandamme, F.-J. Ulm, P. Fonollosa, Nanogranular packing of C–S–H at substochiometric conditions, Cement and Concrete Research, 40 (2010) 14-26.

[16] P.J.M. Monteiro, A.P. Kirchheim, S. Chae, P. Fischer, A.A. MacDowell, E. Schaible, H.R. Wenk, Characterizing the nano and micro structure of concrete to improve its durability, Cement and Concrete Composites, 31 (2009) 577-584.

[17] K. Tosun, B. Baradan, Effect of ettringite morphology on DEF-related expansion, Cement and Concrete Composites, 32 (2010) 271-280.

[18] P.E. Stutzman, J.R. Clifton, Specimen Preparation for Scanning Electron Microscopy, Twenty-First International Conference on Cement Microscopy, Las Vegas, NV, April 25-29, 1999, 1999, pp. 10-22.

[19] K.O. Kjellsen, A. Monsøy, K. Isachsen, R.J. Detwiler, Preparation of flat-polished specimens for SEM-backscattered electron imaging and x-ray microanalysis—importance of epoxy impregnation, Cement and Concrete Research, 33 (2003) 611-616.

[20] V. Cnudde, M.N. Boone, High-resolution x-ray computed tomography in geosciences: A review of the current technology and applications, Earth-Science Reviews, 123 (2013) 1-17.

[21] J. Dewanckele, T. De Kock, G. Fronteau, H. Derluyn, P. Vontobel, M. Dierick, L. Van Hoorebeke, P. Jacobs, V. Cnudde, Neutron radiography and x-ray computed tomography for quantifying weathering and water uptake processes inside porous limestone used as building material, Materials Characterization, 88 (2014) 86-99.

[22] D. Wildenschild, A.P. Sheppard, X-ray imaging and analysis techniques for quantifying pore-scale structure and processes in subsurface porous medium systems, Advances in Water Resources, 51 (2013) 217-246.

[23] E.N. Landis, D.T. Keane, X-ray microtomography, Materials Characterization, 61 (2010) 1305-1316.

[24] R.A. Ketcham, W.D. Carlson, Acquisition, optimization and interpretation of x-ray computed tomographic imagery: aApplications to the geosciences, Computers & Geosciences, 27 (2001) 381-400.

[25] D. Derome, M. Griffa, M. Koebel, J. Carmeliet, Hysteretic swelling of wood at cellular scale probed by phase-contrast x-ray tomography, Journal of Structural Biology, 173 (2011) 180-190.

[26] N. Limodin, L. Salvo, E. Boller, M. Suéry, M. Felberbaum, S. Gailliègue, K. Madi, In situ and real-time 3-D microtomography investigation of dendritic solidification in an Al–10 wt.% Cu alloy, Acta Materialia, 57 (2009) 2300-2310.

[27] L.O. Lindgren, Medical CAT-scanning: X-ray absorption coefficients, CT-numbers and their relation to wood density, Wood Science and Technology, 25 (1991) 341-349.

[28] P.J. Schilling, B.R. Karedla, A.K. Tatiparthi, M.A. Verges, P.D. Herrington, X-ray computed microtomography of internal damage in fiber reinforced polymer matrix composites, Composites Science and Technology, 65 (2005) 2071-2078.

[29] S. Terzi, L. Salvo, M. Suéry, N. Limodin, J. Adrien, E. Maire, Y. Pannier, M. Bornert, D. Bernard, M. Felberbaum, M. Rappaz, E. Boller, In situ x-ray tomography observation of inhomogeneous deformation in semi-solid aluminium alloys, Scripta Materialia, 61 (2009) 449-452.

[30] W.R. Webb, W.E. Brant, N.M. Major, Fundamentals of body CT, 4th ed., Saunders Elsevier, Philadelphia, PA, 2014.

[31] U. Rattanasak, K. Kendall, Pore structure of cement/pozzolan composites by x-ray microtomography, Cement and Concrete Research, 35 (2005) 637-640.

[32] J.L. Provis, R.J. Myers, C.E. White, V. Rose, J.S.J. van Deventer, X-ray microtomography shows pore structure and tortuosity in alkali-activated binders, Cement and Concrete Research, 42 (2012) 855-864.

[33] T.S. Yun, K.Y. Kim, J. Choo, D.H. Kang, Quantifying the distribution of paste-void spacing of hardened cement paste using x-ray computed tomography, Materials Characterization, 73 (2012) 137-143.

[34] S. Lu, E.N. Landis, D.T. Keane, X-ray microtomographic studies of pore structure and permeability in portland cement concrete, Materials and Structures, 39 (2006) 611-620.

[35] N. Bossa, P. Chaurand, J. Vicente, D. Borschneck, C. Levard, O. Aguerre-Chariol, J. Rose, Micro- and nano-x-ray computed-tomography: A step forward in the characterization of the pore network of a leached cement paste, Cement and Concrete Research, 67 (2015) 138-147.

[36] K.Y. Kim, T.S. Yun, K.P. Park, Evaluation of pore structures and cracking in cement paste exposed to elevated temperatures by x-ray computed tomography, Cement and Concrete Research, 50 (2013) 34-40.

[37] M.A.B. Promentilla, T. Sugiyama, T. Hitomi, N. Takeda, Characterizing the 3D pore structure of hardened cement paste with synchrotron microtomography, Journal of Advanced Concrete Technology, 6 (2008) 273-286.

[38] M.A.B. Promentilla, T. Sugiyama, T. Hitomi, N. Takeda, Quantification of tortuosity in hardened cement pastes using synchrotron-based x-ray computed microtomography, Cement and Concrete Research, 39 (2009) 548-557.

[39] M. Lanzón, V. Cnudde, T. de Kock, J. Dewanckele, X-ray microtomography (μ-CT) to evaluate microstructure of mortars containing low density additions, Cement and Concrete Composites, 34 (2012) 993-1000.

[40] T. Sugiyama, M.A.B. Promentilla, T. Hitomi, N. Takeda, Application of synchrotron microtomography for pore structure characterization of deteriorated cementitious materials due to leaching, Cement and Concrete Research, 40 (2010) 1265-1270.

[41] D. Asahina, E.N. Landis, J.E. Bolander, Modeling of phase interfaces during pre-critical crack growth in concrete, Cement and Concrete Composites, 33 (2011) 966-977.

[42] H. Elaqra, N. Godin, G. Peix, M. R'Mili, G. Fantozzi, Damage evolution analysis in mortar, during compressive loading using acoustic emission and x-ray tomography: Effects of the sand/cement ratio, Cement and Concrete Research, 37 (2007) 703-713.

[43] T. Rougelot, N. Burlion, D. Bernard, F. Skoczylas, About microcracking due to leaching in cementitious composites: X-ray microtomography description and numerical approach, Cement and Concrete Research, 40 (2010) 271-283.

[44] J.S. Lawler, D.T. Keane, S.P. Shah, Measuring three-dimensional damage of mortar in compression with x-ray microtomography and digital image correlation, American Concrete Institute SP 189, (2000) 187-202.

[45] H.F.W. Taylor, Cement Chemistry, 2nd Edition ed., Thomas Telford Publishing, London, England, 1997.

[46] A.M. Neville, Properties of Concrete, 4th Edition ed., John Wiley & Sons, Inc., New York, NY, 1996.

[47] P.K. Mehta, P.J.M. Monteiro, Concrete: Microstructure, properties and materials, Third ed., New York, 2006.

[48] Lea's Chemistry of Cement and Concrete, Elsevier - Butterworth-Heinemann, Oxford, UK, 1998.

[49] R.F. Feldman, P.J. Sereda, A model for hydrated Portland cement paste as deduced from sorption-length change and mechanical properties, Matériaux et Construction, 1 (1968) 509-520.

[50] R.B. Williamson, Solidification of portland cement, Progress in Materials Science, 15 (1972) 189-286.

[51] G.W. Groves, TEM studies of cement hydration, MRS Online Proceedings Library, 85 (1986) 3-12.

[52] H.M. Jennings, B.J. Dalgleish, P.L. Pratt, Morphological development of hydrating tricalcium silicate as examined by electron microscopy techniques, Journal of the American Ceramic Society, 64 (1981) 567-572.

[53] T.D. Ciach, J.E. Gillott, E.G. Swenson, P.J. Sereda, Microstructure of calcium silicate hydrates, Cement and Concrete Research, 1 (1971) 13-25.

[54] P. Hewlett, Lea's Chemistry of Cement and Concrete, 4th ed., Burlington : Elsevier Science, Burlington, 2003.

[55] I.G. Richardson, Tobermorite/jennite- and tobermorite/calcium hydroxide-based models for the structure of C-S-H: Applicability to hardened pastes of tricalcium silicate, β-dicalcium silicate, portland cement, and blends of portland cement with blast-furnace slag, metakaolin, or silica fume, Cement and Concrete Research, 34 (2004) 1733-1777.

[56] I.G. Richardson, The nature of C-S-H in hardened cements, Cement and Concrete Research, 29 (1999) 1131-1147.

[57] J.-B. Champenois, A. Mesbah, C. Cau Dit Coumes, G. Renaudin, F. Leroux, C. Mercier, B. Revel, D. Damidot, Crystal structures of Boro-AFm and sBoro-AFt phases, Cement and Concrete Research, 42 (2012) 1362-1370.

[58] A.E. Moore, H.F.W. Taylor, Crystal structure of ettringite, Acta Crystallographica Section B, 26 (1970) 386-393.

[59] D.J. Hassett, G.J. McCarthy, P. Kumarathasan, D. Pflughoeft-Hassett, Synthesis and characterization of selenate and sulfate-selenate ettringite structure phases, Materials Research Bulletin, 25 (1990) 1347-1354.

[60] L.J. Struble, P.W. Brown, An evaluation of ettringite and related compounds for use in the solar energy storage, US Department of Commerce, 1982, pp. 11.

[61] F.M. Lea, The chemistry of cement and concrete, 3rd edition, Chemical Publishing Company, Inc., Ney York, NY, 1971.

[62] G.J. McCarthy, D.J. Hassett, J.A. Bender, Synthesis, Crystal chemistry and stability of ettringite, a material with potential applications in hazardous waste immobilization, MRS Online Proceedings Library, 245 (1991) 129-140.

[63] T. Matschei, B. Lothenbach, F.P. Glasser, The AFm phase in portland cement, Cement and Concrete Research, 37 (2007) 118-130.

[64] D. Zhang, Y. Jia, J. Ma, Z. Li, Removal of arsenic from water by Friedel's salt (FS: $3CaO{\cdot}Al_2O_3{\cdot}CaCl_2{\cdot}10H_2O$), Journal of Hazardous Materials, 195 (2011) 398-404.

[65] K.-H. Goh, T.-T. Lim, Z. Dong, Application of layered double hydroxides for removal of oxyanions: A review, Water Research, 42 (2008) 1343-1368.

[66] S. Miyata, Anion-exchange properties of hydrotalcite-like compounds, Clays and Clay Minerals, 31 (1983) 305-311.

[67] T. Kwon, G.A. Tsigdinos, T.J. Pinnavaia, Pillaring of layered double hydroxides (LDH's) by polyoxometalate anions, Journal of the American Chemical Society, 110 (1988) 3653-3654.

[68] U.A. Birnin-Yauri, F.P. Glasser, Friedel's salt, $Ca_2Al(OH)_6(Cl,OH){\cdot}2H_2O$: Its solid solutions and their role in chloride binding, Cement and Concrete Research, 28 (1998) 1713-1723.

[69] B.E. Warren, X-ray diffraction, Addison-Wesley Publication Company, Reading, MA, 1969.

[70] V.S. Ramachandran, J.J. Beaudoin, Handbook of analytical techniques in concrete science and technology, William Andrew Publishing, LLC, Norwich, New York.

[71] M.E. Brown, Introduction to thermal analysis, Chapman and Hall, UK, 1988.

[72] H. Lusic, M.W. Grinstaff, X-ray-computed tomography contrast agents, Chemical Reviews, 113 (2012) 1641-1666.

[73] L. Salvo, P. Cloetens, E. Maire, S. Zabler, J.J. Blandin, J.Y. Buffière, W. Ludwig, E. Boller, D. Bellet, C. Josserond, X-ray micro-tomography an attractive characterisation technique in materials science, Nuclear Instruments and Methods in Physics Research Section B: Beam Interactions with Materials and Atoms, 200 (2003) 273-286.

[74] J.H. Kinney, M.C. Nichols, X-Ray Tomographic microscopy (XTM) using synchrotron radiation, Annual Review of Materials Science, 22 (1992) 121-152.

[75] K. Wan, Q. Xu, Y. Wang, G. Pan, 3D spatial distribution of the calcium carbonate caused by carbonation of cement paste, Cement and Concrete Composites, 45 (2014) 255-263.

[76] F. Batool, V. Bindiganavile, Air-void size distribution of cement based foam and its effect on thermal conductivity, Construction and Building Materials, 149 (2017) 17-28.

[77] J. Schock, S. Liebl, K. Achterhold, F. Pfeiffer, Obtaining the spacing factor of microporous concrete using high-resolution dual energy x-ray micro CT, Cement and Concrete Research, 89 (2016) 200-205.

[78] S. Diamond, E. Landis, Microstructural features of a mortar as seen by computed microtomography, Mater Struct, 40 (2007) 989-993.

[79] D.A. Lange, Y. Jia, Y.S. Liu, X-ray nanotomography of cement microstructure, American Concrete Institute SP 270, (2010) 9-16.

[80] R. Cepuritis, B.J. Wigum, E.J. Garboczi, E. Mørtsell, S. Jacobsen, Filler from crushed aggregate for concrete: Pore structure, specific surface, particle shape and size distribution, Cement and Concrete Composites, 54 (2014) 2-16.

[81] S.T. Erdogan, P.N. Quiroga, D.W. Fowler, H.A. Saleh, R.A. Livingston, E.J. Garboczi, P.M. Ketcham, J.G. Hagedorn, S.G. Satterfield, Three-dimensional shape analysis of coarse aggregates: New techniques for and preliminary results on several different coarse aggregates and reference rocks, Cement and Concrete Research, 36 (2006) 1619-1627.

[82] E.J. Garboczi, Three-dimensional mathematical analysis of particle shape using x-ray tomography and spherical harmonics: Application to aggregates used in concrete, Cement and Concrete Research, 32 (2002) 1621-1638.

[83] P. Trtik, B. Münch, W.J. Weiss, A. Kaestner, I. Jerjen, L. Josic, E. Lehmann, P. Lura, Release of internal curing water from lightweight aggregates in cement paste investigated by neutron and x-ray tomography, Nuclear Instruments and Methods in Physics Research Section A: Accelerators, Spectrometers, Detectors and Associated Equipment, 651 (2011) 244-249.

[84] S.C. de Wolski, J.E. Bolander, E.N. Landis, An in-situ x-ray microtomography study of split cylinder fracture in cement-based materials, Experimental Mechanics, 54 (2014) 1227-1235.

[85] D. Fukuda, Y. Nara, Y. Kobayashi, M. Maruyama, M. Koketsu, D. Hayashi, H. Ogawa, K. Kaneko, Investigation of self-sealing in high-strength and ultra-low-permeability concrete in water using micro-focus x-ray CT, Cement and Concrete Research, 42 (2012) 1494-1500.

[86] J. Wang, J. Dewanckele, V. Cnudde, S. Van Vlierberghe, W. Verstraete, N. De Belie, X-ray computed tomography proof of bacterial-based self-healing in concrete, Cement and Concrete Composites, 53 (2014) 289-304.

[87] E.N. Landis, D.T. Keane, X-ray microtomography for fracture studies in cement-based materials, Proceedings of SPIE 3772: Developments in x-ray tomography II, 1999, pp. 105-113.

[88] E.N. Landis, E.N. Nagy, D.T. Keane, Microstructure and fracture in three dimensions, Engineering Fracture Mechanics, 70 (2003) 911-925.

[89] G.L. Balázs, O. Czoboly, É. Lublóy, K. Kapitány, Á. Barsi, Observation of steel fibres in concrete with computed tomography, Construction and Building Materials, 140 (2017) 534-541.

[90] A.C. Bordelon, J.R. Roesler, Spatial distribution of synthetic fibers in concrete with x-ray computed tomography, Cement and Concrete Composites, 53 (2014) 35-43.

[91] A. Qsymah, R. Sharma, Z. Yang, L. Margetts, P. Mummery, Micro x-ray computed tomography image-based two-scale homogenisation of ultra high performance fibre reinforced concrete, Construction and Building Materials, 130 (2017) 230-240.

[92] J. Adrien, S. Meille, S. Tadier, E. Maire, L. Sasaki, In-situ x-ray tomographic monitoring of gypsum plaster setting, Cement and Concrete Research, 82 (2016) 107-116.

[93] T.J. Chotard, M.P. Boncoeur-Martel, A. Smith, J.P. Dupuy, C. Gault, Application of x-ray computed tomography to characterise the early hydration of calcium aluminate cement, Cement and Concrete Composites, 25 (2003) 145-152.

[94] D. Gastaldi, F. Canonico, L. Capelli, E. Boccaleri, M. Milanesio, L. Palin, G. Croce, F. Marone, K. Mader, M. Stampanoni, In situ tomographic investigation on the early hydration behaviors of cementing systems, Construction and Building Materials, 29 (2012) 284-290.

[95] S. Das, P. Yang, S.S. Singh, J.C.E. Mertens, X. Xiao, N. Chawla, N. Neithalath, Effective properties of a fly ash geopolymer: Synergistic application of x-ray synchrotron tomography, nanoindentation, and homogenization models, Cement and Concrete Research, 78 (2015) 252-262.

[96] E. Gallucci, K. Scrivener, A. Groso, M. Stampanoni, G. Margaritondo, 3D experimental investigation of the microstructure of cement pastes using synchrotron x-ray microtomography (μCT), Cement and Concrete Research, 37 (2007) 360-368.

[97] J. Han, W. Sun, G. Pan, C. Wang, H. Rong, Application of x-ray computed tomography in characterization microstructure changes of cement pastes in carbonation process, Journal of Wuhan University Technology-Materials Science Editition, 27 (2012) 358-363.

[98] M.B. Leite, P.J.M. Monteiro, Microstructural analysis of recycled concrete using x-ray microtomography, Cement and Concrete Research, 81 (2016) 38-48.

[99] J.L. Provis, A. Hajimohammadi, C.E. White, S.A. Bernal, R.J. Myers, R.P. Winarski, V. Rose, T.E. Proffen, A. Llobet, J.S.J. van Deventer, Nanostructural characterization of geopolymers by advanced beamline techniques, Cement and Concrete Composites, 36 (2013) 56-64.

[100] S. Erdem, X-ray computed tomography and fractal analysis for the evaluation of segregation resistance, strength response and accelerated corrosion behaviour of self-compacting lightweight concrete, Construction and Building Materials, 61 (2014) 10-17.

[101] M. Zhang, Y. He, G. Ye, D.A. Lange, K.v. Breugel, Computational investigation on mass diffusivity in portland cement paste based on x-ray computed microtomography (μCT) image, Construction and Building Materials, 27 (2012) 472-481.

[102] T. Suzuki, H. Ogata, R. Takada, M. Aoki, M. Ohtsu, Use of acoustic emission and x-ray computed tomography for damage evaluation of freeze-thawed concrete, Construction and Building Materials, 24 (2010) 2347-2352.

[103] D. Hernández-Cruz, C.W. Hargis, J. Dominowski, M.J. Radler, P.J.M. Monteiro, Fiber reinforced mortar affected by alkali-silica reaction: A study by synchrotron microtomography, Cement and Concrete Composites, 68 (2016) 123-130.

[104] B. Dong, G. Fang, Y. Liu, P. Dong, J. Zhang, F. Xing, S. Hong, Monitoring reinforcement corrosion and corrosion-induced cracking by x-ray microcomputed tomography method, Cement and Concrete Research, 100 (2017) 311-321.

[105] H.E. Martz, D.J. Scheberk, G. Patrick Roberson, P.J.M. Montiero, Computerized tomography analysis of reinforced concrete, ACI Materials Journal, 90 (1993) 259-264.

[106] A. Michel, B.J. Pease, M.R. Geiker, H. Stang, J.F. Olesen, Monitoring reinforcement corrosion and corrosion-induced cracking using non-destructive x-ray attenuation measurements, Cement and Concrete Research, 41 (2011) 1085-1094.

[107] N.N. Naik, A.C. Jupe, S.R. Stock, A.P. Wilkinson, P.L. Lee, K.E. Kurtis, Sulfate attack monitored by microCT and EDXRD: Influence of cement type, water-to-cement ratio, and aggregate, Cement and Concrete Research, 36 (2006) 144-159.

[108] N.N. Naik, K.E. Kurtis, A.P. Wilkinson, A.C. Jupe, S.R. Stock, Sulfate deterioration of cement-based materials examined by x-ray microtomography, Proceedings of SPIE 5535, 2004, pp. 442-452.

[109] S.R. Stock, N.K. Naik, A.P. Wilkinson, K.E. Kurtis, X-ray microtomography (microCT) of the progression of sulfate attack of cement paste, Cement and Concrete Research, 32 (2002) 1673-1675.

[110] N. Burlion, D. Bernard, D. Chen, X-ray microtomography: Application to microstructure analysis of a cementitious material during leaching process, Cement and Concrete Research, 36 (2006) 346-357.

[111] K. Wan, Y. Li, W. Sun, Application of tomography for solid calcium distributions in calcium leaching cement paste, Construction and Building Materials, 36 (2012) 913-917.

[112] K. Wan, Y. Li, W. Sun, Experimental and modelling research of the accelerated calcium leaching of cement paste in ammonium nitrate solution, Construction and Building Materials, 40 (2013) 832-846.

[113] Q. Hu, M.T. Ley, J. Davis, J.C. Hanan, R. Frazier, Y. Zhang, 3D chemical segmentation of fly ash particles with X-ray computed tomography and electron probe microanalysis, Fuel, 116 (2014) 229-236.

[114] M.A. Le Gros, G. McDermott, C.A. Larabell, X-ray tomography of whole cells, Current Opinion in Structural Biology, 15 (2005) 593-600.

[115] P. Trtik, A. Diaz, M. Guizar-Sicairos, A. Menzel, O. Bunk, Density mapping of hardened cement paste using ptychographic x-ray computed tomography, Cement and Concrete Composites, 36 (2013) 71-77.

[116] M. Dierolf, A. Menzel, P. Thibault, P. Schneider, C.M. Kewish, R. Wepf, O. Bunk, F. Pfeiffer, Ptychographic x-ray computed tomography at the nanoscale, Nature, 467 (2010) 436.

[117] A. Cuesta, A.G. De la Torre, I. Santacruz, P. Trtik, J.C. da Silva, A. Diaz, M. Holler, M.A.G. Aranda, Chemistry and mass density of aluminum hydroxide gel in eco-cements by ptychographic x-ray computed tomography, The Journal of Physical Chemistry C, 121 (2017) 3044-3054.

[118] J.C. da Silva, P. Trtik, A. Diaz, M. Holler, M. Guizar-Sicairos, J. Raabe, O. Bunk, A. Menzel, Mass density and water content of saturated never-dried calcium silicate hydrates, Langmuir, 31 (2015) 3779-3783.

[119] A. Diaz, P. Trtik, M. Guizar-Sicairos, A. Menzel, P. Thibault, O. Bunk, Quantitative x-ray phase nanotomography, Physical Review B, 85 (2012) 020104.

[120] M. Rajczakowska, A. Różański, M. Sobótka, Imaging of cement based composites with use of contrast x-ray microCT, Accessed August 8, 2015; http://bruker-microct.com/company/UM2014/024_Magdalena_Rajczakowska.pdf, pp. 4.

[121] M. Khanzadeh Moradllo, M.T. Ley, Quantitative measurement of the influence of degree of saturation on ion penetration in cement paste by using x-ray imaging, Construction and Building Materials, 141 (2017) 113-129.

[122] M.L.D. Gougar, B.E. Scheetz, D.M. Roy, Ettringite and C-S-H portland cement phases for waste ion immobilization: A review, Waste Management, 16 (1996) 295-303.

[123] D.L. Cocke, M.Y. Mollah, The chemistry and leaching mechanism of hazardous substances in cementitious solidification/stabilization systems, Chemistry and Microstructure of Solidified Waste Forms, (1993) 187-242.

[124] M. Chrysochoou, D. Dermatas, Evaluation of ettringite and hydrocalumite formation for heavy metal immobilization: Literature review and experimental study, Journal of Hazardous Materials, 136 (2006) 20-33.

[125] F.P. Glasser, A. Kindness, S.A. Stronach, Stability and solubility relationships in AFm phases: Part I. Chloride, sulfate and hydroxide, Cement and Concrete Research, 29 (1999) 861-866.

[126] P. Kumarathasan, G.J. McCarthy, D.J. Hassett, D.F. Pflughoeft-Hassett, Oxyanion substituted ettringites: Synthesis and characterization and their potential role in immobilization of As, B, Cr, Se and V, MRS Online Proceedings Library, 178 (1989) 83-104.

[127] J.J. Beaudoin, H. Dramé, L. Raki, R. Alizadeh, Formation and characterization of calcium silicate hydrate-hexadecyltrimethylammonium nanostructure, Journal of Materials Research, 23 (2008) 2804-2815.

[128] J.J. Beaudoin, B. Patarachao, L. Raki, R. Alizadeh, The interaction of methylene blue dye with calcium–silicate–hydrate, Journal of the American Ceramic Society, 92 (2009) 204-208.

[129] R. Żak, J. Deja, Spectroscopy study of Zn, Cd, Pb and Cr ions immobilization on C–S–H phase, Spectrochimica Acta Part A: Molecular and Biomolecular Spectroscopy, 134 (2015) 614-620.

[130] I.G. Richardson, G.W. Groves, The incorporation of minor and trace elements into calcium silicate hydrate (C-S-H) gel in hardened cement pastes, Cement and Concrete Research, 23 (1993) 131-138.

[131] J. Deja, Immobilization of $Cr^{6+}$, $Cd^{2+}$, $Zn^{2+}$ and $Pb^{2+}$ in alkali-activated slag binders, Cement and Concrete Research, 32 (2002) 1971-1979.

[132] D. Bonen, S.L. Sarkar, The present state-of-the-art of immobilization of hazardous heavy metals in cement-based materials, in: M.W.G.a.S. L.Sarkar (Ed.) Advances in Cement and Concrete, Proceedings of an Engineering Foundation Conference, American Society of Civil Engineers, New York, 1994, pp. 481-498.

[133] F.K. Cartledge, L.G. Butler, D. Chalasani, H.C. Eaton, F.P. Frey, E. Herrera, M.E. Tittlebaum, S.L. Yang, Immobilization mechanisms in solidification/stabilization of Cd and Pb salts using portland cement fixing agents, Environmental Science and Technology, 24 (1990) 867-873.

[134] M. Atkins, F.P. Glasser, L.P. Moroni, J.J. Jack, Thermodynamic modeling of blended cements at elevated temperatures (50-90C), 1993.

[135] O.P. Shrivastava, F.P. Glasser, Ion-exchange properties of $Ca_5Si_6O_{18}H_2{\cdot}4H_2O$, Journal of Materials Science Letters, 4 (1985) 1122-1124.

[136] H. Poellmann, H.J. Kuzel, R. Wenda, Solid solution of ettringites part I: Incorporation of $OH^-$ and $CO_3^{2-}$ in $3CaO{\cdot}Al_2O_3{\cdot}3CaSO_4{\cdot}32H_2O$, Cement and Concrete Research, 20 (1990) 941-947.

[137] H. Poellmann, S. Auer, H.J. Kuzel, R. Wenda, Solid solution of ettringites: Part II: Incorporation of $B(OH)_4^-$ and $CrO_4^{2-}$ in $3CaO{\cdot}Al_2O_3{\cdot}3CaSO_4{\cdot}32H_2O$, Cement and Concrete Research, 23 (1993) 422-430.

[138] R. Wenda, H.J. Kuzel, Proceedings of the 8th International Congress on the Chemistry of Cement, Rio de Janeiro, 1983, pp. 37-38.

[139] L.J. Csetenyi, Stability of borate-containing wastes encapsulated in cement, University of Aberdeen, Abereen, UK, 1993, pp. 170.

[140] J. Bensted, V. Prakash, Studies of ettringite and its derivatives, part I, Cement Technology, 2 (1971) 73-76.

[141] D.J. Hassett, D.F. Pflughoeft-Hassett, P. Kumarathasan, G.J. Mcarthy, Ettringite as agent for the fixation of hazardous oxyanions, Proceedings of the Twelfth Annual Madison Waste Conference, University of Wisconsin-Madison, 1989.

[142] W. Klemm, J.I. Bhatty, Fixation of heavy metals as oxyanion-substituted ettringites, in: P.C.A. R&D (Ed.)Serial No. 2431a, 2002.

[143] J. Bensted, S.P. Varma, Sulfoaluminate phase, Klei Keram, 23 (1973) 161-163.

[144] F.P. Glasser, Chemistry of cement solidified waste forms, in: R.D. Spence (Ed.) Chemistry and Microstructre of Solidified Waste Forms, 1993, pp. 1-39.

[145] L. Aimoz, E. Wieland, C. Taviot-Guého, R. Dähn, M. Vespa, S.V. Churakov, Structural insight into iodide uptake by AFm phases, Environmental Science and Technology, 46 (2012) 3874-3881.

[146] R. Allmann, Refinement of the hybrid layer structure hexahydroxoaluminodicalcium hemisulfate tryhydrate [$Ca_2Al(OH)_6$] [$1/2SO_4$ $3H_20$], Neues Jahrbuch für Mineralogie, 3 (1977) 136-144.

[147] J.P. Rapin, G. Renaudin, E. Elkaim, M. Francois, Structural transition of Friedel's salt $3CaO{\cdot}Al_2O_3{\cdot}CaCl_2{\cdot}10H_2O$ studied by synchrotron powder diffraction, Cement and Concrete Research, 32 (2002) 513-519.

[148] G. Renaudin, F. Kubel, J.P. Rivera, M. Francois, Structural phase transition and high temperature phase structure of Friedels salt, $3CaO{\cdot}Al_2O_3{\cdot}CaCl_2{\cdot}10H_2O$, Cement and Concrete Research, 29 (1999) 1937-1942.

[149] A. Terzis, S. Filippakis, H.-J. Kuzel, H. Burzlaff, The crystal structure of $Ca_2Al(OH)_6Cl \cdot 2H_2O$, Zeitschrift für Kristallographie - Crystalline Materials, 181 (1987) 29.

[150] A. Mesbah, C. Cau-dit-Coumes, G. Renaudin, F. Frizon, F. Leroux, Uptake of chloride and carbonate ions by calcium monosulfoaluminate hydrate, Cement and Concrete Research, 42 (2012) 1157-1165.

[151] G. Renaudin, M. Francois, O. Evrard, Order and disorder in the lamellar hydrated tetracalcium monocarboaluminate compound, Cement and Concrete Research, 29 (1999) 63-69.

[152] M. Francois, G. Renaudin, O. Evrard, A Cementitious Compound with Composition $3CaO.Al_2O_3.CaCO_3.11H_2O$, Acta Crystallographica Section C, 54 (1998) 1214-1217.

[153] G. Renaudin, J.P. Rapin, B. Humbert, M. François, Thermal behaviour of the nitrated AFm phase $Ca_4Al_2(OH)_{12}(NO_3)_2{\cdot}4H_2O$ and structure determination of the intermediate hydrate $Ca_4Al_2(OH)_{12}(NO_3)_2{\cdot}2H_2O$, Cement and Concrete Research, 30 (2000) 307-314.

[154] G. Renaudin, M. Francois, The lamellar double-hydroxide (LDH) compound with composition $3CaO{\cdot}Al_2O_3{\cdot}Ca(NO_3)_2{\cdot}10H_2O$, Acta Crystallographica Section C, 55 (1999) 835-838.

[155] G. Renaudin, J.P. Rapin, E. Elkaim, M. François, Polytypes and polymorphs in the related Friedel's salt $[Ca_2Al(OH)_6]^+[X{\cdot}2H_2O]^-$ halide series, Cement and Concrete Research, 34 (2004) 1845-1852.

[156] J.P. Rapin, A. Walcarius, G. Lefevre, M. Francois, A double-layered hydroxide, $3CaO{\cdot}Al_2O_3{\cdot}CaI_2{\cdot}10H_2O$, Acta Crystallographica Section C, 55 (1999) 1957-1959.

[157] A. Walcarius, G. Lefevre, J.-P. Rapin, G. Renaudin, M. Francois, Voltammetric detection of iodide after accumulation by Friedel's salt, Electroanalysis, 13 (2001) 313-320.

[158] R. Fischer, H.J. Kuzel, Reinvestigation of the system $C_4A.nH_2O{\cdot}C_4A.CO_2.nH_2O$, Cement and Concrete Research, 12 (1982) 517-526.

[159] A. Mesbah, C. Cau-dit-Coumes, F. Frizon, F. Leroux, J. Ravaux, G. Renaudin, A new investigation of the $Cl^-$–$CO_3^{2-}$ substitution in AFm phases, Journal of the American Ceramic Society, 94 (2011) 1901-1910.

[160] A. Mesbah, J.-P. Rapin, M. François, C. Cau-dit-Coumes, F. Frizon, F. Leroux, G. Renaudin, Crystal structures and phase transition of cementitious bi-anionic AFm-($Cl^-$, $CO_3^{2-}$) compounds, Journal of the American Ceramic Society, 94 (2011) 261-268.

[161] M. Sacerdoti, E. Passaglia, Hydrocalumite from Latium, Italy: Its crystal structure and relationship wih related synthetic phases, Neues Jahrbuch für Mineralogie, 10 (1988) 462-475.

[162] A. Mesbah, M. François, C. Cau-dit-Coumes, F. Frizon, Y. Filinchuk, F. Leroux, J. Ravaux, G. Renaudin, Crystal structure of Kuzel's salt $3CaO{\cdot}Al_2O_3{\cdot}1/2CaSO_4{\cdot}1/2CaCl_2{\cdot}11H_2O$ determined by synchrotron powder diffraction, Cement and Concrete Research, 41 (2011) 504-509.

# 2. Experimental methods

This section describes both the experimental methods and analytical techniques used throughout the dissertation. In instances where information is specific to a particular manuscript, the reader will be directed to the manuscripts for more information.

## 2.1. Materials – Synthesis of phases

The following sections describe the procedures to synthesize and condition the phases studied in this research. Specifics for the pure and doped phases are outlined for each phase.

### *2.1.1. Synthesis of pure C-S-H*

Synthesis of calcium silicate hydrate was done using the pozzolanic reaction technique [1]. Stoichiometric amounts of reactive, amorphous silica (CAB-O-SIL, grade M-5 from Cabot Corporation) and calcium oxide were mixed in an excess of water with to create C-S-H with a C/S = 1.7. The C-S-H formed due to the hydration of $C_3S$ and $C_2S$ in the hydrated cement paste normally has an average Ca/Si of about 1.7 [2]. Calcium oxide was created by heating reagent grade calcium carbonate to 900 °C and holding for 24 hours. The silica was dried in an oven at 80 °C overnight to remove any adsorbed water. The dry materials were mixed manually in an HDPE bottle. De-gassed, de-ionized water was added to create a solid to liquid ratio of approximately 10. The mixture was placed on a rotation rack at 6 rpm for 21 days. It has been reported that the reaction is nearly complete after one week, and longer time allows for a well ordered crystalline structure representative of an aged C-S-H material [1]. After 21 days of rotation, the material was vacuum filtered, and the samples were placed in a vacuum desiccator at 11% relative humidity (RH).

### *2.1.2. Synthesis of pure ettringite*

AFt was created using procedures outlined by Strubel and Brown [3]. Stoichiometric amounts of reagent grade aluminum sulfate and calcium oxide were mixed to create ettringite. The calcium oxide was created using the procedures described in section 2.1.1. The calcium oxide was dissolved in a 10% sucrose solution, whereas the aluminum sulfate was dissolved in de-gassed, de-ionized water. The two solutions were then mixed on a magnetic stirring plate for 60 hours.

The precipitate was then vacuum filtered. After filtering, the samples were placed in a desiccator and conditioned at 11% RH.

### *2.1.3. Synthesis of pure monosulfate*

AFm was synthesized following the general procedures described by Kuzel [4]. Stoichiometric amounts of $C_3A$ and reagent grade gypsum were mixed in an excess of water in a hydrothermal pressure vessel to create pure AFm. $C_3A$ was created by mixing stoichiometric amounts of calcium carbonate and aluminum oxide. The material was heated to 1400 °C for 12 hours and allowed to cool. After cooling the material was ground and passed through a 75 μm screen and remixed. The material was then heated for 12 hours at 1400 °C for 12 hours. The dry $C_3A$ and gypsum were mixed with de-gassed, de-ionized water and placed in the hydrothermal pressure vessel and heated to 150 °C for four days. After 4 days, the excess water was discharged and the material was vacuum filtered and placed in a vacuum desiccator at 11% RH.

### *2.1.4. Synthesis of iodine substituted monosulfate*

A modified monosulfate was also synthesized by substituting iodine ($I^-$) for $SO_4^{2-}$ as the dopant for improved contrast in x-ray tomography. Several researchers have indicated that $I^-$ can be substituted into the $SO_4^{2-}$ lattice site [5-7]. The preparation of the modified AFm (AFm-I) was done by mixing stoichiometric amounts of $C_3A$ and reagent grade gypsum in a 2 M potassium iodide solution. The $C_3A$ was created using the aforementioned procedures. The dry materials were placed in the vessel and manually mixed. The potassium iodide solution was created with de-gassed, de-ionized water and then added to the dry materials. The resultant solution was then placed in the hydrothermal pressure vessel and heated to 150 °C for four days. After 4 days, the excess water was discharged and the material was vacuum dried, and then conditioned over 11% RH prior to compaction.

## 2.2. Sample preparation for x-ray CT

To prepare for x-ray CT, preconditioned, pure phases were compacted in a hardened steel die using a piston and hydraulic press loaded to 515 MPa. The load was applied at 0.10 MPa/second until the desired pressure was achieved. The load was held for 30 seconds once the pressure was reached. The compacted sample was extruded and placed in a glass tube with nominal dimensions

of 6 mm OD and 3.73 mm ID and sealed at each end to minimize the interaction between the environment and the sample. Overall height of the samples was minimized to try to scan the entire sample in one scan to reduce the total number of scans.

Three types of samples were created. One sample type contained individual layers of the synthesized phases. Each layer was compacted to 515 MPa before the next material was added. The second sample type was a mixture of two phases. A known mass of each material was placed in the hydraulic press prior to compaction. The purpose of the binary mixtures was to establish the potential of segmentation between phases. Each phase was paired with a different one in order to determine such potential difficulties in segmentation. The third sample type was a quaternary blend of four phases, to represent a hydrated portland cement paste at two different ages. Known amounts of each phase were mixed together and placed in the hydraulic press prior to compaction. All blended samples were created by intermixing the materials by hand, and then the powder mixture was placed in the die and hydraulic press. The load was applied until 515 MPa was achieved.

## 2.3. Analytical techniques

To ensure the formation of desired synthetic phases and the proper incorporation of the contrast agents, the composition of the produced materials will need to be characterized. This section describes the experimental procedures used throughout the dissertation.

### *2.3.1. X-ray diffraction (XRD)*

XRD was used to determine whether the correct phases were formed. XRD patterns of synthetic AFt and AFm phases are well documented in the literature [8, 9]. In addition, it was shown in previous studies that changes in the interlayer space (d-spacing) of different C-S-H phases can be detected by XRD [10]. In the specimens with contrast agents, there is usually an increase in the interlayer space; therefore, XRD was used in detecting potential changes in the crystalline structure when contrast agents were incorporated.

A Bruker-AXS D8 Discovery XRD was used for the characterization of all materials. Diffraction angle range of $6° < 2\Theta < 60°$ with a step size of 0.08° with a scan speed of 0.96˚/min was used to characterize the AFt and AFm with an accelerating voltage of 40 kV and current of 40 mA. For

the analysis of C-S-H, a diffraction angle of 4˚<2Θ<15˚ with a step size of 0.03˚ and a scan speed of 0.36˚/min was used. The XRD diffractometer used for analysis is seen in Figure 2-1.

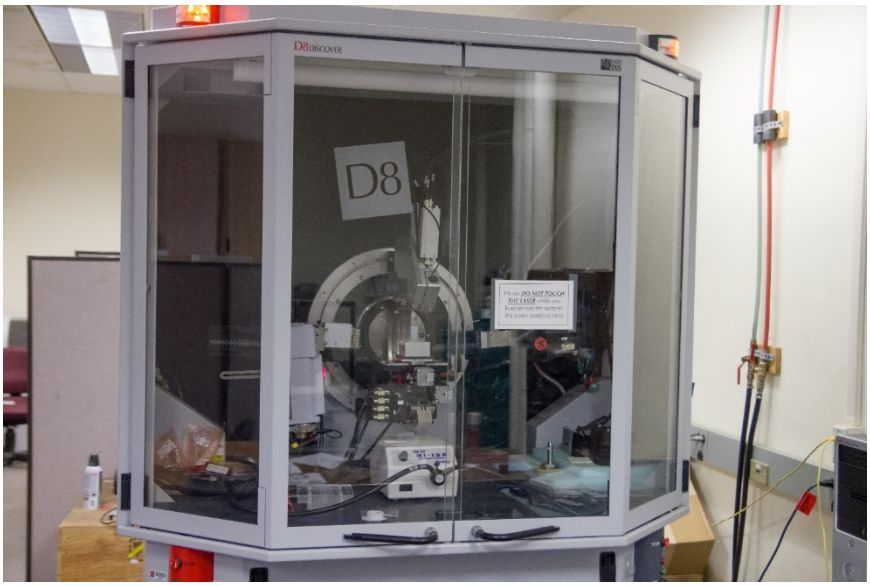


Figure 2-1: Bruker-AXS D8 discovery diffractometer

### *2.3.2. Thermogravimetric analysis and differential thermogravimetric analysis (TGA/DTG)*

TGA/DTG methods can be used to detect changes in chemical composition or decomposition when a sample is subjected to increasing thermal load. It may be done by measuring the reduction in the mass of the compound during heating, or by estimation of the heat that is adsorbed or generated through endothermic or exothermic changes of the compound. Differential mass-loss measurements can be used to estimate the amount of each chemical compound. Various types of materials can also be identified based on the heat flow during the physicochemical changes.

A TA Instruments Q50 was used with a sample size ranging from 20-35 mg. The material was heated from ambient temperature (23 ˚C) to 1000 ˚C with a heating rate of 10 ˚C/min under a flow of nitrogen gas (60 ml/min). The TGA instrument used is found in Figure 2-2.

Figure 2-2: TA Instruments Q50 TGA

### *2.3.3. X-ray computed tomography*

X-ray CT scans were done using the GeoSoilEnviroCARS (GSECARS) bending magnet beam-line, sector 13 at the Advanced Photon Source at the Argonne National Laboratory. This facility provides a fan-beam of high-brilliance radiation, collimated to a parallel beam with a vertical beam size of approximately 5 mm. The energies at which a scan can be conducted range from 8 to ~60 keV. For a sample size of approximately 1 cm outside diameter it is possible to achieve a resolution on the order of 5-10 μm/pixel. Smaller samples sizes allow for finer resolution, currently limited to approximately 1 micron. The raw data (2D projections) generated at GSECARS was reconstructed with a filtered back-projection algorithm using the programming language IDL™ to form a 3D volume of greyscale data [11]. The compacted samples, as discussed in section 2.2, used for x-ray CT are seen in Figure 2-3. The compacted samples were transported to the Advanced Photon Source and placed on the rotation stage with a drill chuck prior to scanning. The experimental set up used for CT scans is shown in Figure 2-4.

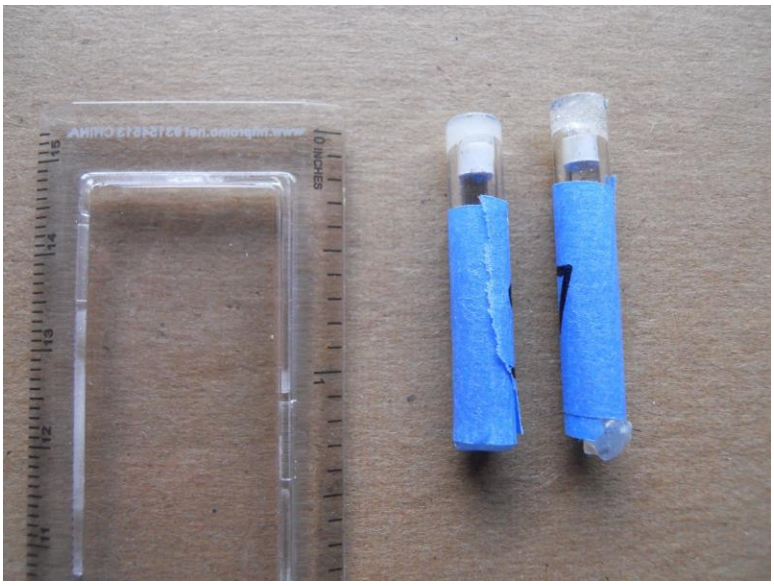

Figure 2-3: Compacted samples used for x-ray CT scans

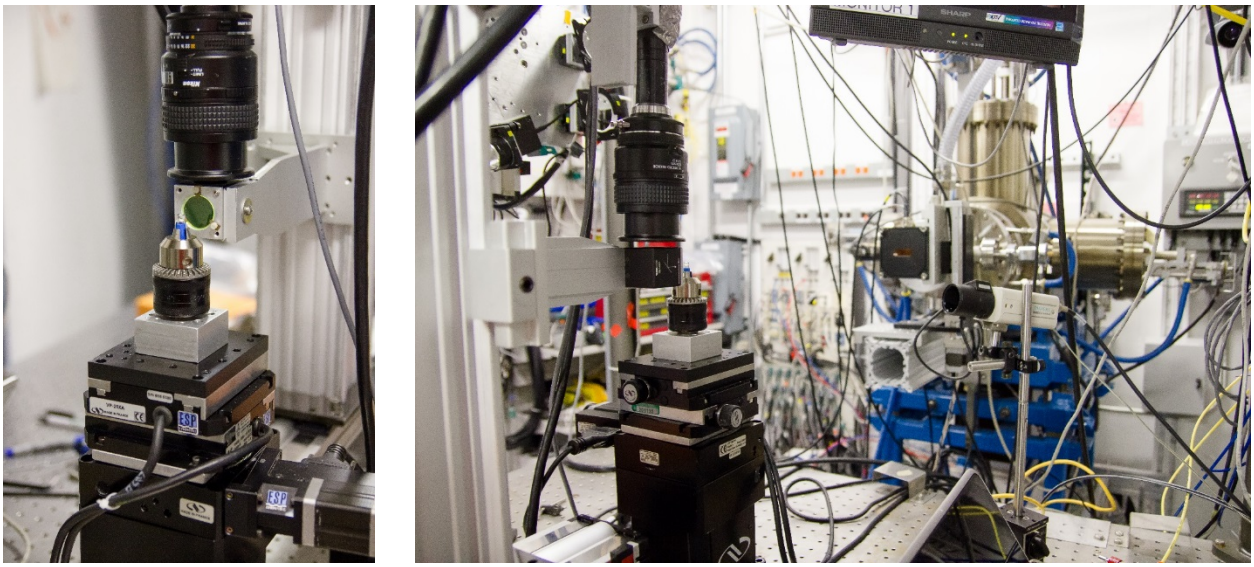

Figure 2-4: Experimental setup used at GSECARS 13-BMD. Left) shows the sample mounted on the rotation stage with the scintillator screen and camera lens behind the sample. Right) shows the set up from the direction of the x-ray source.

## 2.4. Image processing

One of the main challenges to extracting quantitative information from the grey-scale images produced with x-ray CT is accurate image processing. The raw data (2D projections) generated at GSECARS was first reconstructed with a filtered back-projection algorithm using the programming language IDL™ to form a 3D volume of greyscale data [11]. The data was then

filtered, using the non-local means filter. This filter was chosen due to its ability to remove image noise while preserving edges. After filtering, the data was segmented using one of three different algorithms; Gaussian deconstruction of histogram, watershed, or the Bayesian Markov random field method (MRF). Analysis of all data sets were processed using a combination of the following software programs: imageJ, Avizo Fire, and Quantim4. Specifics for analysis of all data sets are outlined in each individual chapter (3-5).

## 2.5. Image segmentation algorithms

The image segmentation process is important for proper classification of voxels in an image volume. This important step can affect the desired outcome if done incorrectly. Global segmentation has been classified as a method of segmentation based on the evaluation of the histogram only. More robust, local segmentation, algorithms exist which account for the spatial arrangement of the greyscale values throughout the domain [12] The local segmentation algorithms offer more flexibility in determine the distribution of phases and often result in more desirable results [13]. Numerous global and local segmentation algorithms exist, and several authors have evaluated their performance in image analysis [14-16]. It should be noted that many of the segmentation algorithms have been developed for two-dimensional image processing in the medical field, images with two phases, or were not developed for true 3D analysis [17, 18]. This research investigates the accuracy in quantifying synthesized hydration products in binary and quaternary mixtures for two local segmentation algorithms (watershed and Bayesian Markov random field) and one global segmentation algorithm developed in this research called the Gaussian deconstruction of histogram. Specifics on the watershed and MRF algorithms are outlined in sections 2.5.1 and 2.5.2, respectively. Details on the Gaussian deconstruction of histogram are outlined in Chapters 3 and 5.

### *2.5.1. Watershed*

The watershed segmentation algorithm uses the principle of catchment basins and watershed lines, derived from how the field of hydrology defines basins and watersheds, to determine how voxels are regionally distributed throughout the sample domain [19, 20]. The watershed lines are determined by the highest gradient between greyscale values, thus determining the borders of the catchment basins locally. These gradient lines can be determined through several different edge

detection methods [12]. In this research, the gradient was identified using Canny-Deriche edge detection filter [21, 22]. The gradient of the image creates watershed lines, defined as the edges between different phases, separating catchment basins, defined as the greyscale values bounded by the watershed lines. Minima are determined as regions where the greyscale value is darker than the surrounding voxels, forming the basis for the catchment basins [19]. Initially, the catchment basins are seeded with simple thresholding to set values for the inundation process. Voxels in the high gradient zones are unclassified at the beginning of the process and are assigned values during the inundation portion of the watershed algorithm. Other voxels which were not classified during the initial thresholding are left unclassified and subsequently determined during the algorithm until a watershed line has been reached. Lastly, the unclassified voxels on the gradient line are determined based on the local distribution of voxels determined in during the algorithm [12].

### *2.5.2. Bayesian Markov random fields (MRF)*

The basis of random field models and the MRF algorithm was developed on the stochastic representation of the attributes of an image volume [23]. The stochastic framework is based on the assumption that the arrangement of specific image attributes, in this case greyscale values and subsequent linear attenuation coefficients (LACs), can be determined by probability distributions. Statistical mean and standard deviation of the LACs must be known or determined through global segmentation or manual seeding of the expected phase [24]. The initial MRF algorithm was developed for two-dimensional (2D) image analysis by Berthod et al. [25], and was expanded to a 3D algorithm by Kulkarni et al. for porous materials [24]. The principle of the segmentation algorithm is to determine the spatial arrangement of class labels (i.e. LACs) by assigning a gray level within the 3D data set to one of the individual classified phases. The method evaluates the interaction between direct neighbors in a probabilistic manner to determine the spatial distribution of the class labels with minimal boundary surface while maintaining grey value data [12, 24]. The determination of class labels is described by:

$$\hat{H} = \underset{\hat{H}}{argmin}\left\{\int_{\Omega}\left(\sqrt{2\pi\sigma_H} + \frac{l'_x - \mu_H}{2\sigma_H^2} + \beta\int_{\Pi}\gamma\left(H_x, H_y\right)\right)\right\} \qquad \text{Equation 2.1}$$

with:

$$\gamma\left(H_x, H_y\right) = \begin{cases} -1 & H_x = H_y \\ 1 & H_x \neq H_y \end{cases}$$

where $\hat{H}$ is the class label, $\Omega$ is the total voxel population, $\Pi$ is the population of all pairs of neighboring voxels x and y, $H_x$ and $H_y$ represent the class label at x and y, respectively, $\mu_H$ and $\sigma_H$ are the class mean and standard deviation, and $\beta$ is a parameter which represents the homogeneity of the region [24].

## 2.6. References


[1] R. Alizadeh, J.J. Beaudoin, L. Raki, Mechanical properties of calcium silicate hydrates, Materials and Structures, 44 (2011) 13-28.

[2] L. Raki, J. Beaudoin, R. Alizadeh, J. Makar, T. Sato, Cement and concrete nanoscience and nanotechnology, Materials, 3 (2010) 918-942.

[3] L.J. Struble, P.W. Brown, An evaluation of ettringite and related compounds for use in the solar energy storage, US Department of Commerce, 1982, pp. 11.

[4] H.J. Kuzel, Synthesis and x-ray study of the crystalline composition $3CaO{\cdot}Al_2O_3{\cdot}CaSO_4{\cdot}12H_2O$, Neues Jahrbuch Mineral Monatsh, 7 (1965) 193-197.

[5] J.P. Rapin, A. Walcarius, G. Lefevre, M. Francois, A double-layered hydroxide, $3CaO{\cdot}Al_2O_3{\cdot}CaI_2{\cdot}10H_2O$, Acta Crystallographica Section C, 55 (1999) 1957-1959.

[6] G. Renaudin, J.P. Rapin, E. Elkaim, M. François, Polytypes and polymorphs in the related Friedel's salt $[Ca_2Al(OH)_6]^+[X{\cdot}2H_2O]^-$ halide series, Cement and Concrete Research, 34 (2004) 1845-1852.

[7] A. Walcarius, G. Lefevre, J.-P. Rapin, G. Renaudin, M. Francois, Voltammetric Detection of iodide after accumulation by Friedel's salt, Electroanalysis, 13 (2001) 313-320.

[8] R. Khoshnazar, L. Raki, J. Beaudoin, R. Alizadeh, Solvent exchange in sulphoaluminate phases. Part I: Ettringite, Advances in Cement Research, 25 (2013) 314-321.

[9] R. Khoshnazar, L. Raki, J. Beaudoin, R. Alizadeh, Solvent exchange in sulfoaluminate phases. Part II: Monosulfate, Advances in Cement Research, 25 (2013) 322-331.

[10] J.J. Beaudoin, R. Alizadeh, Detection of nanostructural anomalies in hydrated cement systems, Cement Concrete Comp, 29 (2007) 63-69.

[11] GSECARS Tomography Processing Software, 2014. http://cars9.uchicago.edu/software/idl/tomography.html.

[12] S. Schlüter, A. Sheppard, K. Brown, D. Wildenschild, Image processing of multiphase images obtained via x-ray microtomography: A review, Water Resources Research, 50 (2014) 3615-3639.

[13] W. Wang, A.N. Kravchenko, A.J.M. Smucker, M.L. Rivers, Comparison of image segmentation methods in simulated 2D and 3D microtomographic images of soil aggregates, Geoderma, 162 (2011) 231-241.

[14] P.K. Sahoo, S. Soltani, A.K.C. Wong, A survey of thresholding techniques, Computer Vision, Graphics, and Image Processing, 41 (1988) 233-260.

[15] N.R. Pal, S.K. Pal, A review on image segmentation techniques, Pattern Recognition, 26 (1993) 1277-1294.

[16] M. Sezgin, B. Sankur, Survey over image thresholding techniques and quantitative performance evaluation, SPIE, 2004, pp. 20.

[17] T.R. Elliot, R.J. Heck, A comparison of 2D vs. 3D thresholding of x-ray CT imagery, Canadian Journal of Soil Science, 87 (2007) 405-412.

[18] S. Schlüter, U. Weller, H.-J. Vogel, Segmentation of x-ray microtomography images of soil using gradient masks, Computers & Geosciences, 36 (2010) 1246-1251.

[19] L. Vincent, P. Soille, Watersheds in digital spaces: an efficient algorithm based on immersion simulations, IEEE Transactions on Pattern Analysis and Machine Intelligence, 13 (1991) 583-598.

[20] S. Beucher, C. Lantuejol, Use of watersheds in contour detection, International Workshop Image Processing, Real-Time Edge and Motion Detection/Estimation, CCETT, Rennes, France, 1979.

[21] R. Deriche, Using Canny's criteria to derive a recursively implemented optimal edge detector, International Journal of Computer Vision, 1 (1987) 167-187.

[22] J. Canny, A Computational Approach to Edge Detection, IEEE Transactions on Pattern Analysis and Machine Intelligence, PAMI-8 (1986) 679-698.

[23] J. Moussouris, Gibbs and Markov random systems with constraints, Journal of Statistical Physics, 10 (1974) 11-33.

[24] R. Kulkarni, M. Tuller, W. Fink, D. Wildenschild, Three-dimensional multiphase segmentation of x-ray CT data of porous materials using a Bayesian Markov random filed framework, Vadose Zone Journal, 11 (2012) 74-85.

[25] M. Berthod, Z. Kato, S. Yu, J. Zerubia, Bayesian image classification using Markov random fields, Image and Vision Computing, 14 (1996) 285-295.

# Manuscript 1

## Quantification of synthesized hydration products using synchrotron microtomography and spectral analysis

Tyler Deboodt, Jason H. Ideker, O. Burkan Isgor, Dorthe Wildenschild

Published in: *Construction and Building Materials,* Volume 157, December 2017, 476-488

# 3. Manuscript 1

## Quantification of synthesized hydration products using synchrotron microtomography and spectral analysis

Tyler Deboodt[1], Jason H. Ideker[2], O. Burkan Isgor[3], Dorthe Wildenschild[4]

**Abstract:**

The use of x-ray computed tomography (CT) has been typically limited to qualitative or semi-quantitative characterization of pore structure, cracking and mechanical damage in cementitious systems due to low contrast in the hydrated phases. These limitations have resulted in the inability to extract quantifiable information on such phases. The goal of this research was to address the limitations caused by low contrast and improving the ability to distinguish the four primary hydrated phases in portland cement; C-S-H, calcium hydroxide, monosulfate, and ettringite. X-ray CT on individual layers, binary mixtures of phases, and quaternary mixtures of phases to represent a hydrated portland cement paste were imaged with synchrotron radiation. Known masses of each phase were converted to a volume and compared to the segmented image volumes. It was observed that adequate contrast in binary mixing of phases allowed for segmentation, and subsequent image analysis indicated quantifiable volumes could be extracted from the tomographic volume. However, low contrast was observed when C-S-H and monosulfate were paired together leading to difficulties segmenting in an unbiased manner. Quantification of phases in quaternary mixtures included larger errors than binary mixes due to histogram overlaps of monosulfate, C-S-H, and calcium hydroxide.

**Keywords:** x-ray tomography, phase quantification, non-destructive testing

---

[1] Graduate Research Assistant, School of Civil and Construction Engineering, Oregon State University

[2] Associate Professor, School of Civil and Construction Engineering, Oregon State University

[3] Professor, School of Civil and Construction Engineering, Oregon State University

[4] Professor, School of Chemical, Biological, and Environmental Engineering, Associate Dean of Graduate School, Oregon State University

## 3.1. Introduction

The use of portland cement will not decrease in the foreseeable future; therefore we must invest in technologies that provide better understanding of existing challenges related to the utilization of this material. This motivation is the driving force behind the increasing number of studies to develop fundamental understanding of hydration and deterioration mechanisms of concrete, and to discover new cementitious materials with superior mechanical and durability properties. Recent interest in the development or improvement of alternative inorganic binders [1-8] and innovative attempts to change the nano-structure of hydrated cement phases for better durability [9-15] are clear indicators of the demand for additional research.

The use of advanced material characterization techniques has had an irrefutable impact on the progress of quantitative understanding of portland cement based materials. Despite the progress enabled by these advanced characterization techniques, further advancement of our understanding of the hydrated phases, and subsequent deterioration of those phases, is hindered by their limitations. One limitation is the inability to non-destructively monitor compositional changes in three-dimensional (3D) samples. For example, it is routine to characterize crystalline phases using x-ray diffraction on powdered samples; however, powder analysis only gives averaged information from the extracted sample domain, and if one wants to monitor changes over a period of time, additional powder samples need to be extracted from different locations from the same specimen, or from different specimens, at different times. Optical and electron microscopic studies on concrete or its components are also limited in that they are performed on two-dimensional (2D) surfaces that need to be prepared for analysis; such sample preparation can induce artifacts in the microstructure [16], such as loss of structure by grinding and polishing [17], changes in structure caused by drying [17, 18], or cracking caused by cutting or drying [19]. After collecting microscopic data from these 2D scans, image analysis can be performed to extract quantitative information on the microstructure of the observed surface. In some cases 3D information can be extrapolated from the 2D microstructural and/or elemental measurements; however, 2D analysis is generally inadequate for accurate characterization when direct 3D information, such as connectivity and distribution of phases within a complex structure is needed. Therefore, a method for extracting 3D information, non-destructively is paramount for further understanding hydrated portland cement phases.

X-ray computed tomography (CT) has been used in the study of portland cement systems in 3D space, primarily for qualitative or semi-quantitative characterization of internal pore structure [20-30], cracking, and mechanical damage [17, 25, 31-34]. Quantitative measures using x-ray CT have been coupled with electron probe microanalysis to identify constituents of cementitious materials [35]. Additionally, mass densities of hydrated phases have been determined using ptychograph x-ray CT on samples prepared using focused ion beam (FIB) milling [36-39]. This method collected coherent diffraction patterns and a tomographic volume is reconstructed based on these patterns. The high resolution (up to 40.8 nm/pixel [39]) allowed for the determination of mass densities based on the measured electron density and the known chemical composition of unhydrated and hydrated phases [37], hydration products of alite [38], and hydration products of alternative, eco-cements [39]. With the recent advances in standalone x-ray CT machines, the potential to quantify hydration products is imperative without being coupled with other highly advanced techniques The potential of x-ray CT to image hydrated phases in a 3D space and the potential to non-destructively identify, quantify, and potentially track changes caused by deterioration processes over time in portland cement based materials, make improvements to this technology an invaluable asset and worthwhile research pursuit.

The goal of this research was to expand the use of x-ray CT beyond its current limited applications in portland cement systems, namely pore structure and crack characterization, to provide quantitative 3D information on hydrated phases at the current expected resolutions, as well as lay the ground work for the ability to potentially to track changes in those phases that may be associated with subsequent deterioration. While the researchers acknowledge that access to synchrotron radiation is limited, this source was used to reduce the scan times to test several variations quickly. The main hydrated phases we studied in this paper were calcium silicate hydrate (C-S-H), calcium hydroxide (CH), ettringite (AFt), and monosulfate (AFm). The ability to non-destructively identify and quantify the main hydrated phases in portland cement systems would result in a paradigm shift in how we characterize these systems. This work focused on determining fundamental x-ray CT signatures of the main hydration products that form in hydrating portland cement. Individual signatures of pure C-S-H, CH, AFt, and AFm were recorded and used to determine quantitative amounts of each phase in both binary mixtures and quaternary mixtures of phases. Binary mixtures were studied to determine the potential for distinguishing one phase from another, whereas the quaternary mixtures were studied to represent a hydrating

portland cement paste. Even though the focus of this research was limited to the major primary and secondary phases that form in portland cement-based materials, the impact of developing techniques to extract distinct and quantitative information from x-ray CT will provide a pathway for enhanced characterization of a wide range of cementitious materials such as portland cement, calcium sulfoaluminate cements, calcium aluminate cements, and alkali-activated systems, as well as future alternative binders.

## 3.2. Materials and methods

### *3.2.1. Synchrotron tomography*

X-ray CT is one method to extract 3D information from solid samples nondestructively. In this approach, a sample is placed between an x-ray source and a detector. Monochromatic x-rays are sent through the sample and the transmitted beams are recorded on a detector after passing through a scintillator to convert the x-rays to visible light [16]. The sample is rotated (up to 360°) along its vertical axis to obtain 3D data. As monochromatic x-rays pass through solid materials, the attenuation follows Beer-Lambert Law [40]:

$$I(x) = I_o e^{(-\mu x)} \qquad \text{Equation 3.1}$$

where $I$ is the attenuated intensity of the x-ray after passing through the solid with a thickness of $x$, $I_o$ is the initial intensity of the radiation, and $\mu$ is the linear attenuation coefficient. According to the Beer-Lambert Law, the ratio of the number of transmitted to incident photons is related to the integral of the linear attenuation coefficient(s) of the materials along the path that the photons travel through the sample. The linear attenuation coefficient is linked to the density, the atomic number, and the energy of the beam [41]. Materials with higher density or high atomic number tend to absorb x-rays better. The relationship between density, atomic number and linear attenuation coefficient of an element is given as [42]:

$$\mu = \frac{\rho Z^4}{AE^3} \qquad \text{Equation 3.2}$$

where $A$ is the atomic mass, $Z$ is the atomic number, $\rho$ is the density, and $E$ is the x-ray energy. Materials with a high linear attenuation coefficient allow x-rays to only penetrate a short distance, whereas materials with a low linear attenuation coefficient allow x-rays to pass through more easily [40].

Upon completion of a tomographic scan, the series of acquired linear attenuation coefficients are mathematically reconstructed into a 3D rendition of the object [42]. Typically, a filtered back-projection algorithm is used to reconstruct the image from the x-rays. The image is composed of a 3D volume of pixels, i.e. voxels, which encapsulate the weighted average linear attenuation coefficient of all of the components within each voxel. This determines the greyscale value, and ultimately the contrast seen in the reconstructed image [43]. The resulting image would be a superimposed projection of a volume in a 2D plane; i.e., a stack of vertical slices within the sample that creates a 3D image of the object [41]. The average greyscale values are counted and plotted as a histogram. The contrast in the histogram is then used for segmentation to isolate certain features in the 3D image stack.

In this study, synchrotron x-ray CT was done on the four main hydrate phases (C-S-H, CH, AFt, and AFm), which were synthesized in the laboratory. The materials were prepared as described in the following sections. The GSECARS 13-BMD beamline of the Advanced Photon Source at the Argonne National Laboratory was used for all scans. The samples were mounted in a drill chuck, which was attached to the rotation stage. A monochromatic beam with energy of 33.299 keV was used for all scans. The beam size was 3.14 mm wide by 5.02 mm tall, resulting in a 2.61 μm/pixel resolution. For each scan, 900 x-ray projection images with a rotation step of 0.18° and exposure time of 2 seconds were collected. The 2D projections were reconstructed to a 3D volume using a filtered back projection algorithm to produce a volume of 16-bit greyscale images.

### *3.2.2. Synthesis of pure phases*

C-S-H was synthesized using the pozzolanic reaction technique [44]. Stoichiometric amounts of reactive, amorphous silica and calcium oxide were mixed in an excess of water with to create C-S-H with a calcium-to-silica ratio (C/S) = 1.7. C-S-H formed due to the hydration of $C_3S$ and β-$C_2S$ in the hydrated cement paste normally ranges from 1.2 – 2.1 and has an average C/S of about 1.75 [45]. Calcium oxide was created by heating reagent grade calcium carbonate at 900 °C for 24 hours. The silica was dried in an oven at 80 °C overnight to remove any adsorbed water. The dry materials were mixed manually in a high density polyethylene bottle. De-gassed, de-ionized water was added to create a solid to liquid ratio of approximately 10. The mixture was placed on a rotation rack at 6 rpm for 21 days. It has been reported that the reaction is nearly complete after one week, and longer rotation times allow for a well ordered crystalline structure representative of

an aged C-S-H material [44]. After 21 days of rotation, the material was vacuum filtered, and the samples were placed in a vacuum desiccator at 11% relative humidity (RH).

AFt was made using procedures described by Strubel and Brown [46]. Stoichiometric amounts of reagent grade aluminum sulfate and calcium oxide were mixed to create ettringite. The calcium oxide was created using the procedures described above. The calcium oxide was dissolved in a 10% sucrose solution, whereas the aluminum sulfate was dissolved in de-gassed, de-ionized water. The two solutions were then mixed on a magnetic stirring plate for 60 hours. The precipitate was then vacuum filtered. After filtering, the samples were placed in a desiccator and conditioned at 11% RH.

AFm was synthesized following procedures described by Kuzel [47]. $C_3A$ was created by mixing stoichiometric amounts of calcium carbonate and aluminum oxide. The material was heated to 1400 °C for 12 hours and allowed to cool. After cooling the material was ground and passed through a 75 μm screen and remixed. The material was then heated for 12 hours at 1400 °C. X-ray diffraction (XRD) indicated nearly pure $C_3A$. Stoichiometric amounts of $C_3A$ and reagent grade gypsum were mixed in an excess of water in a hydrothermal pressure vessel to create pure AFm. Then the dry $C_3A$ and reagent grade gypsum were mixed with de-gassed, de-ionized water and placed in the hydrothermal pressure vessel and heated at 150 °C for four days. After 4 days, the hydrothermal pressure vessel was removed from the heat. After thermal equilibrium had been achieved with room temperature, the excess water was discharged and the material was vacuum filtered. The filtered material was placed in a vacuum desiccator at 11% RH. Lastly, commercially available reagent grade calcium hydroxide (>95% purity) was used to represent portlandite (CH).

All materials were conditioned over a saturated lithium chloride solution (11%) at 23 ˚C. This method of drying was chosen to reduce the potential for phase transformation at elevated temperatures, particularly for AFm and AFt. Additionally, the synthesized phases were kept at 11% RH under a partial vacuum, to minimize the potential for carbonation. The materials were characterized using XRD and TGA/DTA to ensure the correct phases were created and proper conditioning was achieved, as described in section 3.2.3.

### *3.2.3. Characterization of materials*

XRD and thermogravimetric analysis\differential thermogravimetric analysis (TGA\DTG) were used to characterize the synthesized phases. A Bruker-AXS D8 Discovery XRD was used for the characterization of all materials. Diffraction angle range of $6° < 2\Theta < 60°$ with a step size of 0.08° with a scan speed of 0.96˚/min was used to characterize the AFt and AFm with an accelerating voltage of 40 kV and current of 40 mA. Basal spacing of 0.973 nm [48] and 0.561 nm [49] was expected for AFt with 32 water molecules in the crystalline structure, while other peaks were classified from Strubel and Brown [46]. An expected basal spacing of 0.893 nm corresponds to an interlayer distance of an AFm crystal with 12 molecules of water [50], and other peaks were classified from Kuzel [47]. For the analysis of C-S-H, a diffraction angle of $4˚<2\Theta<15˚$ with a step size of 0.03˚ and a scan speed of 0.36˚/min was used.

TGA\DTG was used to further characterize the synthesized phases. A TA Instruments Q50 was used with a sample size ranging from 20-35 mg. The material was heated from ambient temperature (23 ˚C) to 1000 ˚C with a heating rate of 10 ˚C/min under a flow of nitrogen gas (60 ml/min). AFt loses water between 120 ˚C and 230 ˚C [49]. Other losses during TGA occurring between 550 ˚C and 1000 ˚C are attributed to the release of sulfur oxides. These have been reported in literature in AFt synthesized in sucrose [51], as well as in natural ettringite [52]. AFm begins losing water around 220 ˚C as the material releases 6 water molecules. The remaining 6 water molecules are released at temperatures above 220 ˚C. Furthermore, a total mass loss of 34.7% corresponds to 12 water molecules in the AFm phase [13].

### *3.2.4. Compaction of powders*

To prepare for x-ray CT, preconditioned, pure phases were compacted in a hardened steel die using a piston and hydraulic press loaded to 515 MPa. The load was applied at 0.10 MPa/second until the desired pressure was achieved. The load was held for 30 seconds once the pressure was reached. The compacted sample was extruded and placed in a glass tube with nominal dimensions of 6 mm OD and 3.73 mm ID and sealed at each end to minimize the interaction between the environment and the sample. Overall height of the samples was less than 3.14 mm to ensure the entire sample was detected in one scan.

Three types of samples were created. One sample type contained individual layers of the synthesized phases. Each layer was compacted to 515 MPa before the next material was added. The second sample type was a mixture of two phases. A known mass of each material was placed in the hydraulic press prior to compaction. The purpose of the binary mixtures was to establish the potential of segmentation between phases. Each phase was paired with a different one in order to determine such potential difficulties in segmentation. The third sample type was a quaternary blend of four phases, to represent a hydrated portland cement paste at two different ages. Known amounts of each phase were mixed together and placed in the hydraulic press prior to compaction. All blended samples were created by intermixing the materials by hand, and then the powder mixture was placed in the die and hydraulic press. The load was applied until 515 MPa was achieved. A summary of all samples tested is seen in Table 3-1.

Table 3-1: Summary of samples tested

| Sample type | Materials | Number of samples |
|---|---|---|
| Layered | C-S-H, CH, AFt, AFm | 3 |
| Binary mixture | C-S-H and CH | 2 |
| | C-S-H and AFt | 2 |
| | C-S-H and AFm | 2 |
| | CH and AFt | 2 |
| | CH and AFm | 2 |
| | AFm and AFt | 2 |
| Quaternary mixture | ~55% C-S-H, ~25% CH, ~15% AFm, ~5% AFt | 3 |
| | ~60% C-S-H, ~25% CH, ~12% AFt, ~3% AFm | 3 |

### *3.2.5. Image processing and analysis*

The raw data (2D projections) generated at the GSECARS beamline were first reconstructed with a filtered back-projection algorithm using the programming language IDL™ to form a 3D volume of greyscale data. The reconstructed image stack was processed using imageJ and Avizo 9.0. All

data was initially filtered using a non-local means filter [53] to improve the contrast and reduce the noise in the images. Due to similar density and minor differences in composition it was expected that the resultant image volume would exhibit similar greyscale values in samples with mixed phases. These similar greyscale values would ultimately result in the overlapping of peaks in the intensity histogram. Therefore, a procedure to deconstruct the histogram into individual Gaussian curves was developed in order to threshold in an unbiased manner. Subsequent phase segmentation of the Gaussian curves in the binary and quaternary mixture samples was done using a watershed algorithm [54]. A selected region of interest (ROI) was chosen to minimize edge effects between the phases and the glass sample holder. Threshold values were chosen as the intersection of individual Gaussian curves that were determined from deconstructed histograms of each sample. In samples where significant overlapping of greyscale values was observed, the histogram was deconstructed into individual Gaussian curves based on the data collected from the layered samples. This histogram deconstruction process is discussed in more detail later. Once the threshold values were determined, a volumetric analysis was done on each dataset after segmentation. Identical labels were assigned to voxels for each phase. The label analysis resulted in a quantity of voxels, and the volume of voxels was then converted to cubic centimeters using information about the image resolution (2.61 micron/voxel). The image processing workflow is illustrated in Figure 3-1.

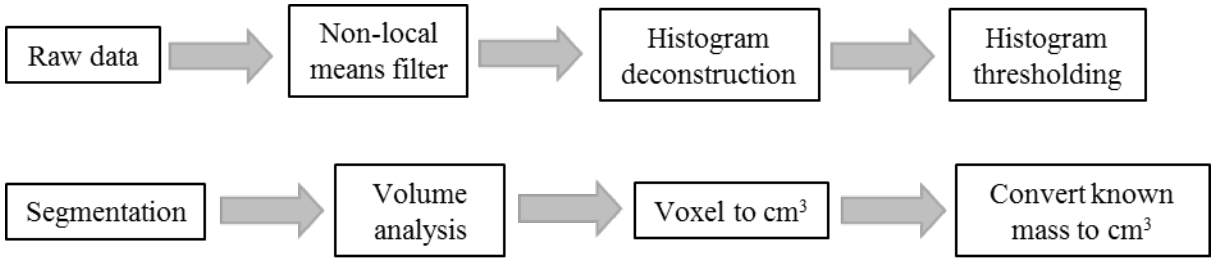


Figure 3-1: Procedures for image analysis

After segmentation, the measured volumes from image analysis were compared to the known amounts of individual phases for each mixed phase sample. The known mass of each phase was converted to a volume through the density of the respective phase. Densities of each phase were determined through reported literature [55], as seen in Table 3-2. The specific gravity of jennite ($9CaO{\cdot}6SiO_2{\cdot}11H_2O$), with a C/S of 1.5 was used for the synthesized C-S-H. Slight variation in the density was expected for the C-S-H phase with a C/S of 1.7, but was considered negligible.

Table 3-2: Density of phases [55]

| Phase | Density (g/cm$^3$) |
|---|---|
| C-S-H | 2.331 |
| CH | 2.251 |
| AFt | 1.778 |
| AFm | 2.015 |

## 3.3. Results and discussion

### *3.3.1. XRD*

Results from XRD analysis for the synthesized powders are shown in Figure 3-2.

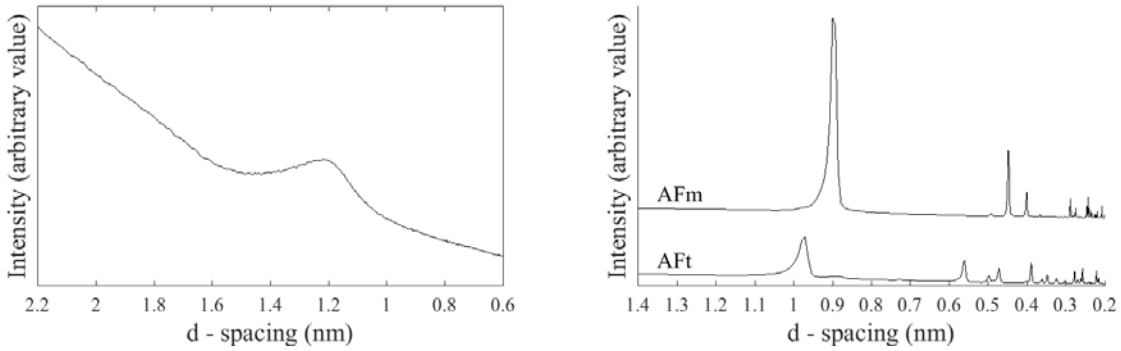


Figure 3-2: Left) C-S-H XRD data. Right) AFm and AFt XRD data.

Three main peaks for C-S-H in XRD depend on the C/S ratio, and have been reported in literature with a d-spacing of 1.250, 0.304, and 0.280 nm. The location of these peaks occur between 5 to 10 degrees 2Θ [49]. It can be seen in Figure 3-2a) that the main peak in the C/S of 1.7 occurred with a d-spacing of 1.21 nm. The broad peak observed was indicative of a semi-crystalline structure, similar to that of an aged C-S-H.

As shown in Figure 3-2b), a large peak in the AFm was observed at a d-spacing of 0.899 nm and a secondary peak was observed at a d-spacing of 0.448 nm. The secondary peak at 0.448 nm was indicative that AFm with 12 molecules of water [47] was synthesized and conditioned properly. The main peak observed in the XRD pattern of AFt occurred at a d-spacing of 0.974 nm and a secondary peak occurred at a d-spacing of 0.561 nm indicated AFt with 32 molecules of water.

Other minor peaks corroborated well with data provided by Strubel and Brown [46] indicating pure ettringite was formed.

### *3.3.2. TGA/DTG*

TGA/DTG was used to further characterize the synthesized phases at the time of compaction, and after preconditioning the powders to 11% RH. Individual TGA/DTG results for the conditioned phases are shown in Figure 3-3

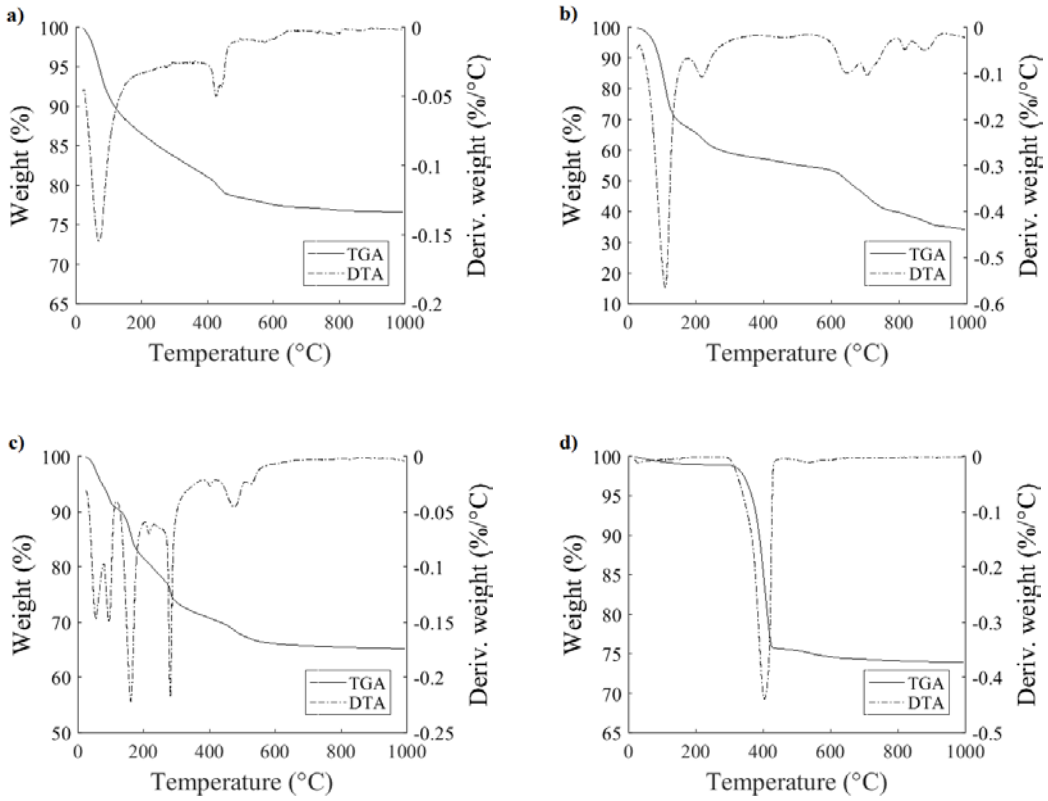


Figure 3-3: TGA/DTA results of phases: a) C-S-H; b) AFt; c) AFm; d) CH

As shown in Figure 3-3a), a sharp decrease in the DTG curve for C-S-H was observed at temperatures lower than 200 ˚C, indicating release of gel water. A smaller decrease, indicating calcium hydroxide, was also observed between 400 ˚C and 600 ˚C. TGA results indicated that there was 6.8% CH and 0.64% $CaCO_3$ in the synthesized C-S-H. Previous research using

quantitative XRD has shown measurable amounts of CH can be observed in C-S-H that is prepared using the pozzolanic method when the C/S > 1.54 [56, 57].

As shown in Figure 3-3b), a large decrease in the DTG curve for AFt was observed at 110 ˚C, a smaller decrease was observed at 220 ˚C, and several smaller decreases above 550 °C. These temperature drops indicated ettringite formation [44, 46]. Calculations from Figure 3-3c) show the synthesized AFm had a total mass loss of 34.8%. This corroborates well with existing literature for AFm with 12 molecules of water [13]. TGA results, as shown in Figure 3-3d), on CH indicated a purity of 95.2%. Results from both XRD and TGA/DTG indicated nearly pure phases were either synthesized or could be used to represent the hydration products found in a hydrated portland cement paste.

### *3.3.3. Reconstructed image volume*

Initially, the reconstructed x-ray CT image volumes for the layered samples were investigated to get a representation of the variation in greyscale values for each individual phase. Representative greyscale values (mean and standard deviation) for each individual phase were then used as a guideline for segmentation of binary and quaternary mixed samples. The average greyscale value and standard deviation were used for histogram deconvolution into individual Gaussian curves, and subsequently to determine segmentation values in samples containing a binary or quaternary mixture of phases. Success using Guassian curves to deconstruct histograms that have overlapping greyscales values representing phases has been shown [24]. It can be seen in Figure 3-4 that there were apparent differences in greyscale intensities, indicating the potential for segmentation between all of the phases.

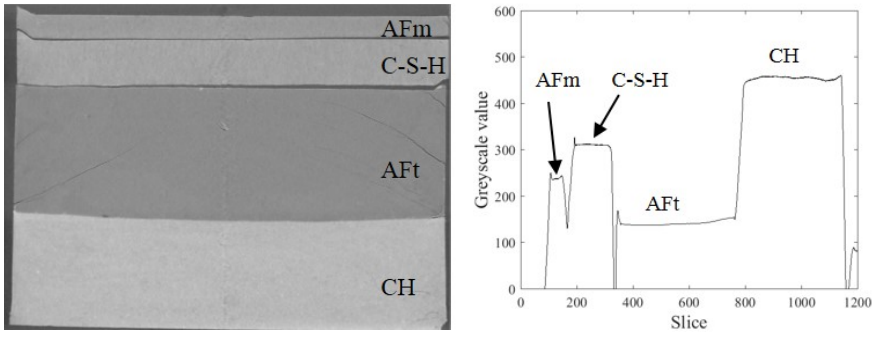


Figure 3-4: Left) Greyscale image of layered phases. Right) Representative greyscale values of image volume

Greyscale orthoslices of the binary and quaternary mixtures of phases were studied, and further showed promise for the ability to segment the phases into individual components. It can be seen in Figure 3-5 that there was contrast among all of the phases in the samples with binary mixtures. However, it was observed in Figure 3-5b), that there was low contrast between C-S-H and AFm with phase boundaries that were hard to differentiate by visual inspection. The raw data was instead filtered using a non-local means filter with different parameters to improve the contrast and distinction between the phase boundaries. However, even after filtering with different parameters, the contrast between these two phases was only slightly improved in one of the two samples. In the second C-S-H and AFm sample, very little contrast was observed, thus leading to difficulties in segmentation of that particular sample.

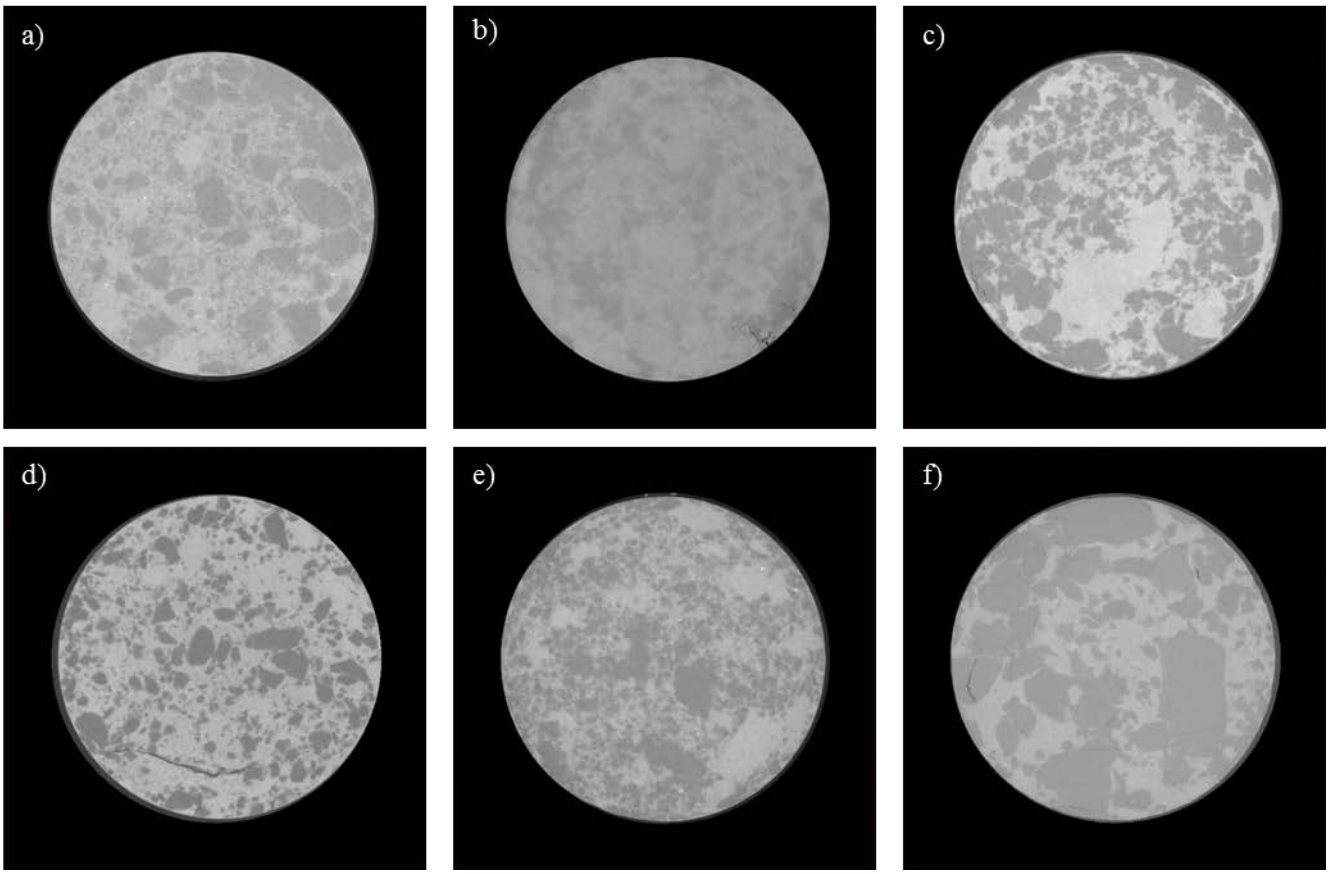


Figure 3-5: Single slice of the reconstructed image volume of binary mixture of phases. a) C-S-H and CH; b) C-S-H and AFm; c) C-S-H and AFt; d) CH and AFt; e) CH and AFm; f) AFm and AFt

Similar to the binary mixtures, quaternary mixtures of phases also showed contrast among phases in greyscale orthoslices upon initial visual inspection, as seen in Figure 3-6. Three distinct phases

were observed visually, with difficulty distinguishing a fourth phase. Similar difficulties segmenting between C-S-H and AFm were expected in the quaternary mixture samples. The low contrast between these two phases prompted use of a method to deconstruct a histogram of either a binary or quaternary mixture into individual Gaussian curves, as discussed in section 3.4.

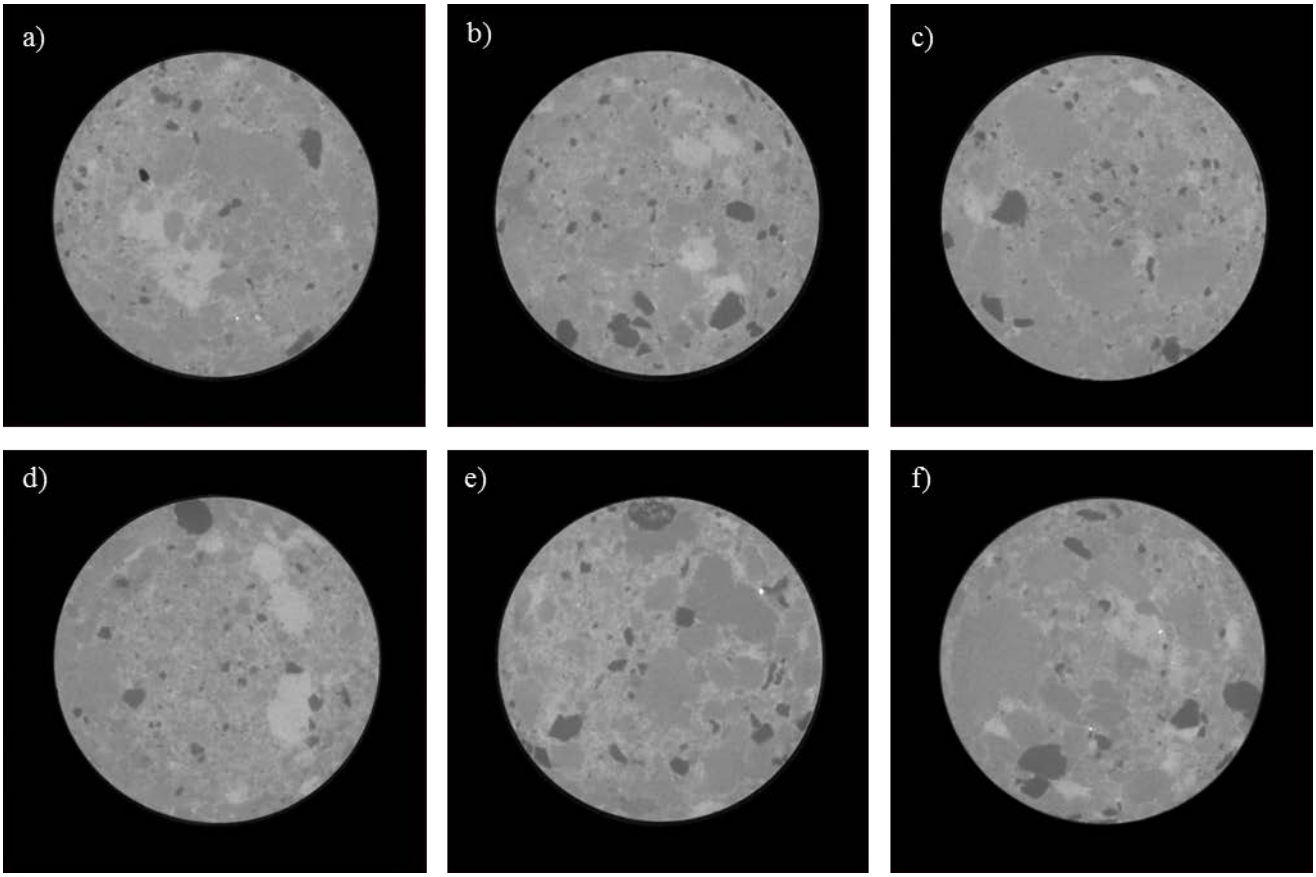


Figure 3-6: Single slice of the reconstructed image volume of quaternary mixture of phases. The top row represents an early-age cement paste, with a composition of ~60% C-S-H, ~25% CH, ~12% AFt, ~3% AFm. The bottom row represents a later-age cement paste, with a composition of ~55% C-S-H, ~25% CH, ~15% AFm, ~5% AFt.

### 3.4. Histogram deconstruction

The histograms for the binary and quaternary mixtures of phases were deconstructed into individual Gaussian curves to properly segment the images in an unbiased manner. A ROI was selected within the data set to analyze the phases while neglecting the sample holder or any void space. The subsequent histogram determined from the ROI was then deconstructed into individual Gaussian curves. Integration was done under each curve of the original histogram, and the area

under each curve was normalized to standardize the section of the histogram for each material. Next, a Gaussian curve was then fit to each normalized area (e.g. two curves for binary mixtures and four curves for quaternary mixtures). Lastly, an automatic process was used to determine the intersection of each curve. The threshold value between two phases was chosen to be the intersection of the Gaussian curves. The typical process for the histogram deconstruction is seen in Figure 3-7.

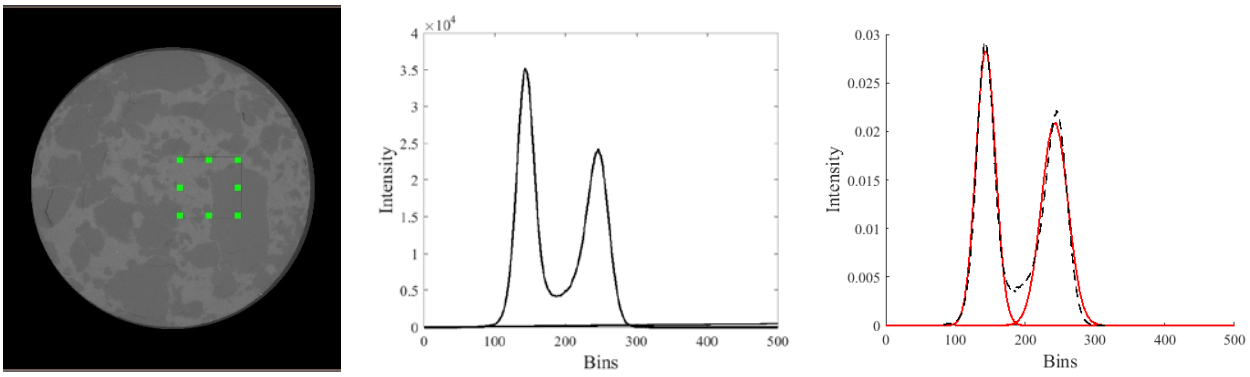


Figure 3-7: Typical histogram deconstruction of a binary mixture of phases. Similar procedures were used for quaternary mixtures. a) ROI selection of the phases only, bounded by the rectangular box. b) Resultant histogram from ROI selection. c) The histogram is normalized, and Gaussian curves are fit to the normalized histogram. The intersection of these curves was determined to be the threshold value

Overall, this method was successful in determining a threshold value for binary mixtures of phases. However, it was difficult to deconstruct the histogram for the binary mixtures with C-S-H and AFm. When these two particular phases were observed by themselves in the layered sample, they exhibited different greyscale values (311 for C-S-H and 238 for AFm), showing promise for segmentation. However, when the two phases were mixed together, the histograms displayed overlapping peaks caused by low contrast at phase boundaries. Deconstruction of the C-S-H/AFm histograms using this procedure was attempted, but ultimately lead to large errors in quantification of each phase. The same approach was applied to the histograms for the quaternary mixtures. Similar difficulties were observed in deconstructing the histograms and determining a threshold value between C-S-H and AFm due to overlapping greyscale intensities.

Therefore, a second approach was used to improve the segmentation of C-S-H and AFm. A histogram was created from a layered sample and used to produce a representative histogram of the pure phases without the influence of partial volume effects and beam attenuation through the

sample. This process was repeated for all three of the layered samples, and the data used to generate an average histogram for each pure phase. Gaussian distribution was applied to each pure phase to determine the mean and standard deviation. The histogram of the mixtures was normalized, and the pure phase Gaussian curves were proportioned to the amount of each phase. The total area under the pure phase Gaussian curves was equal to the area under the histogram of the mixture samples. This resultant pure phase histogram was then overlaid on the histogram of the mixture sample. Similar to before, a simplified approach for thresholding was used such that the intersection of the normalized Gaussian curves was determined to be the threshold value for segmentation. Typical histogram overlays for the binary and quaternary mixtures are seen in Figure 3-8.

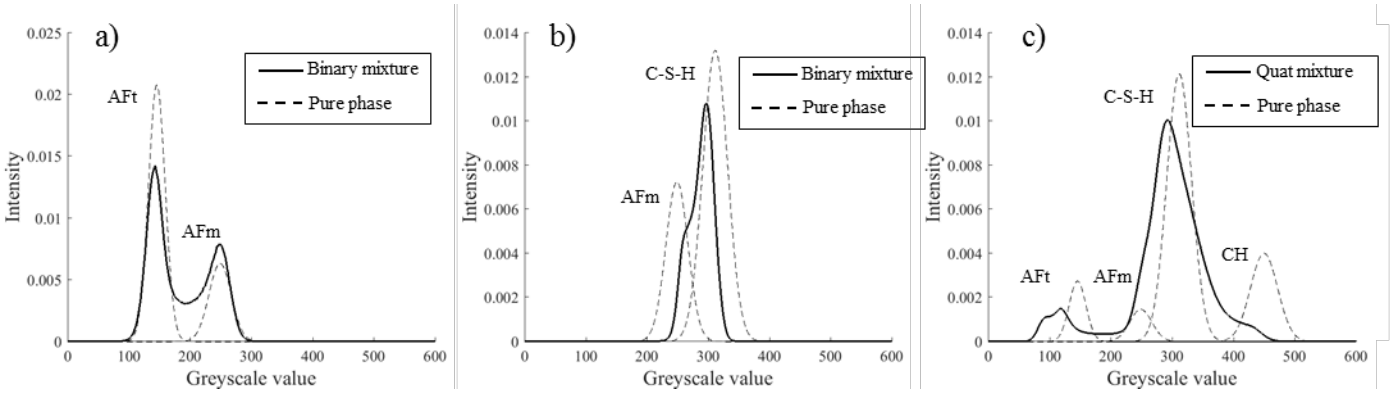


Figure 3-8: a) Normalized pure phase histogram overlaid on an AFt/AFm sample showing the success of this method. The total area under the binary mixture histogram is equal to total area under the pure phase Gaussian curves. b) Normalized pure phase histogram overlaid on a C-S-H/AFm sample. Low contrast between these two phases and partial volume effects resulted in shifts of the peaks for both AFm and C-S-H. c) Pure phase histogram overlaid on quaternary mixture sample.

In summary, histograms were deconstructed in one of two ways. In samples where the histograms could easily be deconstructed into individual Gaussian curves, the threshold value was determined by the intersection of the respective Gaussian curves. In samples where there was significant overlap in adjacent histogram peaks, a simulated pure phase histogram was created from Gaussian curves determined from the layered samples and overlaid on the histogram of the mixed sample. The intersection of the pure phase curves was used as the threshold values. A summary of binary and quaternary mixture threshold values is given in Table 3-3.

Table 3-3: Threshold values for segmentation

| **Binary mixtures** | | | | | | |
|---|---|---|---|---|---|---|
| Sample composition | CH, C-S-H | AFm, C-S-H* | AFt, C-S-H | AFt, CH | AFm, CH | AFm, AFt |
| Average threshold value | 321 | 275 | 218 | 267 | 343 | 179 |
| **Quaternary mixtures** | | | | | | |
| Sample composition | ~55% C-S-H, ~25% CH, ~15% AFm, ~5% AFt | | | ~60% C-S-H, ~25% CH, ~12% AFt, ~3% AFm | | |
| Phase boundary | AFt/ AFm* | AFm/ C-S-H* | C-S-H/ CH* | AFt/ AFm* | AFm/ C-S-H* | C-S-H/ CH* |
| Average threshold value* | 188 | 275 | 378 | 191 | 268 | 379 |

**Use of pure phase histogram for threshold value*

### 3.5. Segmentation

After the histograms were deconstructed and a threshold value was determined, the images were segmented. First, a representative ROI was selected to remove the glass sample holder and to include as much of the compacted powder as possible. After the ROI was chosen, the unwanted data was removed and set to a known greyscale value that would not interfere with subsequent segmentation. Initial visual inspection of the image volume in all samples showed minor cracking within the phase mixture resulting in void space. This void space likely occurred due to stress relaxation after the sample was compacted and extruded. The additional void space within the mixture of phases, as well as the void space between the compacted material and sample holder was also segmented. After the void space was segmented, the threshold value determined from each sample was applied. Upon segmentation of each phase, including the void space, a label value was applied to each segmented phase to determine the total voxels of each phase. Representative segmented samples for the binary and quaternary samples can be seen in Figure 3-9 and Figure 3-10 respectively. These segmented image volumes were used for volume analysis. It should be noted that the void space was ignored for the volume analysis.

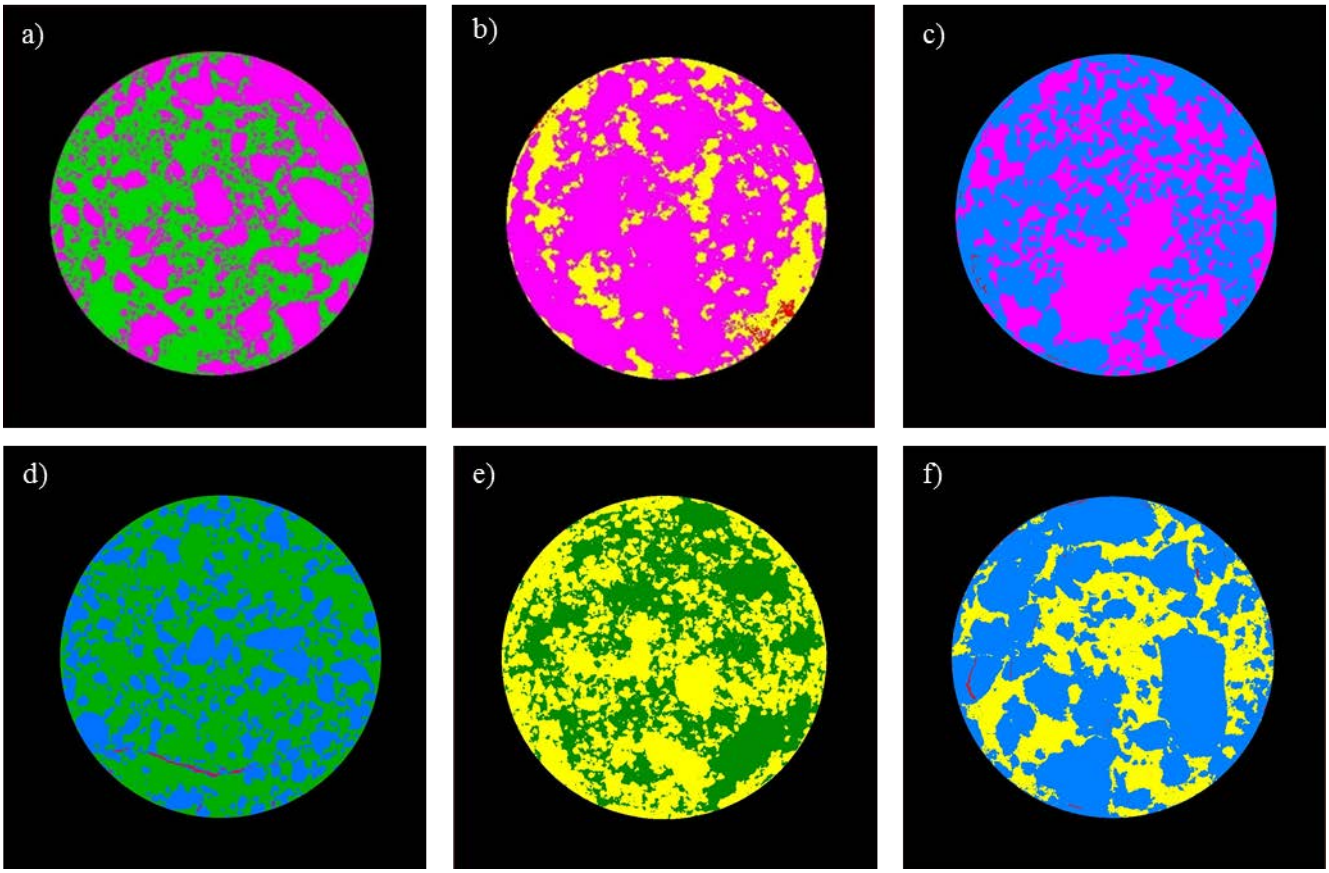


Figure 3-9: Segmented images of binary mixtures with a fixed color value for each material. Red represents void space, purple represents C-S-H, green represents CH, blue represents AFt, and yellow represents AFm. a) CH-C-S-H, b) C-S-H-AFm, c) C-S-H-AFt, d) CH-AFt, e) CH-AFm, f) AFt-AFm

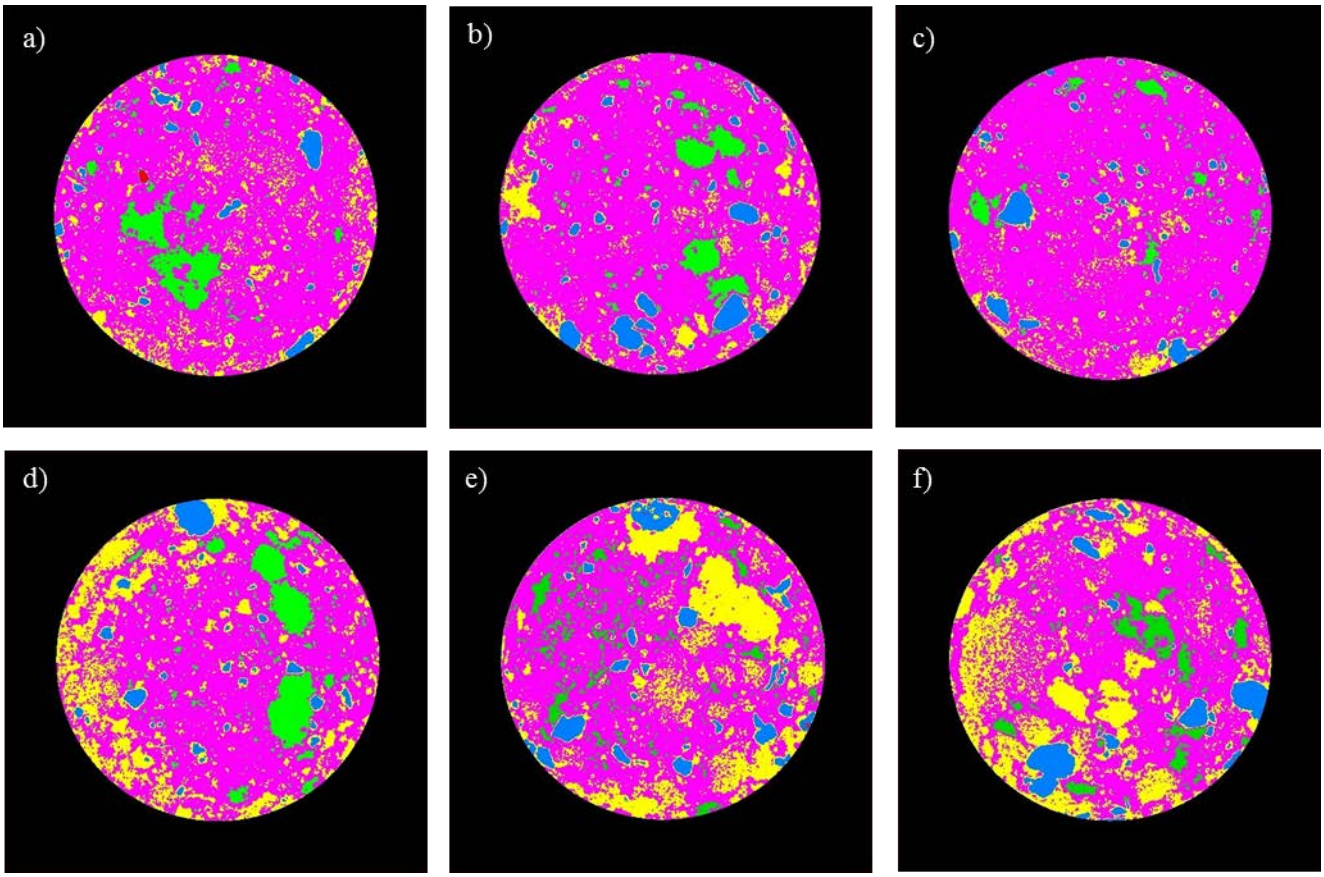


Figure 3-10: Segmented images of quaternary mixtures with a fixed color value for each material. Red represents void space, purple represents C-S-H, green represents CH, blue represents AFt, and yellow represents AFm. The top row represents an early-age cement paste, with a composition of ~60% C-S-H, ~25% CH, ~12% AFt, ~3% AFm. The bottom row represents a later-age cement paste, with a composition of ~55% C-S-H, ~25% CH, ~15% AFm, ~5% AFt.

### 3.6. Volume analysis

Table 3-4 shows the comparison of the volumetric results from the image analysis done on the segmented images of the binary phase mixtures, and the volume determined through the density of the pure phase and the known mass quantity for each sample.

Table 3-4: Comparison of volume of individual phases in binary mixtures

| Phases | Mass (g) | Volume From Mass ($cm^3$) | Image Analysis Volume ($cm^3$) | Error (%) |
|---|---|---|---|---|
| CH | 0.026 | 0.0116 | 0.0133 | -14.9 |
| C-S-H | 0.040 | 0.0172 | 0.0206 | -19.8 |
| CH | 0.016 | 0.0071 | 0.0071 | 0.7 |
| C-S-H | 0.027 | 0.0121 | 0.0141 | -16.2 |
| AFm | 0.014 | 0.0069 | 0.0080 | -15.5 |
| C-S-H | 0.033 | 0.0142 | 0.0101 | 28.8 |
| AFm | 0.022 | 0.0109 | 0.0234 | -114.5 |
| C-S-H | 0.045 | 0.0193 | 0.0089 | 54.0 |
| AFt | 0.034 | 0.0191 | 0.0173 | 9.8 |
| C-S-H | 0.023 | 0.0103 | 0.0093 | 10.4 |
| AFt | 0.018 | 0.0101 | 0.0086 | 14.7 |
| C-S-H | 0.020 | 0.0086 | 0.007 | 18.2 |
| AFt | 0.015 | 0.0084 | 0.008 | 5.8 |
| CH | 0.024 | 0.0107 | 0.0124 | -16.3 |
| AFt | 0.015 | 0.0084 | 0.0079 | 6.7 |
| CH | 0.028 | 0.0124 | 0.0133 | -6.6 |
| AFm | 0.011 | 0.0055 | 0.0054 | 0.9 |
| CH | 0.038 | 0.0169 | 0.0188 | -11.4 |
| AFm | 0.020 | 0.0099 | 0.0102 | -2.7 |
| CH | 0.019 | 0.0084 | 0.0079 | 6.5 |
| AFm | 0.016 | 0.0079 | 0.0069 | 12.9 |
| AFt | 0.035 | 0.0197 | 0.0181 | 7.8 |
| AFm | 0.026 | 0.0129 | 0.0113 | 12.1 |
| AFt | 0.020 | 0.0112 | 0.0106 | 5.5 |

It can be seen the method for thresholding the histograms for the binary mixture of phases was successful, within 20% error, at determining the volume of individual phases. However, due to low contrast in one of the AFm and C-S-H samples, difficulties in segmentation between these two phases led to significant errors in the determining the amounts of each phase in this particular sample. Although the image analysis did not produce exact volumes of each phase, it can be seen in Table 3-5 that the ratio between each phase resulted in small differences between the measured volume from the image analysis and the calculated volume from the mass of each phase. These ratios were determined by taking the volume of one of the phases and dividing by the total volume in the sample. This was done for both the volumes determined from known mass quantities, as

well as the volumes determined from the image analysis. The accuracy in determining phase ratios suggested the ability to determine quantities of phases in the quaternary mixtures. It should be noted minor discrepancies with the difference are presented in Table 3-5 due to rounding.

Table 3-5: Comparison of phase ratios in binary mixtures

| Phases | Single Phase /Total Volume from Mass | Single Phase /Total Volume from Image | Difference |
|---|---|---|---|
| CH | 40.3% | 39.2% | 1.0% |
| C-S-H | 59.7% | 60.8% | -1.0% |
| CH | 37.2% | 37.0% | 0.2% |
| C-S-H | 62.8% | 63.0% | -0.2% |
| AFm | 32.7% | 44.3% | -11.6% |
| C-S-H | 67.3% | 55.7% | 11.6% |
| AFm | 36.1% | 72.4% | -36.4% |
| C-S-H | 63.9% | 27.6% | 36.4% |
| AFt | 65.0% | 65.0% | -0.1% |
| C-S-H | 35.0% | 35.0% | 0.1% |
| AFt | 54.0% | 55.1% | -1.1% |
| C-S-H | 46.0% | 44.9% | 1.1% |
| AFt | 44.0% | 39.2% | 4.8% |
| CH | 56.0% | 60.8% | -4.8% |
| AFt | 40.4% | 37.3% | 3.1% |
| CH | 59.6% | 62.7% | -3.1% |
| AFm | 24.6% | 22.3% | 2.2% |
| CH | 75.4% | 77.7% | -2.2% |
| AFm | 54.1% | 56.4% | -2.3% |
| CH | 45.9% | 43.6% | 2.3% |
| AFm | 28.6% | 27.6% | 1.0% |
| AFt | 71.4% | 72.4% | -1.0% |
| AFm | 53.5% | 51.6% | 1.9% |
| AFt | 46.5% | 48.4% | -1.9% |

Table 3-6 shows the comparison of the volumetric results from the label analysis done on the segmented quaternary phase mixtures, as well as the volume determined through the density of the pure phase and then known mass quantity for each sample.

Table 3-6: Comparison of volume of individual phases in quaternary mixtures

| Phases | Mass (g) | Volume From Mass ($cm^3$) | Image Analysis Volume ($cm^3$) | Error (%) |
|---|---|---|---|---|
| AFt | 0.005 | 0.0028 | 0.0017 | 39.3 |
| CH | 0.015 | 0.0067 | 0.0020 | 69.7 |
| AFm | 0.004 | 0.0020 | 0.0060 | -203.6 |
| C-S-H | 0.043 | 0.0184 | 0.0234 | -26.6 |
| AFt | 0.006 | 0.0034 | 0.0031 | 8.8 |
| CH | 0.014 | 0.0062 | 0.0017 | 71.9 |
| AFm | 0.004 | 0.0020 | 0.0061 | -208.6 |
| C-S-H | 0.046 | 0.0197 | 0.0238 | -20.8 |
| AFt | 0.005 | 0.0028 | 0.0026 | 7.1 |
| CH | 0.014 | 0.0062 | 0.0017 | 72.4 |
| AFm | 0.004 | 0.0020 | 0.0056 | -184.5 |
| C-S-H | 0.043 | 0.0184 | 0.0236 | -28.1 |
| AFt | 0.002 | 0.0011 | 0.0013 | -2.1 |
| CH | 0.015 | 0.0067 | 0.0022 | 99.1 |
| AFm | 0.009 | 0.0045 | 0.0064 | 57.5 |
| C-S-H | 0.033 | 0.0142 | 0.0201 | 60.1 |
| AFt | 0.004 | 0.0022 | 0.0021 | 8.5 |
| CH | 0.016 | 0.0071 | 0.0024 | 66.2 |
| AFm | 0.008 | 0.0040 | 0.0069 | -73.9 |
| C-S-H | 0.033 | 0.0142 | 0.0191 | -35.2 |
| AFt | 0.003 | 0.0017 | 0.0019 | -10.0 |
| CH | 0.014 | 0.0062 | 0.0019 | 68.8 |
| AFm | 0.009 | 0.0045 | 0.0077 | -73.0 |
| C-S-H | 0.036 | 0.0154 | 0.0199 | -28.6 |

Segmentation of the quaternary mixtures of phases produced larger errors than segmentation of the binary phases. It was observed that AFt was the most successful at being quantified compared to the other three phases. Significant histogram overlap between AFm and C-S-H and moderate overlap between C-S-H and CH was observed in all of the quaternary samples, thus leading to difficulties in segmentation. The use of the normalized, pure phase histogram provided guidance on threshold values, but ultimately resulted in larger errors in determining quantities of CH, AFm, and C-S-H. Visual inspection of the histograms of these samples showed minor peaks on the main curve, indicating AFm and CH, but ultimately there was not enough contrast in the phases to get accurate, quantifiable information. Analyzing the ratio of an individual phase to the total volume

determined from the mass proportions and the image analysis showed the correct proportion of AFt could be determined, within 4%. An underestimate of CH was determined in all the samples, whereas quantities of both AFm and C-S-H were overestimated. Significant overlap of the AFm and C-S-H curves for all the samples resulted in difficulties in determining a proper threshold value. Similarly, in most of the samples, there was an overlap of the CH and C-S-H curves.

Table 3-7: Comparison of phase ratios in quaternary mixtures

| Phases | Single Phase /Total Volume from Mass | Single Phase /Total Volume from Image | Difference |
|---|---|---|---|
| AFt | 9.4% | 5.2% | 4.2% |
| CH | 22.3% | 6.1% | 16.2% |
| AFm | 6.6% | 18.2% | -11.6% |
| C-S-H | 61.7% | 70.5% | -8.9% |
| AFt | 10.8% | 8.8% | 1.9% |
| CH | 19.9% | 5.0% | 14.8% |
| AFm | 6.3% | 17.6% | -11.3% |
| C-S-H | 63.0% | 68.5% | -5.5% |
| AFt | 9.5% | 7.8% | 1.8% |
| CH | 21.1% | 5.1% | 16.0% |
| AFm | 6.7% | 16.8% | -10.1% |
| C-S-H | 62.6% | 70.3% | -7.7% |
| AFt | 4.3% | 4.3% | -0.1% |
| CH | 25.2% | 7.2% | 18.0% |
| AFm | 16.9% | 21.4% | -4.5% |
| C-S-H | 53.6% | 67.1% | -13.5% |
| AFt | 8.2% | 6.7% | 1.4% |
| CH | 25.9% | 7.9% | 18.0% |
| AFm | 14.4% | 22.6% | -8.2% |
| C-S-H | 51.5% | 62.7% | -11.2% |
| AFt | 6.1% | 5.9% | 0.2% |
| CH | 22.4% | 6.2% | 16.2% |
| AFm | 16.1% | 24.6% | -8.6% |
| C-S-H | 55.5% | 63.3% | -7.8% |

### 3.7. Causes of error

It was observed that binary mixtures of phases could be segmented to determine the appropriate ratio of each phase, with the exception of AFm and C-S-H. However, the exact quantities of individual phases were either overestimated or underestimated. In quaternary mixtures of phases, segmentation of AFt was successful at determining the amount and ratio of this phase. Both C-S-H and AFm were overestimated and CH was underestimated due to overlap of individual histogram curves caused by low contrast.

Several possible reasons contributed to the inability to get exact quantities of each phase in the binary samples. One contributing factor was the possibility of loss of material during the sample preparation. Loss during loading of the material into the compaction device, as well as small amounts of material left in the compaction device during extrusion may have led to errors in the actual mass of each material in all of the samples. Additionally, published values of phase densities were used to convert the known mass of individual phases to a volume. Minor variations in the actual density of the synthesized phases could attribute to errors in determining the volume of each phase from the known mass.

Additionally, a simplified approach was used for determining the threshold between different phases during the segmentation process. The threshold value between two phases was chosen to be the intersection of the Gaussian curves of individual phases. This simplified approach likely contributed to the observed errors in regions where greyscale values were similar. Several advanced thresholding algorithms exist that help improve the classification of voxels in regions of overlapping peaks in histograms [54, 58-60] with each having benefits and deficits, depending on the situation they are used [61]. The use of one or more of these advanced thresholding techniques might reduce the errors observed in the quaternary mixtures of phases, but this was out of the scope of this research.

Another difficulty that led to possible error in the quantities of each phase was attributed to the limitations of the setup and equipment used for scanning samples. One contributing factor was the limitation of spatial resolution. A resolution of 2.61 μm/voxel was achieved, but any material smaller than 2.61 μm would not be detected, or would result in partial volume effects. Partial volume effects occur when two or more materials are present in a voxel, and the resultant greyscale

value is the average of all of the materials present in that particular voxel [62]. Since significant overlap of AFm and C-S-H and partial overlap of C-S-H and CH were observed, significant partial volume effects could have been present resulting in incorrect greyscale values. While the ability to image at higher resolution would result in lower amounts of partial volume effects, current limitations on spatial resolution are approximately 0.45 micron/voxel at synchrotron facilities using standard procedures [63]. Variations in spatial resolution between facilities are dependent on the available detectors, magnification capabilities, and sample size. These limitations allowed for imaging at 2.61 μm/voxel for this research.

Lastly, the top and bottom of the compacted sample were not aligned to the beam. Slight variations in the verticality of the compacted sample in the glass tube when placed on the rotation stage resulted in a region of voxels that were likely improperly segmented at the void/phase boundary due to partial volume effects. This region affected 20-30 slices at the top and bottom of each sample. These potential voxel misclassifications needed to be incorporated since the entire image volume needed to be analyzed to compare to the known mass. This source of error was expected to be minor and contribute to less than 0.5% error.

### 3.8. Conclusions

The use of x-ray CT has typically been done on void and crack characterization of portland cement systems due to limitations in greyscale values in the hydrated phases. This research analyzed the ability to quantify synthesized phases of the four main hydrated phases (AFt, AFm, C-S-H, and CH) of portland cement using synchrotron x-ray CT. Quantifying samples with two materials through non-destructive image analysis was successfully done. However, low contrast between several phases reduced the ability to properly quantify samples with mixtures of 4 materials. The following conclusions were found from this research:

- Segmentation and volume analysis of binary mixtures of phases was successfully done. Comparison of the volume determined from image analysis closely matched the volume determined by the mass and density of each phase. In most cases the error between the image analysis volume and volume calculated from the quantity of mass and densities was within 15%. Additionally, accurate proportions of each phase were determined in all combinations within 4.8% or less, with the exception of AFm and C-S-H.

- In quaternary mixtures of phases representative of a hydrated portland cement system, quantifiable volumes of AFt, with 4% error, were measured when compared to the calculated volume based on the mass and density. The volume of AFm and C-S-H were overestimated and CH was underestimated, typically. However, proportions of each phase were determined within 18% for all phases.
- Low contrast was observed between AFm and C-S-H, and to a minor extent between CH and C-S-H, resulting in increased errors in the quaternary mixtures of phases when compared to the binary mixtures.

Work presented herein provided a crucial first step to advance traditional x-ray CT beyond its current primary role in porosity and microstructure characterization and into quantitative phase characterization. The authors are currently working on several ways to further improve segmentation in these phases and reduce the percent error.

### 3.9. Acknowledgments

The authors would like to thank the staff, in particular Dr. Mark Rivers, at Sector 13 (GSECARS) at the Advanced Photon Source at the Argonne National Lab. Their support and technical expertise was greatly appreciated. Additionally, the authors would like to thank Dr. Prannoy Suraneni for his assistance on material characterization.

### 3.10. References

[1] I. Chen, M.G. Juenger, Synthesis and hydration of calcium sulfoaluminate-belite cements with varied phase compositions, Journal of Materials Science, 46 (2011) 2568-2577.

[2] P. Duxson, A. Fernández-Jiménez, J.L. Provis, G.C. Lukey, A. Palomo, J.S.J. van Deventer, Geopolymer technology: The current state of the art, Journal of Materials Science, 42 (2007) 2917-2933.

[3] E. Gartner, Are there any practical alternatives to the manufacture of portland cement clinker?, Journal of the Chinese Ceramic Society, 40 (2012) 61-68.

[4] C. Gosselin, E. Gallucci, K. Scrivener, Influence of self heating and $Li_2SO_4$ addition on the microstructural development of calcium aluminate cement, Cement and Concrete Research, 40 (2010) 1555-1570.

[5] J.H. Ideker, C.G. Gosselin, R. Barborak, An alternative repair material: Basics and practical testing of calcium aluminate cements, Concrete International, 35 (2013) 33-37.

[6] M.C.G. Juenger, F. Winnefeld, J.L. Provis, J.H. Ideker, Advances in alternative cementitious binders, Cement and Concrete Research, 41 (2011) 1232-1243.

[7] A. Radlińska, J. Yost, M. Salera, Material properties of structurally viable alkali-activated fly ash concrete, Journal of Materials in Civil Engineering, 25 (2013) 1456-1464.

[8] C. Shi, A.F. Jiménez, A. Palomo, New cements for the 21st century: The pursuit of an alternative to portland cement, Cement and Concrete Research, 41 (2011) 750-763.

[9] R. Alizadeh, J.J. Beaudoin, L. Raki, V. Terskikh, C-S-H/polyaniline nanocomposites prepared by in situ polymerization, Journal of Materials Science, 46 (2011) 460-467.

[10] J.J. Beaudoin, H. Drame, L. Raki, R. Alizadeh, Formation and characterization of calcium silicate hydrate-hexadecyltrimethylammonium nanostructure, Journal of Materials Research, 23 (2008) 2804-2815.

[11] J.J. Beaudoin, H. Drame, L. Raki, R. Alizadeh, Formation and properties of C-S-H-PEG nano-structures, Materials and Structures, 42 (2009) 1003-1014.

[12] R. Khoshnazar, L. Raki, J. Beaudoin, R. Alizadeh, Solvent exchange in sulphoaluminate phases. Part I: Ettringite, Advances in Cement Research, 25 (2013) 314-321.

[13] R. Khoshnazar, L. Raki, J. Beaudoin, R. Alizadeh, Solvent exchange in sulfoaluminate phases. Part II: Monosulfate, Advances in Cement Research, 25 (2013) 322-331.

[14] F. Sanchez, K. Sobolev, Nanotechnology in concrete – A review, Construction and Building Materials, 24 (2010) 2060-2071.

[15] M. Vandamme, F.-J. Ulm, P. Fonollosa, Nanogranular packing of C–S–H at substochiometric conditions, Cement and Concrete Research, 40 (2010) 14-26.

[16] P.J.M. Monteiro, A.P. Kirchheim, S. Chae, P. Fischer, A.A. MacDowell, E. Schaible, H.R. Wenk, Characterizing the nano and micro structure of concrete to improve its durability, Cement and Concrete Composites, 31 (2009) 577-584.

[17] K. Tosun, B. Baradan, Effect of ettringite morphology on DEF-related expansion, Cement and Concrete Composites, 32 (2010) 271-280.

[18] P.E. Stutzman, J.R. Clifton, Specimen preparation for scanning electron microscopy, Twenty-First International Conference on Cement Microscopy, Las Vegas, NV, April 25-29, 1999, 1999, pp. 10-22.

[19] K.O. Kjellsen, A. Monsøy, K. Isachsen, R.J. Detwiler, Preparation of flat-polished specimens for SEM-backscattered electron imaging and x-ray microanalysis—importance of epoxy impregnation, Cement and Concrete Research, 33 (2003) 611-616.

[20] U. Rattanasak, K. Kendall, Pore structure of cement/pozzolan composites by x-ray microtomography, Cement and Concrete Research, 35 (2005) 637-640.

[21] J.L. Provis, R.J. Myers, C.E. White, V. Rose, J.S.J. van Deventer, X-ray microtomography shows pore structure and tortuosity in alkali-activated binders, Cement and Concrete Research, 42 (2012) 855-864.

[22] T.S. Yun, K.Y. Kim, J. Choo, D.H. Kang, Quantifying the distribution of paste-void spacing of hardened cement paste using x-ray computed tomography, Materials Characterization, 73 (2012) 137-143.

[23] S. Lu, E.N. Landis, D.T. Keane, X-ray microtomographic studies of pore structure and permeability in portland cement concrete, Materials and Structures, 39 (2006) 611-620.

[24] N. Bossa, P. Chaurand, J. Vicente, D. Borschneck, C. Levard, O. Aguerre-Chariol, J. Rose, Micro- and nano-x-ray computed-tomography: A step forward in the characterization of the pore network of a leached cement paste, Cement and Concrete Research, 67 (2015) 138-147.

[25] K.Y. Kim, T.S. Yun, K.P. Park, Evaluation of pore structures and cracking in cement paste exposed to elevated temperatures by x-ray computed tomography, Cement and Concrete Research, 50 (2013) 34-40.

[26] M.A.B. Promentilla, T. Sugiyama, T. Hitomi, N. Takeda, Characterizing the 3D pore structure of hardened cement paste with synchrotron microtomography, Journal of Advanced Concrete Technology, 6 (2008) 273-286.

[27] M.A.B. Promentilla, T. Sugiyama, T. Hitomi, N. Takeda, Quantification of tortuosity in hardened cement pastes using synchrotron-based x-ray computed microtomography, Cement and Concrete Research, 39 (2009) 548-557.

[28] M. Lanzón, V. Cnudde, T. de Kock, J. Dewanckele, X-ray microtomography (μ-CT) to evaluate microstructure of mortars containing low density additions, Cement and Concrete Composites, 34 (2012) 993-1000.

[29] T. Sugiyama, M.A.B. Promentilla, T. Hitomi, N. Takeda, Application of synchrotron microtomography for pore structure characterization of deteriorated cementitious materials due to leaching, Cement and Concrete Research, 40 (2010) 1265-1270.

[30] E. Gallucci, K. Scrivener, A. Groso, M. Stampanoni, G. Margaritondo, 3D experimental investigation of the microstructure of cement pastes using synchrotron x-ray microtomography (μCT), Cement and Concrete Research, 37 (2007) 360-368.

[31] D. Asahina, E.N. Landis, J.E. Bolander, Modeling of phase interfaces during pre-critical crack growth in concrete, Cement and Concrete Composites, 33 (2011) 966-977.

[32] H. Elaqra, N. Godin, G. Peix, M. R'Mili, G. Fantozzi, Damage evolution analysis in mortar, during compressive loading using acoustic emission and x-ray tomography: Effects of the sand/cement ratio, Cement and Concrete Research, 37 (2007) 703-713.

[33] T. Rougelot, N. Burlion, D. Bernard, F. Skoczylas, About microcracking due to leaching in cementitious composites: X-ray microtomography description and numerical approach, Cement and Concrete Research, 40 (2010) 271-283.

[34] J.S. Lawler, D.T. Keane, S.P. Shah, Measuring three-dimensional damage of mortar in compression with x-ray microtomography and digital image correlation, American Concrete Institute SP 189, (2000) 187-202.

[35] Q. Hu, M.T. Ley, J. Davis, J.C. Hanan, R. Frazier, Y. Zhang, 3D chemical segmentation of fly ash particles with x-ray computed tomography and electron probe microanalysis, Fuel, 116 (2014) 229-236.

[36] A. Diaz, P. Trtik, M. Guizar-Sicairos, A. Menzel, P. Thibault, O. Bunk, Quantitative x-ray phase nanotomography, Physical Review B, 85 (2012).

[37] P. Trtik, A. Diaz, M. Guizar-Sicairos, A. Menzel, O. Bunk, Density mapping of hardened cement paste using ptychographic x-ray computed tomography, Cement and Concrete Composites, 36 (2013) 71-77.

[38] J.C. da Silva, P. Trtik, A. Diaz, M. Holler, M. Guizar-Sicairos, J. Raabe, O. Bunk, A. Menzel, Mass density and water content of saturated never-dried calcium silicate hydrates, Langmuir, 31 (2015) 3779-3783.

[39] A. Cuesta, A.G. De la Torre, I. Santacruz, P. Trtik, J.C. da Silva, A. Diaz, M. Holler, M.A.G. Aranda, Chemistry and mass density of aluminum hydroxide gel in eco-cements by ptychographic x-ray computed tomography, The Journal of Physical Chemistry C, 121 (2017) 3044-3054.

[40] D. Wildenschild, A.P. Sheppard, X-ray imaging and analysis techniques for quantifying pore-scale structure and processes in subsurface porous medium systems, Advances in Water Resources, 51 (2013) 217-246.

[41] L. Salvo, P. Cloetens, E. Maire, S. Zabler, J.J. Blandin, J.Y. Buffière, W. Ludwig, E. Boller, D. Bellet, C. Josserond, X-ray micro-tomography an attractive characterisation technique in materials science, Nuclear Instruments and Methods in Physics Research Section B: Beam Interactions with Materials and Atoms, 200 (2003) 273-286.

[42] H. Lusic, M.W. Grinstaff, X-ray-computed tomography contrast agents, Chemical Reviews, 113 (2012) 1641-1666.

[43] K. Wan, Q. Xu, Y. Wang, G. Pan, 3D spatial distribution of the calcium carbonate caused by carbonation of cement paste, Cement and Concrete Composites, 45 (2014) 255-263.

[44] R. Alizadeh, J.J. Beaudoin, L. Raki, Mechanical properties of calcium silicate hydrates, Materials and Structures, 44 (2011) 13-28.

[45] I.G. Richardson, The nature of C-S-H in hardened cements, Cement and Concrete Research, 29 (1999) 1131-1147.

[46] L.J. Struble, P.W. Brown, An evaluation of ettringite and related compounds for use in the solar energy storage, US Department of Commerce, 1982, pp. 11.

[47] H.J. Kuzel, Synthesis and x-ray study of the crystalline composition $3CaO{\cdot}Al_2O_3{\cdot}CaSO_4{\cdot}12H_2O$, Neues Jahrbuch Mineral Monatsh, 7 (1965) 193-197.

[48] N.N. Skoblinskaya, K.G. Krasilnikov, L.V. Nikitina, V.P. Varlamov, Changes in crystal structure of ettringite on dehydration. 2, Cement and Concrete Research, 5 (1975) 419-431.

[49] H.F.W. Taylor, Cement Chemistry, 2nd Edition ed., Thomas Telford Publishing, London, England, 1997.

[50] R. Allman, Refinement of the hybrid layer structure $[Ca_2Al(OH)_6]^{+}{\cdot}[1/2SO_4{\cdot}3H_2O]^{-}$, Neues Jahrbuch für Mineralogie Monatsheft, (1977) 136-144.

[51] F. Goetz-Neunhoeffer, J. Neubauer, P. Schwesig, Mineralogical characteristics of ettringites synthesized from solutions and suspensions, Cement and Concrete Research, 36 (2006) 65-70.

[52] S.M. Antao, M.J. Duane, I. Hassan, DTA, TG, and RD studies of sturmanite and ettringite, The Canadian Mineralogist, 40 (2002) 1403-1409.

[53] A. Buades, B. Coll, J.M. Morel, A non-local algorithm for image denoising, 2005 IEEE Computer Society Conference on Computer Vision and Pattern Recognition (CVPR'05), 2005, pp. 60-65 vol. 62.

[54] L. Vincent, P. Soille, Watersheds in digital spaces: an efficient algorithm based on immersion simulations, IEEE Transactions on Pattern Analysis and Machine Intelligence, 13 (1991) 583-598.

[55] M. Balonis, F.P. Glasser, The density of cement phases, Cement and Concrete Research, 39 (2009) 733-739.

[56] P. Yu, Kirkpatrick, R. J., Poe, B., McMillan, P. F. and Cong, X. , Structure of calcium silicate hydrate (C-S-H): Near-, mid-, and far-infrared spectroscopy, Journal of the American Ceramic Society, 82 (1999) 742-748.

[57] X. Cong, R.J. Kirkpatrick, $^{29}$Si MAS NMR study of the structure of calcium silicate hydrate, Advanced Cement Based Materials, 3 (1996) 144-156.

[58] W. Oh, W.B. Lindquist, Image Thresholding by Indicator Kriging, IEEE Transactions on Pattern Analysis and Machine Intelligence, 21 (1999) 590-602.

[59] M. Berthod, Z. Kato, S. Yu, J. Zerubia, Bayesian image classification using Markov random fields, Image and Vision Computing, 14 (1996) 285-295.

[60] A.P. Sheppard, R.M. Sok, H. Averdunk, Techniques for image enhancement and segmentation of tomographic images of porous materials, Physica A: Statistical Mechanics and its Applications, 339 (2004) 145-151.

[61] S. Schlüter, A. Sheppard, K. Brown, D. Wildenschild, Image processing of multiphase images obtained via x-ray microtomography: A review, Water Resources Research, 50 (2014) 3615-3639.

[62] E.J. Hoffman, S.-C. Huang, M.E. Phelps, Quantitation in positron emission computed tomography: 1. Effect of object size, Journal of Computer Assisted Tomography, 3 (1979) 299-308.

[63] M.B. Leite, P.J.M. Monteiro, Microstructural analysis of recycled concrete using x-ray microtomography, Cement and Concrete Research, 81 (2016) 38-48.

# Manuscript 2

## Use of iodine for improving phase quantification using x-ray tomography

Tyler Deboodt, Dorthe Wildenschild, Jason H. Ideker, O. Burkan Isgor

Submitted and under review in: *Cement and Concrete Research*

# 4. Manuscript 2

## Use of iodine for improving phase quantification using x-ray tomography

Tyler Deboodt[1], Dorthe Wildenschild[2], Jason H. Ideker[2], O. Burkan Isgor[3]

**Abstract:**

X-ray computed tomography (CT) has been successfully used to quantify pore structure and crack characterization in cementitious materials. However, the similar contrast (greyscale values) of the hydration products in the reconstructed image volume has limited the ability to quantify these phases, and this remains a significant need to further the impact of this experimental method. The goal of this research was to improve the ability to quantify synthesized hydration products by incorporating a contrast agent to improve segmentation between the four main hydration products in portland cement; C-S-H, calcium hydroxide, monosulfate, and ettringite. Pure C-S-H, CH, and AFt, and a pure and modified AFm, with iodine as a contrast agent, were synthesized for investigation by x-ray CT. Multi-energy scans were used to isolate individual phases using a synchrotron radiation facility. Using iodine as a contrast agent resulted in accurate quantification of the four main hydration products was achieved.

**Keywords:** image analysis (B), hydration products (B), cement (D), composite (E), x-ray tomography

---

[1] Graduate Research Assistant, School of Civil and Construction Engineering, Oregon State University

[2] Professor, School of Chemical, Biological, and Environmental Engineering, Associate Dean of Graduate School, Oregon State University

[3] Associate Professor, School of Civil and Construction Engineering, Oregon State University

[4] Professor, School of Civil and Construction Engineering, Oregon State University

## 4.1. Introduction

There is a growing interest in using x-ray computed tomography (CT) to study a variety of properties of cement and concrete. These include characterizing physical properties, such as internal pore structure and tortuosity [1-14], morphology of aggregates [15-18], crack formation, propagation, and subsequent healing of cracks [6, 19-27], distribution of fiber reinforcement [28-30], microstructure formation during hydration [31-33], microstructure development [4, 9, 14, 34-38], segregation resistance [39], and mass diffusivity [40]. Furthermore, x-ray CT has been used to study deterioration of the cement paste matrix. These studies include detection of freeze-thaw damage [41, 42], alkali-silica reaction [41, 43], formation of calcium carbonate caused by carbonation [44], rebar location and formation corrosion products [45-47], delayed ettringite formation [48], sulfate attack [49-51], and leaching of calcium hydroxide [5, 25, 52-54].

A major issue related to the application of x-ray CT as a standalone method to characterize cementitious systems is the inability to distinguish different solid phases due to relatively similar greyscale values [48]. Due to this difficulty, there have been a limited number of studies that attempted to identify different solid phases in hydrated cement [5, 25, 33, 35, 55]. In addition to low contrast, often spatial resolution is the limiting factor in resolving individual solid phases. With the steady improvement in the capabilities of lab based systems and access to synchrotron radiation centers, the ability to distinguish such phases using these systems would allow researchers an invaluable tool to characterize current and novel alternative cementitious systems. Currently, maximum resolution achievable in x-ray CT is approximately 50 nm/voxel, and it is expected to be reduced as low as 15 nm/voxel with emerging technologies [56]. These challenges have often resulted in the limitations of x-ray CT for extracting quantifiable information on cementitious materials, and resulted in many of the aforementioned studies being limited to qualitative or semi-quantitative analysis.

Previous research investigating synthesized, pure hydration products has shown that there was low contrast between monosulfate (AFm) and calcium silicate hydrate (C-S-H) when combined in a binary mixture, thus leading to difficulties in accurately quantifying these particular phases. The errors were further compounded when AFm and C-S-H were combined in a quaternary mixture with ettringite (AFt) and calcium hydroxide (CH) in proportions that represented a hydrated cement paste due to similar greyscale values observed in AFm, C-S-H, and CH to a lesser extent

[55]. Difficulties in segmenting phases is a common problem, although there has been limited success. This has been achieved in distinguishing zones of decalcification [25, 52], as well as distinguishing unhydrated and hydrated phases [33, 35].

A common approach used in the medical field for research and clinical applications to improve image contrast, and subsequent histogram segmentation, is to implement contrast agents [57]. Success has been achieved when using x-ray CT with contrast agents to differentiate interfaces in tissues to improve imaging and diagnosis [58]. Recent work on the use of contrast agents in geosciences [59-63] has allowed the utilization of x-ray CT to differentiate materials in environmental and biological applications, as well as ion transport in portland cement [64]. The success of these applications forms the motivation of the present study to resolve the limitations of low contrast in hydrated cement phases by focusing on using contrast agents to differentiate phases in cementitious systems. The goal of this research was to address the low contrast between hydration products, particularly AFm and C-S-H. This was achieved by determining a method to implement a contrast agent in AFm, while not changing the crystalline structure. Selective use of such contrast agents would resolve the issue with low image contrast amongst C-S-H and AFm.

## 4.2. Experimental

### *4.2.1. Synchrotron x-ray CT*

X-ray CT is a non-destructive, non-contact technique that uses computer-processed x-rays to produce three-dimensional (3D) tomographic images of specific zones of a scanned object, allowing the user to see inside the object without damaging the specimen [20-23]. A sample is placed between an x-ray source and a detector. Incident x-rays with a known energy are sent through a sample and an image is recorded on a detector after the attenuated x-rays are converted to visible light in a scintillator [41]. 3D image volumes can be created by collecting a series of orthographic projects. These projections are collected by rotating the sample (up to 360°) along its vertical axis.

Synchrotron radiation sources are well suited for high-resolution, high-speed tomographic imaging because of the extremely high photon flux, and the ability for the white synchrotron light to be filtered to specific energy levels with a monochromator. This can be used to enhance the contrast between different phases in an object by scanning at the peak absorption energy of materials. A

sudden increase in absorption coefficient is observed when an x-ray passes through a sample with an energy equal to or slightly greater than the binding energy of the K-shell electrons of the atom. This energy level is known as the absorption edge (k-edge) and increases with the atomic number of the element. To generate images with the highest contrast, the energy of the x-ray source can be adjusted closely to match the k-edge value [58].

In this study, synchrotron x-ray tomography was used in conjunction with a contrast agent to enhance the contrast between the four main hydrate phases (C-S-H, CH, AFt, and AFm). Previous research has indicated low contrast between C-S-H and AFm, thus leading to difficulties segmenting such phase to gain quantifiable information [55]. Pure and doped AFm phases with iodine as a contrast agent were synthesized in the laboratory and compacted to a density that represents a hydrated portland cement paste. Dual energy scans above and below the absorption edge (k-edge) were used to distinguish the contrast agent. Through image subtraction, the material containing the contrast agent can be quantified quickly and accurately [65]. The beam energy was tuned with a monochromator to scan above and below the k-edge of the contrast agent used, iodine, which were 33.069 keV and 33.269 keV, respectively.

The GeoSoilEnviroCARS (GSECARS) 13-BMD beamline of the Advanced Photon Source at the Argonne National Laboratory was used for all scans. The samples were mounted in a drill chuck, which was attached to the rotation stage. The beam size was 3.14 mm wide by 5.02 mm tall, resulting in a 2.60 μm/pixel resolution. For each scan, 900 x-ray projection images with a rotation step of 0.18° and exposure time of 2 seconds were collected. The 2D projections were reconstructed to a 3D volume using a filtered back projection algorithm to produce a volume of 16-bit greyscale images.

### *4.2.2. Potential for phase substitution in AFm as contrast agent*

This research focused on improving the contrast between AFm and C-S-H by incorporating a contrast agent into AFm. This phase was selected for its ability to accommodate various changes in chemical composition without changing the crystalline structure. The AFm phases belong to the lamellar double hydroxide (LDH) family, which is a type of anionic clay material with cationic brucite layers with exchangeable interlayer anions [66]. Most LDHs have relatively weak interlayer bonding, which results in the ability to capture inorganic anions by both surface

adsorption and anion exchange [67, 68]. The structure is composed of positively charged outer layers $[Ca_2Al(OH)_6]^+$ and negatively charged interlayers $[X{\cdot}xH_2O]^-$, where X is an exchangeable singly charged (e.g. chloride) or half-doubly charged anion (e.g. sulfate, carbonate, aluminosilicate). The anion present in the AFm phase is sensitive to the cement composition, as well as the service environment. Anions that may be present in portland cement systems are hydroxide, sulfate, and carbonate. In blended cements, such as portland cement and slag cement, aluminosilicate anions are typically present [69]. Several studies have shown that the AFm phase has successfully incorporated singly charged anions [70-78], half-doubly charged anions [70, 79-82], and multiple anionic compounds [75, 83-87]. The incorporation of $I^-$ [72, 75, 78] into the AFm phase was chosen as the contrast agent in this work due to its ability to ionically substitute for $SO_4^{2-}$ without changing the crystalline structure, and has a k-edge (33.169 keV), which is within the scanning energy range of the synchrotron radiation source at GSECARS 13-BMD.

### *4.2.3. Synthesis of phases*

C-S-H formed due to the hydration of $C_3S$ and β-$C_2S$ in the hydrated cement paste normally ranges from 1.2 – 2.1 and has an average C/S of about 1.75 [88]. The C-S-H created in this research was synthesized using the pozzolanic reaction technique to create a calcium-to-silica ratio (C/S) = 1.7 [89]. Fresh calcium oxide (CaO) was created by heating reagent grade calcium carbonate at 900 °C for 24 hours. Reactive, amorphous silica was dried in an oven at 80 °C overnight to remove any adsorbed water. After the materials cooled, stoichiometric amounts of silica and CaO were mixed manually in a high-density polyethylene bottle. De-gassed, de-ionized water was added to the powder mixture to create a solid to liquid ratio of approximately 10. The mixture was placed on a rotation rack at 6 rpm for 21 days. It has been reported that the reaction is nearly complete after one week, and longer rotation times allow for a well ordered crystalline structure representative of an aged C-S-H material that can be detected using x-ray diffraction (XRD) [89]. After 21 days of rotation, the material was vacuum filtered, and the samples were placed in a vacuum desiccator at 11% relative humidity (RH).

AFt was made using procedures described by Struble and Brown [90]. Stoichiometric amounts of reagent grade $Al_2(SO_4)_3$ and CaO were mixed to create ettringite. The CaO was created using the procedures described above, and was dissolved in a 10% sucrose solution. A solution of $Al_2(SO_4)_3$ was created with de-gassed, de-ionized water. The two solutions were then mixed on a magnetic

stirring plate for 60 hours. The precipitate was then vacuum filtered. After filtering, the samples were placed in a vacuum desiccator and conditioned at 11% RH.

AFm with iodine as a contrast agent was synthesized by modifying the general procedures described by Kuzel [91] to synthesize pure AFm. The preparation of the modified AFm (AFm-I) was done by mixing stoichiometric amounts of $C_3A$ and reagent grade gypsum in a 2 M potassium iodide solution. The dry materials were placed in the vessel and manually mixed. The potassium iodide solution was created with de-gassed, de-ionized water and then added to the dry materials. The resultant solution was then placed in the hydrothermal pressure vessel and heated to 150 °C for four days. After 4 days, the excess water was discharged and the material was vacuum dried and placed in a vacuum desiccator and conditioned at 11% RH. Similar procedures were used to create a pure AFm, but the dry materials were mixed in an abundance of de-gassed, de-ionized water before being heated to 150 ˚C.

Lastly, commercially available, reagent grade calcium hydroxide (>95% purity) was used to represent portlandite. The material was conditioned at 11% RH in a vacuum desiccator prior to compaction for x-ray CT scans.

### *4.2.4. Characterization of materials*

XRD and thermogravimetric analysis\differential thermogravimetric analysis (TGA\DTG) were used to characterize the synthesized phases. A Bruker-AXS D8 Discovery XRD was also used for the characterization of the synthesized phases. Diffraction angle range of $6° < 2\Theta < 60°$ with a step size of 0.08° and a scan speed of 0.96˚/min with an accelerating voltage of 40 kV and current of 40 mA was used for analysis of AFm, AFm-I, and AFt. For the analysis of C-S-H, a diffraction angle of $4˚<2\Theta<15˚$ with a step size of 0.03˚ and a scan speed of 0.36˚/min was used. In pure AFm, a basal spacing of 0.893 nm corresponds to an interlayer distance in the AFm crystal with 12 molecules of water [92]. A reduction of the d-spacing at the *006* reflection in AFm phases occurs with $I^-$ substituting for $SO_4^{2-}$ [93]. AFt with 32 molecules of water has an expected basal spacing of 0.973 nm [94] and 0.561 nm [95].

A TA Instruments Q50 was used to characterize the synthesized phases for TGA/DTG analysis. A sample size ranging from 20-35 mg was used for all materials. A heating rate of 10 ˚C/min under a flow of nitrogen gas (60 ml/min) heated the materials from ambient temperature (23 ˚C) to 1000

˚C. In TGA, the mass loss occurring between 120 ˚C and 230 ˚C indicates water loss in AFt [95]. Other losses in AFt during TGA occur between 550 ˚C and 1000 ˚C, and these losses are attributed to the release of sulfur oxides. These have been reported in literature in AFt synthesized in sucrose [96], as well as in natural ettringite [97]. Water loss in AFm begins around 220 ˚C as the material releases 6 water molecules with the remaining 6 water molecules being released at temperatures above 220 ˚C. A total mass loss of 34.7% corresponds to AFm with 12 water molecules [98].

### *4.2.5. Sample preparation for x-ray CT*

Preconditioned, pure phases were compacted in a hardened steel die using a piston and hydraulic press loaded to 515 MPa. The load was applied at 10 MPa/second until the desired pressure was achieved, and the load was held for 30 seconds once the pressure was reached. The compaction pressure was chosen to create a material with a porosity similar to that of hydrated portland cement paste [99]. Two types of samples were created. One sample type was a binary mixture of AFm (with and without contrast agents) and C-S-H. This sample type was created to determine whether the addition of the iodine as a contrast agent would improve segmentation and quantification of each phase. The second sample type was a quaternary blend of four phases, consisting of C-S-H, CH, AFm (with and without contrast agents), and AFt. For both sample types known amounts of each phase were intermixed by hand prior to compaction, and then the powder mixture was placed in the die and hydraulic press. The load was applied until the desired pressure was achieved. The compacted sample was extruded and placed in a glass tube with nominal dimensions of 6 mm OD and 3.73 mm ID. The tube was sealed at each end to minimize the interaction between the environment and the sample. A summary of the samples tested is found in Table 4-1.

Table 4-1: Summary of samples tested

| Sample type | Materials | Number of samples |
|---|---|---|
| Binary mixtures | C-S-H and AFm-I | 3 |
| | C-S-H and AFm | 2 |
| Quaternary mixtures | C-S-H, CH, AFm, AFt | 6 |
| | C-S-H, CH, AFm-I, AFt | 5 |

### *4.2.6. Image processing and analysis*

The raw data (2D projections) generated at the GSECARS beamline were first reconstructed with a filtered back-projection algorithm using the programming language IDL™ to form a 3D volume of greyscale data. The reconstructed image stack was processed using Avizo Fire 9.3. All data was initially filtered using a non-local means filter [100] to improve the contrast and reduce the noise in the images. Image subtraction was used to segment the binary mixtures. Dual energy scans above and below the k-edge allowed for image subtraction on the image volume. This method allowed for quantification of phases containing the contrast agent. An unsharp mask was applied to the resultant image volume from the image subtraction to enhance the edge boundary for segmentation. The binary mixtures were processed solely using image subtraction. A region of interest (ROI) was chosen to remove the sample holder and void space between the sample and the holder. The quantity of AFm-I was determined by directly measuring the quantity of voxels determined through image subtraction. The quantity of C-S-H was determined by subtracting the quantity of voxels of AFm-I from the total volume of all the solid phases. Figure 4-1 represents the workflow implemented to successfully segment AFm-I in a binary mixture of phases.

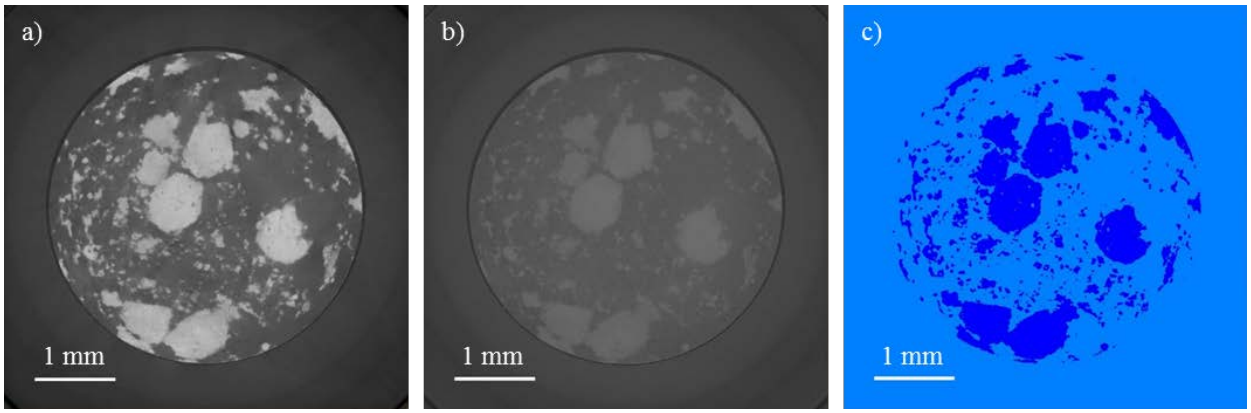


Figure 4-1: Procedure for image subtraction. a) shows a reconstructed image of a binary mixture of AFm-I and C-S-H scanned above the k-edge of iodine (scanning energy = 33.269 keV), whereas b) displays a reconstructed image of the same mixture of phases scanned below the k-edge of iodine (scanning energy = 33.069 keV). Image volume b) was subtracted from image volume a) which resulted in an image volume that contained iodine bearing material only (c). Similarly, the quaternary mixtures were analyzed using a combination of image subtraction for the AFm-I phases and the procedures for segmenting AFt, C-S-H, and CH phases outlined in [55]. The AFm-I phase was quantified using the image subtraction procedure discussed above. Quantification of the remaining phases was done based on pure phase data to determine the threshold values.

The volume of each phase was determined through two different means. The volume of voxels of each phase determined through image analysis was converted to cubic centimeters through the known voxel size, based on the image resolution of 2.60 microns/voxel. This volume was compared to the volume determined by converting the known mass of each phase to a volume based on the density (g/cm$^3$) of each phase. Published values of densities were used for C-S-H [33, 101], CH, AFm, and AFt [102]. An estimated density of AFm-I was determined by relating the molar mass of AFm ($3CaO{\cdot}Al_2O_3{\cdot}CaSO_4{\cdot}12H_2O$ = 622.51 g/mol) and its density (2.015 g/cm$^3$) to the molar mass of AFm-I ($3CaO{\cdot}Al_2O_3{\cdot}CaI_2{\cdot}12H_2O$ = 653.33 g/mol) and its theoretical density. Values for densities of phases used for analysis are found in Table 4-2.

Table 4-2: Phase densities used for analysis

| **Phase** | **Density (g/cm$^3$)** |
|---|---|
| C-S-H | 2.440 |
| CH | 2.251 |
| AFt | 1.778 |
| AFm | 2.015 |
| AFm-I | 2.115 |

## 4.3. Results and discussion

### *4.3.1. XRD*

Results from XRD analysis on the synthesized phases are presented in Figure 4-2.

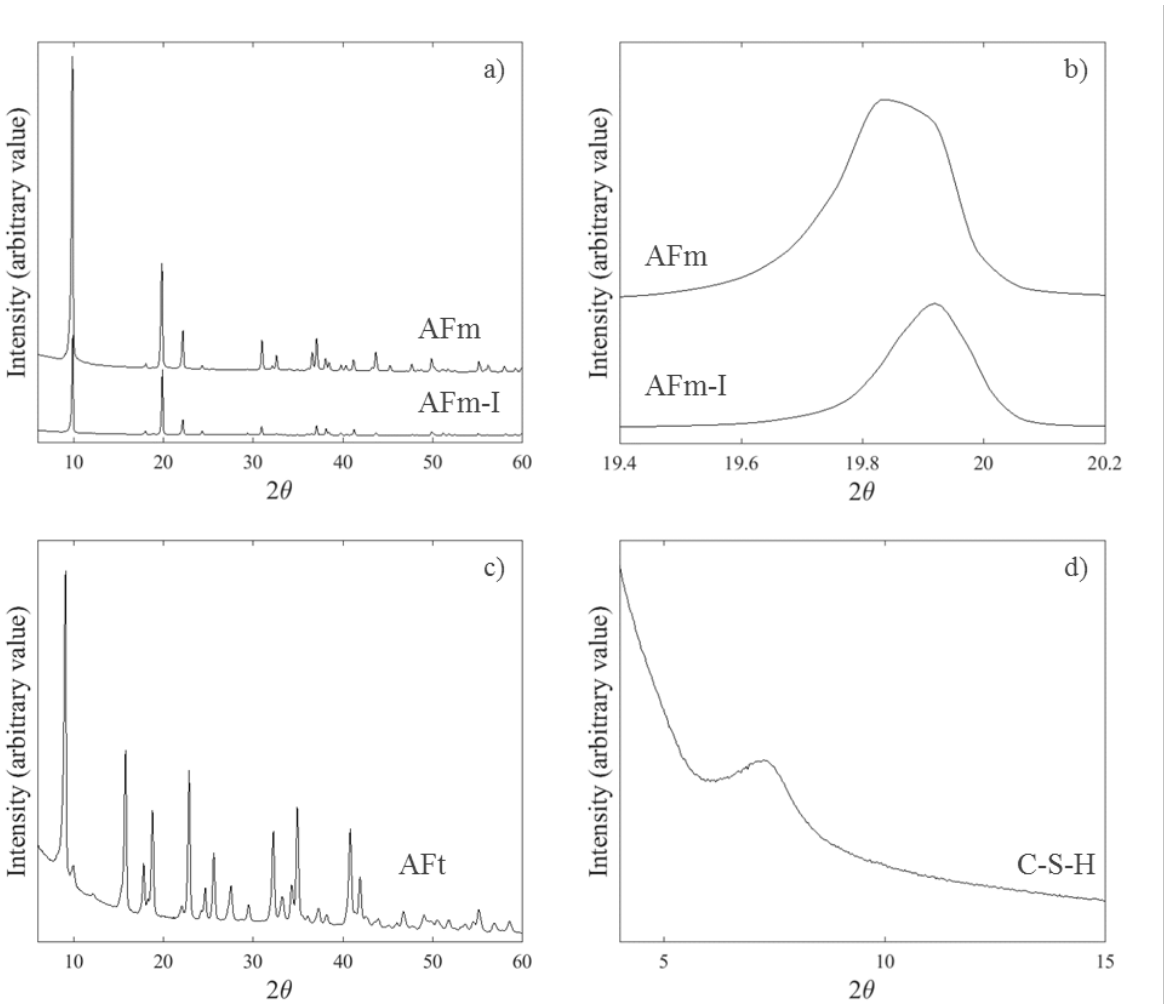


Figure 4-2: XRD patterns for synthesized phases

The major peaks observed in pure AFm match reported values [91]. As seen in Figure 4-12a), the major peaks in the pure and doped AFm are nearly identical, thus indicating similar crystallinity of the two phases. Furthermore, as observed in Figure 4-12b), the interlayer spacing at the *006* reflection (~20˚ 2Θ) was reduced, indicating the uptake of $I^-$, and replacing $SO_4^{2-}$ [93]. A reduction in the interlayer spacing of 0.02 Å was observed at the *006* reflection. Major peaks observed in the synthesized AFt phase occurred at 2θ values of 9.08 degrees and 15.80 degrees, which correspond to interlayer spacing of 0.974 nm and 0.561 nm, respectively. These values of spacing correspond

well with published literature on AFt synthesized using the method described for by Struble and Brown [90]. The major peak of C-S-H occurred at a 2θ value of 7.20 degrees, corresponding to an interlayer distance of 1.228 nm.

### *4.3.2. TGA/DTG*

TGA/DTG was used to further characterize the materials. Individual TGA/DTG results are presented in Figure 4-3.

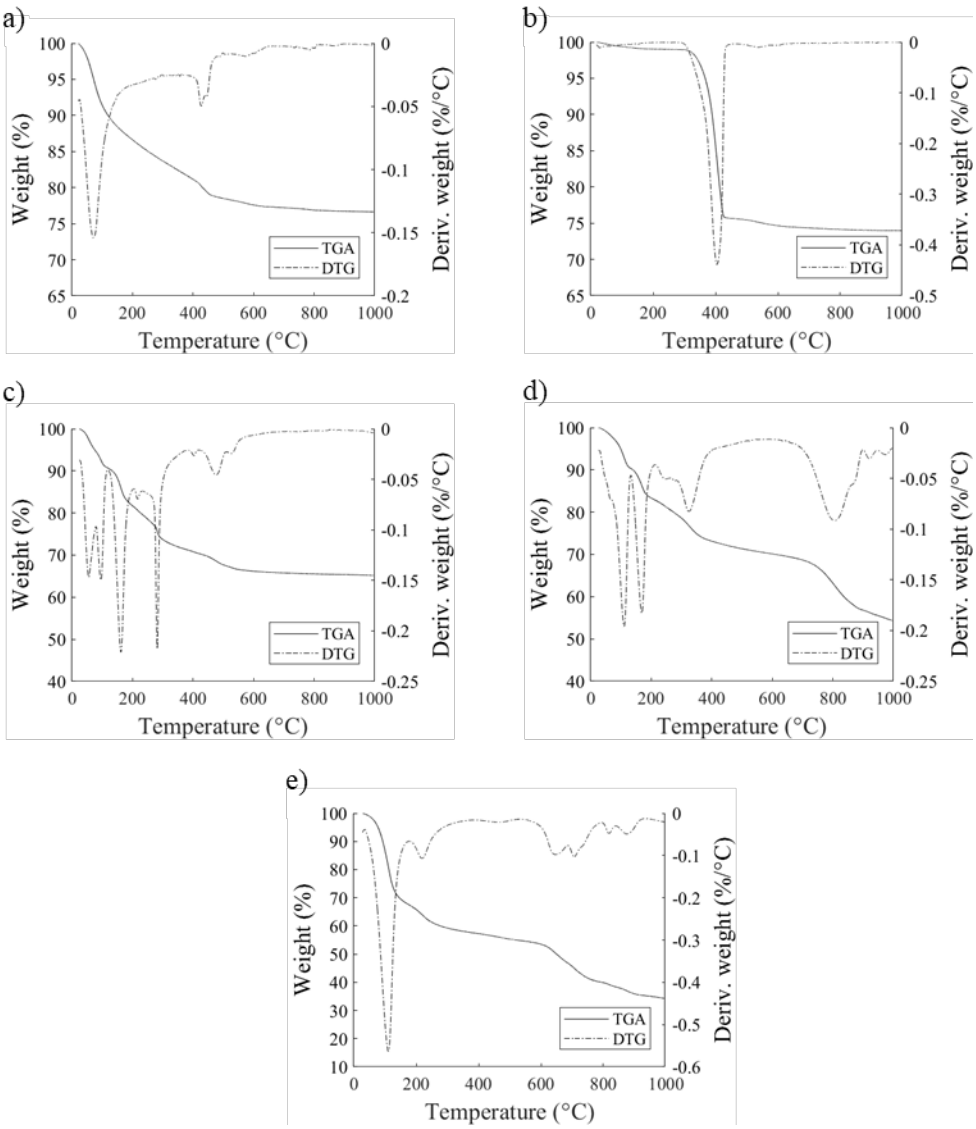


Figure 4-3: TGA/DTG results for individual phases: a) C-S-H; b) CH; c) AFm; d) AFm-I; e) AFt

Results from the analysis of C-S-H indicated the release of gel water in temperatures lower than 200 ˚C, decomposition of calcium hydroxide between 400 ˚C and 600 ˚C, and decomposition of calcium carbonate between 600 ˚C and 800 ˚C. The C-S-H was observed to have 6.8% CH and 0.64% $CaCO_3$. It has been reported that measureable amounts of CH is detected using quantitative XRD in C-S-H that is synthesized using the pozzolanic method [103, 104]. TGA/DTG results of the CH indicated a purity of 95.2%. When comparing AFm-I to a pure AFm, it was found the mass loss increased from 34.8% in a pure AFm to 45.6% in AFm-I. Similar trends in mass loss were observed in the pure AFm and AFm-I until 750 ˚C when an additional mass loss occurred in AFm-I. The mass loss in AFt at 110 ˚C, 220 ˚C, and above 550 ˚C indicated the formation of AFt [89, 90].

### *4.3.3. Improvement to histogram for segmentation*

The ability to segment AFm and C-S-H phases was greatly improved with the incorporation of a contrast agent in the AFm phase in both binary and quaternary mixtures. Figure 4-4 shows a selected image slice from the reconstructed volume and the corresponding histogram for a binary mixture of C-S-H and AFm (Figure 4-4a), and a binary mixture of C-S-H and AFm-I (Figure 4-4b).

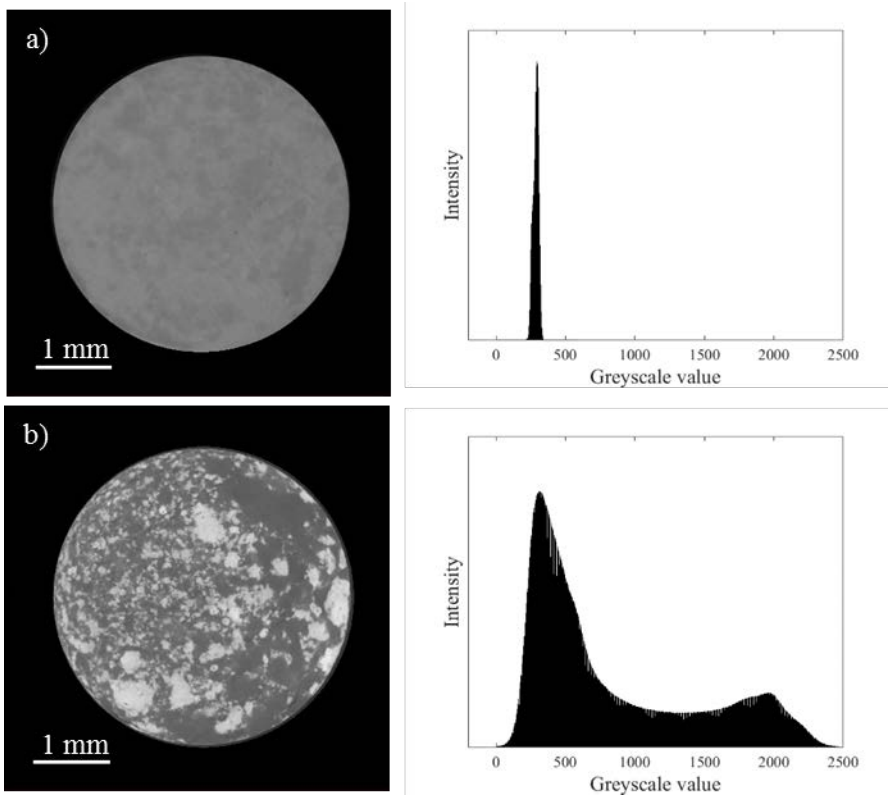


Figure 4-4: Improvements to histogram for segmentation in a binary mixture of AFm and C-S-H phases with the incorporation of iodine as a contrast agent in the AFm phase: a) shows an image slice and corresponding histogram of a binary mixture of pure AFm and C-S-H: b) shows an image slice and corresponding histogram of a binary mixture of pure C-S-H and AFm-I. Both data sets were scanned at 33.269 keV.

As seen Figure 4-14a), the range of greyscale values was narrow in the corresponding histogram of pure AFm and C-S-H. Furthermore, there was only one major peak indicating significant overlap in the greyscale values of pure AFm and C-S-H, making segmentation difficult and leading to significant errors in the quantification of each phase [55]. The incorporation of a contrast agent in the AFm-I phase resulted in two distinct peaks in the histogram and a wider range of greyscale values, as seen in Figure 4-14b). The spreading of the histogram allows for easier segmentation between the two phases. However, the broad region between the two peaks (greyscale values of ~1000 to 1500) could result in misclassification of those particular voxels. In this research, the application of image subtraction using dual energy scans eliminated this potential issue and allowed for quick and rapid quantification of these phases in the binary mixtures.

Similar to the binary mixtures, the histogram in the quaternary mixtures was changed significantly, as seen in Figure 4-5.

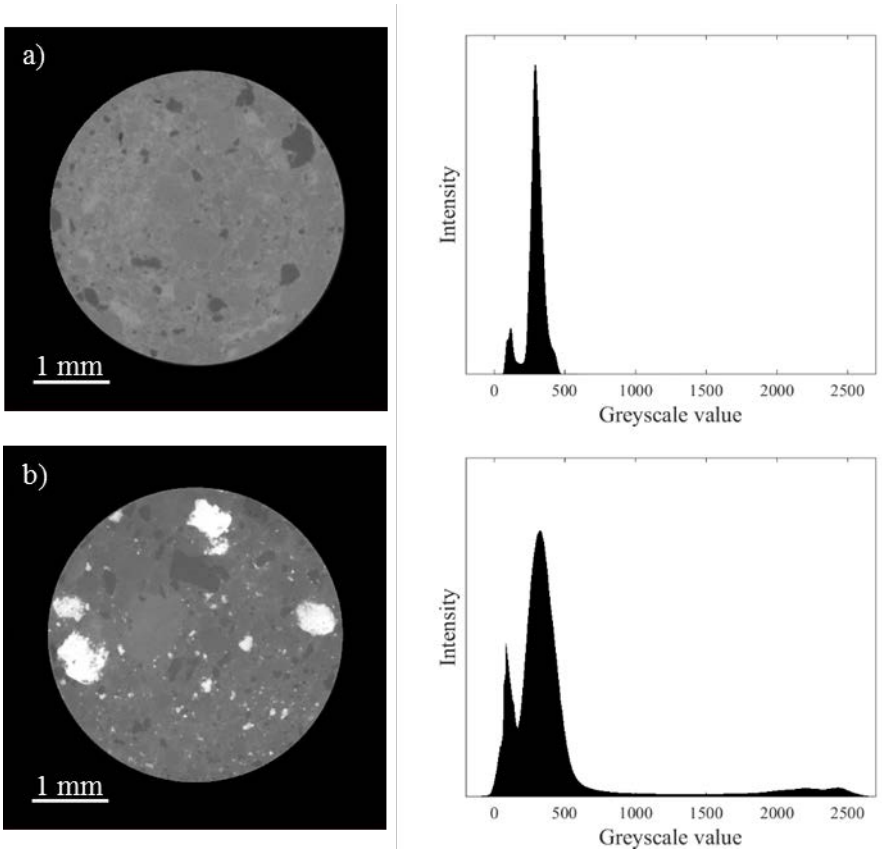


Figure 4-5: Changes to the histograms in quaternary mixtures of phases. a) displays the histogram and image slice of a quaternary mixture of C-S-H, CH, AFm, and AFt. b) shows an image slice and histogram of a quaternary mixture of C-S-H, CH, AFm-I, and AFt. The shift of the greyscale values between 2,000 and 2,500 for the AFm-I phase allowed for improved segmentation of the four phases.

In the mixture of pure phases only, Figure 4-5a), AFt was the only phase that was successfully quantified. Significant overlap of AFm, C-S-H, and CH in the major peak, between greyscale values of 200 and 500, resulted in large errors in quantifying each phase, respectively [55]. Incorporating a contrast agent resulted in a change of the major peak in the quaternary mixture of phases with AFm-I, as seen in Figure 4-5b). However, it was observed there was overlap of the expected C-S-H and CH peaks, thus potentially resulting in the inability to accurately quantify each of these phases.

### *4.3.4. Phase quantification*

Image analysis results and comparison to the volume determined from the mass and density of each phase for the binary mixtures of AFm-I and C-S-H are presented in Table 4-3.

Table 4-3: Binary mixture of AFm-I and C-S-H image analysis results

| Method | Material | Volume determined from mass ($cm^3$) | Volume determined from image analysis ($cm^3$) | Error (%) |
|---|---|---|---|---|
| Sample 1 | C-S-H | 0.0120 | 0.0132 | -14.8 |
| | AFm-I | 0.0043 | 0.0039 | 9.3 |
| Sample 2 | C-S-H | 0.0142 | 0.0156 | -15.5 |
| | AFm-I | 0.0085 | 0.0081 | 4.5 |
| Sample 3 | C-S-H | 0.0124 | 0.0115 | 3.1 |
| | AFm-I | 0.0128 | 0.0126 | 0.9 |

The use of a contrast agent in the AFm-I phase, coupled with dual energy scans to highlight the AFm-I phase, allowed for quick and accurate quantification of the two phases. The maximum error observed was 15.5%. Whereas, when pure C-S-H and AFm are combined, the errors ranged from 15.5% up to 114.5% [55], as seen in Figure 4-6. The use of a contrast agent successfully produced significant improvements to quantifying phases in quaternary mixtures.

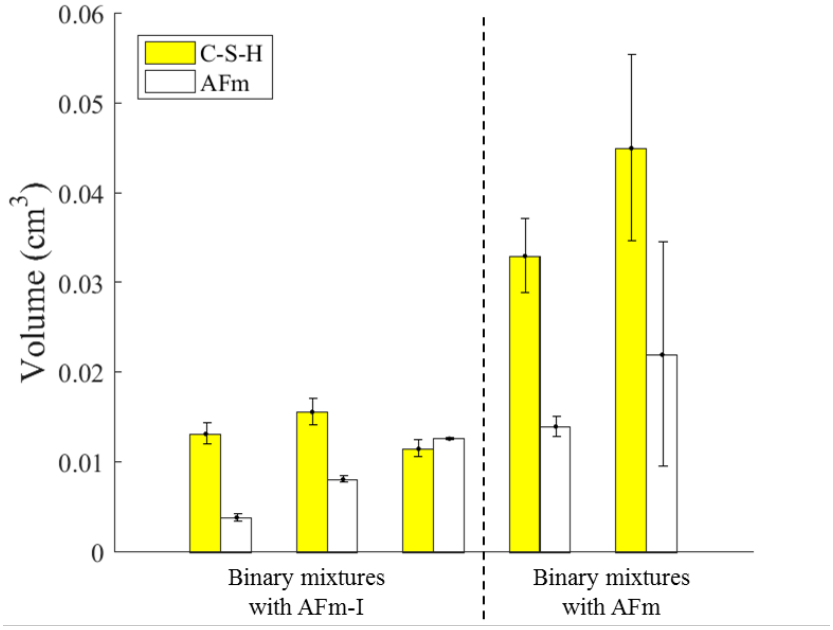


Figure 4-6: Comparison of binary mixtures of C-S-H and AFm phases. The errors when determining volumes were reduced significantly when a contrast agent was incorporated into AFm-I when compared to mixtures of C-S-H and AFm without a contrast agent.

One major benefit of the reduction in errors was the ability to view the phases in 3D. The ability to differentiate phases would allow for continual monitoring of phase formation and the potential for changes in these phases caused by deterioration mechanisms. A 3D rendition of each phase in

a quaternary mixture of phases with quantities being representative of a hydrated portland cement is shown in Figure 4-7.

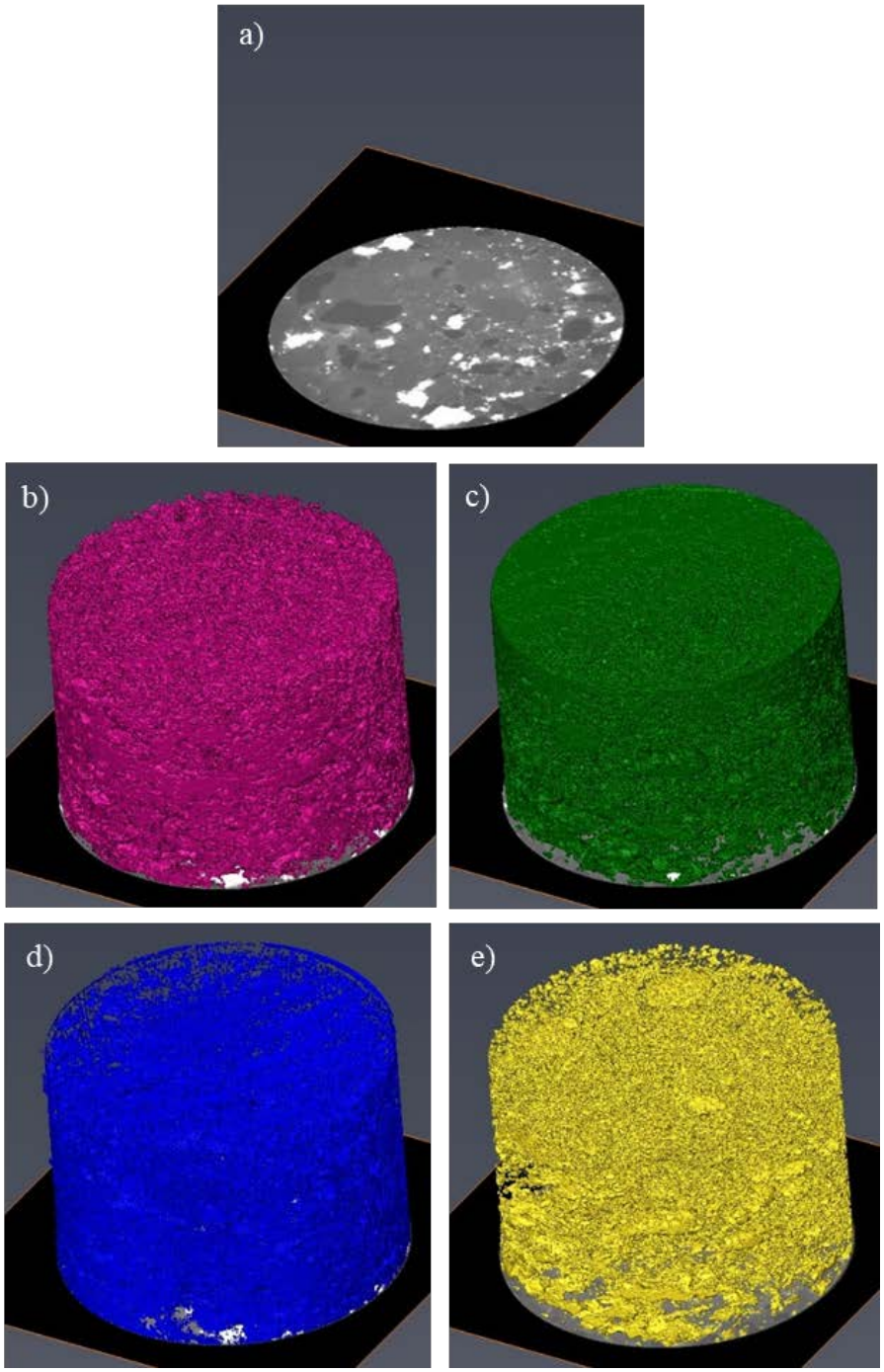


Figure 4-7: 3D rendition of each phase. a) represents a grayscale orthoslice. Figure 4-7b) reperesents C-S-H and was 47% of the total volume. c) represents CH and was 30% of the total volume. d) represents AFt and was 13% of the total volume. e) represents AFm-I and was 11% of the total volume.

The improved ability to accurately quantify AFm-I and C-S-H was extrapolated to segment phases in quaternary mixtures of the synthesized phases. Results from the volume analysis of the quaternary mixtures are presented in Table 4-4.

Table 4-4: Volume analysis determined through image processing and density calculations

| Method | Material | Volume determined from mass ($cm^3$) | Volume determined from image analysis ($cm^3$) | Error (%) |
|---|---|---|---|---|
| Sample 1 | C-S-H | 0.0172 | 0.0200 | -22.1 |
| | CH | 0.0044 | 0.0053 | -20.4 |
| | AFt | 0.0034 | 0.0023 | 33.0 |
| | AFm-I | 0.0014 | 0.0014 | 1.5 |
| Sample 2 | C-S-H | 0.0154 | 0.0177 | -19.7 |
| | CH | 0.0053 | 0.0062 | -16.4 |
| | AFt | 0.0039 | 0.0029 | 25.5 |
| | AFm-I | 0.0043 | 0.0038 | 11.2 |
| Sample 3 | C-S-H | 0.0210 | 0.0234 | -16.3 |
| | CH | 0.0049 | 0.0066 | -36.1 |
| | AFt | 0.0067 | 0.0060 | -4.7 |
| | AFm-I | 0.0014 | 0.0015 | 10.5 |
| Sample 4 | C-S-H | 0.0189 | 0.0203 | -12.6 |
| | CH | 0.0067 | 0.0066 | 0.5 |
| | AFt | 0.0067 | 0.0027 | 5.9 |
| | AFm-I | 0.0028 | 0.0060 | 10.9 |
| Sample 5 | C-S-H | 0.0176 | 0.0154 | 8.4 |
| | CH | 0.0040 | 0.0097 | -142.8 |
| | AFt | 0.0045 | 0.0042 | 6.6 |
| | AFm-I | 0.0038 | 0.0036 | 5.8 |

As seen in Table 4-4, the errors in certain phases were greatly reduced in quantifying each phase in the quaternary mixtures when a contrast agent was added to AFm when compared to the data analyzing quaternary mixtures of pure C-S-H, CH, AFt, and AFm, as seen in Figure 4-8.

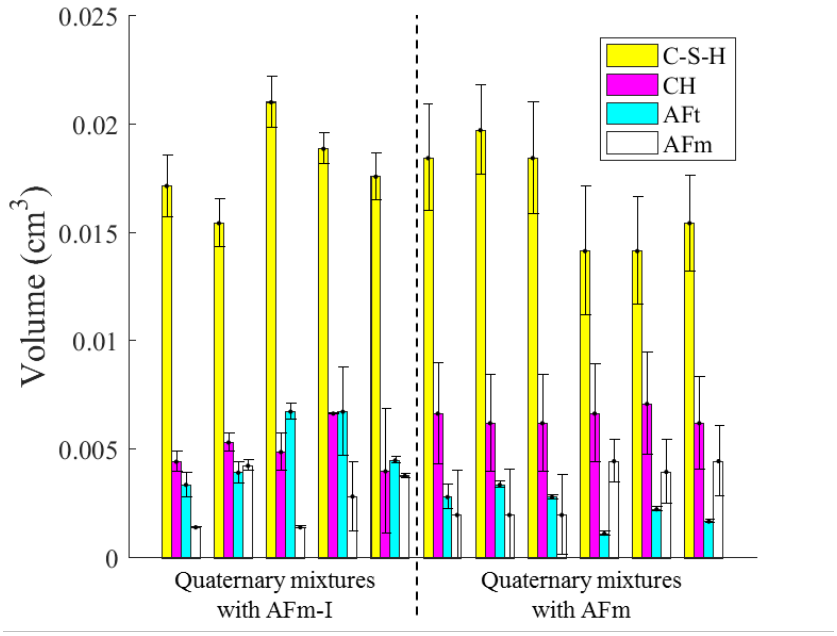


Figure 4-8: Comparison of volume calculations from image analysis in quaternary mixtures with AFm-I as a contrast agent and quaternary mixtures with no contrast agent. Results for the volume analysis of quaternary mixtures with AFm were determined in [55].

Quantification of AFt was nearly similar in the quaternary mixtures with and without a contrast agent due to no changes in the portion of the histogram that represented AFt. The most significant reduction in error was observed in the AFm phases. Errors greater than 200% were observed in the quaternary mixtures of pure phases [55]. The addition of a contrast agent by substituting $I^-$ for $SO_4^{2-}$ in the crystalline structure of AFm allowed for this significant reduction in the error when determining the quantity of AFm phases present. The maximum error observed in quaternary mixtures with AFm-I was 11.2% and as low as 1.5%.

The errors in quantifying C-S-H were reduced from a maximum of 60.1% and minimum of 20.8% in the analysis of the quaternary mixtures without a contrast agent to a maximum of 16.7% and minimum of 7.6% when AFm-I replaced AFm. Errors in quantifying CH were also reduced by similar amounts. However, the errors were widely different in all five samples. Sample 5 had a significant error when determining the amount of CH. This increased error was contributed to the overlap of grayscale values in C-S-H and CH. This overlap leads to recommending alternatives in segmentation algorithms, or for the addition of contrast agents to C-S-H. It is suggested to incorporate contrast agents into C-S-H for its large number of structural sites for cations and anions

to bind [105]. Furthermore, CH has a distinct stoichiometry of $CaOH_2$ [106], therefore it is not a good candidate for incorporating contrast agents. Several studies have shown the ability for C-S-H to capture ions, including but not limited to sodium, hexadecyltrimethylammonium [107], zinc, cadmium, lead, and chromium [108]. The same theory of multi-energy scans can be applied to a modified C-S-H phase as the AFm-I phase to further improve segmentation between C-S-H and CH.

### 4.4. Conclusions

In this research, the limitations of quantifying hydration products due to low contrast, particularly between AFm and C-S-H, in x-ray CT was investigated. Synthesized C-S-H and AFt and commercially available CH were used to represent three of the four hydration products. A doped AFm phase was synthesized by substituting $I^-$ for $SO_4^{2-}$, which allowed for accurate quantification of the four phases. The following conclusions were made:

- A doped AFm phase with iodine was successfully synthesized. Characterization of the phase using XRD indicated no major changes to the crystalline structure with a reduction in the interlayer spacing of 0.02 Å at the *006* reflection.
- Dual energy scans above and below the k-edge of iodine allowed for quick and accurate quantification of C-S-H and AFm-I when combined in binary mixtures. The errors observed in pure C-S-H and AFm were as high as 114%, whereas errors of 10% or less were observed in both phases in the binary mixtures containing AFm-I and C-S-H. This reduction in error was also found in quaternary mixtures of phases that included AFm-I. The ability to accurately determine AFm-I and C-S-H was observed, with maximum errors of 11.2% and 22.1% were observed, respectively in the quaternary mixtures.
- While three phases had consistent results in the error determined during analysis, error in quantifying CH varied. This was attributed to the overlap of grayscale values of C-S-H and CH in the major peak found in the histogram of the quaternary mixtures. A proposed method of incorporating a contrast agent into C-S-H was introduced, and the research detailed in this manuscript lays the groundwork for improvements in segmenting CH and C-S-H.

## 4.5. Acknowledgements

This research used resources of the Advanced Photon Source, a U.S. Department of Energy (DOE) Office of Science User Facility operated for the DOE Office of Science by Argonne National Laboratory under Contract No. DE-AC02-06CH11357. We acknowledge the support of GeoSoilEnviroCARS (Sector 13), which is supported by the National Science Foundation - Earth Sciences (EAR-1128799), and the Department of Energy, Geosciences (DE-FG02-94ER14466). Special thanks to the staff at GSECARS for their assistance with the experimental work, particularly the help of Dr. Mark Rivers.

## 4.6. References

[1] U. Rattanasak, K. Kendall, Pore structure of cement/pozzolan composites by x-ray microtomography, Cement and Concrete Research, 35 (2005) 637-640.

[2] J.L. Provis, R.J. Myers, C.E. White, V. Rose, J.S.J. van Deventer, X-ray microtomography shows pore structure and tortuosity in alkali-activated binders, Cement and Concrete Research, 42 (2012) 855-864.

[3] T.S. Yun, K.Y. Kim, J. Choo, D.H. Kang, Quantifying the distribution of paste-void spacing of hardened cement paste using x-ray computed tomography, Materials Characterization, 73 (2012) 137-143.

[4] S. Lu, E.N. Landis, D.T. Keane, X-ray microtomographic studies of pore structure and permeability in Portland cement concrete, Materials and Structures, 39 (2006) 611-620.

[5] N. Bossa, P. Chaurand, J. Vicente, D. Borschneck, C. Levard, O. Aguerre-Chariol, J. Rose, Micro- and nano-x-ray computed-tomography: A step forward in the characterization of the pore network of a leached cement paste, Cement and Concrete Research, 67 (2015) 138-147.

[6] K.Y. Kim, T.S. Yun, K.P. Park, Evaluation of pore structures and cracking in cement paste exposed to elevated temperatures by x-ray computed tomography, Cement and Concrete Research, 50 (2013) 34-40.

[7] M.A.B. Promentilla, T. Sugiyama, T. Hitomi, N. Takeda, Characterizing the 3D pore structure of hardened cement paste with synchrotron microtomography, Journal of Advanced Concrete Technology, 6 (2008) 273-286.

[8] M.A.B. Promentilla, T. Sugiyama, T. Hitomi, N. Takeda, Quantification of tortuosity in hardened cement pastes using synchrotron-based x-ray computed microtomography, Cement and Concrete Research, 39 (2009) 548-557.

[9] M. Lanzón, V. Cnudde, T. de Kock, J. Dewanckele, X-ray microtomography (μ-CT) to evaluate microstructure of mortars containing low density additions, Cement and Concrete Composites, 34 (2012) 993-1000.

[10] T. Sugiyama, M.A.B. Promentilla, T. Hitomi, N. Takeda, Application of synchrotron microtomography for pore structure characterization of deteriorated cementitious materials due to leaching, Cement and Concrete Research, 40 (2010) 1265-1270.

[11] F. Batool, V. Bindiganavile, Air-void size distribution of cement based foam and its effect on thermal conductivity, Construction and Building Materials, 149 (2017) 17-28.

[12] J. Schock, S. Liebl, K. Achterhold, F. Pfeiffer, Obtaining the spacing factor of microporous concrete using high-resolution dual energy x-ray micro CT, Cement and Concrete Research, 89 (2016) 200-205.

[13] S. Diamond, E. Landis, Microstructural features of a mortar as seen by computed microtomography, Materials and Structures, 40 (2007) 989-993.

[14] D.A. Lange, Y. Jia, Y.S. Liu, X-ray nanotomography of cement microstructure, American Concrete Institute SP 270, (2010) 9-16.

[15] R. Cepuritis, B.J. Wigum, E.J. Garboczi, E. Mørtsell, S. Jacobsen, Filler from crushed aggregate for concrete: Pore structure, specific surface, particle shape and size distribution, Cement and Concrete Composites, 54 (2014) 2-16.

[16] S.T. Erdogan, P.N. Quiroga, D.W. Fowler, H.A. Saleh, R.A. Livingston, E.J. Garboczi, P.M. Ketcham, J.G. Hagedorn, S.G. Satterfield, Three-dimensional shape analysis of coarse aggregates: New techniques for and preliminary results on several different coarse aggregates and reference rocks, Cement and Concrete Research, 36 (2006) 1619-1627.

[17] E.J. Garboczi, Three-dimensional mathematical analysis of particle shape using x-ray tomography and spherical harmonics: Application to aggregates used in concrete, Cement and Concrete Research, 32 (2002) 1621-1638.

[18] P. Trtik, B. Münch, W.J. Weiss, A. Kaestner, I. Jerjen, L. Josic, E. Lehmann, P. Lura, Release of internal curing water from lightweight aggregates in cement paste investigated by neutron and x-ray tomography, Nuclear Instruments and Methods in Physics Research Section A: Accelerators, Spectrometers, Detectors and Associated Equipment, 651 (2011) 244-249.

[19] D. Asahina, E.N. Landis, J.E. Bolander, Modeling of phase interfaces during pre-critical crack growth in concrete, Cement and Concrete Composites, 33 (2011) 966-977.

[20] S.C. de Wolski, J.E. Bolander, E.N. Landis, An in-situ x-ray microtomography study of split cylinder fracture in cement-based materials, Experimental Mechanics, 54 (2014) 1227-1235.

[21] H. Elaqra, N. Godin, G. Peix, M. R'Mili, G. Fantozzi, Damage evolution analysis in mortar, during compressive loading using acoustic emission and x-ray tomography: Effects of the sand/cement ratio, Cement and Concrete Research, 37 (2007) 703-713.

[22] D. Fukuda, Y. Nara, Y. Kobayashi, M. Maruyama, M. Koketsu, D. Hayashi, H. Ogawa, K. Kaneko, Investigation of self-sealing in high-strength and ultra-low-permeability concrete in water using micro-focus x-ray CT, Cement and Concrete Research, 42 (2012) 1494-1500.

[23] J.S. Lawler, D.T. Keane, S.P. Shah, Measuring three-dimensional damage of mortar in compression with x-ray microtomography and digital image correlation, American Concrete Institute SP 189, (2000) 187-202.

[24] J. Wang, J. Dewanckele, V. Cnudde, S. Van Vlierberghe, W. Verstraete, N. De Belie, X-ray computed tomography proof of bacterial-based self-healing in concrete, Cement and Concrete Composites, 53 (2014) 289-304.

[25] T. Rougelot, N. Burlion, D. Bernard, F. Skoczylas, About microcracking due to leaching in cementitious composites: X-ray microtomography description and numerical approach, Cement and Concrete Research, 40 (2010) 271-283.

[26] E.N. Landis, D.T. Keane, X-ray microtomography for fracture studies in cement-based materials, Proceedings of SPIE 3772: Developments in x-ray tomography II, 1999, pp. 105-113.

[27] E.N. Landis, E.N. Nagy, D.T. Keane, Microstructure and fracture in three dimensions, Engineering Fracture Mechanics, 70 (2003) 911-925.

[28] G.L. Balázs, O. Czoboly, É. Lublóy, K. Kapitány, Á. Barsi, Observation of steel fibres in concrete with computed tomography, Construction and Building Materials, 140 (2017) 534-541.

[29] A.C. Bordelon, J.R. Roesler, Spatial distribution of synthetic fibers in concrete with x-ray computed tomography, Cement and Concrete Composites, 53 (2014) 35-43.

[30] A. Qsymah, R. Sharma, Z. Yang, L. Margetts, P. Mummery, Micro x-ray computed tomography image-based two-scale homogenisation of ultra high performance fibre reinforced concrete, Construction and Building Materials, 130 (2017) 230-240.

[31] J. Adrien, S. Meille, S. Tadier, E. Maire, L. Sasaki, In-situ x-ray tomographic monitoring of gypsum plaster setting, Cement and Concrete Research, 82 (2016) 107-116.

[32] T.J. Chotard, M.P. Boncoeur-Martel, A. Smith, J.P. Dupuy, C. Gault, Application of x-ray computed tomography to characterise the early hydration of calcium aluminate cement, Cement and Concrete Composites, 25 (2003) 145-152.

[33] D. Gastaldi, F. Canonico, L. Capelli, E. Boccaleri, M. Milanesio, L. Palin, G. Croce, F. Marone, K. Mader, M. Stampanoni, In situ tomographic investigation on the early hydration behaviors of cementing systems, Construction and Building Materials, 29 (2012) 284-290.

[34] S. Das, P. Yang, S.S. Singh, J.C.E. Mertens, X. Xiao, N. Chawla, N. Neithalath, Effective properties of a fly ash geopolymer: Synergistic application of x-ray synchrotron tomography, nanoindentation, and homogenization models, Cement and Concrete Research, 78 (2015) 252-262.

[35] E. Gallucci, K. Scrivener, A. Groso, M. Stampanoni, G. Margaritondo, 3D experimental investigation of the microstructure of cement pastes using synchrotron x-ray microtomography (μCT), Cement and Concrete Research, 37 (2007) 360-368.

[36] J. Han, W. Sun, G. Pan, C. Wang, H. Rong, Application of x-ray computed tomography in characterization microstructure changes of cement pastes in carbonation process, Journal of Wuhan University of Technology-Materials Science Edition, 27 (2012) 358-363.

[37] M.B. Leite, P.J.M. Monteiro, Microstructural analysis of recycled concrete using x-ray microtomography, Cement and Concrete Research, 81 (2016) 38-48.

[38] J.L. Provis, A. Hajimohammadi, C.E. White, S.A. Bernal, R.J. Myers, R.P. Winarski, V. Rose, T.E. Proffen, A. Llobet, J.S.J. van Deventer, Nanostructural characterization of geopolymers by advanced beamline techniques, Cement and Concrete Composites, 36 (2013) 56-64.

[39] S. Erdem, X-ray computed tomography and fractal analysis for the evaluation of segregation resistance, strength response and accelerated corrosion behaviour of self-compacting lightweight concrete, Construction and Building Materials, 61 (2014) 10-17.

[40] M. Zhang, Y. He, G. Ye, D.A. Lange, K.v. Breugel, Computational investigation on mass diffusivity in Portland cement paste based on x-ray computed microtomography (μCT) image, Construction and Building Materials, 27 (2012) 472-481.

[41] P.J.M. Monteiro, A.P. Kirchheim, S. Chae, P. Fischer, A.A. MacDowell, E. Schaible, H.R. Wenk, Characterizing the nano and micro structure of concrete to improve its durability, Cement and Concrete Composites, 31 (2009) 577-584.

[42] T. Suzuki, H. Ogata, R. Takada, M. Aoki, M. Ohtsu, Use of acoustic emission and x-ray computed tomography for damage evaluation of freeze-thawed concrete, Construction and Building Materials, 24 (2010) 2347-2352.

[43] D. Hernández-Cruz, C.W. Hargis, J. Dominowski, M.J. Radler, P.J.M. Monteiro, Fiber reinforced mortar affected by alkali-silica reaction: A study by synchrotron microtomography, Cement and Concrete Composites, 68 (2016) 123-130.

[44] K. Wan, Q. Xu, Y. Wang, G. Pan, 3D spatial distribution of the calcium carbonate caused by carbonation of cement paste, Cement and Concrete Composites, 45 (2014) 255-263.

[45] B. Dong, G. Fang, Y. Liu, P. Dong, J. Zhang, F. Xing, S. Hong, Monitoring reinforcement corrosion and corrosion-induced cracking by x-ray microcomputed tomography method, Cement and Concrete Research, 100 (2017) 311-321.

[46] H.E. Martz, D.J. Scheberk, G. Patrick Roberson, P.J.M. Montiero, Computerized tomography analysis of reinforced concrete, ACI Materials Journal, 90 (1993) 259-264.

[47] A. Michel, B.J. Pease, M.R. Geiker, H. Stang, J.F. Olesen, Monitoring reinforcement corrosion and corrosion-induced cracking using non-destructive x-ray attenuation measurements, Cement and Concrete Research, 41 (2011) 1085-1094.

[48] K. Tosun, B. Baradan, Effect of ettringite morphology on DEF-related expansion, Cement and Concrete Composites, 32 (2010) 271-280.

[49] N.N. Naik, A.C. Jupe, S.R. Stock, A.P. Wilkinson, P.L. Lee, K.E. Kurtis, Sulfate attack monitored by microCT and EDXRD: Influence of cement type, water-to-cement ratio, and aggregate, Cement and Concrete Research, 36 (2006) 144-159.

[50] N.N. Naik, K.E. Kurtis, A.P. Wilkinson, A.C. Jupe, S.R. Stock, Sulfate deterioration of cement-based materials examined by x-ray microtomography, Proceedings of SPIE 5535, 2004, pp. 442-452.

[51] S.R. Stock, N.K. Naik, A.P. Wilkinson, K.E. Kurtis, X-ray microtomography (microCT) of the progression of sulfate attack of cement paste, Cement and Concrete Research, 32 (2002) 1673-1675.

[52] N. Burlion, D. Bernard, D. Chen, X-ray microtomography: Application to microstructure analysis of a cementitious material during leaching process, Cement and Concrete Research, 36 (2006) 346-357.

[53] K. Wan, Y. Li, W. Sun, Application of tomography for solid calcium distributions in calcium leaching cement paste, Construction and Building Materials, 36 (2012) 913-917.

[54] K. Wan, Y. Li, W. Sun, Experimental and modelling research of the accelerated calcium leaching of cement paste in ammonium nitrate solution, Construction and Building Materials, 40 (2013) 832-846.

[55] T. Deboodt, J.H. Ideker, O.B. Isgor, D. Wildenschild, Quantification of synthesized hydration products using synchrotron microtomography and spectral analysis, Construction and Building Materials, 157 (2017) 476-488.

[56] M.A. Le Gros, G. McDermott, C.A. Larabell, X-ray tomography of whole cells, Current Opinion in Structural Biology, 15 (2005) 593-600.

[57] W.R. Webb, W.E. Brant, N.M. Major, Fundamentals of Body CT, 4th ed., Saunders Elsevier, Philadelphia, PA, 2014.

[58] H. Lusic, M.W. Grinstaff, X-ray-computed tomography contrast agents, Chemical Reviews, 113 (2012) 1641-1666.

[59] Y. Davit, G. Iltis, G. Debenest, S. Veran-Tissoires, D. Wildenschild, M. Gerino, M. Quintard, Imaging biofilm in porous media using x-ray computed microtomography, Journal of Microscopy, 242 (2011) 15-25.

[60] K.A. Culligan, D. Wildenschild, B.S.B. Christensen, W.G. Gray, M.L. Rivers, Pore-scale characteristics of multiphase flow in porous media: A comparison of air–water and oil–water experiments, Advances in Water Resources, 29 (2006) 227-238.

[61] D. Wildenschild, A.P. Sheppard, X-ray imaging and analysis techniques for quantifying pore-scale structure and processes in subsurface porous medium systems, Advances in Water Resources, 51 (2013) 217-246.

[62] D. Wildenschild, C.M.P. Vaz, M.L. Rivers, D. Rikard, B.S.B. Christensen, Using x-ray computed tomography in hydrology: Systems, resolutions, and limitations, Journal of Hydrology, 267 (2002) 285-297.

[63] G.C. Iltis, R.T. Armstrong, D.P. Jansik, B.D. Wood, D. Wildenschild, Imaging biofilm architecture within porous media using synchrotron-based x-ray computed microtomography, Water Resources Research, 47 (2011) W02601.

[64] M. Khanzadeh Moradllo, M.T. Ley, Quantitative measurement of the influence of degree of saturation on ion penetration in cement paste by using x-ray imaging, Construction and Building Materials, 141 (2017) 113-129.

[65] B.P. Flannery, H.W. Deckman, W.G. Roberge, K.L. D'Amico, Three-dimensional x-ray nicrotomography, Science, 237 (1987) 1439-1444.

[66] D. Zhang, Y. Jia, J. Ma, Z. Li, Removal of arsenic from water by Friedel's salt (FS: $3CaO{\cdot}Al_2O_3{\cdot}CaCl_2{\cdot}10H_2O$), Journal of Hazardous Materials, 195 (2011) 398-404.

[67] K.-H. Goh, T.-T. Lim, Z. Dong, Application of layered double hydroxides for removal of oxyanions: A review, Water Research, 42 (2008) 1343-1368.

[68] S. Miyata, Anion-exchange properties of hydrotalcite-like compounds, Clays and Clay Minerals, 31 (1983) 305-311.

[69] T. Matschei, B. Lothenbach, F.P. Glasser, The AFm phase in portland cement, Cement and Concrete Research, 37 (2007) 118-130.

[70] A. Mesbah, C. Cau-dit-Coumes, G. Renaudin, F. Frizon, F. Leroux, Uptake of chloride and carbonate ions by calcium monosulfoaluminate hydrate, Cement and Concrete Research, 42 (2012) 1157-1165.

[71] J.P. Rapin, G. Renaudin, E. Elkaim, M. Francois, Structural transition of Friedel's salt $3CaO{\cdot}Al_2O_3{\cdot}CaCl_2{\cdot}10H_2O$ studied by synchrotron powder diffraction, Cement and Concrete Research, 32 (2002) 513-519.

[72] J.P. Rapin, A. Walcarius, G. Lefevre, M. Francois, A double-layered hydroxide, $3CaO{\cdot}Al_2O_3{\cdot}CaI_2{\cdot}10H_2O$, Acta Crystallographica Section C, 55 (1999) 1957-1959.

[73] G. Renaudin, M. Francois, The lamellar double-hydroxide (LDH) compound with composition $3CaO{\cdot}Al_2O_3{\cdot}Ca(NO_3)_2{\cdot}10H_2O$, Acta Crystallographica Section C, 55 (1999) 835-838.

[74] G. Renaudin, F. Kubel, J.P. Rivera, M. Francois, Structural phase transition and high temperature phase structure of Friedels salt, $3CaO{\cdot}Al_2O_3{\cdot}CaCl_2{\cdot}10H_2O$, Cement and Concrete Research, 29 (1999) 1937-1942.

[75] G. Renaudin, J.P. Rapin, E. Elkaim, M. François, Polytypes and polymorphs in the related Friedel's salt $[Ca_2Al(OH)_6]^+[X{\cdot}2H_2O]^-$ halide series, Cement and Concrete Research, 34 (2004) 1845-1852.

[76] G. Renaudin, J.P. Rapin, B. Humbert, M. François, Thermal behaviour of the nitrated AFm phase $Ca_4Al_2(OH)_{12}(NO_3)_2{\cdot}4H_2O$ and structure determination of the intermediate hydrate $Ca_4Al_2(OH)_{12}(NO_3)_2{\cdot}2H_2O$, Cement and Concrete Research, 30 (2000) 307-314.

[77] A. Terzis, S. Filippakis, H.-J. Kuzel, H. Burzlaff, The crystal structure of $Ca_2Al(OH)_6Cl \cdot 2H_2O$, Zeitschrift für Kristallographie - Crystalline Materials, 181 (1987) 29.

[78] A. Walcarius, G. Lefevre, J.-P. Rapin, G. Renaudin, M. Francois, Voltammetric detection of iodide after accumulation by friedel's salt, Electroanalysis, 13 (2001) 313-320.

[79] R. Allmann, Refinement of the hybrid layer structure hexahydroxoaluminodicalcium hemisulfate tryhydrate $[Ca_2Al\ (OH)_6]\ [1/2SO_4\ 3H_20]$, Neues Jahrbuch für Mineralogie, 3 (1977) 136-144.

[80] J.-B. Champenois, A. Mesbah, C. Cau Dit Coumes, G. Renaudin, F. Leroux, C. Mercier, B. Revel, D. Damidot, Crystal structures of Boro-AFm and sBoro-AFt phases, Cement and Concrete Research, 42 (2012) 1362-1370.

[81] M. Francois, G. Renaudin, O. Evrard, A Cementitious Compound with Composition $3CaO{\cdot}Al_2O_3{\cdot}CaCO_3{\cdot}11H_2O$, Acta Crystallographica Section C, 54 (1998) 1214-1217.

[82] G. Renaudin, M. Francois, O. Evrard, Order and disorder in the lamellar hydrated tetracalcium monocarboaluminate compound, Cement and Concrete Research, 29 (1999) 63-69.

[83] R. Fischer, H.J. Kuzel, Reinvestigation of the system $C_4A.nH_2O{\cdot}C_4A{\cdot}CO_2{\cdot}nH_2O$, Cement and Concrete Research, 12 (1982) 517-526.

[84] A. Mesbah, C. Cau-dit-Coumes, F. Frizon, F. Leroux, J. Ravaux, G. Renaudin, A new investigation of the $Cl^{-}$–$CO_3^{2-}$ substitution in AFm phases, Journal of the American Ceramic Society, 94 (2011) 1901-1910.

[85] A. Mesbah, M. François, C. Cau-dit-Coumes, F. Frizon, Y. Filinchuk, F. Leroux, J. Ravaux, G. Renaudin, Crystal structure of Kuzel's salt $3CaO{\cdot}Al_2O_3{\cdot}1/2CaSO_4{\cdot}1/2CaCl_2{\cdot}11H_2O$ determined by synchrotron powder diffraction, Cement and Concrete Research, 41 (2011) 504-509.

[86] A. Mesbah, J.-P. Rapin, M. François, C. Cau-dit-Coumes, F. Frizon, F. Leroux, G. Renaudin, Crystal structures and phase transition of cementitious bi-anionic AFm-($Cl^{-}$, $CO_3^{2-}$) compounds, Journal of the American Ceramic Society, 94 (2011) 261-268.

[87] M. Sacerdoti, E. Passaglia, Hydrocalumite from Latium, Italy: Its crystal structure and relationship wih related synthetic phases, Neues Jahrbuch für Mineralogie, 10 (1988) 462-475.

[88] I.G. Richardson, The nature of C-S-H in hardened cements, Cement and Concrete Research, 29 (1999) 1131-1147.

[89] R. Alizadeh, J.J. Beaudoin, L. Raki, Mechanical properties of calcium silicate hydrates, Materials and Structures, 44 (2011) 13-28.

[90] L.J. Struble, P.W. Brown, An evaluation of ettringite and related compounds for use in the solar energy storage, US Department of Commerce, 1982, pp. 11.

[91] H.J. Kuzel, Synthesis and x-ray study of the crystalline composition $3CaO{\cdot}Al_2O_3{\cdot}CaSO_4{\cdot}12H_2O$, Neues Jahrbuch Mineral Monatsh, 7 (1965) 193-197.

[92] R. Allman, Refinement of the hybrid layer structure $[Ca_2Al(OH)_6]^{+}{\cdot}[1/2SO_4{\cdot}3H_2O]^{-}$, Neues Jahrbuch für Mineralogie Monatsheft, (1977) 136-144.

[93] L. Aimoz, D.A. Kulik, E. Wieland, E. Curti, B. Lothenbach, U. Mäder, Thermodynamics of AFm-($I_2$, $SO_4$) solid solution and of its end-members in aqueous media, Applied Geochemistry, 27 (2012) 2117-2129.

[94] N.N. Skoblinskaya, K.G. Krasilnikov, L.V. Nikitina, V.P. Varlamov, Changes in crystal structure of ettringite on dehydration. 2, Cement and Concrete Research, 5 (1975) 419-431.

[95] H.F.W. Taylor, Cement Chemistry, 2nd Edition ed., Thomas Telford Publishing, London, England, 1997.

[96] F. Goetz-Neunhoeffer, J. Neubauer, P. Schwesig, Mineralogical characteristics of ettringites synthesized from solutions and suspensions, Cement and Concrete Research, 36 (2006) 65-70.

[97] S.M. Antao, M.J. Duane, I. Hassan, DTA, TG, and RD studies of sturmanite and ettringite, The Canadian Mineralogist, 40 (2002) 1403-1409.

[98] R. Khoshnazar, L. Raki, J. Beaudoin, R. Alizadeh, Solvent exchange in sulfoaluminate phases. Part II: Monosulfate, Advances in Cement Research, 25 (2013) 322-331.

[99] R. Alizadeh, J.J. Beaudoin, L. Raki, V. Terskikh, C-S-H/polyaniline nanocomposites prepared by in situ polymerization, Journal of Materials Science, 46 (2011) 460-467.

[100] A. Buades, B. Coll, J.M. Morel, A non-local algorithm for image denoising, 2005 IEEE Computer Society Conference on Computer Vision and Pattern Recognition (CVPR'05), 2005, pp. 60-65 vol. 62.

[101] T. Powers, T. Brownyard, Studies of the physical properties of hardened portland cement paste (Bulletin 22), Portland Cement Association, Chicago, IL, 1948.

[102] M. Balonis, F.P. Glasser, The density of cement phases, Cement and Concrete Research, 39 (2009) 733-739.

[103] X. Cong, R.J. Kirkpatrick, $^{29}$Si MAS NMR study of the structure of calcium silicate hydrate, Advanced Cement Based Materials, 3 (1996) 144-156.

[104] P. Yu, Kirkpatrick, R. J., Poe, B., McMillan, P. F. and Cong, X. , Structure of calcium silicate hydrate (C-S-H): Near-, mid-, and far-infrared spectroscopy, Journal of the American Ceramic Society, 82 (1999) 742-748.

[105] M.L.D. Gougar, B.E. Scheetz, D.M. Roy, Ettringite and C-S-H portland cement phases for waste ion immobilization: A review, Waste Management, 16 (1996) 295-303.

[106] P.K. Mehta, P.J.M. Monteiro, Concrete: Microstructure, properties and materials, Third ed., New York, 2006.

[107] J.J. Beaudoin, H. Dramé, L. Raki, R. Alizadeh, Formation and characterization of calcium silicate hydrate-hexadecyltrimethylammonium nanostructure, Journal of Materials Research, 23 (2008) 2804-2815.

[108] R. Żak, J. Deja, Spectroscopy study of Zn, Cd, Pb and Cr ions immobilization on C–S–H phase, Spectrochimica Acta Part A: Molecular and Biomolecular Spectroscopy, 134 (2015) 614-620.

# Manuscript 3

## Comparison of segmentation algorithms for quantifying portland cement hydrates using synchrotron microtomography

Tyler Deboodt, Dorthe Wildenschild, Jason H. Ideker, O. Burkan Isgor

To be submitted to: *Cement and Concrete Composites*

# 5. Manuscript 3

## Comparison of segmentation algorithms for quantifying portland cement hydrates using synchrotron microtomography

Tyler Deboodt[1], Dorthe Wildenschild[2], Jason H. Ideker[3], O. Burkan Isgor[4]

**Abstract:**

X-ray computed tomography (CT) has become increasingly popular for non-destructive investigation of cementitious systems. Differentiating solid phases due to similar greyscale value in the image volume has been reported as a challenge, thus x-ray CT has been predominately limited to crack and void quantification and qualitative or semi-quantitative analysis for solid phases. The goal of this research was to investigate image preprocessing and segmentation algorithms in quantifying synthesized hydration products. C-S-H, calcium hydroxide, monosulfate, and ettringite were created in the laboratory for investigation. Many segmentation algorithms exist and can lead to differing results during image processing. In this research, Markov random fields, watershed, and a Gaussian histogram deconstruction algorithms were studied for their ability to quantify the solid phases. It was found that misclassification of voxels occurred when using the Gaussian deconstruction. An average reduction of 50%, and as high as 180%, in the quantification errors were observed when using local segmentation algorithms.

**Keywords:** image analysis, x-ray computed tomography, synchrotron, non-destructive testing

---

[1] Graduate Research Assistant, School of Civil and Construction Engineering, Oregon State University

[2] Professor, School of Chemical, Biological, and Environmental Engineering, Associate Dean of Graduate School, Oregon State University

[3] Associate Professor, School of Civil and Construction Engineering, Oregon State University

[4] Professor, School of Civil and Construction Engineering, Oregon State University

## 5.1. Introduction

A major challenge related to the application of x-ray computed tomography (CT) to characterize hydration products of cementitious systems is the difficulty to distinguish different solid phases due to relatively similar greyscale values [1], particularly differentiating individual unhydrated and hydrated phases. This challenge has limited the use of x-ray CT to extract quantifiable information on cementitious materials, and resulted in studies on the solid phases often being limited to qualitative or semi-quantitative analysis [2-6].

One limitation in using x-ray CT is obtaining adequate spatial resolution in the reconstructed image volume. Spatial resolution depends on the sample size, the optics used for magnification, and the resolution of the detector. In order to increase the accuracy of quantitative measurements (e.g. porosity), the resolution needs to be optimized as well, which typically implies the use of a smaller samples. Distinction between phases in a bulk system (e.g. hydrated cement paste, void, or aggregate) becomes challenging as the size of the voxel is increased. If a particular phase does not encompass an entire voxel, bias in segmentation of the image may occur. This artifact, called partial volume effects, increases as the voxel size increases [7], and a high spatial resolution is key to extracting accurate pore structure information from an image stack [5, 8]. Therefore, a compromise between sample size and resolution must be found for x-ray CT imaging in cementitious systems, particularly in systems where aggregate-cement interaction and identification of phases in hydrated cement are of interest [9].

One method to resolve the spatial resolution limitation is to implement the use of ptychographic x-ray CT. A focused x-ray beam is transmitted through a sample with a thickness of tens of nanometers. A coherent diffraction pattern is recorded and a tomographic volume is recreated from such patterns. Recent advances include the determination and quantification of mass densities of hydrated and unhydrated phases [10], hydration products created from alite [11], and hydration products of alternative cements [12]. While these recent advances allow for the ability to extract quantifiable information on solid phases in cementitious materials, the authors acknowledge the limitations on spatial resolution using traditional x-ray CT methods for use in cementitious materials and is not a focus of this manuscript. Advances in x-ray CT resolution are improving for both x-ray tube and synchrotron sources. Currently, maximum resolution achievable in x-ray CT

is approximately 50 nm/voxel, and it is expected to be reduced as low as 15 nm/voxel with emerging technologies [13].

The second limitation and primary focus of this research was to consider methods to resolve segmentation challenges in low contrast materials by investigating different global and local segmentation algorithms. The lack of contrast between solid phases has proven to be difficult to determine an unbiased threshold value to segment the image volume. Often times the resultant histogram of the image volume is a series of overlapping peaks constituting the greyscale values of each phase. An arbitrary threshold value can be used for segmentation purposes [14]. However, these values may be biased, particularly if greyscale values of specific phases are not known. This may result in misclassification of voxels, particularly if phase attenuation values overlap [15]. One approach used for segmentation is to deconstruct the histogram into separate Gaussian curves that represent the greyscale distribution of each phase and determining the threshold value for segmentation as the intersection of adjacent Gaussian curve [2, 6]. Other successes in quantifying solid phases in portland cement include determining zones of calcium leaching in calcium silicate hydrate (C-S-H) and calcium hydroxide (CH) phases [3, 16]. However, these histogram based, global segmentation algorithms often does not account for the spatial distribution of the local voxel neighborhood and can lead to misclassification of voxels [15, 17].

Furthermore, work done on hydrating portland cement paste allowed for distinct quantification of unhydrated phases, hydrated cement paste, and porosity [5]. Similar work investigating hydration behaviors of ordinary portland cement (OPC), calcium sufloaluminate cement (CSA), and a mix of OPC and CSA determined the formation of hydration products. Four pure solid phases were investigated using x-ray CT to correlate the measured greyscale value to the expected linear attenuation coefficient of each phase. Theoretical greyscale values were determined for the remaining expected hydrated and unhydrated phases based on the assumed linear attenuation coefficient. Changes in the histogram were discovered for specific phases that were expected to change over time at particular greyscale values as the cement paste hydrated in all three sample types. While the authors were able to quantify the changes in porosity of all three sample types, the quantity of individual hydration products was not reported. This research began investigating the ability to measure greyscale values of individual phases, however the ability to segment each

phase became difficult due to the similar greyscale values reported and overlapping peaks in the histogram [4].

An alternative to improving the image contrast is to include the use of contrast agents in the system. Several of the main hydrates found in portland cement have the ability to incorporate ions that, when scanned at appropriate scanning energies, can greatly improve the contrast and reduce the errors in quantification of hydration products. Error was reduced in C-S-H and AFm mixtures from as high as 114.5% to 15.5% by incorporating iodine into AFm as a contrast agent [18]. However, the use of contrast agents likely need to be a forethought when creating new cementitious systems instead of an afterthought in existing systems.

The ability to extract quantifiable 3D information of cementitious systems using x-ray CT has been successful in determining porosity and tortuosity [2, 8, 14, 19-27]. Furthermore, the method has shown promise at characterizing individual phases [4, 6], but errors in quantification of phases was observed. One challenge in extracting quantifiable information is determining appropriate image processing and segmentation procedures. These challenges form the focus of this research by investigating several segmentation algorithms and their applicability to the calcium-silica bearing minerals that form during the hydration of portland cement, including calcium silicate hydrate (C-S-H), calcium hydroxide (CH), ettringite (AFt), and monosulfate (AFm). These four main hydration products of portland cement were synthesized and intermixed to investigate the applicability of one histogram based, global segmentation algorithm for phase quantification, and two local segmentation algorithms (watershed and Bayesian Markov random fields). This research provides the groundwork to determine an appropriate segmentation algorithm for quantifying phases in portland cement.

### 5.2. Image segmentation algorithms

The image segmentation process is important for proper classification of voxels in an image volume, which can affect the desired outcome if done incorrectly. Global segmentation has been classified as a method of segmentation based on the evaluation of the histogram only to determine threshold values. More robust, local segmentation, algorithms exist which offer more flexibility in determining the distribution of phases and often result in more desirable results [28]. However, these methods rely on intensity thresholding for segmentation. Instead of relying on a single

threshold value, a variable thresholding surface is created from the local sample domain to account for the spatial arrangement of the greyscale values throughout the image volume [17, 29]. Numerous global and local segmentation algorithms exist, and several authors have evaluated their performance in image analysis [30-32]. This the accuracy in quantifying synthesized hydration products in binary and quaternary mixtures for one global segmentation algorithm (Gaussian deconstruction of histogram) and two local segmentation algorithms (watershed and Bayesian Markov random field) was investigated. Preliminary threshold values for all algorithms were determined by measuring the linear attenuation coefficient (LAC) of C-S-H, CH, AFt, and AFm.

### *5.2.1. Measurement of linear attenuation coefficient*

As the monochromatic x-rays generated by a synchrotron radiation source pass through solid materials, their intensities attenuate to varying degrees as a function of the materials along the path of the beam, a phenomenon described by the Beer-Lambert Law [33]:

$$I(x) = I_o e^{(-\mu x)} \qquad \text{Equation 5.3}$$

where, $I$ is the attenuated intensity of the x-ray after passing through the solid with a thickness of $x$, $I_o$ is the initial intensity of the radiation, and $\mu$ is the linear attenuation coefficient. According to the Beer-Lambert Law, the ratio of the number of transmitted to incident photons is related to the integral of the LAC of the materials along the path that the photons travel through the sample. The LAC is linked to the density, the atomic number, and the energy of the beam [34]. Materials with higher density or high atomic number tend to absorb x-rays better. The relationship between density, atomic number, and LAC of an element is given as [35]:

$$\mu = \frac{\rho Z^4}{AE^3} \qquad \text{Equation 5.4}$$

where, $A$ is the atomic mass, $Z$ is the atomic number, $\rho$ is the density, and $E$ is the x-ray energy. Materials with a high LAC allow x-rays to only penetrate a short distance, whereas materials with a low LAC allow x-rays to pass through more easily [33]. The measured LAC of each pure phase was determined. This information was then used to determine potential threshold values when using the segmentation algorithms in the binary and quaternary mixtures of phases discussed below.

### *5.2.2. Gaussian deconstruction of histogram for segmentation*

It has been reported that the distribution of greyscale values, and subsequent LACs, can be assumed to have a Gaussian distribution [2, 6] with a probability density function (PDF) of:

$$f(x) = \frac{1}{\sqrt{2\pi\sigma^2}} e^{\frac{-(x-\mu)^2}{2\sigma^2}} \qquad \text{Equation 5.5}$$

where: $\mu$ is the mean of the distribution and $\sigma$ is the standard deviation. This method assumes each individual phase has a distinct distribution of LACs in the reconstructed image volume. In this research, the Gaussian PDF of each phase was determined by fitting a Gaussian curve to the LACs extracted from the reconstructed image volume of individual pure phases; C-S-H, CH, AFm, and AFt. The next step was to unitize the histogram of each sample that was composed of a mixture of phases. Next, the Gaussian curves of the pure phases were proportioned to the known mass of each phase in the sample to generate a pure phase histogram. The pure phase histogram was then overlaid on the histogram of the mixture samples. The total area of the pure phase histogram was equivalent to histogram of the mixture sample. The threshold value was chosen as the intersection of two adjacent Gaussian curves.

### *5.2.3. Watershed segmentation*

The watershed segmentation algorithm uses the principle of catchment basins and watershed lines derived from the hydrology field to determine how voxels are regionally distributed throughout the sample domain [36, 37]. The watershed lines are determined as the highest gradient between greyscale values, thus determining the borders of the catchment basins locally. These gradient lines can be determined through several different edge detection methods [17]. In this research, the gradient was identified using Canny-Deriche edge detection filter [38, 39]. The gradient of the image creates watershed lines, which separate catchment basins. Minima are determined as regions where the greyscale value is darker than the surrounding voxels and are bound by the watershed lines, forming the basis for the catchment basins [36]. Initially, the catchment basins are seeded with simple thresholding to set values for the inundation process. The basins are filled until a watershed line is reached, filling the catchment basin. Voxels not initially classified during thresholding are left unclassified, which include voxels in zones near the watershed lines. These regions are assigned values during the inundation portion of the watershed algorithm when a

watershed line has been reached. Lastly, the unclassified voxels on the watershed lines are determined based on the local, 3D distribution of voxels [17].

### *5.2.4. Bayesian Markov random fields segmentation*

The basis of random field models and the Bayesian Markov random fields (MRF) algorithm was developed on the stochastic representation of the attributes in an image volume [40]. The stochastic framework is based on the assumption that the arrangement of specific image attributes, in this case greyscale values and subsequent LACs, can be determined by probability distributions. Statistical mean and standard deviation of the LACs must be known or determined through global segmentation or manual seeding of the expected phase [15]. The initial MRF algorithm was developed for two-dimensional (2D) image analysis by Berthod et al. [41], and was expanded to a 3D algorithm by Kulkarni et al. for porous materials [15]. The principle of the segmentation algorithm is to determine the spatial arrangement of class labels (i.e. LACs) by assigning a value within the 3D data set to one of the individual classified phases. The method evaluates the interaction between direct neighbors in a probabilistic manner to determine the spatial distribution of the class labels with minimal boundary surface while maintaining grey value data [15, 17]. The determination of class labels is described by:

$$\hat{H} = \underset{\hat{H}}{\operatorname{argmin}} \left\{ \int_{\Omega} \left( \sqrt{2\pi\sigma_H} + \frac{I'_x - \mu_H}{2\sigma_H^2} + \beta \int_{\Pi} \gamma(H_x, H_y) \right) \right\} \qquad \text{Equation 5.6}$$

with:

$$\gamma(H_x, H_y) = \begin{cases} -1 & H_x = H_y \\ 1 & H_x \neq H_y \end{cases} \qquad \text{Equation 5.7}$$

where $\hat{H}$ is the class label, $\Omega$ is the total voxel population, $\Pi$ is the population of all pairs of neighboring voxels x and y, $H_x$ and $H_y$ represent the class label at x and y, respectively, $\mu_H$ and $\sigma_H$ are the class mean and standard deviation, and $\beta$ is a parameter which represents the homogeneity of the region. The first term of Equation 5.4 defines the statistics for individual phases, and the second term defines the boundaries between phases [15].

## 5.3. Experimental methods and materials

### *5.3.1. Synchrotron x-ray CT*

In this study, synchrotron x-ray CT was done one the four main hydrate phases (C-S-H, CH, AFt, and AFm), which were synthesized to determine the feasibility of different segmentation algorithms to discern each phase. The materials were synthesized and prepared as described in the following section. The GeoSoilEnviroCARS (GSECARS) 13-BMD beamline of the Advanced Photon Source at the Argonne National Laboratory was used for all scans. The samples were mounted in a drill chuck, which was attached to the rotation stage. The beam size was 3.14 mm wide by 5.02 mm tall, resulting in a 2.61 μm/pixel resolution. For each scan, 900 x-ray projection images with a rotation step of 0.18° and exposure time of 2 seconds were collected. All samples were scanned at 33.299 keV.

### *5.3.2. Sample preparation*

The four main hydration products of portland cement concrete were synthesized and investigated for this research. C-S-H was synthesized using the pozzolanic method with a calcium-to-silica ratio of 1.7 [42]. Pure CaO was created by heating reagent grade $CaCO_3$ to 900 °C for 24 hours. The cooled CaO was mixed in stoichiometric proportions with reactive $SiO_2$ in an excess of de-aired, de-ionized water and mixed on a rotation rack for 21 days at 6 rpm. The material was then vacuum filtered. AFt was created by mixing stoichiometric amounts of $Al_2(SO_4)_3$ and CaO. The fresh CaO was dissolved in a 10% sucrose solution and combined with a solution of $Al_2(SO_4)_3$ on a magnetic stirring plate for 60 hours [43]. The precipitate was vacuum filtered. AFm was created by mixing stoichiometric amounts of $C_3A$ and reagent grade gypsum ($CaSO_4 \cdot 2H_2O$) in excess de-aired, de-ionized water. The solution was placed in a hydrothermal pressure vessel and heated to 150 °C for 4 days [44]. After 4 days, the solution was allowed to cool to room temperature and the precipitate was vacuum filtered. A commercially available, reagent grade calcium hydroxide (>95% purity) was used to represent portlandite (CH). All materials were placed in a vacuum desiccator and conditioned at 11% relative humidity.

After conditioning, the powder materials were compacted to a pressure of 515 MPa using a die and hydraulic press for x-ray CT studies. This compaction pressure resulted in a density with similar porosity to that of a hydrated portland cement paste [45]. Three different sample types were

created. The first sample type was individual layers of pure phases, approximately 1-2 mm per layer, to determine the linear attenuation coefficient (LAC). Three layered samples were scanned. The second sample type was a binary mixture of two phases. Each phase was paired with a different one to determine potential segmentation limitations. A known mass of each phases was intermixed with another prior to compaction. Two samples per pair were scanned, for a total of twelve binary mixtures scanned. The third sample type was a quaternary mixture of four phases. A known mass of each phase was proportioned to represent a hydrated portland cement paste, and intermixed prior to compaction. Six quaternary mixtures were scanned. A summary of the binary and quaternary samples tested are presented in Table 5-1.

Table 5-1: Summary of samples scanned

| Sample type | Materials | Sample ID |
|---|---|---|
| Binary mixture | C-S-H and CH | B1-1 |
| | | B1-2 |
| | AFm and C-S-H | B2-1 |
| | | B2-2 |
| | AFt and C-S-H | B3-1 |
| | | B3-2 |
| | AFt and CH | B4-1 |
| | | B4-2 |
| | AFm and CH | B5-1 |
| | | B5-2 |
| | AFt and AFm | B6-1 |
| | | B6-2 |
| Quaternary mixture | ~55% C-S-H, ~25% CH, ~15% AFm, ~5% AFt | Q1-1 |
| | | Q1-2 |
| | | Q1-3 |
| | ~60% C-S-H, ~25% CH, ~12% AFt, ~3% AFm | Q2-1 |
| | | Q2-2 |
| | | Q2-3 |

## 5.4. Results and discussion

### *5.4.1. Characterization of materials*

XRD and thermogravimetric analysis\differential thermogravimetric analysis (TGA\DTG) were used to characterize the synthesized phases. A Bruker-AXS D8 Discovery XRD was also used for the characterization of the synthesized phases. Diffraction angle range of $6° < 2\Theta < 60°$ with a step size of 0.08° with a scan speed of 0.96˚/min with an accelerating voltage of 40 kV and current of 40 mA was used for analysis of AFm and AFt. For the analysis of C-S-H, a diffraction angle of

4˚<2Θ<15˚ with a step size of 0.03˚ and a scan speed of 0.36˚/min was used. XRD patterns for the synthesized phases are seen in Figure 5-1.

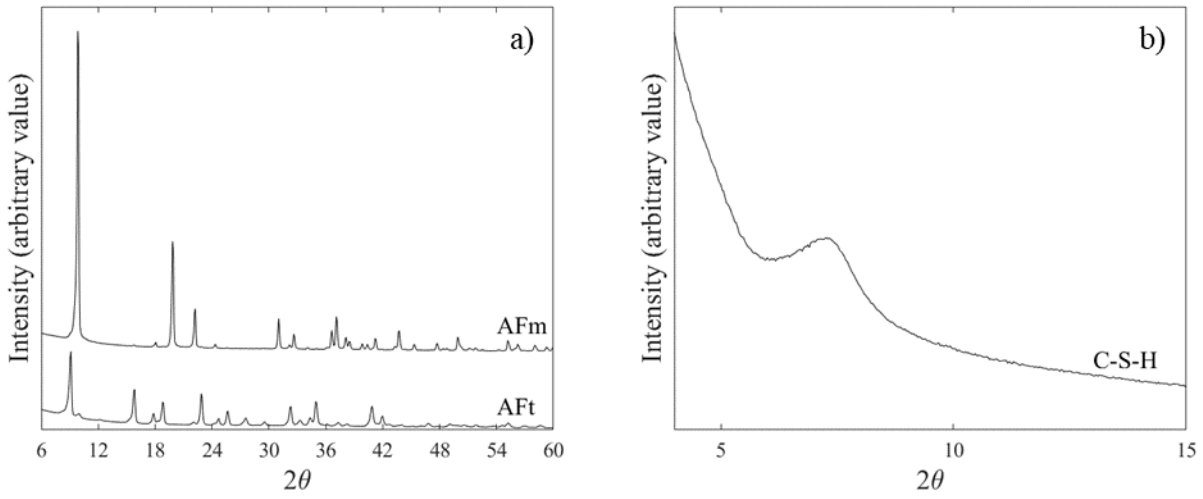


Figure 5-1: XRD patterns of synthesized materials

In pure AFm, a basal spacing of 0.893 nm corresponds to an interlayer distance in the AFm crystal with 12 molecules of water [46], as indicated by the main peak occurring at a 2θ value of 9.9 degrees seen in Figure 5-1a). The secondary peak observed at 19.9 degrees 2θ indicated a basal spacing of 0.448 nm, further verifying AFm with 12 water molecules was synthesized [44]. AFt with 32 molecules of water has an expected basal spacing of 0.973 nm [47] and 0.561 nm [48]. The XRD pattern in Figure 5-1a) indicated the proper d-spacing of AFt with peaks occurring at 2θ values of 9.1 and 15.8 degrees, respectively. Other peaks observed in the XRD pattern of AFt matched published literature of synthesized AFt [43]. The major peak observed in C-S-H varies, depending on the Ca/Si ratio, and occur between 5 to 10 degrees 2θ [48]. The synthesized C-S-H with a Ca/Si ratio of 1.7 had a major peak occurring at 7.3 degrees.

Further characterization of the synthesized materials was done using a TA Instruments Q50 for TGA/DTG analysis. A sample size ranging from 20-35 mg was used for all materials. A heating rate of 10 ˚C/min, under a flow of nitrogen gas (60 ml/min), heated the materials from ambient temperature (23 ˚C) to 1000 ˚C. Results of the TGA/DTG analysis of the four phases used in this study are seen in Figure 5-2.

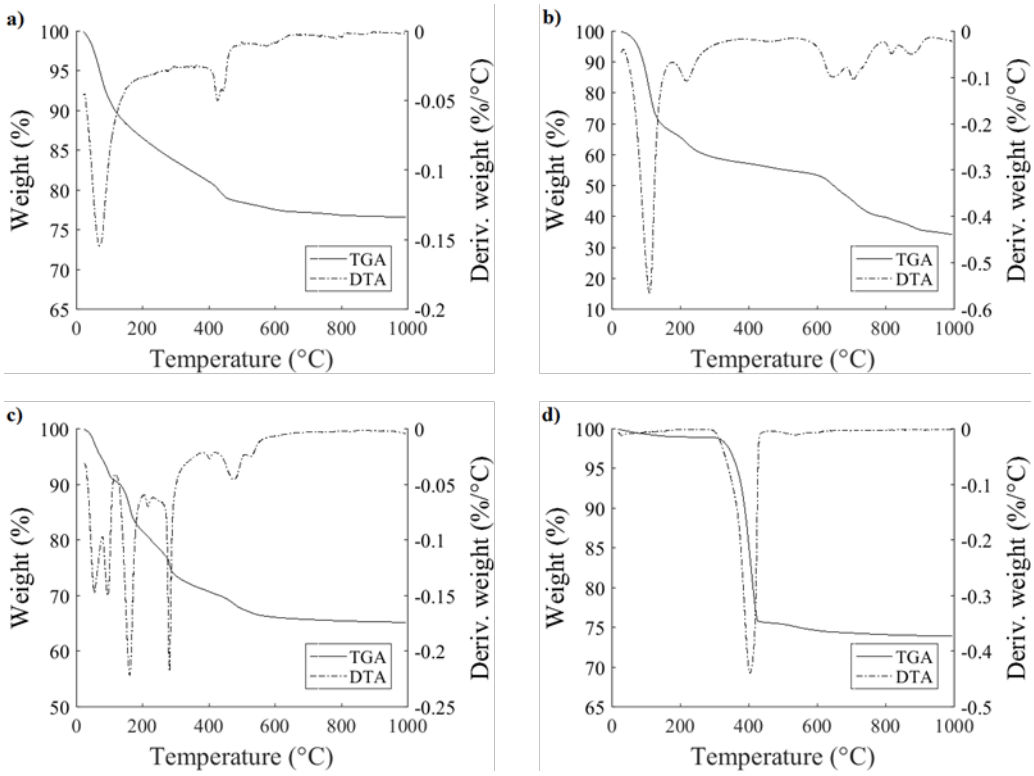


Figure 5-2 - TGA/DTG analysis of phases: a) C-S-H, b) AFt, c) AFm, d) CH

The major loss in C-S-H occurring at temperatures less than 200 °C were attributed to the release of gel water, as seen in Figure 5-2a). A secondary loss occurring between 400 °C and 600 °C indicated decomposition of calcium hydroxide. Additional losses were attributed to the formation of $CaCO_3$. TGA analysis indicated 6.8% CH and 0.64% $CaCO_3$ in the synthesized C-S-H. The presence of CH was expected in synthesized C-S-H with a Ca/Si ratio > 1.54 using the pozzolanic method [49, 50]. Mass loss in AFt occurring between 120 ˚C and 230 ˚C indicated water loss [48], while other losses occurring between 550 ˚C and 1000 ˚C were attributed to the release of sulfur oxides, as seen in Figure 5-2b). These losses have been reported in literature for AFt synthesized in sucrose [51], as well as in natural ettringite [52]. As observed in Figure 5-2c), water loss in AFm began around 220 ˚C as the material released 6 water molecules with the remaining 6 water molecules being released at temperatures above 220 ˚C. A measured mass loss of 34.8% indicated AFm was created and conditioned with 12 water molecules [53]. TGA/DTG analysis of CH, seen in Figure 5-2d), indicated a purity of 95.2%.

### *5.4.2. Pre-segmentation processing*

The raw data (2D projections) generated at the GSECARS beamline were first reconstructed with a filtered back-projection algorithm using the programming language IDL™ to form a 3D volume of greyscale data. The reconstructed image stack was processed using Avizo Fire 9.3 and Quantim4. The data was first processed using a non-local means filter [54] to remove image noise from the volume. While several de-noising filters exist, the non-local means filter was chosen due to the robustness of the algorithm to remove noise while preserving edges and improving contrast at edge boundaries [55-57]. Further improvements were made to edge detection for the watershed segmentation by applying an unsharp mask filter to enhance edge boundaries. A comparison of the distribution of greyscale values and ability to detect edges is presented in Figure 5-3. It can be seen that applying a non-local means filter resulted in a separation of greyscale values in a binary mixture of C-S-H and CH, thus resulting in the ability to determine a threshold values for the two phases in an unbiased manner. The separation of the peaks allowed for verification of proportioning the LAC of each phase for the Gaussian deconstruction of the histogram segmentation algorithm.

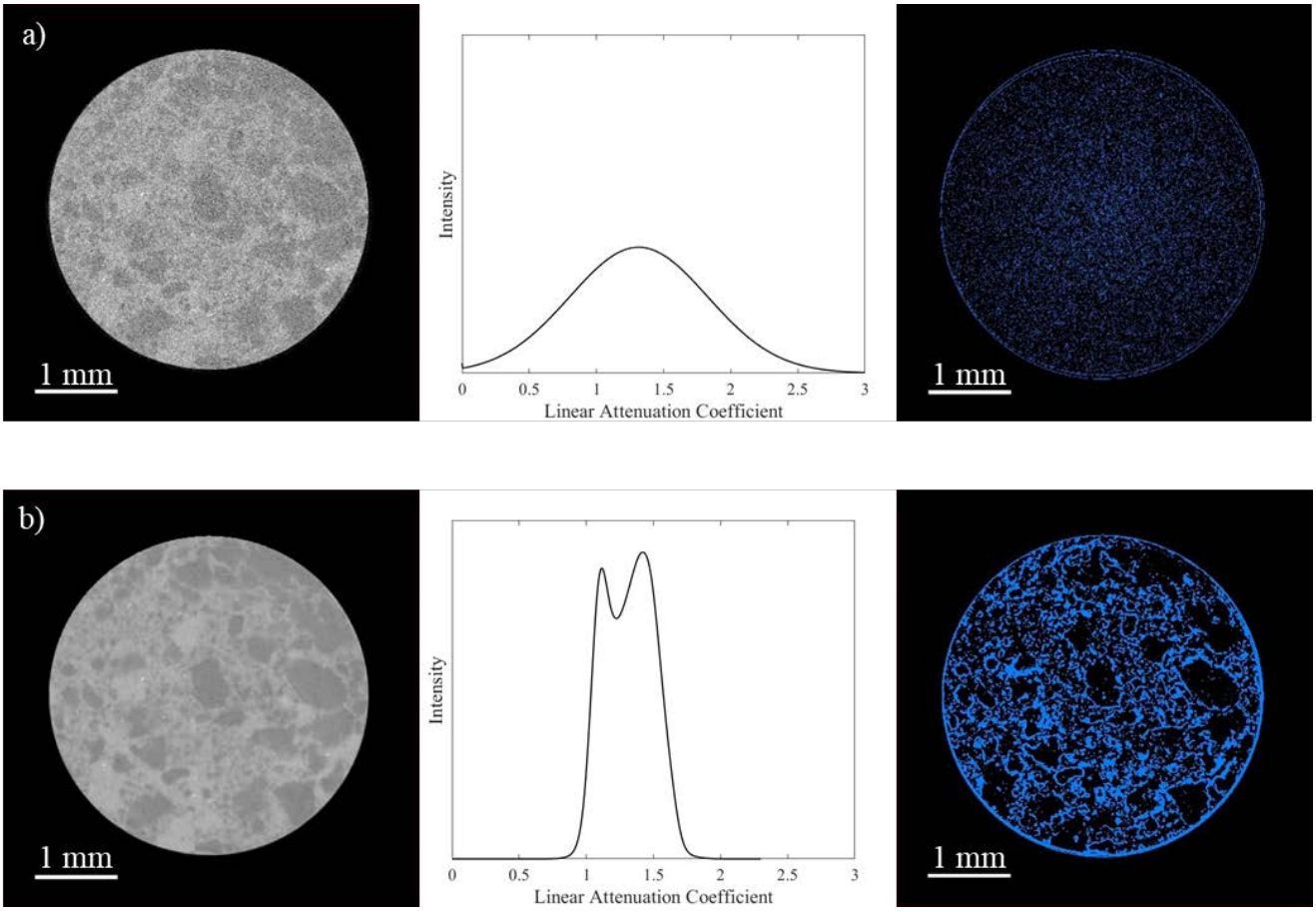


Figure 5-3: Importance of filtering before attempting to segment data: a) Greyscale slice of raw data of a binary mixture of C-S-H and CH, resulting in a histogram with overlap of the greyscale values (center) and an inability to distinguish edges, as seen in the upper right. b) Greyscale slice of the same data after non-local means filtering, resulting in a histogram with two distinct peaks and distinct edges between phases, as seen in the lower right.

Once the data sets were preprocessed, the volume of each phase in the binary and quaternary mixtures was determined through two different means for each segmentation algorithm. One method for determining the volume was done through image analysis by converting the volume of voxels of each phase, determined through the different segmentation algorithms, to cubic centimeters. The image resolution of 2.61 microns/voxel was used to convert the voxels into cubic centimeters. This volume was compared to the volume determined by converting the known mass of each phase to a volume based on its respective density ($g/cm^3$). Published values of densities were used for C-S-H [4, 58], CH, AFm, and AFt [59]. Densities of phases used for analysis are shown in Table 5-2.

Table 5-2: Phase densities used for analysis

| Phase | Density (g/cm$^3$) |
|---|---|
| C-S-H | 2.440 |
| CH | 2.251 |
| AFt | 1.778 |
| AFm | 2.015 |

### *5.4.3. LAC of pure phases and threshold determination*

The measured LAC of the preprocessed image volume for each pure phase was determined to provide an understanding for potential threshold values for segmentation. The average LAC and standard deviation of each phase was measured and fit to a Gaussian distribution. The measured LAC for each phase were 0.549 cm$^{-1}$ for AFt, 0.963 cm$^{-1}$ for AFm, 1.193 cm$^{-1}$ for C-S-H, and 1.733 cm$^{-1}$ for CH. As seen in Figure 5-4, it was observed there was a potential for overlap of LACs between AFm and C-S-H. This overlap could lead to difficulties segmenting accurately for quantification of these phases in both binary and quaternary mixtures. The mean and standard deviation of each pure phase was used to determine potential threshold values for the Gaussian deconstruction algorithm, ranges for minima of catchment basins used in the watershed algorithm, and seeding values for the MRF algorithm.

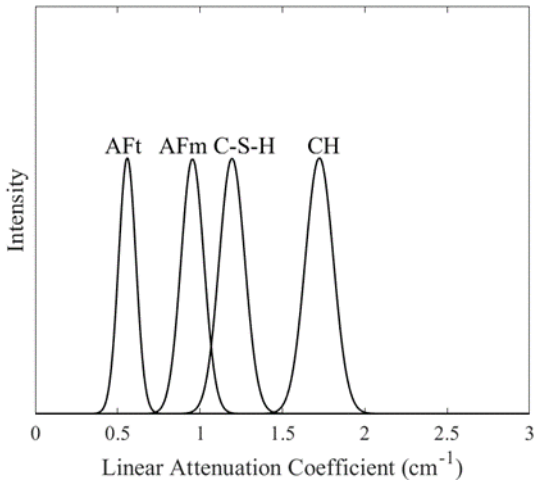


Figure 5-4: Distribution of measured LAC for each phase

The measured LACs were used as a reference to provide threshold values for the three segmentation algorithms. This was done by using the Gaussian deconstruction of the histogram of

each sample. The intersection of the adjacent curves was determined to be an initial seeding value for watershed and MRF. A schematic for this method is shown in Figure 5-5.

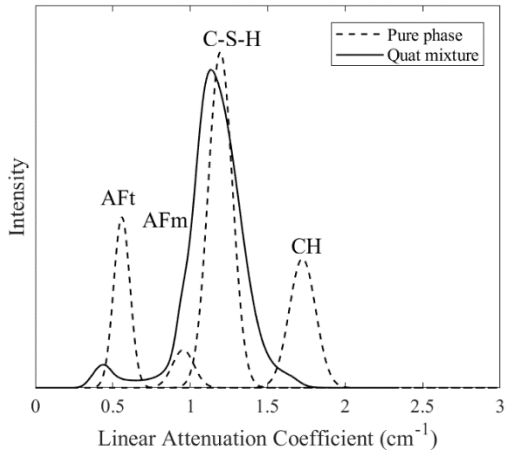


Figure 5-5: Proportioning individual quantities of the respective mass of each phase to the expected distribution of LACs for a quaternary mixture. The total area under the quaternary histogram is equivalent to the area under the four pure phase Gaussian curves.

As seen in Figure 5-23, overlapping LACs for all of the phases in the quaternary mixtures was observed. The major peaks for AFt and CH were overestimated when using the pure phase LAC to estimate the quantity of each of those respective phases. Furthermore, overlap of AFm, C-S-H, and CH, LACs was observed in all of the quaternary mixtures, likely attributed to partial volume effects.

### *5.4.4. Segmentation results of binary mixtures*

Results of the volume analysis for the three segmentation algorithms for the binary mixtures are presented in Figure 5-6. The error from the measured volume from the image analysis compared to the expected volume based on the mass and density of each phase is plotted for each binary sample type. An overestimate was determined when the volume determined from the image analysis resulted in a higher quantity of each phase when compared to the expected volume determined from the mass and density of each phase. Similarly, an underestimate was determined when the volume calculated from the image analysis was lower than the expected volume.

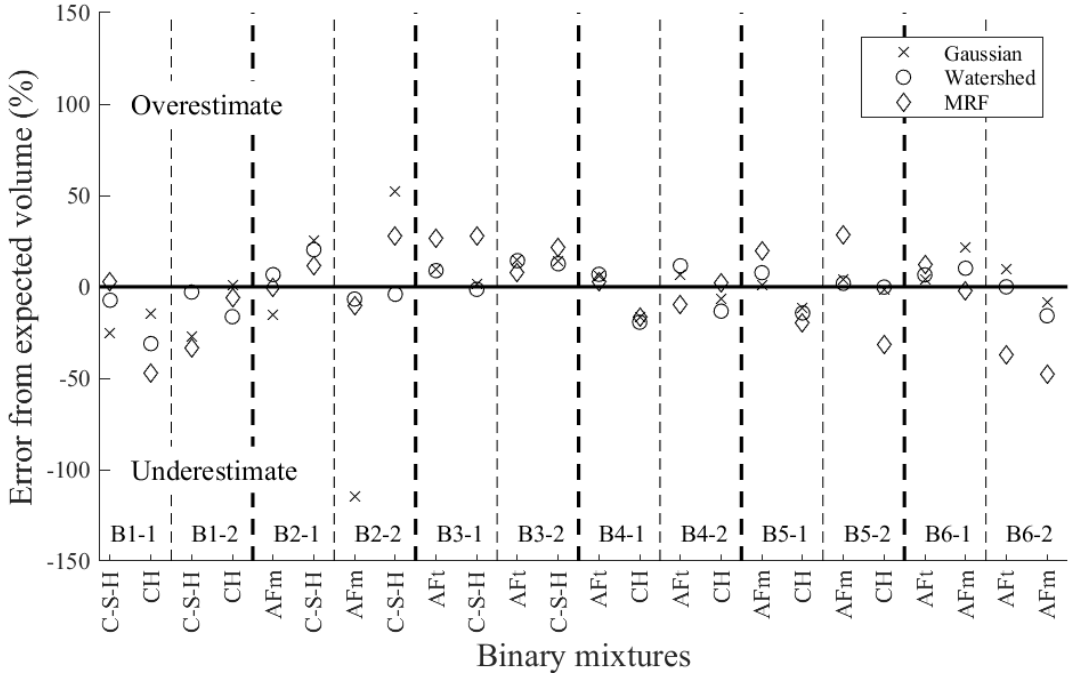


Figure 5-6: Comparison of the three segmentation algorithms on the binary mixtures. Errors were determined by the difference between the volume determined through image analysis and the expected volume from the mass-density relationship of each respective phase.

In general, good correlation was achieved in all of the segmentation algorithms when determining quantities of phases in the binary mixtures. The Gaussian deconstruction method resulted in higher deviations, typically, than the watershed and MRF methods. This was particularly apparent in the AFm and C-S-H mixtures where errors when comparing the two volumes varied greatly and were as high as 115%. Both watershed and MRF better resolved the low contrast between the two phases and eliminated much of the variation in error calculations when compared to the Gaussian deconstruction method. This was attributed to the robustness of both algorithms ability to proportion voxels based on the local neighborhood, whereas the threshold value for segmentation of the Gaussian deconstruction method was based solely on the histogram. In the AFm and C-S-H mixtures, the Gaussian deconstruction method often misclassified the voxels for both phases throughout the image volume for both samples. Image slices from segmentation of the three algorithms are presented in Figure 5-7.

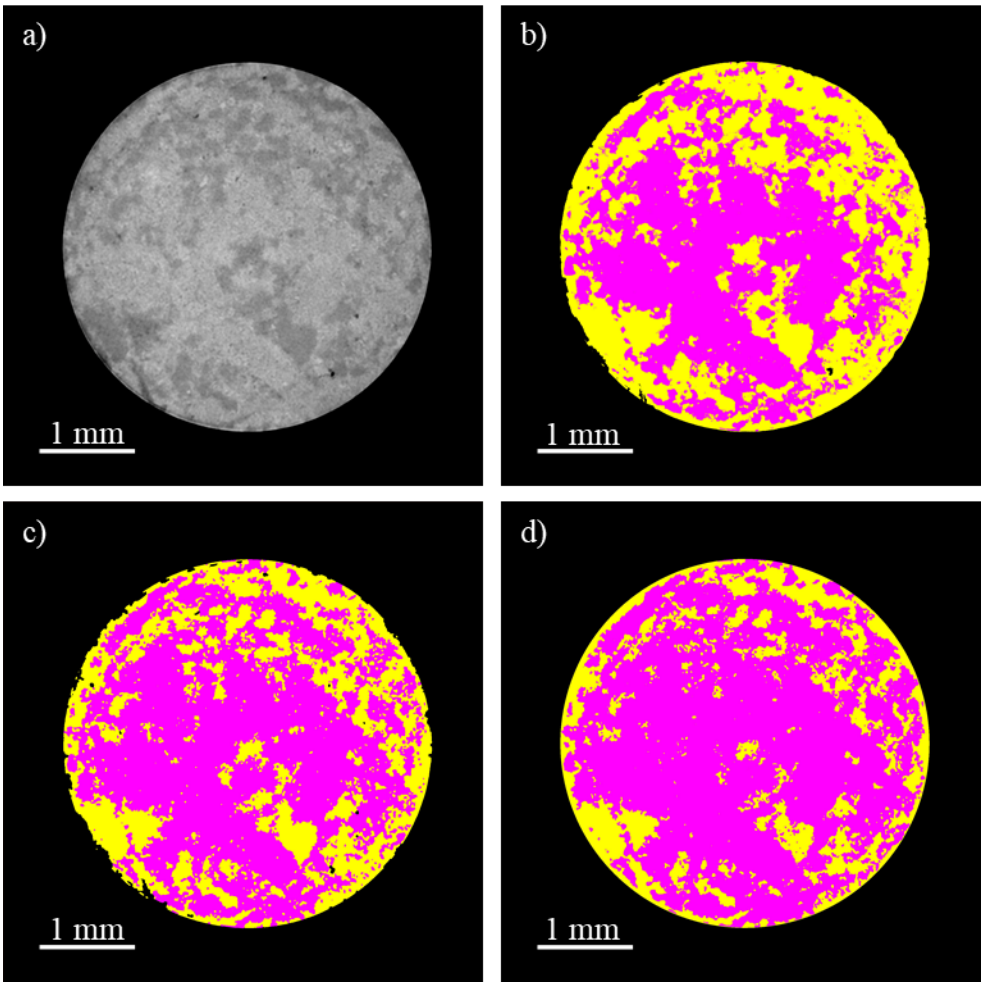


Figure 5-7: Segmentation of AFm and C-S-H mixtures where purple represents C-S-H and yellow represents AFm: a) Greyscale orthoslice, b) Segmented using Gaussian deconstruction, c) Segmented using watershed, d) segmented using MRF

As shown in Figure 5-6, AFm was underestimated and C-S-H was overestimated using the Gaussian deconstruction method for both samples. The voxels were often misclassified, as shown in Figure 5-7b), where there was more AFm by visual observation, yet the analysis of the entire image volume resulted in an overestimation of C-S-H and underestimation of AFm. The watershed algorithm best resolved the low contrast between the two phases, shown in Figure 5-7c). The MRF algorithm resulted in an underestimation of AFm and overestimation of C-S-H, which was copacetic with the results shown in Figure 5-6.

### *5.4.5. Segmentation results of quaternary mixtures*

An overview of the three algorithms for segmenting the quaternary mixture image volumes is shown in Figure 5-8.

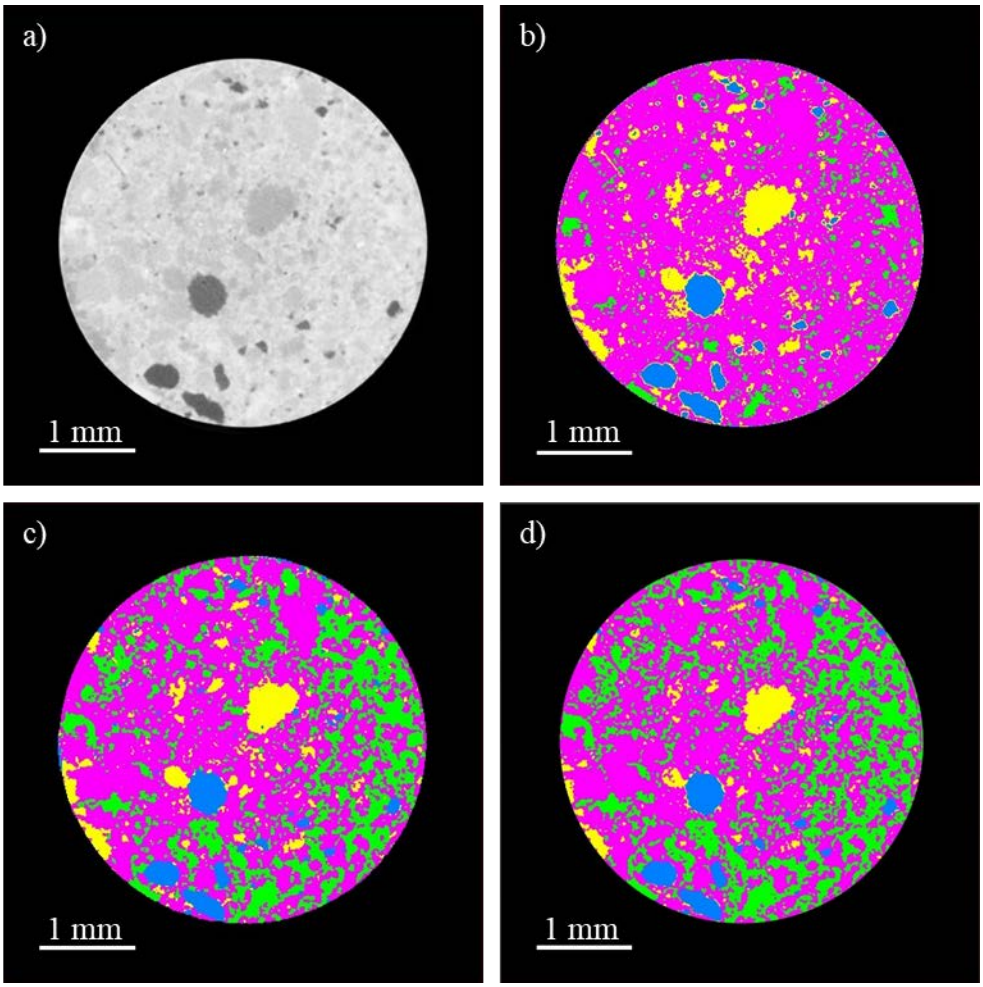


Figure 5-8: Comparison of segmentation algorithms in a quaternary mixture of phases. Blue represents AFt, yellow represents AFm, purple represents C-S-H, and green represents CH. a) Greyscale orthoslice of a quaternary mixture. b) Segmented using Gaussian deconstruction. c) Segmented using watershed. d) Segmented using MRF

As seen in Figure 5-8b), the majority of the volume determined using the Gaussian deconstruction was C-S-H. The major peak in the histogram was difficult to determine appropriate threshold values solely based on the histogram information in order to resolve individual phases. The watershed and MRF algorithms better resolved the major peak, particularly in determining the quantities of C-S-H (purple) and CH (green), as shown in Figure 5-8c) and d), respectively.

Furthermore, smaller quantities of AFm were visually observed in the watershed and MRF segmented images, and predominately classified as C-S-H.

Volume analysis results on the six quaternary mixtures for the three segmentation algorithms are presented in Figure 5-9. Errors were determined by the difference between the volume determined through image analysis and the expected volume from the mass-density relationship of each respective phase.

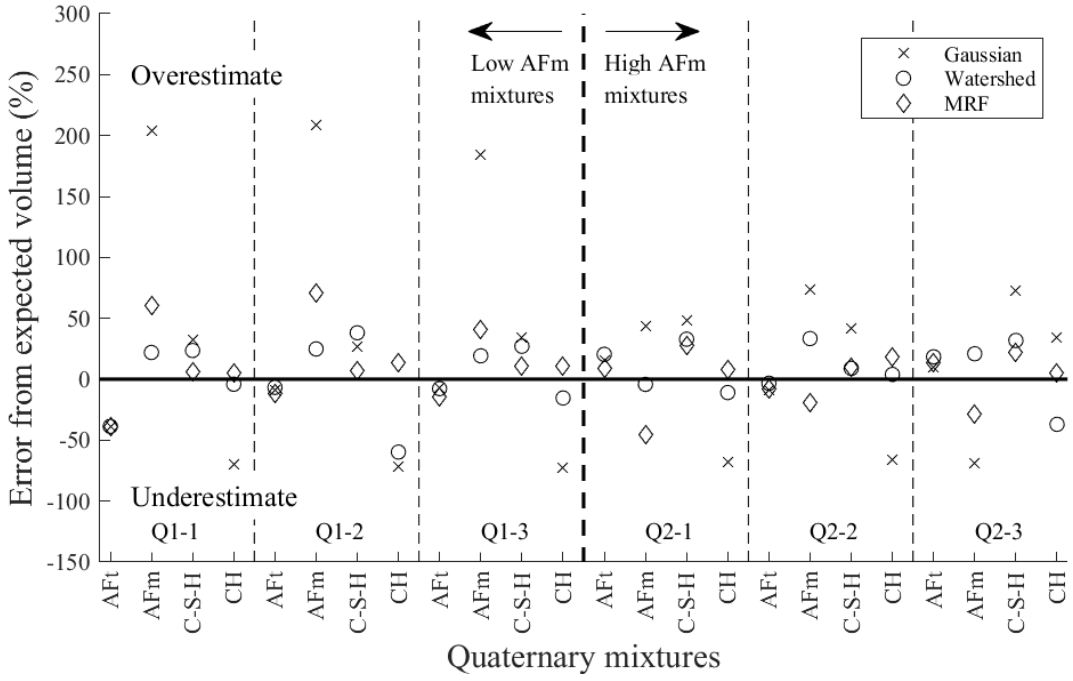


Figure 5-9: Comparison of the three segmentation algorithms on the quaternary mixtures.

The errors observed in the binary mixtures were compounded when the Gaussian deconstruction method was used on the quaternary mixtures, due to the significant overlap of the LACs of AFm, C-S-H, and CH. Errors as high as 39%, 210%, 73%, and 74%, were observed in AFt, AFm, C-S-H, and CH, respectively when the Gaussian deconstruction method was used. As expected, based on the visual inspection of the segmented image volumes, the errors in quantifying individual phases were reduced when using the watershed and MRF algorithms. Maximum errors of 38%, 24%, 38%, and 60%, for AFt, AFm, C-S-H, and CH, were observed in the watershed algorithm results. Similar errors were observed in the phases when MRF was used, with a reduction in the error for CH. A maximum error of 19% was observed for CH. Furthermore when comparing the

MRF to watershed in low AFm quaternary mixtures, as observed in Figure 5-27, the errors were higher in quantifying AFm when using MRF compared to watershed, with errors as high as 70% when using MRF and 25% when using watershed. The errors for quantifying CH for the same mixtures were lower when using MRF than watershed, thus reiterating the potential to run multiple algorithms to accurately quantify various phases.

In general, the use of the Gaussian deconstruction method worked well to quantify AFt. The observed errors were comparable for all three methods at quantifying this phase. Vast improvements in quantifying AFm, C-S-H, and CH, were observed for all samples when the data was segmented using the watershed or MRF algorithms. When using the Gaussian deconstruction method, significant errors were observed in quantifying AFm and CH. Furthermore, the variation in errors was reduced when using watershed and MRF. CH and AFm were underestimated when using watershed and MRF, respectively. The other phases were generally overestimated when using both of these algorithms.

In addition to reducing the errors in image volume calculations, the watershed and MRF algorithms better resolved the transition zones where high gradients were observed between phases, particularly AFt and the other phases, as seen in Figure 5-10.

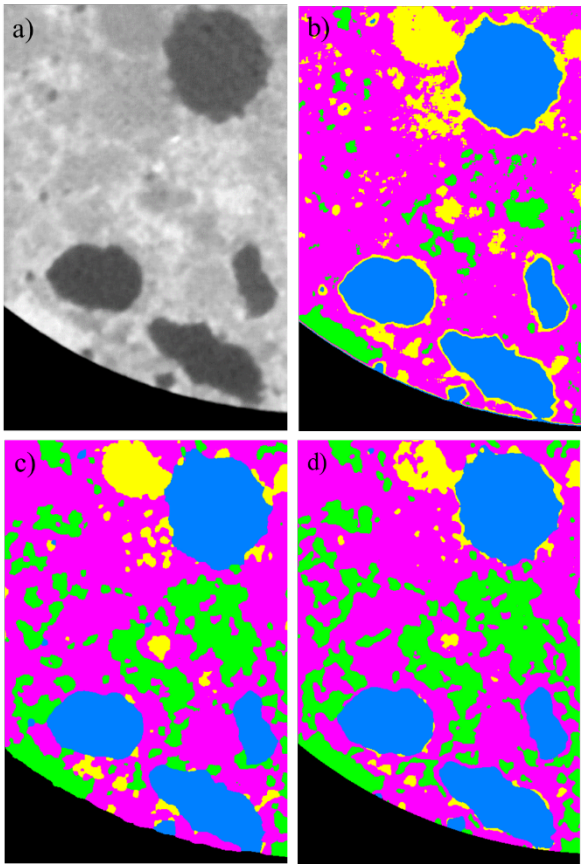


Figure 5-10: Comparison of edge boundaries after segmentation using different algorithms. a) Greyscale image with three AFt phases represented by the darkest grey values. b) Segmented using the Gaussian deconstruction method. c) Segmented using the watershed algorithm. d) Segmented using the MRF algorithm. Color schemes representing phases are similar to what is presented in Figure 5-8.

When using the Gaussian deconstruction method, each AFt (blue) region had a rim of AFt (yellow) voxels throughout the image volume, as seen in Figure 5-10b). The use of watershed and MRF better resolved the edges between adjacent phases in high gradient zones, particularly between AFt and AFm. However, smaller, discrete regions of AFm were present near many of the AFt regions in the segmented image volumes using watershed and MRF.

There is promise in using local segmentation algorithms to quantify hydration products, however, care must still be taken to determine appropriate threshold or seeding values for segmentation. Knowledge of expected LACs for each phase should be measured or calculated to provide a starting point for segmentation. If only histogram data is available, deconstructing the histogram into individual Gaussian curves for the expected peaks was a viable alternative for determining threshold values. Furthermore, one challenge with the watershed algorithm is the necessity for

edge detection. This may attribute to the variation in errors when using this method for the binary and quaternary mixtures where low contrast between phases was observed. When low contrast is present between phases, such as AFm and C-S-H, or as expected in a hydrating cementitious system, where potentially inadequate resolution and additional phases forming, difficulties may arise when attempting to use this segmentation algorithm since object identification through edge detection is a critical step when using watershed [29]. Therefore, a stochastic approach to determining phases, such as MRF, can help resolve such phases. Other segmentation algorithms may further refine the errors, such as converging active contours, which combines image gradient and image intensity simultaneously [60]. Algorithms such as this may help resolve greyscale issues in hydrating cementitious systems where the significantly more phases are present, and are finer in scale.

## 5.5. Conclusions

It is well known that low contrast can be expected in both the hydrated and unhydrated phases of portland cement in reconstructed x-ray CT image volumes. The image processing and analysis can be overlooked as trivial, but the image analysis can provide differing results based on the procedures followed. This research investigated one global thresholding algorithm and two local segmentation algorithms to determine the feasibility to accurately differentiate and quantify synthesized hydration products found in portland cement. The following conclusions were made from this research:

- Histogram based, global thresholding, algorithms can accurately quantify phases when adequate contrast is observed in the reconstructed image volume. This method for segmentation worked well for most binary mixtures with the exception of C-S-H and AFm, where errors in quantification exceeded 100%. Global thresholding was successful at quantifying AFt phases in quaternary mixtures, but errors increased when determining the amounts of AFm, C-S-H, and CH. Difficulties determining an appropriate threshold value when the LAC of phases are similar resulted in the large errors.
- Statistically based, local thresholding, algorithms reduced the errors in binary mixtures of AFm and C-S-H from as high as 115% in the global, Gaussian histogram deconstruction to as low as 14% and 37% when using watershed and MRF, respectively. Similar trends in errors were observed in all three algorithms for the other binary mixture combinations.

- The watershed algorithm reduced the errors in quaternary mixtures of phases. Variations in errors were observed between AFm/C-S-H and C-S-H/CH. This was likely attributed to the inability to properly define edges between low contrast phases. Therefore, appropriate image preprocessing, such as filtering and sharpening, may be needed in order for edge detection to appropriately run watershed.
- The MRF algorithm performed similarly to watershed in quantifying the phases in the quaternary mixtures. In general, the variation in errors were reduced, as well as the overall error in quantifying each phase. A stochastic algorithm such as MRF may be appropriate for resolving phases when edges cannot be detected.

## 5.6. Acknowledgements

This research used resources of the Advanced Photon Source, a U.S. Department of Energy (DOE) Office of Science User Facility operated for the DOE Office of Science by Argonne National Laboratory under Contract No. DE-AC02-06CH11357. We acknowledge the support of GeoSoilEnviroCARS (Sector 13), which is supported by the National Science Foundation - Earth Sciences (EAR-1128799), and the Department of Energy, Geosciences (DE-FG02-94ER14466). Special thanks to the staff at GSECARS for their assistance with the experimental work, particularly the help of Dr. Mark Rivers.

## 5.7. References

[1] K. Tosun, B. Baradan, Effect of ettringite morphology on DEF-related expansion, Cement and Concrete Composites, 32 (2010) 271-280.

[2] N. Bossa, P. Chaurand, J. Vicente, D. Borschneck, C. Levard, O. Aguerre-Chariol, J. Rose, Micro- and nano-x-ray computed-tomography: A step forward in the characterization of the pore network of a leached cement paste, Cement and Concrete Research, 67 (2015) 138-147.

[3] T. Rougelot, N. Burlion, D. Bernard, F. Skoczylas, About microcracking due to leaching in cementitious composites: X-ray microtomography description and numerical approach, Cement and Concrete Research, 40 (2010) 271-283.

[4] D. Gastaldi, F. Canonico, L. Capelli, E. Boccaleri, M. Milanesio, L. Palin, G. Croce, F. Marone, K. Mader, M. Stampanoni, In situ tomographic investigation on the early hydration behaviors of cementing systems, Construction and Building Materials, 29 (2012) 284-290.

[5] E. Gallucci, K. Scrivener, A. Groso, M. Stampanoni, G. Margaritondo, 3D experimental investigation of the microstructure of cement pastes using synchrotron x-ray microtomography (μCT), Cement and Concrete Research, 37 (2007) 360-368.

[6] T. Deboodt, J.H. Ideker, O.B. Isgor, D. Wildenschild, Quantification of synthesized hydration products using synchrotron microtomography and spectral analysis, Construction and Building Materials, 157 (2017) 476-488.

[7] J.L. Provis, A. Hajimohammadi, C.E. White, S.A. Bernal, R.J. Myers, R.P. Winarski, V. Rose, T.E. Proffen, A. Llobet, J.S.J. van Deventer, Nanostructural characterization of geopolymers by advanced beamline techniques, Cement and Concrete Composites, 36 (2013) 56-64.

[8] M.A.B. Promentilla, T. Sugiyama, T. Hitomi, N. Takeda, Quantification of tortuosity in hardened cement pastes using synchrotron-based x-ray computed microtomography, Cement and Concrete Research, 39 (2009) 548-557.

[9] P.J.M. Monteiro, A.P. Kirchheim, S. Chae, P. Fischer, A.A. MacDowell, E. Schaible, H.R. Wenk, Characterizing the nano and micro structure of concrete to improve its durability, Cement and Concrete Composites, 31 (2009) 577-584.

[10] P. Trtik, A. Diaz, M. Guizar-Sicairos, A. Menzel, O. Bunk, Density mapping of hardened cement paste using ptychographic x-ray computed tomography, Cement and Concrete Composites, 36 (2013) 71-77.

[11] J.C. da Silva, P. Trtik, A. Diaz, M. Holler, M. Guizar-Sicairos, J. Raabe, O. Bunk, A. Menzel, Mass density and water content of saturated never-dried calcium silicate hydrates, Langmuir, 31 (2015) 3779-3783.

[12] A. Cuesta, A.G. De la Torre, I. Santacruz, P. Trtik, J.C. da Silva, A. Diaz, M. Holler, M.A.G. Aranda, Chemistry and mass density of aluminum hydroxide gel in eco-cements by ptychographic x-ray computed tomography, The Journal of Physical Chemistry C, 121 (2017) 3044-3054.

[13] M.A. Le Gros, G. McDermott, C.A. Larabell, X-ray tomography of whole cells, Current Opinion in Structural Biology, 15 (2005) 593-600.

[14] J.L. Provis, R.J. Myers, C.E. White, V. Rose, J.S.J. van Deventer, X-ray microtomography shows pore structure and tortuosity in alkali-activated binders, Cement and Concrete Research, 42 (2012) 855-864.

[15] R. Kulkarni, M. Tuller, W. Fink, D. Wildenschild, Three-dimensional multiphase segmentation of x-ray CT data of porous materials using a Bayesian Markov random filed framework, Vadose Zone Journal, 11 (2012) 74-85.

[16] N. Burlion, D. Bernard, D. Chen, X-ray microtomography: Application to microstructure analysis of a cementitious material during leaching process, Cement and Concrete Research, 36 (2006) 346-357.

[17] S. Schlüter, A. Sheppard, K. Brown, D. Wildenschild, Image processing of multiphase images obtained via x-ray microtomography: A review, Water Resources Research, 50 (2014) 3615-3639.

[18] T. Deboodt, D. Wildenschild, J.H. Ideker, O.B. Isgor, Use of iodine for improving phase quantification using x-ray tomography, Submitted to Cement and Concrete Research, (2018).

[19] U. Rattanasak, K. Kendall, Pore structure of cement/pozzolan composites by x-ray microtomography, Cement and Concrete Research, 35 (2005) 637-640.

[20] T.S. Yun, K.Y. Kim, J. Choo, D.H. Kang, Quantifying the distribution of paste-void spacing of hardened cement paste using x-ray computed tomography, Materials Characterization, 73 (2012) 137-143.

[21] S. Lu, E.N. Landis, D.T. Keane, X-ray microtomographic studies of pore structure and permeability in Portland cement concrete, Materials and Structures, 39 (2006) 611-620.

[22] K.Y. Kim, T.S. Yun, K.P. Park, Evaluation of pore structures and cracking in cement paste exposed to elevated temperatures by x-ray computed tomography, Cement and Concrete Research, 50 (2013) 34-40.

[23] M.A.B. Promentilla, T. Sugiyama, T. Hitomi, N. Takeda, Characterizing the 3D pore structure of hardened cement paste with synchrotron microtomography, Journal of Advanced Concrete Technology, 6 (2008) 273-286.

[24] M. Lanzón, V. Cnudde, T. de Kock, J. Dewanckele, X-ray microtomography (μ-CT) to evaluate microstructure of mortars containing low density additions, Cement and Concrete Composites, 34 (2012) 993-1000.

[25] T. Sugiyama, M.A.B. Promentilla, T. Hitomi, N. Takeda, Application of synchrotron microtomography for pore structure characterization of deteriorated cementitious materials due to leaching, Cement and Concrete Research, 40 (2010) 1265-1270.

[26] F. Batool, V. Bindiganavile, Air-void size distribution of cement based foam and its effect on thermal conductivity, Construction and Building Materials, 149 (2017) 17-28.

[27] J. Schock, S. Liebl, K. Achterhold, F. Pfeiffer, Obtaining the spacing factor of microporous concrete using high-resolution dual energy x-ray micro CT, Cement and Concrete Research, 89 (2016) 200-205.

[28] W. Wang, A.N. Kravchenko, A.J.M. Smucker, M.L. Rivers, Comparison of image segmentation methods in simulated 2D and 3D microtomographic images of soil aggregates, Geoderma, 162 (2011) 231-241.

[29] P. Iassonov, T. Gebrenegus, M. Tuller, Segmentation of x-ray computed tomography images of porous materials: A crucial step for characterization and quantitative analysis of pore structures, Water Resources Research, 45 (2009).

[30] P.K. Sahoo, S. Soltani, A.K.C. Wong, A survey of thresholding techniques, Computer Vision, Graphics, and Image Processing, 41 (1988) 233-260.

[31] N.R. Pal, S.K. Pal, A review on image segmentation techniques, Pattern Recognition, 26 (1993) 1277-1294.

[32] M. Sezgin, B. Sankur, Survey over image thresholding techniques and quantitative performance evaluation, SPIE, 2004, pp. 20.

[33] D. Wildenschild, A.P. Sheppard, X-ray imaging and analysis techniques for quantifying pore-scale structure and processes in subsurface porous medium systems, Advances in Water Resources, 51 (2013) 217-246.

[34] L. Salvo, P. Cloetens, E. Maire, S. Zabler, J.J. Blandin, J.Y. Buffière, W. Ludwig, E. Boller, D. Bellet, C. Josserond, X-ray micro-tomography an attractive characterisation technique in

materials science, Nuclear Instruments and Methods in Physics Research Section B: Beam Interactions with Materials and Atoms, 200 (2003) 273-286.

[35] H. Lusic, M.W. Grinstaff, X-ray-computed tomography contrast agents, Chemical Reviews, 113 (2012) 1641-1666.

[36] L. Vincent, P. Soille, Watersheds in digital spaces: An efficient algorithm based on immersion simulations, IEEE Transactions on Pattern Analysis and Machine Intelligence, 13 (1991) 583-598.

[37] S. Beucher, C. Lantuejol, Use of watersheds in contour detection, International Workshop Image Processing, Real-Time Edge and Motion Detection/Estimation, CCETT, Rennes, France, 1979.

[38] R. Deriche, Using Canny's criteria to derive a recursively implemented optimal edge detector, International Journal of Computer Vision, 1 (1987) 167-187.

[39] J. Canny, A computational approach to edge detection, IEEE Transactions on Pattern Analysis and Machine Intelligence, PAMI-8 (1986) 679-698.

[40] J. Moussouris, Gibbs and Markov random systems with constraints, Journal of Statistical Physics, 10 (1974) 11-33.

[41] M. Berthod, Z. Kato, S. Yu, J. Zerubia, Bayesian image classification using Markov random fields, Image and Vision Computing, 14 (1996) 285-295.

[42] R. Alizadeh, J.J. Beaudoin, L. Raki, Mechanical properties of calcium silicate hydrates, Materials and Structures, 44 (2011) 13-28.

[43] L.J. Struble, P.W. Brown, An evaluation of ettringite and related compounds for use in the solar energy storage, US Department of Commerce, 1982, pp. 11.

[44] H.J. Kuzel, Synthesis and x-ray study of the crystalline composition $3CaO{\cdot}Al_2O_3{\cdot}CaSO_4{\cdot}12H_2O$, Neues Jahrbuch Mineral Monatsh, 7 (1965) 193-197.

[45] R. Alizadeh, J.J. Beaudoin, L. Raki, V. Terskikh, C-S-H/polyaniline nanocomposites prepared by in situ polymerization, Journal of Materials Science, 46 (2011) 460-467.

[46] R. Allman, Refinement of the hybrid layer structure $[Ca_2Al(OH)_6]^{+}{\cdot}[1/2SO_4{\cdot}3H_2O]^{-}$, Neues Jahrbuch für Mineralogie Monatsheft, (1977) 136-144.

[47] N.N. Skoblinskaya, K.G. Krasilnikov, L.V. Nikitina, V.P. Varlamov, Changes in crystal structure of ettringite on dehydration. 2, Cement and Concrete Research, 5 (1975) 419-431.

[48] H.F.W. Taylor, Cement Chemistry, 2nd Edition ed., Thomas Telford Publishing, London, England, 1997.

[49] P. Yu, Kirkpatrick, R. J., Poe, B., McMillan, P. F. and Cong, X. , Structure of calcium silicate hydrate (C-S-H): Near-, mid-, and far-infrared spectroscopy, Journal of the American Ceramic Society, 82 (1999) 742-748.

[50] X. Cong, R.J. Kirkpatrick, $^{29}Si$ MAS NMR study of the structure of calcium silicate hydrate, Advanced Cement Based Materials, 3 (1996) 144-156.

[51] F. Goetz-Neunhoeffer, J. Neubauer, P. Schwesig, Mineralogical characteristics of ettringites synthesized from solutions and suspensions, Cement and Concrete Research, 36 (2006) 65-70.

[52] S.M. Antao, M.J. Duane, I. Hassan, DTA, TG, and RD studies of sturmanite and ettringite, The Canadian Mineralogist, 40 (2002) 1403-1409.

[53] R. Khoshnazar, L. Raki, J. Beaudoin, R. Alizadeh, Solvent exchange in sulfoaluminate phases. Part II: Monosulfate, Advances in Cement Research, 25 (2013) 322-331.

[54] A. Buades, B. Coll, J.M. Morel, A non-local algorithm for image denoising, 2005 IEEE Computer Society Conference on Computer Vision and Pattern Recognition (CVPR'05), 2005, pp. 60-65 vol. 62.

[55] P. Coupé, P. Hellier, C. Kervrann, C. Barillot, Nonlocal means-based speckle filtering for ultrasound images, IEEE Transactions on Image Processing, 18 (2009) 2221-2229.

[56] M.S. Rana, K. Sarker, T. Bhuiyan, M.M. Hassan, Comparing the performance of different ultrasonic images enhancement for speckle noise reduction in ultrasound images using techniques: A preference study, Proceedings from the Second International Workshop on Pattern Recognition, SPIE, Singapore, Singapore, 2017, pp. 7.

[57] T. Xia, W. Qi, X. Niu, E. Asma, M. Winkler, W. Wang, Quantitative comparison of anisotropic diffusion, non-local means and gaussian post-filtering effects on FDG-PET lesions, Journal of Nuclear Medicine, 56 (2015).

[58] T. Powers, T. Brownyard, Studies of the physical properties of hardened portland cement paste (Bulletin 22), Portland Cement Association, Chicago, IL, 1948.

[59] M. Balonis, F.P. Glasser, The density of cement phases, Cement and Concrete Research, 39 (2009) 733-739.

[60] A.P. Sheppard, R.M. Sok, H. Averdunk, Techniques for image enhancement and segmentation of tomographic images of porous materials, Physica A: Statistical Mechanics and its Applications, 339 (2004) 145-151.

# 6. Conclusions

X-ray CT is a powerful analytical technique that can be used to extract 3D, quantifiable information non-destructively. One of the primary challenges of using x-ray CT in cementitious materials was researched through an investigation on methods to resolve low contrast amongst the four main hydration products. The work presented in this dissertation provided new data on methods to determine threshold values in an unbiased manner based through deconstruction of the histogram in binary and quaternary mixtures, methods to incorporate contrast agents into the crystalline structure of specific hydration products, and a study to assess global and local segmentation algorithms to quantify hydration products in cementitious systems. Key findings and recommended future work are summarized in sections 6.1 and 6.2, respectively.

## 6.1. Key findings

The key findings from this work are listed below:

- Synthesized AFt, AFm, C-S-H, and CH exhibited different greyscale values in reconstructed image volumes generated from synchrotron x-ray CT, affirming the potential to quantify individual hydration products.
- A global segmentation method to determine threshold values in an unbiased manner using a histogram of greyscale values was developed. Initial information on the expected greyscale value of each phase needs to be measured, or calculated based on an expected linear attenuation coefficient. Each phase was proportioned to a known amount and a Gaussian probability density function was applied to each phase. The intersection of adjacent Gaussian curves was then determined automatically.
- Successful segmentation using the developed algorithm was achieved in quantifying individual all binary mixtures of synthesized phases, with the exception of C-S-H and AFm. The use of the algorithm in quaternary mixtures resulted in higher errors during quantification of individual phases when compared to the binary mixtures. However, the method was successful at determining proportions of individual phases in both the binary and quaternary mixtures.

- In general, the developed global segmentation algorithm is less computationally intense than the assessed local segmentation algorithms, watershed and MRF. A summary of the findings of this method include:
    - The Gaussian deconstruction of histogram provided a method to determine threshold values in an unbiased manner. These threshold values could be applied to both watershed and MRF.
    - Initial knowledge of expected greyscale values or LACs needs to be measured. Additionally, the expected LAC can be calculated for phases in the event they cannot be directly measured.
    - However, in quaternary mixtures, the error in quantifying AFm, C-S-H, and CH, were compounded. Typically, quantities of CH was underestimated, while quantities of AFm and C-S-H were overestimated.
    - This developed algorithm was successful in determining proportions of phases in binary and quaternary mixtures.
- Initial investigations using contrast agents to resolve low contrast between C-S-H and AFm resulted in a quick and accurate method to quantify these two phases. Iodine was substituted into the AFm crystalline structure at the $SO_4^{2-}$ lattice site. Confirmation on the substitution was determined using XRD ensuring the crystalline structure was not changed.
- Quantities of the AFm-I phase was determined through image subtraction. This method resulted in quick and accurate assessment of the AFm-I phase.
- Inconsistencies when quantifying C-S-H and CH were presented when using the global segmentation algorithm developed in this dissertation, even when a contrast agent was used to distinguish C-S-H and AFm phases. This resulted in an investigation in using local segmentation algorithms to account for the spatial distribution of greyscale values.
- The use of local segmentation algorithms generally improved the ability to quantify phases. The watershed algorithm reduced the errors from over 200% in quantifying AFm to below 50% in quaternary mixtures. The MRF and watershed algorithms more accurately quantified phases in the quaternary mixtures. Better refinement in determining quantities of CH was observed in the MRF algorithm.
    - Many additional global and local segmentation algorithms exist, and a further investigation into these should be done in order to determine methods to resolve

these low contrast issues. Several algorithms may need to be run on the same data set to accurately quantify all phases present.

## 6.2. Future work

The following list is of recommendations for future work to build upon what was learned through the work presented in this dissertation:

- Further investigation on synthesized hydration products with various stoichiometry for C-S-H and other crystalline AFm and AFt phases, such as Friedel's salt, is necessary to account for the inherent variability of the hydration products found in portland cement. This variability is typically due to the service environment.
- A parametric study should be completed to determine optimal scanning energies to achieve high-contrast with good signal-to-noise.
- Determination of greyscale values and linear attenuation coefficients of unhydrated phases, $C_3S$, $C_2S$, $C_3A$, and $C_4AF$, need to be done. Once completed, x-ray CT scans for combinations of unhydrated and hydrated phases can begin to lay the ground work for monitoring changes to phases during hydration.
- A study on deterioration mechanisms of hydration products should be done. Examples include sulfate attack, thermal decomposition, and alkali-silica reaction. These deterioration mechanisms can be monitored using fast tomography, which is presented with preliminary work in Appendix A.
- A more robust study on determining potential contrast agents to use for isolating individual phases in x-ray CT should be done. A preliminary investigation into contrast agents for AFt and C-S-H are presented in Appendix A. Several contrast agents for each synthesized phase should be studied for use in both synchrotron and lab based x-ray CT systems.
- Once selected contrast agents are determined, further experimental work should be done to target specific phases in a hydrating portland cement system. The effects on hydration, setting time, strength, and durability should also be investigated.
- A more thorough study on resolving low contrast with segmentation algorithms would likely further improvements for quantifying phases. The use of local segmentation algorithms generally reduced the error in quantification. Algorithms such as watershed,

rely on well-defined edges, worked well in mixtures with high contrast. However, there was difficulty distinguishing edges in phases with low contrast, such as AFm and C-S-H.

# 7. References

This section provides a compiled list of all of the cited references used throughout this dissertation, in alphabetical order.

J. Adrien, S. Meille, S. Tadier, E. Maire, L. Sasaki, In-situ x-ray tomographic monitoring of gypsum plaster setting, Cement and Concrete Research, 82 (2016) 107-116.

L. Aimoz, D.A. Kulik, E. Wieland, E. Curti, B. Lothenbach, U. Mäder, Thermodynamics of AFm-($I_2$, $SO_4$) solid solution and of its end-members in aqueous media, Applied Geochemistry, 27 (2012) 2117-2129.

L. Aimoz, E. Wieland, C. Taviot-Guého, R. Dähn, M. Vespa, S.V. Churakov, Structural insight into iodide uptake by AFm phases, Environmental Science & Technology, 46 (2012) 3874-3881.

R. Alizadeh, J.J. Beaudoin, L. Raki, Mechanical properties of calcium silicate hydrates, Materials and Structures, 44 (2011) 13-28.

R. Alizadeh, J.J. Beaudoin, L. Raki, V. Terskikh, C-S-H/polyaniline nanocomposites prepared by in situ polymerization, Journal of Materials Science, 46 (2011) 460-467.

R. Allman, Refinement of the hybrid layer structure $[Ca_2Al(OH)_6]^{+}\cdot[1/2SO_4\cdot 3H_2O]^{-}$, Neues Jahrbuch für Mineralogie Monatsheft, (1977) 136-144.

S.M. Antao, M.J. Duane, I. Hassan, DTA, TG, and RD studies of sturmanite and ettringite, The Canadian Mineralogist, 40 (2002) 1403-1409.

D. Asahina, E.N. Landis, J.E. Bolander, Modeling of phase interfaces during pre-critical crack growth in concrete, Cement and Concrete Composites, 33 (2011) 966-977.

M. Atkins, F.P. Glasser, L.P. Moroni, J.J. Jack, Thermodynamic modeling of blended cements at elevated temperatures (50-90C), 1993.

G.L. Balázs, O. Czoboly, É. Lublóy, K. Kapitány, Á. Barsi, Observation of steel fibres in concrete with computed tomography, Construction and Building Materials, 140 (2017) 534-541.

M. Balonis, F.P. Glasser, The density of cement phases, Cement and Concrete Research, 39 (2009) 733-739.

F. Batool, V. Bindiganavile, Air-void size distribution of cement based foam and its effect on thermal conductivity, Construction and Building Materials, 149 (2017) 17-28.

J.J. Beaudoin, R. Alizadeh, Detection of nanostructural anomalies in hydrated cement systems, Cement Concrete Comp, 29 (2007) 63-69.

J.J. Beaudoin, H. Drame, L. Raki, R. Alizadeh, Formation and characterization of calcium silicate hydrate-hexadecyltrimethylammonium nanostructure, Journal of Materials Research, 23 (2008) 2804-2815.

J.J. Beaudoin, H. Drame, L. Raki, R. Alizadeh, Formation and properties of C-S-H-PEG nano-structures, Materials and Structures, 42 (2009) 1003-1014.

J.J. Beaudoin, H. Dramé, L. Raki, R. Alizadeh, Formation and characterization of calcium silicate hydrate-hexadecyltrimethylammonium nanostructure, Journal of Materials Research, 23 (2008) 2804-2815.

J.J. Beaudoin, B. Patarachao, L. Raki, R. Alizadeh, The interaction of methylene blue dye with calcium–silicate–hydrate, Journal of the American Ceramic Society, 92 (2009) 204-208.

J. Bensted, V. Prakash, Studies of ettringite and its derivatives, part I, Cement Technology, 2 (1971) 73-76.

J. Bensted, S.P. Varma, Sulfoaluminate phase, Klei Keram, 23 (1973) 161-163.

M. Berthod, Z. Kato, S. Yu, J. Zerubia, Bayesian image classification using Markov random fields, Image and Vision Computing, 14 (1996) 285-295.

S. Beucher, C. Lantuejol, Use of watersheds in contour detection, International Workshop Image Processing, Real-Time Edge and Motion Detection/Estimation, CCETT, Rennes, France, 1979.

U.A. Birnin-Yauri, F.P. Glasser, Friedel's salt, $Ca_2Al(OH)_6(Cl,OH)\cdot 2H_2O$: Its solid solutions and their role in chloride binding, Cement and Concrete Research, 28 (1998) 1713-1723.

D. Bonen, S.L. Sarkar, The present state-of-the-art of immobilization of hazardous heavy metals in cement-based materials, in: M.W.G.a.S. L.Sarkar (Ed.) Advances in Cement and Concrete, Proceedings of an Engineering Foundation Conference, American Society of Civil Engineers, New York, 1994, pp. 481-498.

A.C. Bordelon, J.R. Roesler, Spatial distribution of synthetic fibers in concrete with x-ray computed tomography, Cement and Concrete Composites, 53 (2014) 35-43.

N. Bossa, P. Chaurand, J. Vicente, D. Borschneck, C. Levard, O. Aguerre-Chariol, J. Rose, Micro- and nano-x-ray computed-tomography: A step forward in the characterization of the pore network of a leached cement paste, Cement and Concrete Research, 67 (2015) 138-147.

M.E. Brown, Introduction to thermal analysis, Chapman and Hall, UK, 1988.

A. Buades, B. Coll, J.M. Morel, A non-local algorithm for image denoising, 2005 IEEE Computer Society Conference on Computer Vision and Pattern Recognition (CVPR'05), 2005, pp. 60-65

N. Burlion, D. Bernard, D. Chen, X-ray microtomography: Application to microstructure analysis of a cementitious material during leaching process, Cement and Concrete Research, 36 (2006) 346-357.

J. Canny, A computational approach to edge detection, IEEE Transactions on Pattern Analysis and Machine Intelligence, PAMI-8 (1986) 679-698.

F.K. Cartledge, L.G. Butler, D. Chalasani, H.C. Eaton, F.P. Frey, E. Herrera, M.E. Tittlebaum, S.L. Yang, Immobilization mechanisms in solidification/stabilization of Cd and Pb salts using portland cement fixing agents, Environmental Science and Technology, 24 (1990) 867-873.

R. Cepuritis, B.J. Wigum, E.J. Garboczi, E. Mørtsell, S. Jacobsen, Filler from crushed aggregate for concrete: Pore structure, specific surface, particle shape and size distribution, Cement and Concrete Composites, 54 (2014) 2-16.

J.-B. Champenois, A. Mesbah, C. Cau Dit Coumes, G. Renaudin, F. Leroux, C. Mercier, B. Revel, D. Damidot, Crystal structures of Boro-AFm and sBoro-AFt phases, Cement and Concrete Research, 42 (2012) 1362-1370.

I. Chen, M.G. Juenger, Synthesis and hydration of calcium sulfoaluminate-belite cements with varied phase compositions, Journal of Materials Science, 46 (2011) 2568-2577.

T.J. Chotard, M.P. Boncoeur-Martel, A. Smith, J.P. Dupuy, C. Gault, Application of x-ray computed tomography to characterise the early hydration of calcium aluminate cement, Cement and Concrete Composites, 25 (2003) 145-152.

M. Chrysochoou, D. Dermatas, Evaluation of ettringite and hydrocalumite formation for heavy metal immobilization: Literature review and experimental study, Journal of Hazardous Materials, 136 (2006) 20-33.

T.D. Ciach, J.E. Gillott, E.G. Swenson, P.J. Sereda, Microstructure of calcium silicate hydrates, Cement and Concrete Research, 1 (1971) 13-25.

V. Cnudde, M.N. Boone, High-resolution X-ray computed tomography in geosciences: A review of the current technology and applications, Earth-Science Reviews, 123 (2013) 1-17.

D.L. Cocke, M.Y. Mollah, The chemistry and leaching mechanism of hazardous substances in cementitious solidification/stabilization systems, Chemistry and Microstructure of Solidified Waste Forms, (1993) 187-242.

X. Cong, R.J. Kirkpatrick, $^{29}$Si MAS NMR study of the structure of calcium silicate hydrate, Advanced Cement Based Materials, 3 (1996) 144-156.

P. Coupé, P. Hellier, C. Kervrann, C. Barillot, Nonlocal means-based speckle filtering for ultrasound images, IEEE Transactions on Image Processing, 18 (2009) 2221-2229.

L.J. Csetenyi, Stability of borate-containing wastes encapsulated in cement, University of Aberdeen, Abereen, UK, 1993, pp. 170.

A. Cuesta, A.G. De la Torre, I. Santacruz, P. Trtik, J.C. da Silva, A. Diaz, M. Holler, M.A.G. Aranda, Chemistry and mass density of aluminum hydroxide gel in eco-Cements by ptychographic x-ray computed tomography, The Journal of Physical Chemistry C, 121 (2017) 3044-3054.

K.A. Culligan, D. Wildenschild, B.S.B. Christensen, W.G. Gray, M.L. Rivers, Pore-scale characteristics of multiphase flow in porous media: A comparison of air–water and oil–water experiments, Advances in Water Resources, 29 (2006) 227-238.

J.C. da Silva, P. Trtik, A. Diaz, M. Holler, M. Guizar-Sicairos, J. Raabe, O. Bunk, A. Menzel, Mass density and water content of saturated never-dried calcium silicate hydrates, Langmuir, 31 (2015) 3779-3783.

S. Das, P. Yang, S.S. Singh, J.C.E. Mertens, X. Xiao, N. Chawla, N. Neithalath, Effective properties of a fly ash geopolymer: Synergistic application of x-ray synchrotron tomography, nanoindentation, and homogenization models, Cement and Concrete Research, 78 (2015) 252-262.

Y. Davit, G. Iltis, G. Debenest, S. Veran-Tissoires, D. Wildenschild, M. Gerino, M. Quintard, Imaging biofilm in porous media using x-ray computed microtomography, Journal of Microscopy, 242 (2011) 15-25.

S.C. de Wolski, J.E. Bolander, E.N. Landis, An in-situ x-ray microtomography study of split cylinder fracture in cement-based materials, Experimental Mechanics, 54 (2014) 1227-1235.

T. Deboodt, J.H. Ideker, O.B. Isgor, D. Wildenschild, Quantification of synthesized hydration products using synchrotron microtomography and spectral analysis, Construction and Building Materials, 157 (2017) 476-488.

T. Deboodt, D. Wildenschild, J.H. Ideker, O.B. Isgor, Use of iodine for improving phase quantification using x-ray tomography, Submitted to Cement and Concrete Research, (2018).

J. Deja, Immobilization of $Cr^{6+}$, $Cd^{2+}$, $Zn^{2+}$ and $Pb^{2+}$ in alkali-activated slag binders, Cement and Concrete Research, 32 (2002) 1971-1979.

R. Deriche, Using Canny's criteria to derive a recursively implemented optimal edge detector, International Journal of Computer Vision, 1 (1987) 167-187.

D. Derome, M. Griffa, M. Koebel, J. Carmeliet, Hysteretic swelling of wood at cellular scale probed by phase-contrast x-ray tomography, Journal of Structural Biology, 173 (2011) 180-190.

J. Dewanckele, T. De Kock, G. Fronteau, H. Derluyn, P. Vontobel, M. Dierick, L. Van Hoorebeke, P. Jacobs, V. Cnudde, Neutron radiography and x-ray computed tomography for quantifying weathering and water uptake processes inside porous limestone used as building material, Materials Characterization, 88 (2014) 86-99.

S. Diamond, E. Landis, Microstructural features of a mortar as seen by computed microtomography, Mater Struct, 40 (2007) 989-993.

A. Diaz, P. Trtik, M. Guizar-Sicairos, A. Menzel, P. Thibault, O. Bunk, Quantitative x-ray phase nanotomography, Physical Review B, 85 (2012) 020104.

M. Dierolf, A. Menzel, P. Thibault, P. Schneider, C.M. Kewish, R. Wepf, O. Bunk, F. Pfeiffer, Ptychographic x-ray computed tomography at the nanoscale, Nature, 467 (2010) 436.

B. Dong, G. Fang, Y. Liu, P. Dong, J. Zhang, F. Xing, S. Hong, Monitoring reinforcement corrosion and corrosion-induced cracking by x-ray microcomputed tomography method, Cement and Concrete Research, 100 (2017) 311-321.

P. Duxson, A. Fernández-Jiménez, J.L. Provis, G.C. Lukey, A. Palomo, J.S.J. van Deventer, Geopolymer technology: The current state of the art, Journal of Materials Science, 42 (2007) 2917-2933.

H. Elaqra, N. Godin, G. Peix, M. R'Mili, G. Fantozzi, Damage evolution analysis in mortar, during compressive loading using acoustic emission and x-ray tomography: Effects of the sand/cement ratio, Cement and Concrete Research, 37 (2007) 703-713.

T.R. Elliot, R.J. Heck, A comparison of 2D vs. 3D thresholding of x-ray CT imagery, Canadian Journal of Soil Science, 87 (2007) 405-412.

S. Erdem, X-ray computed tomography and fractal analysis for the evaluation of segregation resistance, strength response and accelerated corrosion behaviour of self-compacting lightweight concrete, Construction and Building Materials, 61 (2014) 10-17.

S.T. Erdogan, P.N. Quiroga, D.W. Fowler, H.A. Saleh, R.A. Livingston, E.J. Garboczi, P.M. Ketcham, J.G. Hagedorn, S.G. Satterfield, Three-dimensional shape analysis of coarse aggregates: New techniques for and preliminary results on several different coarse aggregates and reference rocks, Cement and Concrete Research, 36 (2006) 1619-1627.

R.F. Feldman, P.J. Sereda, A model for hydrated portland cement paste as deduced from sorption-length change and mechanical properties, Matériaux et Construction, 1 (1968) 509-520.

R. Fischer, H.J. Kuzel, Reinvestigation of the system $C_4A.nH_2O \cdot C_4A.CO_2 \cdot nH_2O$, Cement and Concrete Research, 12 (1982) 517-526.

B.P. Flannery, H.W. Deckman, W.G. Roberge, K.L. D'Amico, Three-dimensional x-ray microtomography, Science, 237 (1987) 1439-1444.

M. Francois, G. Renaudin, O. Evrard, A Cementitious Compound with Composition $3CaO \cdot Al_2O_3 \cdot CaCO_3 \cdot 11H_2O$, Acta Crystallographica Section C, 54 (1998) 1214-1217.

D. Fukuda, Y. Nara, Y. Kobayashi, M. Maruyama, M. Koketsu, D. Hayashi, H. Ogawa, K. Kaneko, Investigation of self-sealing in high-strength and ultra-low-permeability concrete in water using micro-focus x-ray CT, Cement and Concrete Research, 42 (2012) 1494-1500.

E. Gallucci, K. Scrivener, A. Groso, M. Stampanoni, G. Margaritondo, 3D experimental investigation of the microstructure of cement pastes using synchrotron x-ray microtomography (μCT), Cement and Concrete Research, 37 (2007) 360-368.

E.J. Garboczi, Three-dimensional mathematical analysis of particle shape using x-ray tomography and spherical harmonics: Application to aggregates used in concrete, Cement and Concrete Research, 32 (2002) 1621-1638.

E. Gartner, Are there any practical alternatives to the manufacture of portland cement clinker?, Journal of the Chinese Ceramic Society, 40 (2012) 61-68.

D. Gastaldi, F. Canonico, L. Capelli, E. Boccaleri, M. Milanesio, L. Palin, G. Croce, F. Marone, K. Mader, M. Stampanoni, In situ tomographic investigation on the early hydration behaviors of cementing systems, Construction and Building Materials, 29 (2012) 284-290.

F.P. Glasser, Chemistry of cement solidified waste forms, in: R.D. Spence (Ed.) Chemistry and Microstructre of Solidified Waste Forms, 1993, pp. 1-39.

F.P. Glasser, A. Kindness, S.A. Stronach, Stability and solubility relationships in AFm phases: Part I. Chloride, sulfate and hydroxide, Cement and Concrete Research, 29 (1999) 861-866.

F. Goetz-Neunhoeffer, J. Neubauer, P. Schwesig, Mineralogical characteristics of ettringites synthesized from solutions and suspensions, Cement and Concrete Research, 36 (2006) 65-70.

K.-H. Goh, T.-T. Lim, Z. Dong, Application of layered double hydroxides for removal of oxyanions: A review, Water Research, 42 (2008) 1343-1368.

C. Gosselin, E. Gallucci, K. Scrivener, Influence of self heating and $Li_2SO_4$ addition on the microstructural development of calcium aluminate cement, Cement and Concrete Research, 40 (2010) 1555-1570.

M.L.D. Gougar, B.E. Scheetz, D.M. Roy, Ettringite and C-S-H portland cement phases for waste ion immobilization: A review, Waste Management, 16 (1996) 295-303.

G.W. Groves, TEM Studies of Cement Hydration, MRS Online Proceedings Library, 85 (1986) 3-12.

GSECARS Tomography Processing Software, 2014, http://cars9.uchicago.edu/software/idl/tomography.html.

J. Han, W. Sun, G. Pan, C. Wang, H. Rong, Application of x-ray computed tomography in characterization microstructure changes of cement pastes in carbonation process, Journal of Wuhan University of Technology-Materals Science Edition, 27 (2012) 358-363.

D.J. Hassett, G.J. McCarthy, P. Kumarathasan, D. Pflughoeft-Hassett, Synthesis and characterization of selenate and sulfate-selenate ettringite structure phases, Materials Research Bulletin, 25 (1990) 1347-1354.

D.J. Hassett, D.F. Pflughoeft-Hassett, P. Kumarathasan, G.J. Mcarthy, Ettringite as agent for the fixation of hazardous oxyanions, Proceedings of the Twelfth Annual Madison Waste Conference, University of Wisconsin-Madison, 1989.

D. Hernández-Cruz, C.W. Hargis, J. Dominowski, M.J. Radler, P.J.M. Monteiro, Fiber reinforced mortar affected by alkali-silica reaction: A study by synchrotron microtomography, Cement and Concrete Composites, 68 (2016) 123-130.

P. Hewlett, Lea's Chemistry of Cement and Concrete, 4th ed. ed., Burlington : Elsevier Science, Burlington, 2003.

E.J. Hoffman, S.-C. Huang, M.E. Phelps, Quantitation in positron emission computed tomography: 1. Effect of object size, Journal of Computer Assisted Tomography, 3 (1979) 299-308.

Q. Hu, M.T. Ley, J. Davis, J.C. Hanan, R. Frazier, Y. Zhang, 3D chemical segmentation of fly ash particles with x-ray computed tomography and electron probe microanalysis, Fuel, 116 (2014) 229-236.

P. Iassonov, T. Gebrenegus, M. Tuller, Segmentation of x-ray computed tomography images of porous materials: A crucial step for characterization and quantitative analysis of pore structures, Water Resources Research, 45 (2009).

J.H. Ideker, C.G. Gosselin, R. Barborak, An alternative repair material: Basics and practical testing of calcium aluminate cements, Concrete International, 35 (2013) 33-37.

G.C. Iltis, R.T. Armstrong, D.P. Jansik, B.D. Wood, D. Wildenschild, Imaging biofilm architecture within porous media using synchrotron-based x-ray computed microtomography, Water Resources Research, 47 (2011).

H.M. Jennings, B.J. Dalgleish, P.L. Pratt, Morphological development of hydrating tricalcium silicate as examined by electron microscopy techniques, Journal of the American Ceramic Society, 64 (1981) 567-572.

M.C.G. Juenger, F. Winnefeld, J.L. Provis, J.H. Ideker, Advances in alternative cementitious binders, Cement and Concrete Research, 41 (2011) 1232-1243.

R.A. Ketcham, W.D. Carlson, Acquisition, optimization and interpretation of x-ray computed tomographic imagery: Applications to the geosciences, Computers & Geosciences, 27 (2001) 381-400.

M. Khanzadeh Moradllo, M.T. Ley, Quantitative measurement of the influence of degree of saturation on ion penetration in cement paste by using x-ray imaging, Construction and Building Materials, 141 (2017) 113-129.

R. Khoshnazar, L. Raki, J. Beaudoin, R. Alizadeh, Solvent exchange in sulfoaluminate phases. Part II: Monosulfate, Advances in Cement Research, 25 (2013) 322-331.

R. Khoshnazar, L. Raki, J. Beaudoin, R. Alizadeh, Solvent exchange in sulphoaluminate phases. Part I: Ettringite, Advances in Cement Research, 25 (2013) 314-321.

K.Y. Kim, T.S. Yun, K.P. Park, Evaluation of pore structures and cracking in cement paste exposed to elevated temperatures by x-ray computed tomography, Cement and Concrete Research, 50 (2013) 34-40.

J.H. Kinney, M.C. Nichols, X-ray tomographic microscopy (XTM) using synchrotron radiation, Annual Review of Materials Science, 22 (1992) 121-152.

K.O. Kjellsen, A. Monsøy, K. Isachsen, R.J. Detwiler, Preparation of flat-polished specimens for SEM-backscattered electron imaging and x-ray microanalysis-Importance of epoxy impregnation, Cement and Concrete Research, 33 (2003) 611-616.

W. Klemm, J.I. Bhatty, Fixation of heavy metals as oxyanion-substituted ettringites, in: P.C.A. R&D (Ed.)Serial No. 2431a, 2002.

R. Kulkarni, M. Tuller, W. Fink, D. Wildenschild, Three-dimensional multiphase segmentation of x-ray CT data of porous materials using a Bayesian Markov random filed framework, Vadose Zone Journal, 11 (2012) 74-85.

P. Kumarathasan, G.J. McCarthy, D.J. Hassett, D.F. Pflughoeft-Hassett, Oxyanion substituted ettringites: Synthesis and characterization; and their potential role in immobilization of As, B, Cr, Se and V, MRS Online Proceedings Library, 178 (1989) 83-104.

H.J. Kuzel, Synthesis and x-ray study of the crystalline composition $3CaO{\cdot}Al_2O_3{\cdot}\ CaSO_4{\cdot}12H_2O$, Neues Jahrbuch Mineral Monatsh, 7 (1965) 193-197.

T. Kwon, G.A. Tsigdinos, T.J. Pinnavaia, Pillaring of layered double hydroxides (LDH's) by polyoxometalate anions, Journal of the American Chemical Society, 110 (1988) 3653-3654.

E.N. Landis, D.T. Keane, X-ray microtomography for fracture studies in cement-based materials, Proceedings of SPIE 3772: Developments in x-ray tomography II, 1999, pp. 105-113.

E.N. Landis, D.T. Keane, X-ray microtomography, Materials Characterization, 61 (2010) 1305-1316.

E.N. Landis, E.N. Nagy, D.T. Keane, Microstructure and fracture in three dimensions, Engineering Fracture Mechanics, 70 (2003) 911-925.

D.A. Lange, Y. Jia, Y.S. Liu, X-Ray nanotomography of cement microstructure, American Concrete Institute SP 270, (2010) 9-16.

M. Lanzón, V. Cnudde, T. de Kock, J. Dewanckele, X-ray microtomography (μ-CT) to evaluate microstructure of mortars containing low density additions, Cement and Concrete Composites, 34 (2012) 993-1000.

J.S. Lawler, D.T. Keane, S.P. Shah, Measuring three-dimensional damage of mortar in compression with x-ray microtomography and digital image correlation, American Concrete Institute SP 189, (2000) 187-202.

M.A. Le Gros, G. McDermott, C.A. Larabell, X-ray tomography of whole cells, Current Opinion in Structural Biology, 15 (2005) 593-600.

Lea's Chemistry of Cement and Concrete, Elsevier - Butterworth-Heinemann, Oxford, UK, 1998.

M.B. Leite, P.J.M. Monteiro, Microstructural analysis of recycled concrete using x-ray microtomography, Cement and Concrete Research, 81 (2016) 38-48.

N. Limodin, L. Salvo, E. Boller, M. Suéry, M. Felberbaum, S. Gailliègue, K. Madi, In situ and real-time 3-D microtomography investigation of dendritic solidification in an Al–10 wt.% Cu alloy, Acta Materialia, 57 (2009) 2300-2310.

L.O. Lindgren, Medical CAT-scanning: X-ray absorption coefficients, CT-numbers and their relation to wood density, Wood Science and Technology, 25 (1991) 341-349.

S. Lu, E.N. Landis, D.T. Keane, X-ray microtomographic studies of pore structure and permeability in portland cement concrete, Mater Struct, 39 (2006) 611-620.

H. Lusic, M.W. Grinstaff, X-ray-computed tomography contrast agents, Chemical Reviews, 113 (2012) 1641-1666.

H.E. Martz, D.J. Scheberk, G. Patrick Roberson, P.J.M. Montiero, Computerized tomography analysis of reinforced concrete, ACI Materials Journal, 90 (1993) 259-264.

T. Matschei, B. Lothenbach, F.P. Glasser, The AFm phase in portland cement, Cement and Concrete Research, 37 (2007) 118-130.

G.J. McCarthy, D.J. Hassett, J.A. Bender, Synthesis, Crystal chemistry and stability of ettringite, A material with potential applications in hazardous waste immobilization, MRS Online Proceedings Library, 245 (1991) 129-140.

P.K. Mehta, P.J.M. Monteiro, Concrete: Microstructure, properties and materials, Third ed., New York, 2006.

A. Mesbah, C. Cau-dit-Coumes, F. Frizon, F. Leroux, J. Ravaux, G. Renaudin, A new investigation of the $Cl^{-}$–$CO_3^{2-}$ substitution in AFm Phases, Journal of the American Ceramic Society, 94 (2011) 1901-1910.

A. Mesbah, C. Cau-dit-Coumes, G. Renaudin, F. Frizon, F. Leroux, Uptake of chloride and carbonate ions by calcium monosulfoaluminate hydrate, Cement and Concrete Research, 42 (2012) 1157-1165.

A. Mesbah, M. François, C. Cau-dit-Coumes, F. Frizon, Y. Filinchuk, F. Leroux, J. Ravaux, G. Renaudin, Crystal structure of Kuzel's salt $3CaO{\cdot}Al_2O_3{\cdot}1/2CaSO_4{\cdot}1/2CaCl_2{\cdot}11H_2O$ determined by synchrotron powder diffraction, Cement and Concrete Research, 41 (2011) 504-509.

A. Mesbah, J.-P. Rapin, M. François, C. Cau-dit-Coumes, F. Frizon, F. Leroux, G. Renaudin, Crystal structures and phase transition of cementitious bi-anionic AFm-($Cl^{-}$, $CO_3^{2-}$) compounds, Journal of the American Ceramic Society, 94 (2011) 261-268.

A. Michel, B.J. Pease, M.R. Geiker, H. Stang, J.F. Olesen, Monitoring reinforcement corrosion and corrosion-induced cracking using non-destructive x-ray attenuation measurements, Cement and Concrete Research, 41 (2011) 1085-1094.

S. Miyata, Anion-exchange properties of hydrotalcite-like compounds, Clays and Clay Minerals, 31 (1983) 305-311.

P.J.M. Monteiro, A.P. Kirchheim, S. Chae, P. Fischer, A.A. MacDowell, E. Schaible, H.R. Wenk, Characterizing the nano and micro structure of concrete to improve its durability, Cement and Concrete Composites, 31 (2009) 577-584.

A.E. Moore, H.F.W. Taylor, Crystal structure of ettringite, Acta Crystallographica Section B, 26 (1970) 386-393.

J. Moussouris, Gibbs and Markov random systems with constraints, Journal of Statistical Physics, 10 (1974) 11-33.

N.N. Naik, A.C. Jupe, S.R. Stock, A.P. Wilkinson, P.L. Lee, K.E. Kurtis, Sulfate attack monitored by microCT and EDXRD: Influence of cement type, water-to-cement ratio, and aggregate, Cement and Concrete Research, 36 (2006) 144-159.

N.N. Naik, K.E. Kurtis, A.P. Wilkinson, A.C. Jupe, S.R. Stock, Sulfate deterioration of cement-based materials examined by x-ray microtomography, Proceedings of SPIE 5535, 2004, pp. 442-452.

A.M. Neville, Properties of concrete, 4th Edition ed., John Wiley & Sons, Inc., New York, NY, 1996.

W. Oh, W.B. Lindquist, Image thresholding by indicator kriging, IEEE Transactions on Pattern Analysis and Machine Intelligence, 21 (1999) 590-602.

N.R. Pal, S.K. Pal, A review on image segmentation techniques, Pattern Recognition, 26 (1993) 1277-1294.

H. Poellmann, S. Auer, H.J. Kuzel, R. Wenda, Solid solution of ettringites: Part II: Incorporation of $B(OH)_4^-$ and $CrO_4^{2-}$ in $3CaO{\cdot}Al_2O_3{\cdot}3CaSO_4{\cdot}32H_2O$, Cement and Concrete Research, 23 (1993) 422-430.

H. Poellmann, H.J. Kuzel, R. Wenda, Solid solution of ettringites: Part I: Incorporation of $OH^-$ and $CO_3^{2-}$ in $3CaO{\cdot}Al_2O_3{\cdot}32H_2O$, Cement and Concrete Research, 20 (1990) 941-947.

T. Powers, T. Brownyard, Studies of the physical properties of hardened portland cement paste (Bulletin 22), Portland Cement Association, Chicago, IL, 1948.

M.A.B. Promentilla, T. Sugiyama, T. Hitomi, N. Takeda, Characterizing the 3D pore structure of hardened cement paste with synchrotron microtomography, Journal of Advanced Concrete Technology, 6 (2008) 273-286.

M.A.B. Promentilla, T. Sugiyama, T. Hitomi, N. Takeda, Quantification of tortuosity in hardened cement pastes using synchrotron-based x-ray computed microtomography, Cement and Concrete Research, 39 (2009) 548-557.

J.L. Provis, A. Hajimohammadi, C.E. White, S.A. Bernal, R.J. Myers, R.P. Winarski, V. Rose, T.E. Proffen, A. Llobet, J.S.J. van Deventer, Nanostructural characterization of geopolymers by advanced beamline techniques, Cement and Concrete Composites, 36 (2013) 56-64.

J.L. Provis, R.J. Myers, C.E. White, V. Rose, J.S.J. van Deventer, X-ray microtomography shows pore structure and tortuosity in alkali-activated binders, Cement and Concrete Research, 42 (2012) 855-864.

A. Qsymah, R. Sharma, Z. Yang, L. Margetts, P. Mummery, Micro X-ray computed tomography image-based two-scale homogenisation of ultra high performance fibre reinforced concrete, Construction and Building Materials, 130 (2017) 230-240.

A. Radlińska, J. Yost, M. Salera, Material properties of structurally viable alkali-activated fly ash concrete, Journal of Materials in Civil Engineering, 25 (2013) 1456-1464.

L. Raki, J. Beaudoin, R. Alizadeh, J. Makar, T. Sato, Cement and concrete nanoscience and nanotechnology, Materials, 3 (2010) 918-942.

V.S. Ramachandran, J.J. Beaudoin, Handbook of analytical techniques in concrete science and rechnology, William Andrew Publishing, LLC, Norwich, New York.

M.S. Rana, K. Sarker, T. Bhuiyan, M.M. Hassan, Comparing the performance of different ultrasonic images enhancement for speckle noise reduction in ultrasound images using techniques: A preference study, Proceedings from the Second International Workshop on Pattern Recognition, SPIE, Singapore, Singapore, 2017, pp. 7.

J.P. Rapin, G. Renaudin, E. Elkaim, M. Francois, Structural transition of Friedel's salt $3CaO{\cdot}Al_2O_3{\cdot}CaCl_2{\cdot}10H_2O$ studied by synchrotron powder diffraction, Cement and Concrete Research, 32 (2002) 513-519.

J.P. Rapin, A. Walcarius, G. Lefevre, M. Francois, A double-layered hydroxide, $3CaO{\cdot}Al_2O_3{\cdot}CaI_2{\cdot}10H_2O$, Acta Crystallographica Section C, 55 (1999) 1957-1959.

U. Rattanasak, K. Kendall, Pore structure of cement/pozzolan composites by x-ray microtomography, Cement and Concrete Research, 35 (2005) 637-640.

G. Renaudin, M. Francois, The lamellar double-hydroxide (LDH) compound with composition $3CaO{\cdot}Al_2O_3{\cdot}Ca(NO_3)_2{\cdot}10H_2O$, Acta Crystallographica Section C, 55 (1999) 835-838.

G. Renaudin, M. Francois, O. Evrard, Order and disorder in the lamellar hydrated tetracalcium monocarboaluminate compound, Cement and Concrete Research, 29 (1999) 63-69.

G. Renaudin, F. Kubel, J.P. Rivera, M. Francois, Structural phase transition and high temperature phase structure of Friedels salt, $3CaO{\cdot}Al_2O_3{\cdot}CaCl_2{\cdot}10H_2O$, Cement and Concrete Research, 29 (1999) 1937-1942.

G. Renaudin, J.P. Rapin, E. Elkaim, M. François, Polytypes and polymorphs in the related Friedel's salt $[Ca_2Al(OH)_6]^+[X{\cdot}2H_2O]^-$ halide series, Cement and Concrete Research, 34 (2004) 1845-1852.

G. Renaudin, J.P. Rapin, B. Humbert, M. François, Thermal behaviour of the nitrated AFm phase $Ca_4Al_2(OH)_{12}(NO_3)_2{\cdot}4H_2O$ and structure determination of the intermediate hydrate $Ca_4Al_2(OH)_{12}(NO_3)_2{\cdot}2H_2O$, Cement and Concrete Research, 30 (2000) 307-314.

I.G. Richardson, The nature of C-S-H in hardened cements, Cement and Concrete Research, 29 (1999) 1131-1147.

I.G. Richardson, Tobermorite/jennite- and tobermorite/calcium hydroxide-based models for the structure of C-S-H: Applicability to hardened pastes of tricalcium silicate, β-dicalcium silicate, portland cement, and blends of portland cement with blast-furnace slag, metakaolin, or silica fume, Cement and Concrete Research, 34 (2004) 1733-1777.

I.G. Richardson, G.W. Groves, The incorporation of minor and trace elements into calcium silicate hydrate (C-S-H) gel in hardened cement pastes, Cement and Concrete Research, 23 (1993) 131-138.

T. Rougelot, N. Burlion, D. Bernard, F. Skoczylas, About microcracking due to leaching in cementitious composites: X-ray microtomography description and numerical approach, Cement and Concrete Research, 40 (2010) 271-283.

M. Sacerdoti, E. Passaglia, Hydrocalumite from Latium, Italy: Its crystal structure and relationship wih related synthetic phases, Neues Jahrbuch für Mineralogie, 10 (1988) 462-475.

P.K. Sahoo, S. Soltani, A.K.C. Wong, A survey of thresholding techniques, Computer Vision, Graphics, and Image Processing, 41 (1988) 233-260.

L. Salvo, P. Cloetens, E. Maire, S. Zabler, J.J. Blandin, J.Y. Buffière, W. Ludwig, E. Boller, D. Bellet, C. Josserond, X-ray micro-tomography an attractive characterisation technique in materials science, Nuclear Instruments and Methods in Physics Research Section B: Beam Interactions with Materials and Atoms, 200 (2003) 273-286.

F. Sanchez, K. Sobolev, Nanotechnology in concrete – A review, Construction and Building Materials, 24 (2010) 2060-2071.

P.J. Schilling, B.R. Karedla, A.K. Tatiparthi, M.A. Verges, P.D. Herrington, X-ray computed microtomography of internal damage in fiber reinforced polymer matrix composites, Composites Science and Technology, 65 (2005) 2071-2078.

S. Schlüter, A. Sheppard, K. Brown, D. Wildenschild, Image processing of multiphase images obtained via x-ray microtomography: A review, Water Resources Research, 50 (2014) 3615-3639.

S. Schlüter, U. Weller, H.-J. Vogel, Segmentation of x-ray microtomography images of soil using gradient masks, Computers & Geosciences, 36 (2010) 1246-1251.

J. Schock, S. Liebl, K. Achterhold, F. Pfeiffer, Obtaining the spacing factor of microporous concrete using high-resolution dual energy x-ray micro CT, Cement and Concrete Research, 89 (2016) 200-205.

M. Sezgin, B. Sankur, Survey over image thresholding techniques and quantitative performance evaluation, SPIE, 2004, pp. 20.

A.P. Sheppard, R.M. Sok, H. Averdunk, Techniques for image enhancement and segmentation of tomographic images of porous materials, Physica A: Statistical Mechanics and its Applications, 339 (2004) 145-151.

C. Shi, A.F. Jiménez, A. Palomo, New cements for the 21st century: The pursuit of an alternative to portland cement, Cement and Concrete Research, 41 (2011) 750-763.

O.P. Shrivastava, F.P. Glasser, Ion-exchange properties of $Ca_5Si_6O_{18}H_2 \cdot 4H_2O$, Journal of Materials Science Letters, 4 (1985) 1122-1124.

N.N. Skoblinskaya, K.G. Krasilnikov, L.V. Nikitina, V.P. Varlamov, Changes in crystal structure of ettringite on dehydration. 2, Cement and Concrete Research, 5 (1975) 419-431.

S.R. Stock, N.K. Naik, A.P. Wilkinson, K.E. Kurtis, X-ray microtomography (microCT) of the progression of sulfate attack of cement paste, Cement and Concrete Research, 32 (2002) 1673-1675.

L.J. Struble, P.W. Brown, An evaluation of ettringite and related compounds for use in the solar energy storage, US Department of Commerce, 1982, pp. 11.

P.E. Stutzman, J.R. Clifton, Specimen Preparation for Scanning Electron Microscopy, in: L.J.a.A. Nisperos (Ed.) Twenty-First International Conference on Cement Microscopy, Las Vegas, NV, April 25-29, 1999, 1999, pp. 10-22.

T. Sugiyama, M.A.B. Promentilla, T. Hitomi, N. Takeda, Application of synchrotron microtomography for pore structure characterization of deteriorated cementitious materials due to leaching, Cement and Concrete Research, 40 (2010) 1265-1270.

T. Suzuki, H. Ogata, R. Takada, M. Aoki, M. Ohtsu, Use of acoustic emission and x-ray computed tomography for damage evaluation of freeze-thawed concrete, Construction and Building Materials, 24 (2010) 2347-2352.

H.F.W. Taylor, Cement Chemistry, 2nd Edition ed., Thomas Telford Publishing, London, England, 1997.

S. Terzi, L. Salvo, M. Suéry, N. Limodin, J. Adrien, E. Maire, Y. Pannier, M. Bornert, D. Bernard, M. Felberbaum, M. Rappaz, E. Boller, In situ x-ray tomography observation of inhomogeneous deformation in semi-solid aluminium alloys, Scripta Materialia, 61 (2009) 449-452.

A. Terzis, S. Filippakis, H.-J. Kuzel, H. Burzlaff, The crystal structure of $Ca_2Al(OH)_6Cl{\cdot}2H_2O$, Zeitschrift für Kristallographie - Crystalline Materials, 181 (1987) 29.

K. Tosun, B. Baradan, Effect of ettringite morphology on DEF-related expansion, Cement and Concrete Composites, 32 (2010) 271-280.

P. Trtik, A. Diaz, M. Guizar-Sicairos, A. Menzel, O. Bunk, Density mapping of hardened cement paste using ptychographic x-ray computed tomography, Cement and Concrete Composites, 36 (2013) 71-77.

P. Trtik, B. Münch, W.J. Weiss, A. Kaestner, I. Jerjen, L. Josic, E. Lehmann, P. Lura, Release of internal curing water from lightweight aggregates in cement paste investigated by neutron and x-ray tomography, Nuclear Instruments and Methods in Physics Research Section A: Accelerators, Spectrometers, Detectors and Associated Equipment, 651 (2011) 244-249.

M. Vandamme, F.-J. Ulm, P. Fonollosa, Nanogranular packing of C–S–H at substochiometric conditions, Cement and Concrete Research, 40 (2010) 14-26.

L. Vincent, P. Soille, Watersheds in digital spaces: An efficient algorithm based on immersion simulations, IEEE Transactions on Pattern Analysis and Machine Intelligence, 13 (1991) 583-598.

A. Walcarius, G. Lefevre, J.-P. Rapin, G. Renaudin, M. Francois, Voltammetric detection of iodide after accumulation by Friedel's salt, Electroanalysis, 13 (2001) 313-320.

K. Wan, Y. Li, W. Sun, Application of tomography for solid calcium distributions in calcium leaching cement paste, Construction and Building Materials, 36 (2012) 913-917.

K. Wan, Y. Li, W. Sun, Experimental and modelling research of the accelerated calcium leaching of cement paste in ammonium nitrate solution, Construction and Building Materials, 40 (2013) 832-846.

K. Wan, Q. Xu, Y. Wang, G. Pan, 3D spatial distribution of the calcium carbonate caused by carbonation of cement paste, Cement and Concrete Composites, 45 (2014) 255-263.

J. Wang, J. Dewanckele, V. Cnudde, S. Van Vlierberghe, W. Verstraete, N. De Belie, X-ray computed tomography proof of bacterial-based self-healing in concrete, Cement and Concrete Composites, 53 (2014) 289-304.

W. Wang, A.N. Kravchenko, A.J.M. Smucker, M.L. Rivers, Comparison of image segmentation methods in simulated 2D and 3D microtomographic images of soil aggregates, Geoderma, 162 (2011) 231-241.

B.E. Warren, X-ray diffraction, Addison-Wesley Publication Company, Reading, MA, 1969.

W.R. Webb, W.E. Brant, N.M. Major, Fundamentals of body CT, 4th ed., Saunders Elsevier, Philadelphia, PA, 2014.

R. Wenda, H.J. Kuzel, Proceedings of the 8th International Congress on the Chemistry of Cement, Rio de Janeiro, 1983, pp. 37-38.

D. Wildenschild, A.P. Sheppard, X-ray imaging and analysis techniques for quantifying pore-scale structure and processes in subsurface porous medium systems, Advances in Water Resources, 51 (2013) 217-246.

D. Wildenschild, C.M.P. Vaz, M.L. Rivers, D. Rikard, B.S.B. Christensen, Using x-ray computed tomography in hydrology: Systems, resolutions, and limitations, Journal of Hydrology, 267 (2002) 285-297.

R.B. Williamson, Solidification of portland cement, Progress in Materials Science, 15 (1972) 189-286.

T. Xia, W. Qi, X. Niu, E. Asma, M. Winkler, W. Wang, Quantitative comparison of anisotropic diffusion, non-local means and gaussian post-filtering effects on FDG-PET Llesions, Journal of Nuclear Medicine, 56 (2015).

P. Yu, Kirkpatrick, R. J., Poe, B., McMillan, P. F. and Cong, X., Structure of calcium silicate hydrate (C-S-H): Near-, mid-, and far-infrared spectroscopy, Journal of the American Ceramic Society, 82 (1999) 742-748.

T.S. Yun, K.Y. Kim, J. Choo, D.H. Kang, Quantifying the distribution of paste-void spacing of hardened cement paste using x-ray computed tomography, Materials Characterization, 73 (2012) 137-143.

R. Żak, J. Deja, Spectroscopy study of Zn, Cd, Pb and Cr ions immobilization on C–S–H phase, Spectrochimica Acta Part A: Molecular and Biomolecular Spectroscopy, 134 (2015) 614-620.

D. Zhang, Y. Jia, J. Ma, Z. Li, Removal of arsenic from water by Friedel's salt (FS: $3CaO{\cdot}Al_2O_3{\cdot}CaCl_2{\cdot}10H_2O$), Journal of Hazardous Materials, 195 (2011) 398-404.

M. Zhang, Y. He, G. Ye, D.A. Lange, K.v. Breugel, Computational investigation on mass diffusivity in portland cement paste based on x-ray computed microtomography (μCT) image, Construction and Building Materials, 27 (2012) 472-481.

# Appendix A

# A. Appendix A

## A.1. Additional x-ray CT data

This section presents additional x-ray CT data on cementitious systems that was completed at the GeoSoilEnviroCARS (GSECARS) 13-BMD beamline of the Advanced Photon Source at the Argonne National Laboratory. Specifics for each investigation are presented below. The following data in sections A.1.1 and A.1.2 will be worked into a publication in *Concrete International*. Further preliminary work on the use of contrast agents for AFt and C-S-H are presented in section A.1.3.

### A.1.1. Use of x-ray CT for alkali-silica reaction damage investigation

X-ray CT can be used to investigate the damage caused by deterioration mechanisms. In this research, alkali-silica reaction (ASR) was investigated. A 0.42 w/cm cement paste with a reactive opal aggregate was exposed to a 1 N NaOH solution for 7 days at 80 °C. At the end of 7 days, the sample was scanned using the GSECARS 13-BMD beamline at the Advanced Photon Source at the Argonne National Laboratory. The sample was 3.14 mm in diameter, and scanned at 33.269 keV. The resultant image volume had a resolution of 2.60 μm/voxel. A slice of the reconstructed image volume of an undamaged aggregate and a cement paste exposed to 1 N NaOH solution for 7 days at 80 °C is seen in Figure A-1.

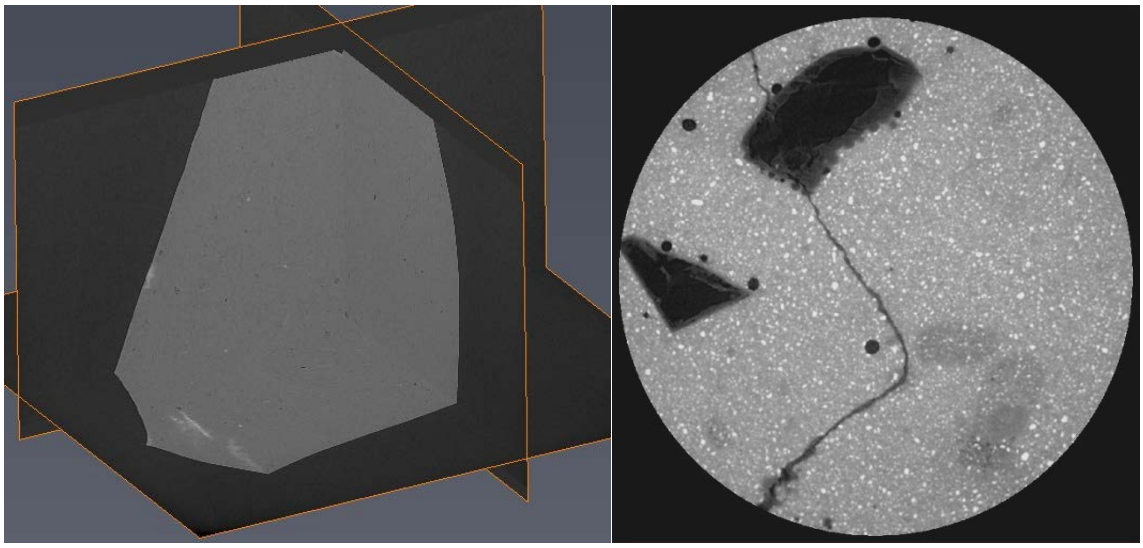

Figure A-1: Reconstructed image slice. Left) shows a 3D series of image slices of an undamaged opal aggregate. Right) shows an orthographic slice of the damaged cement paste. Clear signs of cracking through the cement paste and damage in the aggregate were observed.

### A.1.2. Use of 'pink-beam' fast tomography

The use of a synchrotron source for x-ray CT typically results in decreased scan times compared to a polychromatic, lab-based system due to the increase in the flux of the x-ray source. However, when using a monochromator to specify a scan energy, much of the total energy of the beam is not filtered out, typically only 0.1% of the energy is transmitted to the sample. Recent developments using pink beam at synchrotron facilities has allowed for a major reduction in scan times. Instead of filtering much of the beam energy through a monochromator, the beam passes through a grazing incidence mirror. The grazing incidence mirror removes some of the higher energy levels of the beam. The energy intensity which is removed is dependent on the mirror coating and angle of the mirror. Further filtering of the beam energy can be achieved with x-ray absorbing filters to remove some of the low energy levels. The resultant beam is tunable to specific energies and has more than 1000 times the x-ray flux than the monochromatic beam tuned to the same energy with a monochromator [1].

A preliminary investigation into using fast tomography with pink beam was done to determine its potential for use in cementitious systems. Typical scan times for x-ray CT were approximately 30 minutes per sample for research done in this dissertation. However, the scan time was reduced to as little as 15 seconds when using pink beam tomography. This reduction in data acquisition time

can allow for real time assessment of various deterioration mechanisms that occur in cementitious systems. An image slice of a reconstructed image volume of a sample scanned using x-ray CT with the beam tuned with a monochromator and scanned using pink beam tomography is presented in Figure A-2.

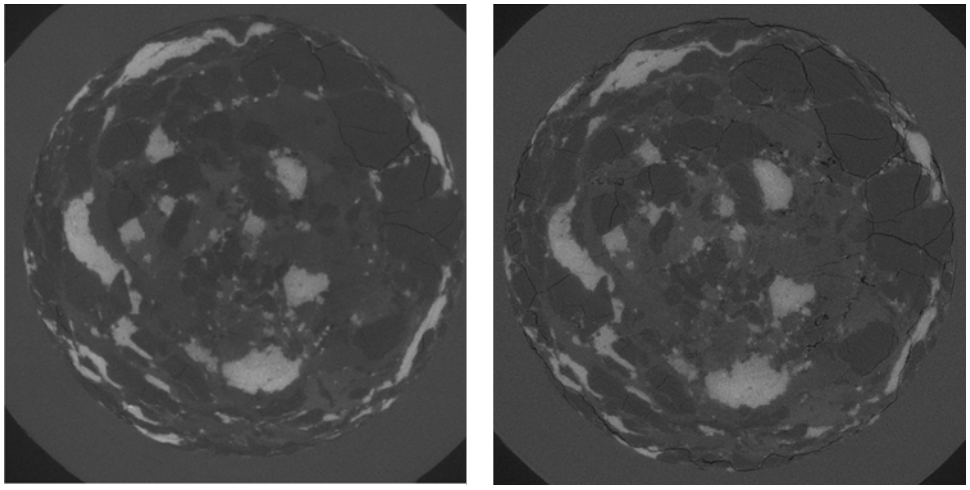

Figure A-2: Two reconstructed image slices of the same sample using traditional synchrotron tomography and fast tomography. Left) reconstructed image slice of a sample using the traditional method with a monochromator. The scan time was 30 minutes. Right) reconstructed image slice of the same sample using fast tomography. The scan time was reduced to 15 seconds, allowing for real time investigation of deterioration mechanisms, such as the development of ASR, as presented in section A.1.1. The images were collected at the Advanced Photon Source at the Argonne National Laboratory by the author and is published in [1].

### A.1.3. Preliminary work on contrast agents in AFt and C-S-H

A preliminary investigation on incorporating contrast agents into AFt and C-S-H was done in conjunction with the research presented in this dissertation. Several challenges for contrast agents exist, namely the long-term stability of the phase that the ion or element substitutes for. For example, in AFt, McCarthy et al. [2] looked at pH stability (<11.5) and stability of substituted AFt phases in the presence of other oxyanions. Potential substituted phases in AFt included sulfate, selenate, and borate ettringites. It was observed at pH levels between 6 and 9, the ettringite dissolved incongruently into calcium, oxyanion species, and noncrystalline solids that were rich in alumina. Significant amounts of alumina were present when the pH was below 5, and complete dissolution occurred at a pH below 2. Furthermore, all types of ettringite was destabilized at a pH higher than 12.5. Hampson and Bailey [3] suggested that in a pH environment less than 11, the stability was limited by the low solubility of $Al(OH)_3$, and at a pH above 12.5 the stability was

limited by the low solubility of $Ca(OH)_2$. Furthermore, McCarthy et al. [2] investigated the stability of a substituted oxyanion in to the ettringite structure in the presence of other oxyanions, which are typically found in service conditions (sulfate or carbonate). In the case of selenate and sulfate, the sulfate oxyanion has a stronger preference to be in the ettringite structure. It was observed that when selenate substituted ettringite was placed in a $Na_2SO_4$ solution, there was a substitution that occurred replacing selenite with sulfate. Most of the substitution had occurred as quickly as one hour, and a plateau effect occurred in sulfate solutions with concentrations higher than 5,000 mg/L.

Based on the literature review (Chapter 1), two potential contrast agents were investigated, one each for C-S-H and AFt. Cesium (Cs) was chosen as the contrast agent for C-S-H and barium (Ba) for AFt due to the k-shell binding energies of 35.985 keV and 37.441 keV, respectively. These scanning energies were appropriate for the use of synchrotron x-ray CT.

#### *A.1.3.1. Synthesis of C-S-H with absorbed Cs*

Pure C-S-H with a Ca/Si ratio of 1/7 was created following the procedures outlined in section 2.1.1 of this dissertation. The material was preconditioned to 11% RH prior to further experimental work. The preconditioned powder was then placed on a magnetic stirring plate in a 2 M CsCl solution for 3 weeks. The resultant material was then vacuum filtered and conditioned to 11% RH prior to compaction for x-ray CT analysis.

#### *A.1.3.2. Synthesis of Ba substituted AFt*

Pure AFt was created following the procedures found in section 2.1.2 of this dissertation. The material was preconditioned to 11% RH prior to further experimental work. The preconditioned powder was placed on a magnetic stirring plate in a 0.02 M $Ba(OH)_2$ solution for 48 hours. The resultant material was vacuum saturated and conditioned to 11% RH prior to compaction for x-ray CT analysis.

#### *A.1.3.3. X-ray CT images of phases with contrast agents*

A quaternary mixture of phases was created for investigation on the applicability of contrast agents in three of the four phases. The four phases investigated were C-S-H with a Cs contrast agent (C-S-H/Cs), AFt with a Ba contrast agent (AFt-Ba), AFm with an iodine (I) contrast agent (AFm-I),

and commercially available CH. These phases were premixed by hand in proportions similar to that found in a hydrated portland cement paste and compacted following the procedures outlined in section 2.2 of this dissertation. The samples were scanned using the GeoSoilEnviroCARS (GSECARS) bending magnet beam-line, 13-BMD at the Advanced Photon Source at the Argonne National Laboratory. Six total scans were done on the sample. Scanning below and above the absorption edge of I, Cs, and Ba were done. These energies were 32.969 keV, 33.269 keV, 35.9 keV, 36.2 keV, 37.34 keV, and 37.54 keV for I, Cs, and Ba, respectively. Reconstructed x-ray CT slices representing scanning above and below each absorption edge is presented in Figure A-3.

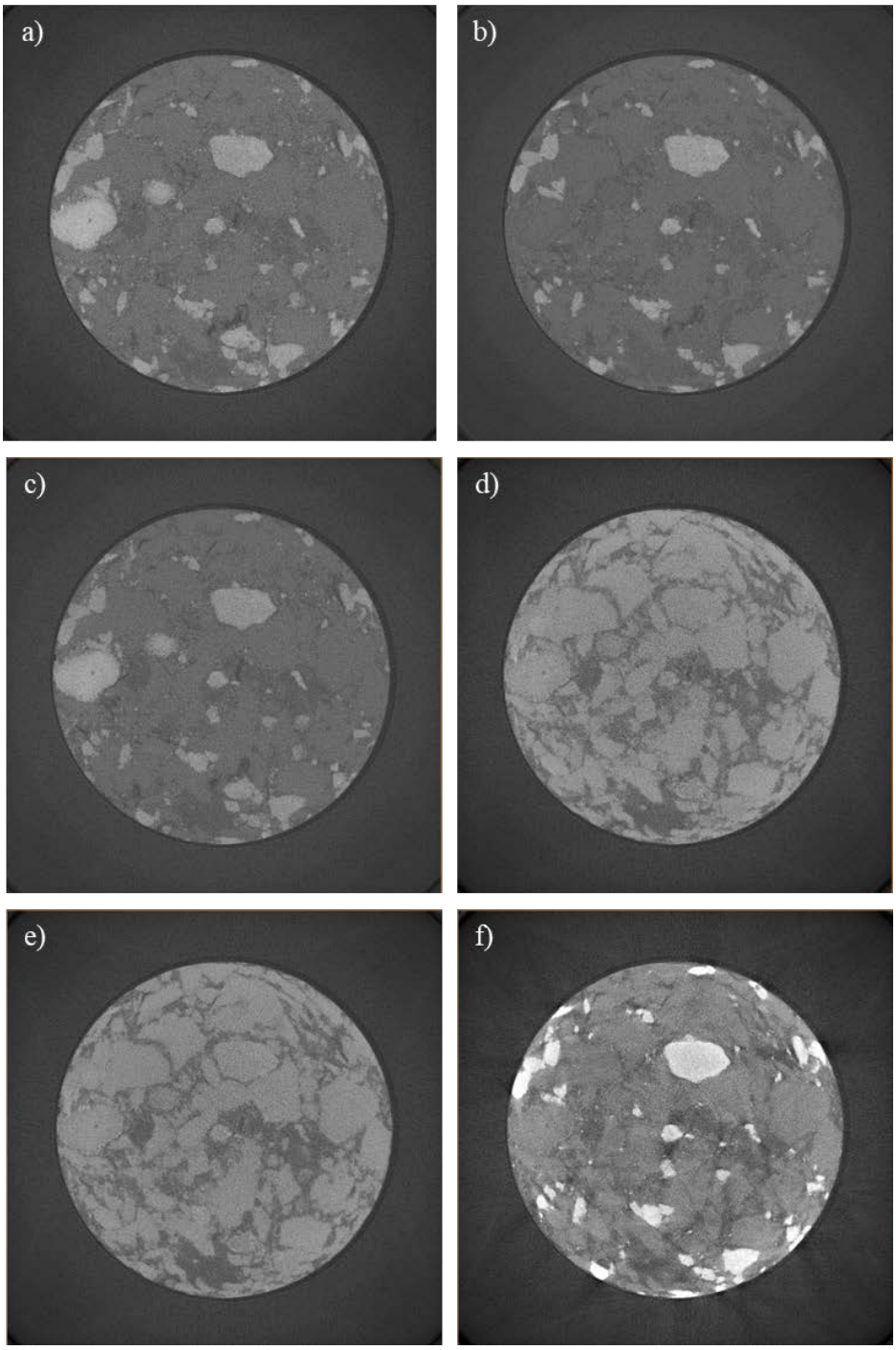


Figure A-3: Reconstructed x-ray CT image slices for quaternary mixture of four phases, three with contrast agents: a) scanned at 32.969 keV, below the I absorption edge, b) scanned at 33.269 keV, above the absorption edge of I. Small portions of AFm-I was observed in the bottom portion of the sample, c) scanned at 35.9 keV, below the absorption edge of Cs, d) scanned at 36.2 keV, above the absorption edge of Cs. Significant improvements to the contrast in the C-S-H/Cs was observed when scanned above and below the Cs absorption edge, e) scanned at 37.34 keV, below the absorption edge of Ba, and f) scanned at 37.54 keV, above the absorption edge of Ba. Similar improvements to isolating the AFt-Ba was observed using the multi-energy scanning above and below the absorption edge of Ba.

As seen in Figure A-3, the ability to isolate individual phases was greatly improved when using selective, multi-energy scanning to isolate specific contrast agents. The concepts presented in Chapter 4 using image subtraction to quantify individual phases can be applied for quick and rapid image analysis. One challenge observed was the propensity for AFt-Ba to have high x-ray absorption, thus creating streaking in the reconstructed image volume, as seen in Figure A-3f). The preliminary investigation proved the contrast agents were successful at isolating specific phases. However, further investigation in to the mechanisms of how the ions were substituted or absorbed into the phases needs further investigation. Preliminary work on characterizing two of the phases with contrast agents is presented in section A.1.3.4.

### *A.1.3.4. XRD data*

Initial characterization of phases incorporating contrast agents was done using XRD. AFm-I and AFt-Ba were investigated and results are presented in Figure A-4.

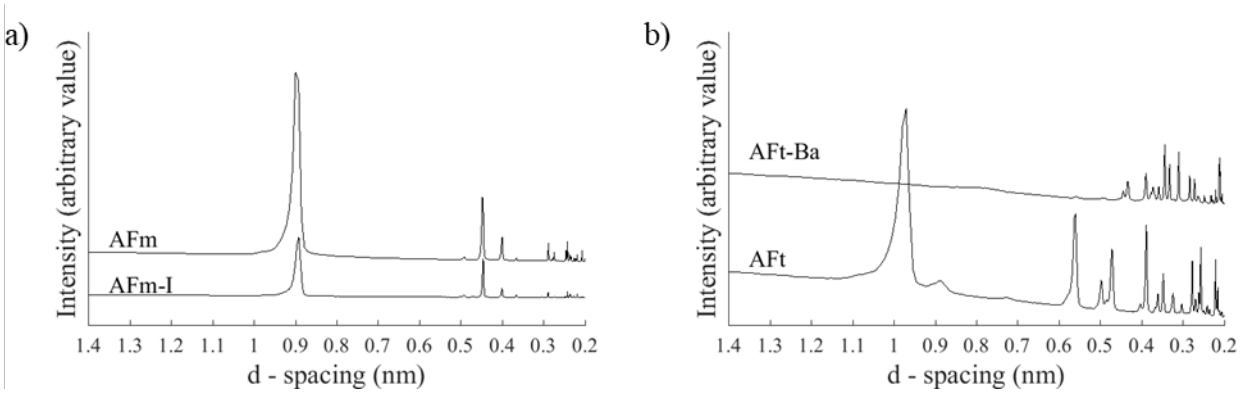


Figure A-4: XRD data on phases with contrast agents

It can be seen in Figure A-4a) that the XRD patterns for pure AFm and AFm-I were nearly identical, with good correlation between the major peaks, indicating the substation of I into the AFm structure did not cause any changes to the crystalline structure. However, as seen in Figure A-4b), the XRD patterns for pure AFt and AFt-Ba were not similar. The AFt was characterized using XRD and TGA/DTG in Chapter 3, and corroborated well with published data for both methods to assure pure AFt was synthesized. Changes to the crystalline structure were observed in the AFt-Ba when compared to pure AFt. This was likely due to the high pH of 0.02 M $Ba(OH)_2$ (~pH = 12.6). As discussed above, all forms of ettringite reported in the literature were destabilized in a pH greater than 12.5. It was likely the material created when trying to make AFt-Ba was not

part of the AFt family. Other Ba containing compounds could be used for future investigations of Ba substitutions into AFt. It should be noted, there was no characterization done on the C-S-H/Cs phase. Future work using XRD, TGA/DTG, and nuclear magnetic resonance are recommended to appropriately characterize the mechanism of Cs binding into C-S-H.

### A.1.4. References

[1] M. Rivers, High-speed tomography using pink beam at GeoSoilEnviroCARS, Proceedings of SPIE Vol. 9967; S. R. Stock; B. Müller; G. Wang; SPIE; 99670X; Argonne National Lab. (ANL), Argonne, IL (United States). Advanced Photon Source (APS)2017.

[2] G.J. McCarthy, D.J. Hassett, J.A. Bender, Synthesis, crystal chemistry and stability of ettringite, a material with potential applications in hazardous waste immobilization, MRS Online Proceedings Library, 245 (1991) 129-140.

[3] C.J. Hampsoim, J.E. Bailey, On the structure of some precipitated calcium alumino-sulphate hydrates, Journal of Materials Science, 17 (1982) 3341-3346.

# Appendix B

# Manuscript 5

## Limitations and recommendations for measuring setting time, autogenous deformation, and chemical shrinkage of paste

Tyler Deboodt, Jason H. Ideker

This manuscript is published in: *Proceedings of the 14th International Congress on Cement Chemistry, Beijing, China, 2015*

## B. Manuscript 5

# Limitations and recommendations for measuring setting time, autogenous deformation, and chemical shrinkage of paste

Tyler Deboodt[1], Jason H. Ideker[2]

**Abstract:** Traditionally, setting time of cement paste is measured using the Vicat setting time test method. However, the rate of hydration and time of initial and final set is affected by the temperature of the paste. Current specifications for the Vicat setting time allows a range of conditioning temperatures during testing. Small changes in temperature can have a significant effect on the time of initial and final set. It is important to know a more exact time of final set, particularly in studies of autogenous deformation. It is known that chemical shrinkage and autogenous deformation are of equal magnitude until rigidity in the paste structure occurs and internal strains can be developed. Adequate rigidity occurs at the time of final set and, at this time, a separation of chemical and autogenous shrinkage can be observed. This study examined the effects of temperature variations in the Vicat setting time test on final set to determine the initiation of autogenous shrinkage measurements. Setting time, autogenous deformation, and chemical shrinkage of portland cement pastes with a w/c = 0.35 were measured. Setting time was measured according to the Vicat method. Volumetric measurements using the membrane method were used for determining autogenous deformation, and an automated dilatometry method per ASTM C1608 was used for chemical shrinkage measurements. Surface temperature of the paste sample was measured during the Vicat test. Variations in final setting time of cement pastes of up to 1.5 h were observed and resulted in variations of up to 30% in the magnitude of autogenous deformation. These variations were caused by inconsistent temperature control for setting time. Recommendations for the three test methods to accurately determine when autogenous deformation measurements should be initiated in the laboratory are presented.

**Keywords**: setting time; autogenous deformation; chemical shrinkage

---

[1]Graduate Research Assistant, School of Civil and Construction Engineering, Oregon State University

[2]Associate Professor, School of Civil and Construction Engineering, Oregon State University

## B.1. Introduction

Autogenous deformation is a phenomenon closely related to changes in internal relative humidity (RH) of the cement paste [1-3]. In ordinary portland cement concretes with high water to cement ratios (w/c) (>0.42) [4], autogenous deformation is negligible when compared to drying shrinkage. While in concrete with low w/c ratio (<0.40) autogenous deformation can result in shrinkage, which be significant enough to induce micro- or macro-cracking and may impair the concrete quality. The amount of autogenous shrinkage is even greater in these low w/c mixtures when coupled with supplementary cementitious materials, such as silica fume [5]. While the mechanisms leading to autogenous shrinkage are not yet fully understood, it is generally agreed upon that a relationship exists between autogenous shrinkage and changes in relative humidity of capillary pores in the cement paste.

This relationship can be explained by the difference in chemical shrinkage between cementitious materials with low w/c ratios. For instance, the chemical shrinkage of ordinary portland cement is typically around 0.07, which means a 7% mass of water per mass of cement is needed to complete the hydration process. The addition of supplementary cementitious materials to the system can increase the magnitude of autogenous shrinkage significantly. The same coefficients of chemical shrinkage in blended portland cement systems with silica fume, slag and fly ash are 0.22, 0.18 and 0.10 to 0.16 (range for fly ash) [6]. This means that for complete hydration in these systems, more water is required. In systems prone to large amounts of chemical shrinkage, the internal RH decreases due to increasing water demand resulting in capillary tension arising from water leaving small capillaries (<50 nm) which can be great enough to cause these pores to collapse. As a result, macroscopic shrinkage occurs [7]. In a hardened microstructure even relative small changes in strain can result in significant stress build-up which may result in cracking, especially at early ages.

To capture the autogenous deformation or to assess the effectiveness of shrinkage mitigation strategies, many measurement techniques and apparatus to assess autogenous deformation have been developed. These techniques include the membrane method [3, 8], corrugated tube method [9], rigid form method [10] are documented. At the time of final set, the microstructure has developed enough rigidity for strains to be induced, and thus the zero point for autogenous

deformation measurements. A common method to measure the time of final set is using the Vicat needle, with procedures outlined in ASTM C191 [11]. Furthermore, divergence between the autogenous deformation and chemical shrinkage occur at the time of final set, thus indicating adequate rigidity in the microstructure [12]. It is postulated that these methods are applicable for determining the zero point for autogenous deformation. This research investigated the variation of final set measured by the standard Vicat needle test, as well as combined autogenous deformation and chemical shrinkage testing to determine the effect on the total amount of autogenous deformation in cement pastes

## B.2. Experimental

### B.2.1. Materials and mixture design

A Type I/II portland cement was used in the study. The chemical composition of the cement is seen in Table B-1. All paste mixtures were created with deaerated, deionized water and the cement was screened over a 0.85 mm sieve prior to mixing. A w/c of 0.35 was used for all experiments.

Table B-1: Oxide analysis of Type I/II portland cement

| Composition | $SiO_2$ | $Al_2O_3$ | $Fe_2O_3$ | CaO | MgO | $Na_2O$ Eq. | $SO_3$ | LOI | $C_3S$ | $C_2S$ | $C_3A$ | $C_4AF$ |
|---|---|---|---|---|---|---|---|---|---|---|---|---|
| Content (%) | 20.51 | 4.72 | 3.23 | 64.2 | 0.80 | 0.49 | 2.70 | 2.62 | 61.51 | 12.40 | 7.03 | 9.84 |

### B.2.2. Experimental procedures

All samples were mixed using ASTM C305 procedures for hydraulic cement paste. Prior to casting, all materials used were brought to 23 °C for 24 h. After casting, the samples were transferred into the appropriate testing environment for the duration of the test. In experiments where combined testing was done, all samples were cast from the same batch of paste to ensure consistency in the samples.

The setting time was measured using the Vicat needle following procedures outlined in ASTM C191. Volumetric autogenous deformation was measured using the membrane method, outlined in by Lura and Jenson [3]. Approximately 70 g (±2 g) of paste was used in all of the autogenous deformation testing. The sample was cast in a polyurethane membrane, and then submerged in temperature controlled paraffin oil at 23 °C to eliminate water transmission. The mass change was

measured for 60 h from time of contact. An automated dilatometry method, per ASTM C1608, was used to measure chemical shrinkage with image analysis. Each chemical shrinkage test was the average of three samples. Procedures are found in work by Fu et al. [13]. Sample height was modified to account for depercolation issues observed in low w/cm pastes [12-14]. A sample height of 3 mm (~3 g of paste) was used. After casting, the samples were placed in a temperature controlled water bath at 23 °C, and monitored for 60 h from time of contact. The recorded images were processed with computer software developed by the Laboratory of Construction Materials at École Polytechnique Fédérale de Laussane to determine the total water uptake. This image analysis provides significant enhancement to the accuracy of chemical shrinkage results [15, 16].

## B.3. Results and Discussion

### B.3.1. Effect of temperature on Vicat setting time

To study the variation in time to initial and final set, five replicates were cast and tested under similar conditions. Conditioning requirements per ASTM C191 allow for a temperature range of 6 °C for the cement and molds, 4 °C for the mixing water and 4 °C for the moist cabinet [11]. Table B-2 shows the results from this study. The average time to initial set was 188 min with a standard deviation of 20.1 min. The average time to final set was 358 min with a standard deviation of 45.9 min.

Table B-2: Variation in initial and final set

| | Initial set (min) | Final set (min) | Initial temperature (°C) | Maximum temperature (°C) |
|---|---|---|---|---|
| Replicate 1 | 196 | 405 | 21.0 | 23.5 |
| Replicate 2 | 208 | 411 | 23.3 | 25.1 |
| Replicate 3 | 203 | 330 | 22.8 | 24.4 |
| Replicate 4 | 166 | 315 | 22.8 | 25.0 |
| Replicate 5 | 167 | 330 | 21.6 | 24.0 |

It can be seen in Table B-2 there was a range of 42 min for initial set and 96 min for final set. These differences were caused by variations in the sample temperature. While all samples met the conditioning requirements in ASTM C191, the range allowable conditioning range may not be acceptable for determining final set for autogenous deformation measurements.

### B.3.2. Effect of final set on autogenous deformation

Samples for autogenous deformation and setting time were cast from the same batch of paste. Three sets of samples were cast to determine the difference in the magnitude of autogenous deformation based on the Vicat final setting time. Figure B-1 shows the variation that final set has on the amount of measured autogenous deformation. One standard deviation of the final set from Table B-2 was taken as the upper and lower bounds of set time variation.

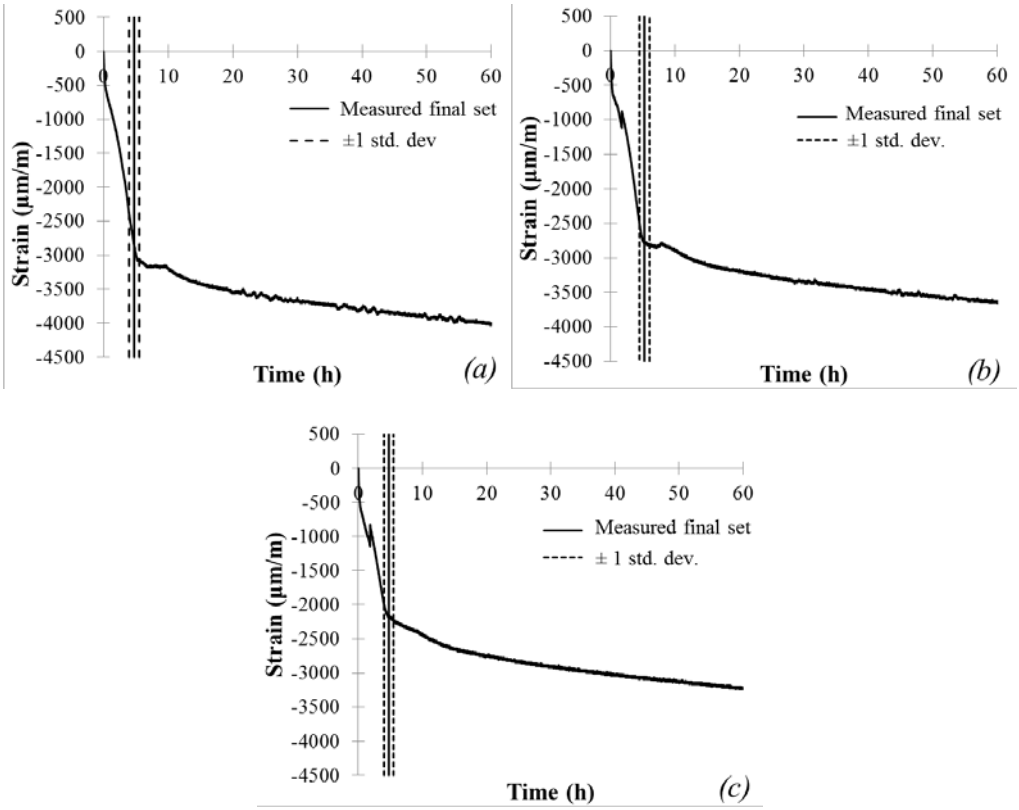


Figure B-1: Effect of setting time on autogenous deformation

Since strain development does not begin until there is sufficient rigidity in the microstructure, the zero strain point was taken as the time of final set. The magnitude of autogenous strain was calculated at 60 h from initial contact between the cement and water for all tests. The average amount of autogenous deformation for samples (a)-(c) at 60 h was -1170, -920, and -880 με for the lower bound, measured, and upper bound of setting time, respectively. The standard deviation for these tests were 60, 115, and 100 με. The variation between the lower bound and measured set time was 32.7% for sample (a), 32.9% for sample (b), and 17.5% for sample (c). The variation between the upper bound and measured set time was 4.1% for sample (a), 3.9% for sample (b),

and 5.8% for sample (c). Therefore, an error in the measured final set per ASTM C191 may result in significant errors in the amount of autogenous deformation. Due to self-heating, it is recommended that active temperature control of the sample for Vicat setting time matches the temperature profile of the autogenous deformation sample.

### B.3.3. Combination testing

An alternative to using the Vicat setting time is to choose where the chemical shrinkage and autogenous deformation curves separate. In this testing, three sets of samples were cast. For each set, the autogenous deformation and chemical shrinkage samples were cast from the same batch. Figure B-2 displays the results from this testing. The average of three tests, and an envelope of ±1 standard deviation are plotted for both the chemical shrinkage and autogenous deformation.

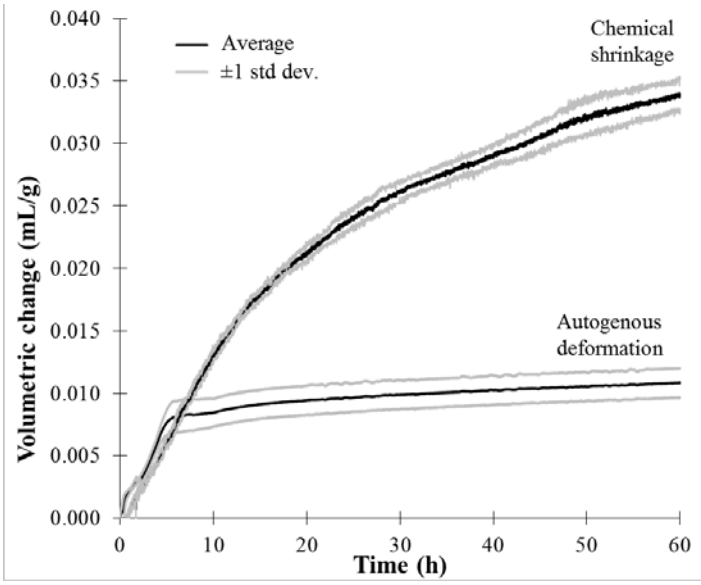


Figure B-2: Chemical shrinkage and autogenous deformation

It can be seen that there is a difference between the chemical shrinkage and autogenous deformation curves, although these are supposed to match until final set occurs. Other researchers have reported this can be determined using the membrane method for autogenous deformation and a buoyancy method for chemical shrinkage. These two methods follow the same fundamental principal of measurement (buoyancy) [12]. Whereas in this research, dilatometry was used for chemical shrinkage and buoyancy was used for autogenous deformation. It is possible similar methods must be used in order for these two curves to align. Further research is needed to confirm.

The error associated with using this method can also be profound due to the error seen in the early age (<10 h) for the autogenous deformation curves. An alternative is to detect when the slope of the curves differ. However, in order to determine this in an unbiased manner, the minimum of the derivative of the curves must be calculated. While there are models to have a best fit curve for chemical shrinkage [13, 17], there currently is not a best fit model for autogenous shrinkage.

## B.4. Conclusions

The Vicat setting time is typically used for the measurement of initial and final set of pastes. Although this is the standardized test method, it has limitations when determining the amount of autogenous deformation. The following conclusions and recommendations were discovered from this research:

- Variation of up to 42 min and 96 min were observed in initial and final set in paste while meeting the conditioning requirements of ASTM C191. Self-heating of the samples was observed, resulting in these variations of setting time. Active temperature control, or reduction in size of the sample to ensure temperature control is recommended for determination of final set for autogenous deformation measurements. Incorrectly measuring the final set may result in an error of 30% or greater in the total amount of autogenous deformation.
- The use of chemical shrinkage, coupled with the membrane method, could be an alternative to Vicat setting time to determine the amount of autogenous deformation. However, modifications to the membrane method (e.g. sample size, buoyancy liquid, membrane type) need to be completed to allow for the chemical shrinkage and autogenous deformation curve to align. It is proposed to determine a best fit model for the autogenous deformation curve. From this curve, a difference in slope between the chemical shrinkage and autogenous deformation curves can be found in an unbiased manner. Furthermore, it is possible different measurement techniques, such as dilatometry and buoyancy, are not compatible to align the chemical shrinkage and autogenous deformation curves. However, further research is needed to confirm.

## B.5. Acknowledgements

The financial help from the Oregon Department of Transportation, under research project SPR-711, as well as Weyerhaeuser is greatly appreciated.

## B.6. References

[1] O.M. Jensen, P.F. Hansen, Autogenous deformation and RH-change in perspective, Cement and Concrete Research, 31 (2001) 1859-1865.

[2] O.M. Jensen , P.F. Hansen, Autogenous deformation and change of relative humidity in silica fume modified cement paste, ACI Materials Journal, 28 (1996) 539-543.

[3] P. Lura, O. Jensen, Measuring techniques for autogenous strain of cement paste, Materials and Structures, 40 (2007) 431-440.

[4] E.E. Holt, Early-age autogenous shrinkage of concrete, Technical Research Centre of Finland, VTT Publications, No. 446, (2001).

[5] P. Lura, Autogenous deformation and internal curing of concrete, DUP Science, Delft, 2003, pp. p. 208.

[6] D.P. Bentz, Internal curing of high-performance blended cement mortar, ACI Materials Journal, 104 (2007) 408-414.

[7] P.K. Mehta, P.J.M. Monteiro, Concrete: Microstructure, properties, and materials, 3 ed., McGraw-Hill, New York, 2006.

[8] J.C. Yates, Effect of calcium chloride on readings of a volumeter inclosing portland cement pastes and on linear changes of concrete, Highway Research Board Proc.21, (1941) 294-304.

[9] B.J. Mohr, K.L. Hood, Influence of bleed water reabsorption on cement paste autogenous deformation, Cement and Concrete Research, 40 (2010) 220-225.

[10] B. Pease, A.B. Hossain, J. Weiss, Quantifying volume change, stress development, and cracking due to early-age autogenous shrinkage, ACI SP 220, (2004) 23-39.

[11] ASTM Standard C191, Standard test methods for time of setting of hydraulic cement by Vicat needle, in: ASTM International (Ed.) ASTM C191-13West Conshocken, PA, 2013, 2013.

[12] G. Sant, P. Lura, J. Weiss, Measurements of volume change in cementitious materials at early ages: Review of testing protocols and interpretation of results, Transportation Research Record: Journal of the Transportation Research Board, (2006) 21-29.

[13] T. Fu, T. Deboodt, J.H. Ideker, A simple procedure on determining long-term chemical shrinkage for cementitious systems using improved chemical shrinkage test, ASCE Journal of Materials, 24 (2012).

[14] G. Sant, D. Bentz, J. Weiss, Capillary porosity depercolation in cement-based materials: Measurement techniques and factors which influence their interpretation, Cement and Concrete Research, 41 (2011) 854-864.

[15] M. Costoya, Effect of particle size on the hydration kinetics and microstructural development of tricalcium silicate, EPFL, Lausanne, Switzerland, 2008.

[16] T. Fu, Autogenous deformation and chemical shrinkage of high-performance cementitious systems, School of Civil and Construction Engineering, Oregon State University, Corvallis, OR, 2011, pp. p. 133.

[17] K.T. Xiao, H.Q. Yang, Y. Dong, Study on the influence of admixture on chemical shrinkage of cement based materials, Key Engineering Materials, 405-406 (2009) 226-233.

# Appendix C

# Manuscript 6

## Re-evaluation of testing parameters in the accelerated mortar bar test

Tyler Deboodt, Andrew Wilson, Jason H. Ideker, Matthew P. Adams

This manuscript is published in: *Proceedings of the 15th International Conference on Alkali-Aggregate Reactivity, São Paulo, Brazil, 2016*

# C. Manuscript 6

## Re-evaluation of testing parameters in the accelerated mortar bar test

Tyler Deboodt[1], Andrew Wilson[2], Jason H. Ideker[3], Matthew P. Adams[4]

**Abstract:** The accelerated mortar bar test (AMBT) is used as a rapid screening method to determine the potential of an aggregate to be alkali-silica reactive. However, aggregate grading, temperature, and the concentration of the NaOH soak solution will affect the observed reactivity of aggregates. This research presents a study of aggregate reactivity using the AMBT in which an examination of the impact of temperature, normality, and aggregate grading on expansion was determined. A siliceous, fine aggregate was tested to assess the impact of each of these parameters in the AMBT (according to ASTM C1260), and ultimately compared to concrete prism tests (CPT-ASTM C1293). Under standard testing procedures this aggregate was determined to be very highly reactive, according to ASTM C1778, with an expansion of 0.49% at 14 days, yet was deemed non-reactive in the CPT with an expansion of 0.02% at 1 year. To assess the effect of temperature and aggregate preparation, a standard 1 N NaOH solution was used. The temperature study was done at 23 °C, 38 °C, 60 °C, and 80 °C. As received and the prescribed grading were used to assess the effect of aggregate preparation. A study of the impact of normality examined NaOH solutions of 0.5 N, 0.75 N, 1 N, 1.25 N, 1.5 N, and 1.75 N at 80 °C. It was found that expansion peaked in a 0.75 N NaOH solution at 14 days. Expansion was shown to increase as temperature increased, particularly above 38°C. It was shown that modifications to the AMBT test typically did not correspond to the results in the CPT.

**Keywords:** temperature, normality, AMBT, ASR, alkali content

---

[1] Graduate Research Assistant, School of Civil and Construction Engineering, Oregon State University
[2] Undergraduate Research Assistant, School of Civil and Construction Engineering, Oregon State University
[3] Associate Professor, School of Civil and Construction Engineering, Oregon State University
[4] Assistant Professor, Department of Civil and Environmental Engineering, New Jersey Institute of Technology

## C.1. Introduction

The accelerated mortar bar test (AMBT) is one of the most widely used methods for rapid assessment of an aggregate's potential for alkali-silica reaction (ASR). However, this test method may indicate an aggregate is reactive, where it determined to be innocuous in other methods, such as the concrete prism test (CPT) [1] or field performance. Similarly, aggregates may be considered innocuous in the AMBT, but have poor field performance. Historically, the development of an accelerated ASR test methods included higher temperatures and increased alkali contents during the testing [2]. Increased alkalis are added either at mixing, or in a soak solution. The alkalis were provided through solutions such as NaOH [3], NaCl [4, 5], KOH [6], and salt water [7]. The development of the current ASTM C1260 [8] was founded on the research by Oberholster and Davies [3] with testing conditions at 1 N NaOH storage solution at 80 °C [8].

During the development of the AMBT, six different aggregates were assessed at different temperatures and normalities of NaOH storage solution on expansion of mortar bars. The aggregates were quartz or silicate bearing. Maximum expansion was observed in three of the six aggregates at 80 °C, while maximum expansion was observed at 90 °C in the others. Furthermore, maximum expansion was observed at 1.0 N NaOH in five of the six aggregates, whereas maximum expansion in the other aggregate was 1.5 N [3]. Similarly in another study, it was found that in a hornfels aggregate, maximum expansion was also observed in a 1 N NaOH solution stored at 80 °C [6], further establishing support for these testing conditions as a worst case scenario for accelerated testing.

However, correlation discrepancies between the AMBT and field performance or other methods to assess ASR potential have arisen [9-11]. The aggressive testing conditions of the AMBT does not represent real world conditions, and thus can result in aggregates that fail in the AMBT and show good field performance [12]. Furthermore, the testing environment was optimized for a quartz, silica, or hornfels aggregates, which could ultimately lead to incorrect expansion values for other types of aggregates. Modifications to the AMBT procedures have been previously reported in literature. It was found that a 1 N NaOH testing environment resulted in higher expansion when compared to a 0.5 N or 0.25 N solution; cements with a higher Na2Oeq had a higher expansion; and prolonging the curing duration had little effect on expansion [13].

Preliminary testing showed a locally sourced siliceous fine aggregate was highly reactive (0.49% at 14 days) when tested under standard testing conditions in the AMBT. Anecdotal reports of field performance of this aggregate were good (i.e. no ASR observed). However, when the same aggregate was tested in the CPT (ASTM C1293) the aggregate was considered innocuous at 1 year (0.02% expansion). The main motivation of this research was to assess the key variables in the AMBT, and their effect on 14-day expansion for this particular aggregate. The variables studied in this research include the effect of storage temperature, normality of the NaOH soak solution, aggregate grading, and initial alkali content of the cement.

## C.2. Materials and methods

### C.2.1. Materials

#### *C.2.1.1. Aggregates*

A siliceous, locally sourced, natural river fine aggregate was tested to determine its potential reactivity in the AMBT and CPT. This aggregate was composed of various igneous rocks and minerals, many of which are known to participate in ASR. These potentially reactive components include fine-grained volcanic rock types (e.g. basalt, andesite, dacite, crystalline rhyolite), glassy volcanic rocks (e.g. rhyolite and tuff), and microcrystalline quartz (e.g. quartzite, microcrystalline silica, optically-strained quartz). A full summary of the aggregate constituents are seen in Table C-1.

Table C-1: Typical composition of fine aggregates

| Component | Mineral Examples | Amount (%) |
|---|---|---|
| Fine-grained basic to intermediate volcanic rocks | Basalt, andesite, dacite, crystalline rhyolite | 44 |
| Medium- to coarse-grained basic to intermediate igneous rocks | Granodiorite, diorite, gabbro | 34 |
| Quartzite and microcrystalline silica | Quartzite, microcrystalline silica, chert | 8 |
| Glassy volcanic rocks | Rhyolite, Tuff | 1 |
| Other | Iron oxides, quartz, feldspar, pyroxene, opaques | 13 |

In order to test the reactivity of the fine aggregate in the CPT, a calcareous coarse aggregate was used as the non-reactive aggregate. This coarse aggregate passed the AMBT and CPT test methods, and was therefore deemed non-reactive.

*C.2.1.2. Cement*

A type I/II portland cement meeting the requirements outlined in ASTM C150 [14] was used for all testing. The Na2Oeq¬ for this cement was 0.83. For all testing the cement was sieved over an 850 µm screen before using. Table C-2 shows the oxide analysis of the cement used in this research.

Table C-2: Cement composition

| | Cement 1 | Cement 2 |
|---|---|---|
| **Constituent** | **Amount (%)** | **Amount (%)** |
| $SiO_2$ | 19.61 | 19.93 |
| $Al_2O_3$ | 4.38 | 4.72 |
| $Fe_2O_3$ | 2.76 | 3.5 |
| CaO | 62.21 | 63.47 |
| MgO | 2.72 | 0.82 |
| $Na_2O$ | 0.28 | 0.29 |
| $K_2O$ | 0.84 | 0.33 |
| $Na_2O_{eq}$ | 0.83 | 0.51 |
| LOI | 2.6 | 3.09 |
| $C_3S$ | 60.16 | 61.33 |
| $C_3A$ | 6.95 | 6.61 |
| $C_2S$ | 10.83 | 10.86 |
| $C_4AF$ | 8.39 | 10.64 |

## C.2.2. Methods

### *C.2.2.1. Accelerated mortar bar test*

The AMBT is a widely used test method to rapidly assess the potential for alkali-silica reactivity in aggregates. Typically, an aggregate with an expansion value greater than 0.20% at 14 days of testing is considered potentially deleterious expansive. If the expansion value is between 0.10% and 0.20% at 14 days, the aggregate could be either innocuous or deleterious, and further testing should be done in order to determine the reactivity of aggregates that fall in this expansion range. Recommendations include continuing the AMBT to 28 days [15, 16], or supplement with ASTM C1293 [17] (CPT) and/or ASTM C289 (chemical method) [18]. If an aggregate has an expansion value less than 0.10% at 14 days, it is considered innocuous. However, due to the aggressive nature of standard AMBT conditions, this test may not accurately predict the potential for reactivity when compared to field testing or the concrete CPT [9-12].

Sampling and preparation of test specimen procedures outlined in ASTM C1260 [8] were used as guidance for all mixtures. For the temperature, normality, and alkali content studies, the aggregates were sieved to the proper gradating and washed per the requirements in the standard. In the

aggregate grading study, the as received aggregates were washed before mixing. After preparation of the aggregates, mixing of mortars occurred per ASTM C305 [19]. After mixing, the samples were cast in 25 mm x 25 mm x 285 mm molds and allowed to cure for 24 hours. The specimens were removed from their respective molds at 24 ± 2 hours and placed into preconditioned water for 24 hours. The water temperature and resultant storage temperature is discussed below. Initial measurements were taken 48 hours after the initial contact and the specimens were transferred into a preconditioned NaOH solution. The normality of the NaOH solution is discussed below. Length change measurements were taken every 2 to 3 days up to 28 days of immersion in the NaOH solution, or until 0.10% expansion was measured. Results from each study were compared to the length change of mortar bars tested under standard conditions (80 °C and 1 N NaOH) at 14 and 28 days of exposure. A summary of the mixtures and all testing parameters is seen in Table C-3.

Table C-3: Mixture identification

| Mixture ID | Aggregate grading | Normality of NaOH | Temperature | Number of bars |
|---|---|---|---|---|
| Control | ASTM C1260 | 1 N | 80 ℃ | 4 |
| 0.5N | ASTM C1260 | 0.5 N | 80 ℃ | 4 |
| 0.75N | ASTM C1260 | 0.75 N | 80 ℃ | 4 |
| 1.25N | ASTM C1260 | 1.25 N | 80 ℃ | 4 |
| 1.5N | ASTM C1260 | 1.5 N | 80 ℃ | 4 |
| 1.75N | ASTM C1260 | 1.75 N | 80 ℃ | 4 |
| 23C | ASTM C1260 | 1 N | 23 ℃ | 4 |
| 38C | ASTM C1260 | 1 N | 38 ℃ | 4 |
| 60C | ASTM C1260 | 1 N | 60 ℃ | 4 |
| AR | As received | 1 N | 80 ℃ | 12 |

*Normality of NaOH solution*

Six different normalities of the NaOH were tested. The normalities tested were 0.5 N, 0.75 N, 1.0 N, 1.25 N, 1.5 N, and 1.75 N. The specimens were stored at 80 °C for all mixtures where normality

was studied. Sieved and washed aggregates were used for this study. Four bars for each normality solution were cast.

*Storage temperature*

Four different storage temperatures were studied to determine the effect on expansion. The temperatures were 23 °C, 38 °C, 60 °C, and 80 °C. Sieved and washed aggregates were used for this study. After the specimens cured for 24 hours, they were transferred to preconditioned water at the respective temperature for 24 hours. For example, if the testing temperature was 38 °C, the specimens were transferred to pre-heated water at 38 °C after demolding. Next, the initial measurement was recorded and the specimens were transferred into a 1 N NaOH solution preconditioned to the correct temperature. The specimens were stored in the NaOH solution until 28 days or an average expansion of 0.10% was observed.

*Aggregate preparation*

A comparison was done between the grading of the aggregates per ASTM C1260 and the as received state of the fine aggregate. Sieve analysis of the as received aggregate compared to the ASTM C1260 graded aggregate is seen in Table C-4. Sampling of the as received aggregates was done according to ASTM D75 [20]. Due to the inherent variability in grading of as received aggregates, three sets of four mortar bars using the as received aggregate were cast and compared to a control set.

Table C-4: Aggregate grading

| | | ASTM C1260 graded | As received |
|---|---|---|---|
| **Passing** | **Retained on** | **Mass (%)** | **Mass (%)** |
| 12.5 mm | 9.53 mm | 0 | 0.04 |
| 9.53 mm | 4.75 mm | 0 | 4.62 |
| 4.75 mm | 2.36 mm | 10 | 18.36 |
| 2.36 mm | 1.18 mm | 25 | 11.87 |
| 1.18 mm | 600 µm | 25 | 12.05 |
| 600 µm | 300 µm | 25 | 31.09 |
| 300 µm | 150 µm | 15 | 19.33 |
| 150 µm | Pan | 0 | 2.64 |

*C.2.2.2. Concrete prism test*

While the AMBT is a rapid test method that can quickly determine the reactivity of an aggregate, it is reported that the concrete prism test is best recommended for determining the potential reactivity [12, 21-23], although there are reported shortcomings of this test method [21]. Procedures outlined in ASTM C1293 [22] were followed for the CPT testing. Expansion results from the 1-year CPT were compared to 14- and 28-day expansion values from all variations of the AMBT.

## C.3. Results

### C.3.1. AMBT results

The control set of mortar bars tested at standard testing conditions (80 °C and 1 N NaOH) and aggregate grading specified in ASTM C1260 had an expansion of 0.49% at 14 days and 0.73% at 28 days. Based on these results, this aggregate is considered to be potentially deleterious. The measured expansion was the average of 4 mortar bars. This measurement was the baseline for comparison of all the parameters studied.

Figure C-1 shows incremental growth of mortar bars stored in various NaOH normalities at 80 °C.

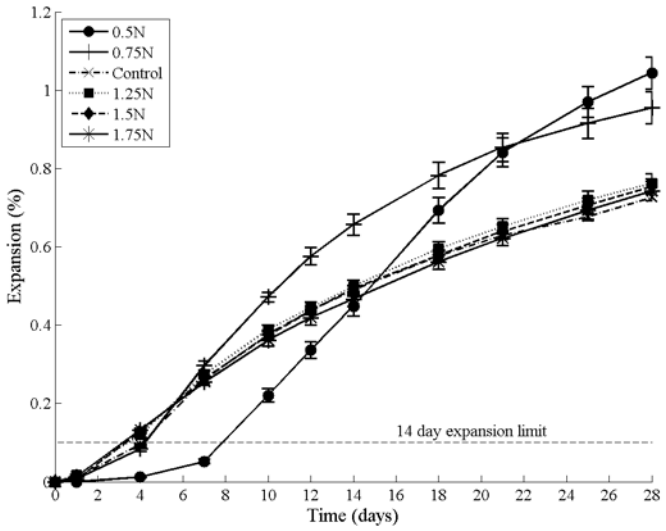


Figure C-1: Expansion as a function of time for ASTM C1260 graded mortar bars with different levels of NaOH normality

It can be seen that storing the mortar bars in a 0.75 N NaOH solution resulted in the highest 14 day expansion (0.66%) and highest rate of expansion up to 14 days of exposure. At 28 days of exposure, the 0.75 N NaOH solution had the second highest expansion (0.96%). When storing the mortar bars in a 0.5 N NaOH solution, the 14 day expansion was the lowest (0.45%) amongst all soak solution normalities. However, the 28 day expansion was the highest (1.04%). As the normality of the NaOH solutions increased, there were similar values in the 14 and 28 day expansion were observed for the 1 N, 1.25 N, 1.5 N, and 1.75 N NaOH solutions. Graphical representation of the 14 and 28 day expansion values for all NaOH solutions is seen in Figure C-2.

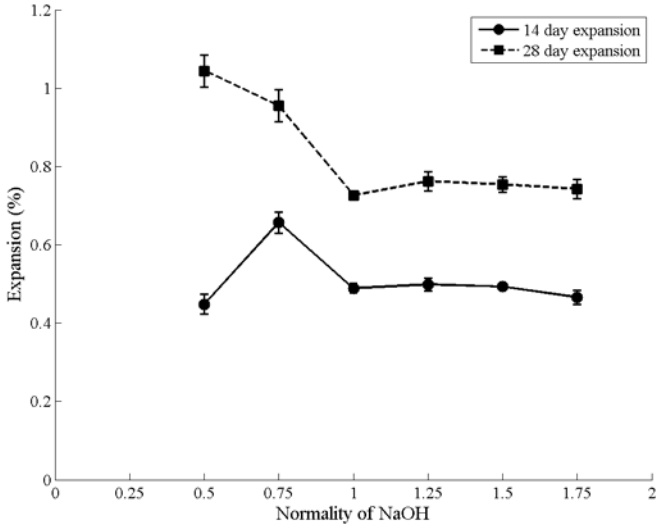


Figure C-2: 14- and 28-day expansion at various levels of NaOH normality on ASTM C1260 mortar bars

The results of the effect of different storage temperatures on length change of mortar bars stored in 1 N NaOH solution are seen in Figure C-3.

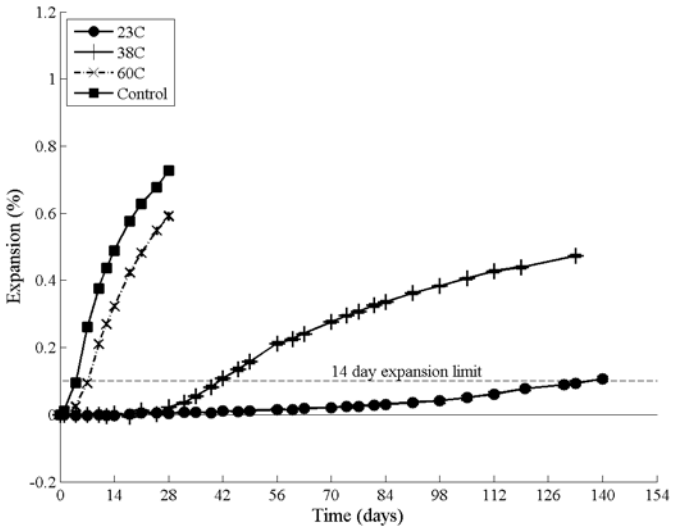


Figure C-3: Effect of temperature and expansion values of ASTM C1260 mortar bars

The amount and rate of expansion increased with an increase in temperature. Minimal expansion was observed at 28 days in mortar bars stored at 23 °C and 38 °C. Measurements of the mortar bars at this temperature were monitored until an average expansion of 0.10% was achieved. An exposure time of 140 days was required for the mortar bars stored at 23 °C to reach an expansion

of 0.10%. Exposure of 42 days in the NaOH solution was required for the mortar bars stored at 38 °C to reach an expansion of 0.10%.

Results for the effect of aggregate grading on length change are seen in Figure C-4. The use of as received aggregates resulted in a range of expansion values at both 14 and 28 days. Expansion at 14 days for the as received samples was 0.56%. . The expansion for the as received samples at 28 days was 0.82%.

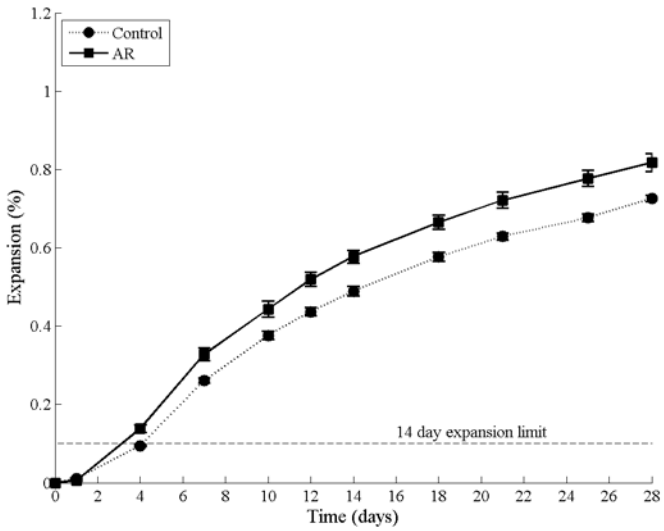


Figure C-4: Effect of grading on expansion values of ASTM C1260 graded and as received fine aggregates

### C.3.2. Comparison of AMBT and CPT results

Figure C-5 shows expansion the 14- and 28-day AMBT expansion values compared to the 1-year CPT expansion. The 1-year CPT expansion was 0.02% whereas the 14-day AMBT expansion was 0.49%. The expansion value from the CPT suggests that the aggregate was innocuous, yet the expansion value from the AMBT suggests the aggregate was potentially deleterious. Comparing all of the AMBT expansion values to the CPT expansion values; it was found that only two AMBT mixtures resulted in a pass-pass relationship with the CPT results. The 14- and 28-day expansion values of the 23 °C and 38 °C AMBT mixtures produced this pass-pass relationship.

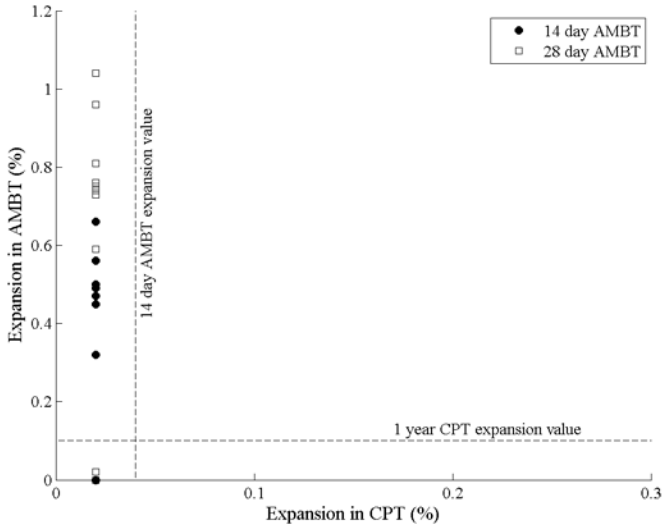


Figure C-5: AMBT vs CPT results

## C.4. Discussion

Decreasing the normality of the NaOH solution to 0.75 N resulted in a higher expansion at both 14 and 28 days compared to the control. Further decreasing the normality to 0.5 N resulted in a lower 14 day expansion, but a higher 28 day expansion when compared to the control. The length change at both 14 and 28 days in mortar bars stored in NaOH solutions that had a normality greater than 1 N was similar to that of the control. The increase in reactivity of the same aggregate when tested at lower normality solutions was caused by a pessimum effect [24], which ultimately resulted in a higher expansion at a lower alkali content. The pessimum effect seen in the AMBT results may also explain the low reactivity in the CPT. Further research on the CPT with this aggregate at various alkali loading levels needs to be completed to ensure whether this aggregate is actually innocuous.

Reducing the temperature below 80 °C resulted in a decreased amount and rate of expansion in all temperatures tested. Decreasing the temperature to 60 °C resulted in a reduction in the 14 and 28 day expansion by 35% and 19% when compared to the mortar bars test at 80 °C, respectively. There was no measured expansion at 14 days for the mortar bars stored at 38 °C and 23 °C. No expansion was observed at 28 days in the mortar bars stored at 23 °C, and an expansion of 0.02% was observed at 28 days in the mortar bars stored at 38 °C. However, when stored long enough, mortar bars stored at both 23 °C and 38 °C eventually reached an expansion of 0.01%, thus

indicating that even at low temperatures this aggregate may still be potentially deleterious in the long-term.

Using the aggregate in an as received state resulted in an increase in variability in both the expansion values, as well as the measured standard deviation. Expansion at 14 days was increased by 12.5% when compared to the control. At 28 days, the expansion was also increased in the as received aggregate mortar bars when compared to the control. However, this increase in expansion was generally lower (10.9%) than at 14 days. Furthermore, the standard deviation amongst the twelve mortar bars was higher than that of the control. This increase in expansion and variation amongst the individual mortar bars was likely caused by an increase in the amount of fine aggregate particles (<600 μm) in the as received aggregates than the ASTM C1260 grading requirements. Previous research has indicated the particle size influences the amount of expansion caused by ASR [11, 25, 26]. However, in that research it was found that the 1.25-2.50 mm size range influenced the expansion the most [11]. In this research the increase in expansion and variation amongst the individual mortar bars was likely caused by an increase in the amount of fine aggregate particles (<600 μm) in the as received aggregates, as seen in Table 2. Furthermore, the increase in standard deviation can be attributed to the inherent variability in the grading of the aggregate in an as received state. Although standardized procedures for aggregate sampling were followed during aggregate sampling, these natural variations in aggregate gradation influenced the total expansion in the mortar bars.

Comparing both the 14- and 28-day expansion values for all of the mixtures tested in the AMBT to the CPT results, it can be seen that the majority of the mixtures failed the AMBT but passed the CPT. Only two different mixtures, 23C and 38C, passed both testing procedures. It can be seen that modifying the normality of the NaOH or changing the aggregate gradation in the AMBT does not result in a pass-pass relationship when compared to the CPT. However, it was observed in the AMBT that decreasing the normality to 0.75 N resulted in a higher expansion at 14-days, while the highest 28-day expansion was observed in mortar bars tested at 0.5 N. This pessimum effect could result in an increase in expansion in the CPT when tested at alkali contents lower than 1.25%. It is recommended that a parametric study on the amount of available alkalis in the CPT be done.

## C.5. Conclusions

This research reassessed several testing parameters of the AMBT method for a locally sourced, siliceous river gravel. The testing parameters studied were the normality of the NaOH solution, storage temperature, aggregate grading, and the alkali content of the cement. The following conclusions were made from this research:

- The original development of the AMBT was optimized through testing six different quartz or silica bearing aggregates. Maximum expansion was observed in five of the six aggregates at the conditions that have been prescribed in ASTM C1260. It is reported that this test method typically results in the highest expansion values, thus a worst case scenario. Results from AMBT on a locally available, siliceous river sand from this study indicated that conditions in ASTM C1260 may not always be the worst case scenario, thus the potential for misclassifying aggregates in either the innocuous or potentially deleterious category.
- A pessimum effect was observed in the AMBT, with a maximum expansion at 14-days in 0.75 N NaOH solution. At 28-days, maximum expansion was measured when mortar bars were tested in a 0.5 N NaOH solution. This result may indicate a pessimum effect may be present when this aggregate is tested in the CPT as well. Results from the CPT indicated this aggregate is innocuous, but had a high degree of reactivity when tested in the AMBT, particularly at lower normalities of NaOH. Therefore, due to these variations in aggregate reactivity caused by alkali loading, a parametric study on several aggregate types should be done in order to determine the appropriate alkali loading in both the AMBT and CPT to ensure maximum expansion.
- Modifications to the AMBT resulted in only two mixtures that passed both the 14-day AMBT and 1-year CPT expansion limits. Significant expansions were observed in all normalities of NaOH tested, aggregate preparation, and in temperatures 60 °C or higher. This indicated that the aggressiveness of the test method may result in an incorrect classification of an aggregate when compared to the more reliable CPT.
- However, further testing on both the AMBT and the CPT should be done in order to assure an accurate assessment of an aggregate and correlation between the test methods is confirmed. While it is typically reported that the CPT is the most accurate laboratory

test method [23], there has been recent research indicating aggregates that pass the CPT have shown significant expansions in both field performance and long-term testing on field exposure sites [27].

## C.6. References

[1] J.H. Ideker, B.L. East, K.J. Folliard, M.D.A. Thomas, B. Fournier, The current state of the accelerated concrete prism test, Cement and Concrete Research, 40 (2010) 550-555.

[2] A. Shayan, Effects of NaOH and NaCl solutions and temperature on the behavior of specimens subjected to accelerated AAR tests 1, Cement and Concrete Research, 28 (1998) 25-31.

[3] R.E. Oberholster, G. Davies, An accelerated method for testing the potential alkali reactivity of siliceous aggregates, Cement and Concrete Research, 16 (1986) 181-189.

[4] S. Chatterji, An accelerated method for the detection of alkali-aggregate reactivities of aggregates, Cement and Concrete Research, 8 (1978) 647-649.

[5] M. Kawamura, K. Takemoto, N. Terashima, Effect of sodium chloride and sodium hydroxide from the surrounding solution on alkali-silica reaction in mortars containing fly ash, Magazine of Concrete Research, 40 (1988) 143-151.

[6] J.H.P. van Aardt, S. Visser, Progress report part 2: CSIR research report BRR 577, 1982.

[7] R.N. Swamy, M.M.A. Asali, New test methods for alkali-silica reaction, Proceedings of the 7th International Conference on Alkali Aggregate Reactivity, Ottowa, 1986, 324-329.

[8] ASTM C1260, ASTM C1260-14: Standard test method for potential alkali reactivity of aggregates (mortar-bar method), West Conshocken, Pennsylvania, ASTM International, 2014.

[9] M. de Grosbois, E. Fontaine, Evaluation of the potential alkali-reactivity of concrete aggregates: Performance of testing methods and a producer's point of view, Proceedings of the 11th International Conference on Alkali-Aggregate Reactivity, Quebec, 2000, 267-276.

[10] B. Fournier, M.A. Bérubé, Alkali-aggregate research in concrete: A review of basic concepts and engineering implications, Canadian Journal of Civil Engineering, 27 (2000) 212-225.

[11] D. Lu, B. Fournier, P.E. Grattan-Bellew, Evaluation of accelerated test methods for determining alkali-silica reactivity of concrete aggregates, Cement and Concrete Composites, 28 (2006) 546-554.

[12] J.H. Ideker, A.F. Bentivegna, K.J. Folliard, M.C.G. Juenger, Do current laboratory test methods accurately predict alkali-silica reactivity?, ACI Materials Journal, 109 (2012) 395-402.

[13] C.S. Shon, D.G. Zollinger, S.L. Sarkar, Evaluation of modified ASTM C1260 accelerated mortar bar test for alkali–silica reactivity, Cement and Concrete Research, 32 (2002) 1981-1987.

[14] ASTM C150, ASTM C150m-12: Standard specification for portland cement, West Conshocken, Pennsylvania, ASTM International, 2012.

[15] R.D. Hooton, New aggregate alkali-reactivity test methods, report MAT-91-14, November 1991, Ontario Ministry of Transportation.

[16] R.D. Hooton, C.A. Rogers, Development of the NBRI rapid mortar bar test leading to its use in North America, Ninth International Conference on AAR in Concrete, London, 1992, 461-467.

[17] ASTM C1293, ASTM C1293-08b: Standard test method for determination of length change of concrete due to alkali-silica reaction, West Conshocken, Pennsylvania, ASTM International, 2008.

[18] ASTM C289, ASTM C289-07: Standard test method for potential alkali-silica reactivity of aggregates (chemical method), West Conshocken, Pennsylvania, ASTM International, 2007.

[19] ASTM C305, ASTM C305-14: Standard practice for mechanical mixing of hydraulic cement pastes and mortars of plastic consistency, West Conshocken, Pennsylvania, ASTM International, 2014.

[20] ASTM D75, ASTM D75-13: Standard practice for sampling aggregates, West Conshocken, Pennsylvania, ASTM International, 2012.

[21] M.D.A. Thomas, B. Fournier, K.J. Folliard, J.H. Ideker, M. Shehata, M., Test methods for evaluating preventive measures for controlling expansion due to alkali–silica reaction in concrete, Cement and Concrete Research, 36 (2006) 1842-1856.

[22] ASTM C1293, ASTM C1293 - 08b: Standard test method for determination of length change of concrete due to alkali-silica reaction, West Conshocken, Pennsylvania, ASTM International, 2015.

[23] J.H. Ideker, A.F. Bentivegna, K.J. Folliard, M.C.G Juenger, Do current laboratory test methods accurately predict alkali-silica reactivity?, ACI Materials Journal, 109 (2012) 395-402.

[24] D.W. Hobbs, Alkali-silica reaction in concrete. London, Thomas Telford Ltd. 1988.

[25] S. Diamond, N. Thaulow, A study of expansion due to alkali-silica reaction as conditioned by the grain size of the reactive aggregate, Cement and Concrete Research, 4 (1974) 591-607.

[26] D.E. Stanton, The expansion of concrete through reaction between cement and aggregate. American Society of Civil Engineers, 66 (1940) 1781-1811.

[27] J.H. Ideker, T. Drimalas, A.F. Bentivegna, K.J. Folliard, B. Fournier, M.D.A. Thomas, R.D. Hooton, C.A. Rogers, The importance of outdoor exposure site testing, 14th International Conference on Alakali-Aggregate Reaction, Austin, TX, 2012, 10.